Electronic Thesis and Dissertation Repository

10-3-2024 10:30 AM

Coordination Chemistry and Reactivity of Biaryl Pd Phosphine 1-Azaallyl Complexes

Leslie S.G. Kelley, *The University of Western Ontario*

Supervisor: Blacquiere, Johanna M., *The University of Western Ontario*
A thesis submitted in partial fulfillment of the requirements for the Master of Science degree in Chemistry
© Leslie S.G. Kelley 2024

Follow this and additional works at: https://ir.lib.uwo.ca/etd

Part of the Inorganic Chemistry Commons

Recommended Citation

Abstract

Structurally responsive ligands (SRLs) are dynamic ligands that can alter coordination mode with a metal centre, to stimulate fundamental organometallic reactions in several catalytic cycles. These dynamic ligand coordination changes can also enable access to unique reaction mechanisms and challenging reaction steps. The Blacquiere group previously synthesized a phosphine 1-azaallyl (P^AzA) ligand, in which the 1-azaallyl (1-AzA) moiety reversibly switches between multiple coordination modes. The previous phenyl-linked P^AzA ligand led to a variety of coordination modes with Pd, however the κ^1-P;η^3-NCC mode was never observed. In pursuit of accessing the κ^1-P;η^3-NCC coordination mode, a new P^AzA ligand bearing a biaryl backbone was targeted. The coordination chemistry of the biaryl P^AzA ligand with Pd was explored. Small molecule reactivity with the biaryl Pd P^AzA complex was examined, with the goal of inducing a change in ligand coordination mode. Preliminary catalysis with the biaryl Pd P^AzA complex was assessed.

Keywords

Summary for Lay Audience

Catalysis is the process of increasing the speed of a chemical reaction with the participation of a compound known as a catalyst. During a chemical reaction, catalysts must be reactive under the given conditions to facilitate a specific chemical transformation. However, there are no permanent chemical changes made to the catalyst itself and the catalyst is not consumed. Transition metal complexes operate as very effective catalysts for several organic reactions. Transition metal catalysts are made up of two components, the metal centre and the ligands bound to the metal centre. The ligands bound to the metal centre of a transition metal catalyst can significantly influence the reactivity of the catalyst. Certain ligand families can dynamically change how they bind to a metal centre, based on the reaction environmental demands, to facilitate and stabilize difficult chemical transformations. This work focuses on expanding a new ligand family, with this dynamic metal binding ability, known as the phosphine 1-azaallyl (P^AzA) ligand family. Specifically, the synthesis of a new P^AzA ligand was conducted and how the P^AzA ligand binds to Pd was analyzed. Several reactivity experiments were investigated with this new Pd P^AzA complex, with the goal of inducing a change in how the P^AzA ligand binds to Pd. The reactivity experiments highlighted the dynamic binding ability of the P^AzA ligand, which suggested that the Pd P^AzA complex could promote desirable chemical transformations. Preliminary catalysis was attempted to try to exploit the unique reactivity of the Pd P^AzA complex.

Co-Authorship Statement

All chapters were written by Leslie Kelley and edited by Johanna Blacquiere.

All experimental work was conducted by Leslie Kelley except for:

- Kyle Jackman contributed to some of the initial experimental procedure for the biaryl phosphine 1-azaallyl ligand. Kyle Jackman also grew crystals of compound **1b** and collected some of the IR and mass spec data for **H[L2]**, **K[L2]**, Pd complex **1**, and Pd complex **2** in Chapter 2.

- Paul Boyle collected and solved the X-ray crystallographic data for Pd complex **1b** in Chapter 2.

- T.K. Sham, Zhiqiang Wang, Yipeng Sun, and Jiaban Xu conducted the EXAFS and XANES experiments and analysis for Pd complex **2** in Chapter 2.

- Viktor Staroverov conducted the energy calculations for Pd complex **2** in Chapter 2.

Acknowledgements

Table of Contents

List of Tables

List of Figures

List of Schemes

List of Abbreviations

1-AzA	1-Azaallyl
Å	Angstrom
˚C	Degrees Celsius
β	Beta
δ	Delta
ε	Epsilon
κ	Kappa
λ	Lambda
η	Eta
π	Pi
σ	Sigma
μ	Upsilon
Ar	Aryl
ATR	Attenuated Total Reflectance
cm	centimetres
COD	1,5-Cyclooctadiene
COSY	Correlation Spectroscopy
Cp*	1,2,3,4,5-Pentamethylcyclopentadienyl
DAP	2,6-Diacetylpyridine
DCM	Dichloromethane
DMAP	4-Dimethylaminopyridine
DMF	Dimethylformamide
^{DMP}DAB	*N,N'*-Bis(2,6-Dimethylphenyl)diazabutadiene
DMSO	Dimethyl Sulfoxide
dppf	1,1'-Bis (diphenylphosphino)ferrocene
Equiv	Equivalents
Et	Ethyl
EXAFS	Extended X-ray Absorption Fine Structure

fac	facial
FTIR	Fourier Transform Infrared Spectroscopy
G	Gibbs Free Energy
h	hours
HMBC	Heteronuclear Multiple Bond Correlation
HMDS	Hexamethyldisilylamide
HOMO	Highest Occupied Molecular Orbital
HSQC	Heteronuclear Single Quantum Coherence
Hz	Hertz
IR	Infrared
K	Kelvin
LUMO	Lowest Unoccupied Molecular Orbital
M	Molarity
MA	Methyl Acrylate
MAH	Maleic Anhydride
MALDI	Matrix Assisted Laser Desorption/Ionization
max	Maximum
Me	Methyl
mer	meridional
mg	Milligrams
MHz	Megahertz
min	Minutes
mL	Millilitres
mmol	Millimoles
mol	Moles
MS	Mass Spectrometry
nm	nanometres
NMR	Nuclear Magnetic Resonance
p	para
P^A	Phosphine Amine

P^AzA	Phosphine 1-Azaallyl
P^I	Phosphine Imine
Ph	Phenyl
ppm	Parts Per Million
Prod	Product
py	Pyridine
rt	Room Temperature
s	Seconds
SRL	Structurally Responsive Ligand
Sub	Substrate
τ	Geometry Index
TBA	Tetrabutylammonium
^{t}Bu	tert-Butyl
TEY	Total Electron Yield
Tf	Triflate
THF	Tetrahydrofuran
UV-Vis	Ultraviolet-Visible Spectroscopy
VT	Variable Temperature
XANES	X-ray Absorption Near Edge Structure

List of Complexes

A[L2]
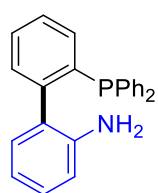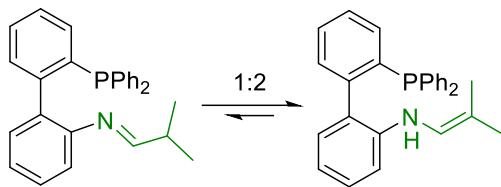
H[L2]a   1:2   **H[L2]b**
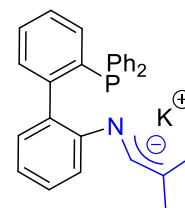
K[L2]
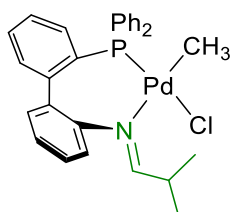
1a
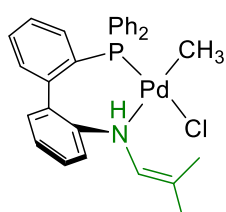
1b
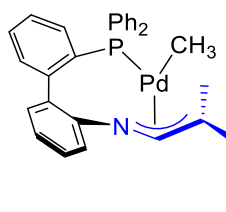
2
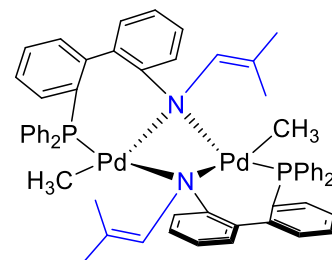
2'
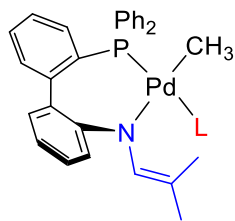
3

3a: L = py
3b: L = PPh₃
3c: L = P(ᵗBu)₃
3d: L = P(NEt₂)₃
3e: L = PEt₃
3f: L= CN⁻
3g: L = H₂O

3c-5

2-3   + PR₃

4

5

6

7a

7b

8a   **8b**   **8c**   **8d**

9a   **9b**   **9c**   **9d**

9e   **10**   **11**

12a   **12b**   **13**   **14**

xviii
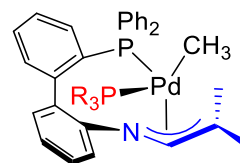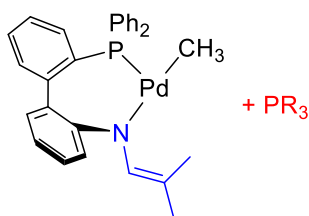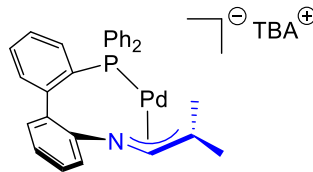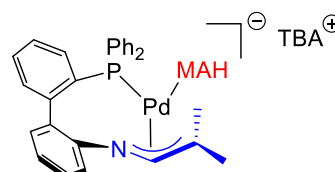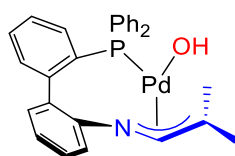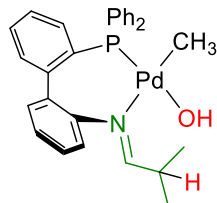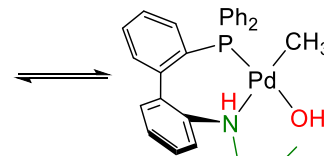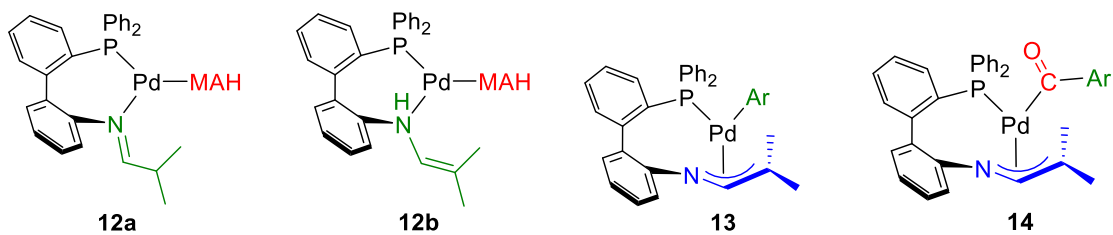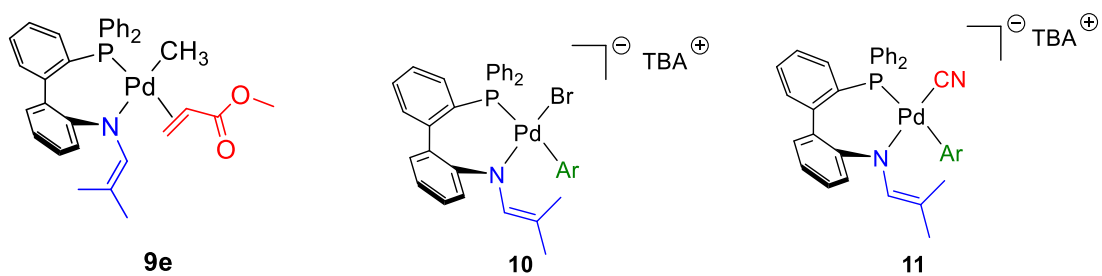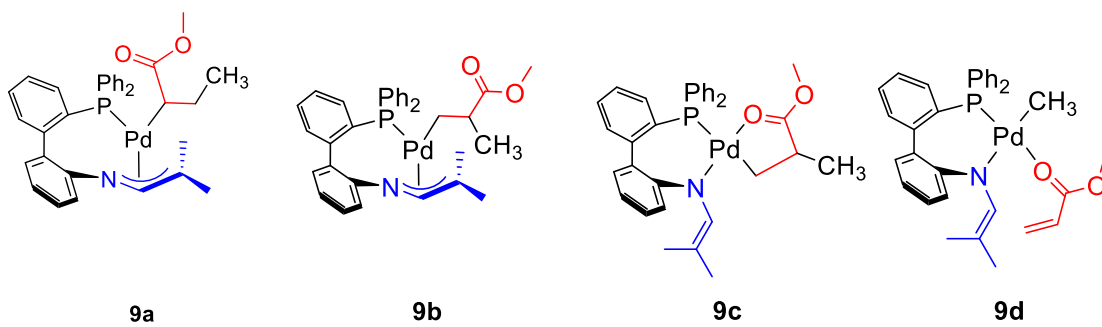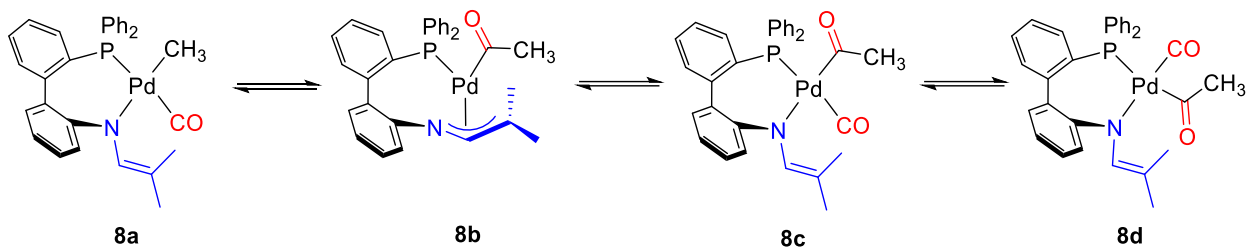
1.0 Introduction

1.1 Homogeneous Catalysis

Homogeneous transition metal catalysts play an important role in several chemical transformations because they lower the energy barrier of chemical transformations without being consumed, which subsequently accelerates the rate of these chemical processes.[1-4] Homogeneous catalysts are specifically advantageous because they operate through well-defined mechanisms, which can allow for relatively straightforward catalyst alteration, and therefore exceptional selectivity towards a distinct product can be achieved.[5] Improved design and selectivity of homogeneous catalysts is typically due to the influence of ligands coordinated to the metal centre, as different ligands enable unique reactivity and selectivity at the metal centre.[6-10]

1.2 Small Molecule Activation

Small molecule activation is the process of triggering and transforming small molecules such as N_2, H_2, O_2, CO, CO_2, H_2O, SO_2, N_2O, CH_4, and NH_3 that are readily abundant in natural geochemical cycles and several metabolic processes in organisms into value-added products, which have significant applications in biology, medicine, industrial catalysis, and environmental protection.[11-13] Small molecule activation/transformation requires a kinetically or thermodynamically unfavoured step such as breaking or forming chemical bonds to alter the molecule's reactivity.[13,14] Small molecule activation is a fundamental step in several catalytic transformations so the ability to efficiently activate small molecules catalytically is of high interest.[13,15] One strategy to improve catalytic small molecule activation involves utilizing catalyst design by fine-tuning the steric and electronic profiles of supporting ligands to enhance catalytic performance.[12, 16-19]

1.3 Hemilabile Ligands in Catalysis

Hemilabile ligands have been exploited in catalysis because they can open coordination sites for catalyst activation and stabilize reactive transition metal centres throughout the duration of a reaction.[20,21] Hemilabile ligands have been successfully utilized in a variety of catalytic reactions including hydrogenation, carbonylation, hydroformylation, polymerization, isomerization, cycloaddition, allylation, and epoxidation.[20] Hemilabile ligands are polydentate chelates that contain at least two different types of bonding groups, where at least one group strongly coordinates to the metal centre while at least one other group is labile or weakly bonding.[20,22] Although all hemilabile ligands have similar properties with regards to bonding groups, they operate and self-tune within three different mechanisms.[20,23] The first type of hemilabile ligand involves spontaneous opening of the chelate bond and often occurs when the metal centre has variable coordination numbers.[20,23] For example, the cationic Ni complex **A** reversibly shifts between coordination numbers five and four (**A** and **A'** respectively), the NEt$_2$ donor (highlighted in blue, Scheme 1.1) spontaneously dissociates and recoordinates at the Ni metal centre.[23]
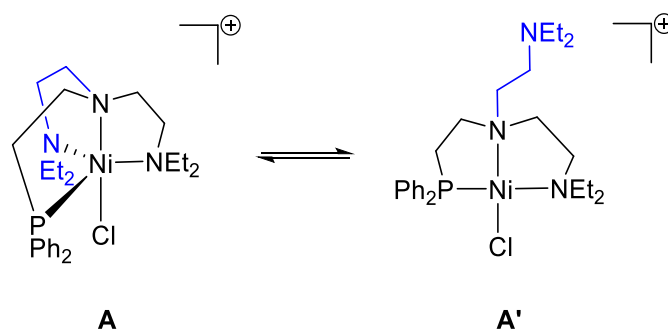
Scheme 1.1. Spontaneous opening of the NEt$_2$ chelate bond on a cationic Ni complex.[23]

The second type of hemilabile ligand involves intramolecular ligand competition between donor groups through a fluxional ligand exchange process.[20,23] This most commonly occurs when a hemilabile ligand has at least two weak donor groups coordinated to a single transition metal centre.[20] In the [ReCl(CO)$_3$(DAP)] complex **B**, coordination exchange of the pendant acyl groups occurs readily at

room temperature (Scheme 1.2).[24] The coordination number at the metal centre remains the same in both complex **B** and **B′.**
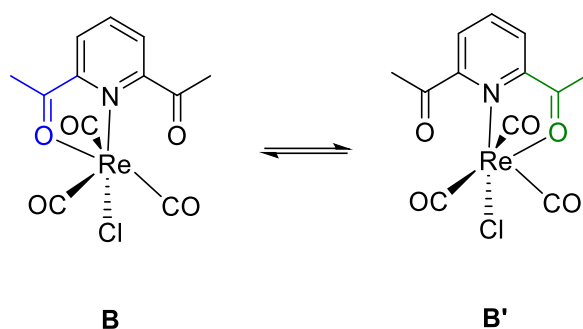
Scheme 1.2. Fluxional ligand exchange between the pendant acyl groups.[24]

The third type of hemilabile ligand involves displacement of a donor group by an exogenous ligand that coordinates to the metal centre, such as CO coordination.[20,23] In a CO atmosphere Rh complex **C** reversibly binds to CO, which displaces the methoxy ligand highlighted in blue to form complex **C′** (Scheme 1.3).[25] In the absence of a CO atmosphere the methoxy ligand highlighted in blue recoordinates to complex **C′** to form complex **C.**[25]
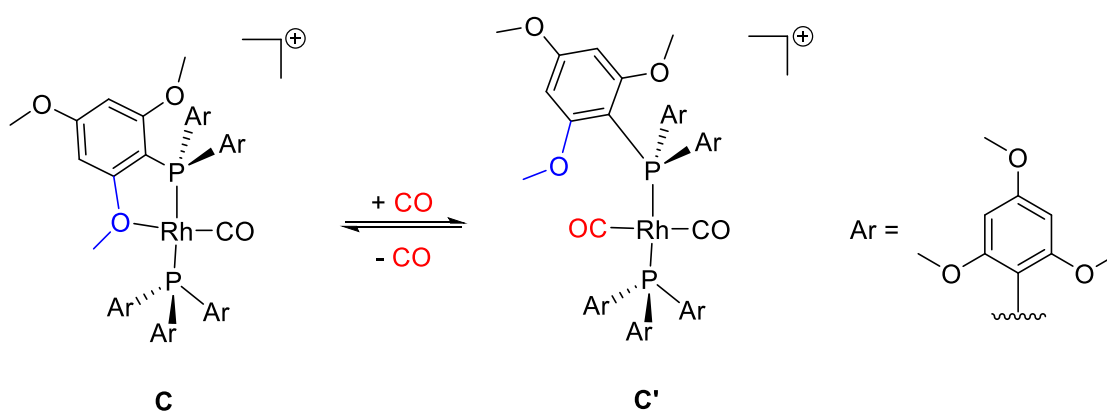
Scheme 1.3. Reversible coordination between CO and a hemilabile methoxy ligand in a Rh(I) complex.[25]

Hemilabile P,O and P,N ligands have been especially prominent in catalysis because they offer a pathway to achieve product selectivity, by their non-symmetric nature, while maintaining the ability to activate and stabilize a reactive transition metal centre.[26-28] P,O and P,N ligands coordinate to

transition metal centres as either neutral LL type ligands or anionic LX type ligands. In late transition metal complexes bearing hemilabile P,O and P,N ligands, the phosphine donor groups are statically anchored to the metal centre and provide stability to a low coordinate metal centre, with their strong σ-donor ability.[26,27] The oxygen and nitrogen donor groups can reversibly dissociate from the metal centre to generate an open coordination site on the metal.[26,27] P,O and P,N ligands can also introduce an element of regiocontrol through the *trans* effect, since nucleophilic substitution will be directed to the position on the metal centre *trans* to the phosphine donor group.[26,27] Bidentate P,O and P,N ligands coordinate to transition metal centres with three distinct coordination modes, which include κ^1-P coordination, κ^2-P,O/N coordination, or μ-(κ^2-P,O/N) coordination (Figure 1.1).[23]
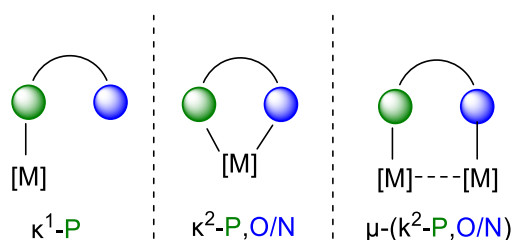
Figure 1.1. Coordination modes of bidentate P,O and P,N ligands.[23]

     Keim and coworkers synthesized a cationic Pd η^3-allyl complex **D** bearing a hemilabile P,O ligand, that demonstrates how reversible dissociation and recoordination of the oxygen donor group can drive reactivity (Scheme 1.4). When **D** was exposed to ethylene at –30 ˚C, the O-donor of the phosphino-ester readily dissociates from Pd, which allows ethylene coordination to form complex **E**. Upon warming, the hemilabile O-donor recoordinates to Pd, which drives allyl ethylene coupling through insertion of ethylene into the Pd-allyl bond to form complex **F**.[29]
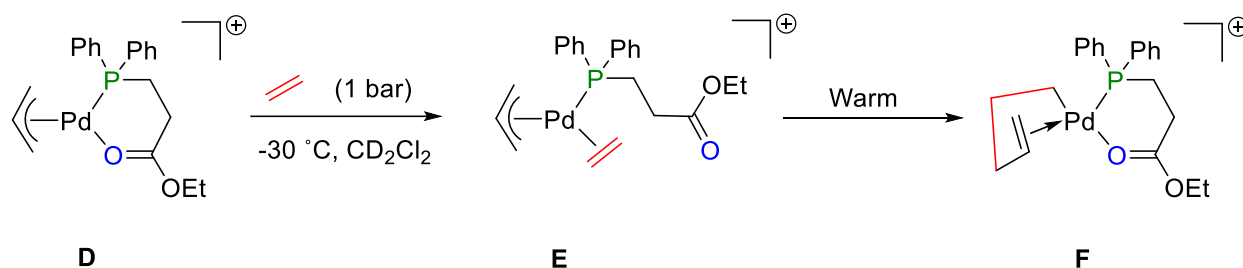
Scheme 1.4. Ligand enabled ethylene insertion into a Pd-allyl bond.[29]

Homogeneous gold catalysis has become a promising area of research due to the functional group tolerance and biocompatibility of gold.[30-33] Gold catalysis often proceeds through a Au(I)/Au(III) redox catalytic cycle, which has been traditionally challenging, due to the instability of the Au(I) intermediate species.[30-33] A popular method to overcome this challenge, has been to incorporate a hemilabile P,N ligand onto the catalyst, to stabilize both the Au(I) and Au(III) catalytic intermediates through changes in ligand coordination mode.[30] In the following gold catalyzed Heck reaction, the P,N ligand is initially coordinated κ^1-P to allow for the favourable linear geometry of the Au(I) complex **G** (Scheme 1.5).[30] Upon oxidative addition of the aryl iodide the N coordinates to the metal centre in a κ^2-P,N coordination mode to stabilize the favourable square planar geometry of the Au(III) intermediate **I**.[30] From here styrene coordinates to Au(III), and complex **J** undergoes 1,2-migratory insertion to form complex **K**.[30] β-H elimination then occurs to produce intermediate **M**, where reductive elimination then occurs along with N ligand dissociation to regenerate Au(I) complex **H**, with the P,N ligand coordinated κ^1-P.[30]
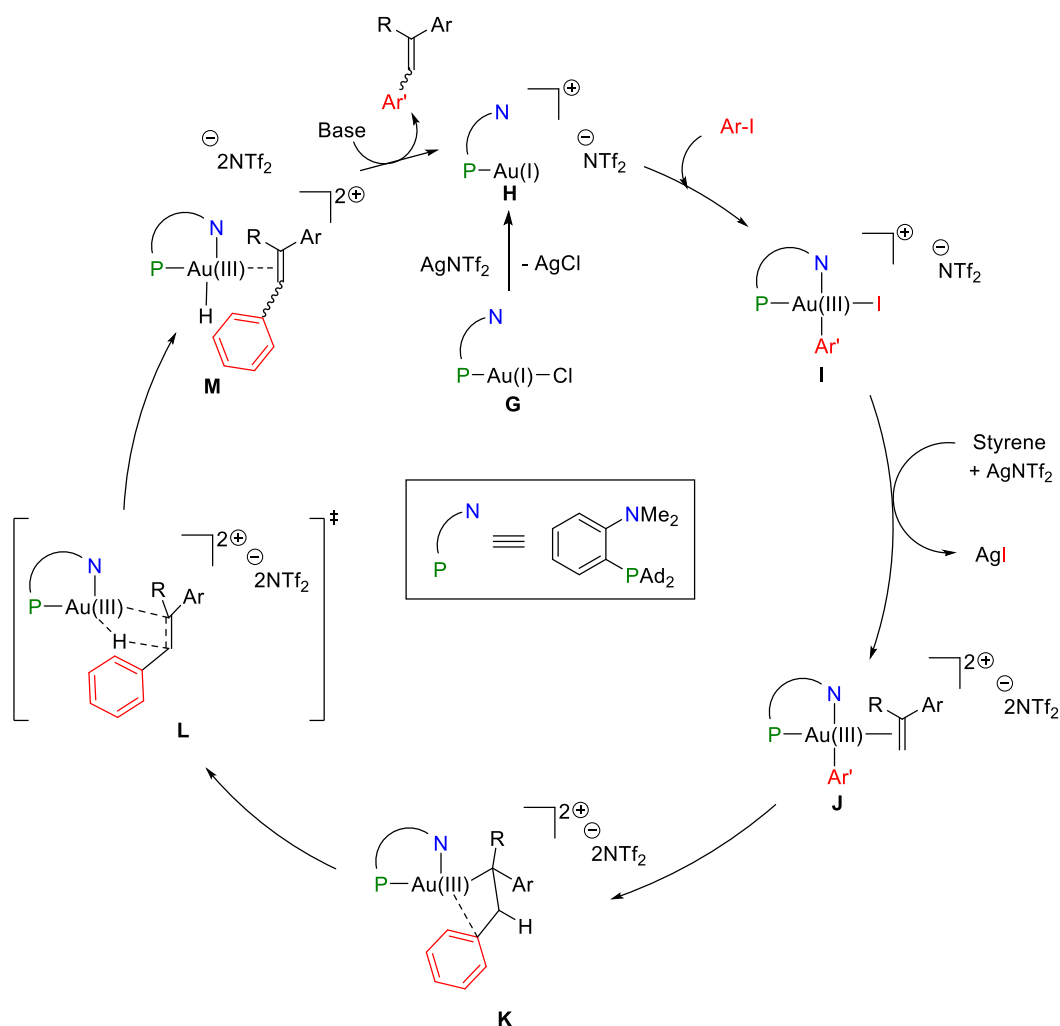
Scheme 1.5. Ligand stabilization of Au(I) and Au(III) intermediates, which enables gold catalyzed Heck reactions of aryl iodides with styrenes.[30]

1.4 Structurally Responsive Ligands

Supporting ligands that dynamically adapt their coordination mode to environmental and structural demands of a reactive intermediate are known as structurally responsive ligands (SRLs).[21] SRLs are valuable in catalysis because they have the capability to provide both an open coordination site for substrate binding and stabilization for a low coordinate intermediate species. Hemilabile ligands are the simplest version of SRLs as they undergo reversible changes in denticity through chelate dissociation/coordination, however SRLs incorporate much more versatile ligand classes that can shapeshift between several coordination modes through reversible changes in denticity, hapticity, or a

combination of both. In each coordination mode, the ligand induces different electronic and steric properties on the metal centre and therefore, the reactivity of the metal changes for each coordination mode.[34]

The 2-azaallyl ligand is a SRL that can shift between a diverse range of coordination modes. In Co(I) complex **N**, the 2-azaallyl ligand highlighted in blue is coordinated to the metal centre with an η^3-CNC coordination mode (Scheme 1.6).[35] When **N** undergoes a reaction with CO the geometry, coordination number, and oxidation state at the metal centre does not change, but the coordination mode of the 2-azaallyl ligand highlighted in blue shifts from η^3-CNC to κ^1-C.[35] The strong π-backbonding interaction between CO and the Co(I) metal centre in complex **O**, induces the change in 2-azaallyl ligand coordination mode, to prevent a change in geometry, coordination number, and oxidation state at the metal centre. [35]
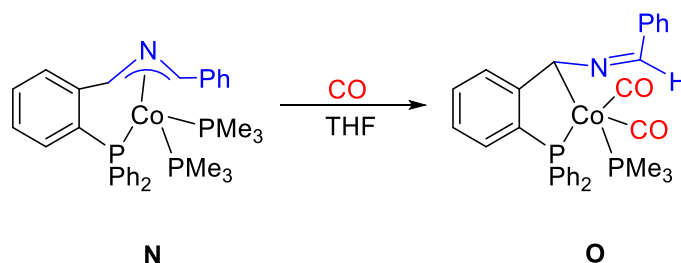
Scheme 1.6. Addition of CO to Co(I) complex **N** to synthesize complex **O**.[35]

1.5 Coordination Chemistry of 1-Azaallyl Ligands

The 1-azaallyl (1-AzA) group is an SRL that is isoelectronic and structurally similar to many common SRLs used in catalysis, including allyls, amidinates, carboxylates, and pyridonates, however it remains underused in catalysis.[36] The 1-AzA moiety has a delocalized negative charge through the π-system that is across the NCC backbone, which allows it to adopt a diverse range of coordination modes with transition metals (Figure 1.2).[34,37,38] In monometallic complexes the 1-AzA moiety will coordinate

in either a κ^1-N, κ^2-NC, or η^3-NCC mode and in bimetallic complexes the 1-AzA will coordinate in either a μ-N, μ-(κ^1-N; κ^1-C), or μ-(κ^1-N;η^2-CC) mode.
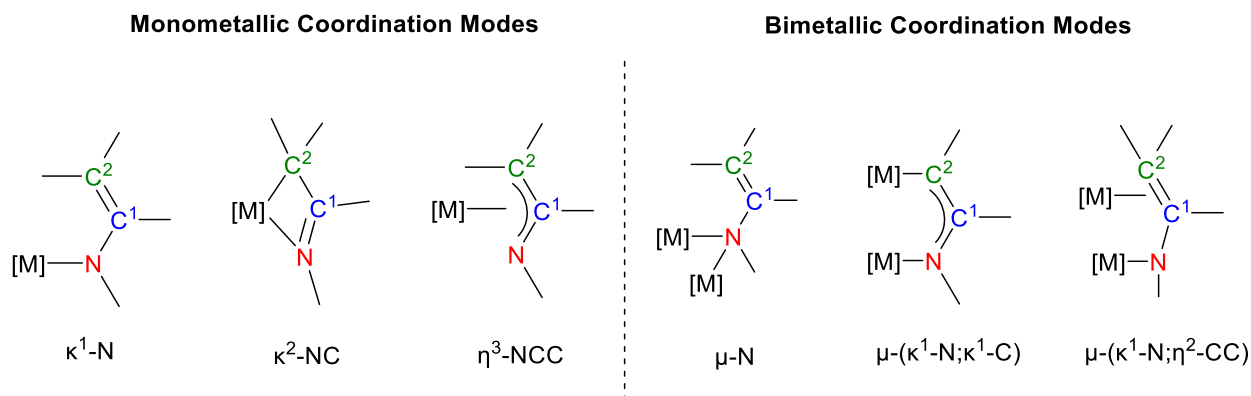
Figure 1.2. General depiction of the diverse range of monometallic (left) and bimetallic (right) coordination modes of the 1-AzA group.

The ability of the 1-AzA ligand to exhibit and switch between various coordination modes is influenced by the identity of the metal, the metal oxidation state, ligand substituents, and solvent.[21] Sterically large 1-AzA ligands on monometallic metal(II) complexes (M = group 2, 13, 14) favour κ^2-NC coordination in low coordinate environments, whereas in the presence of a strong neutral donor such as THF or pyridine, 1-AzA ligands on monometallic complexes favour the κ^1-N coordination mode.[37] One important isomerization in monometallic complexes is the shift between the η^3-NCC mode, which occupies two coordination sites and the κ^1-N mode, which occupies one coordination site (Scheme 1.7).[39] In a catalytic cycle, the 1-AzA moiety could isomerize from the η^3-NCC mode to the κ^1-N mode, which would open a coordination site on the metal centre for substrate binding. Conversely, isomerization from the κ^1-N mode to the η^3-NCC mode could occur after product release or any step that opens a coordination site to stabilize the low coordinate intermediate.
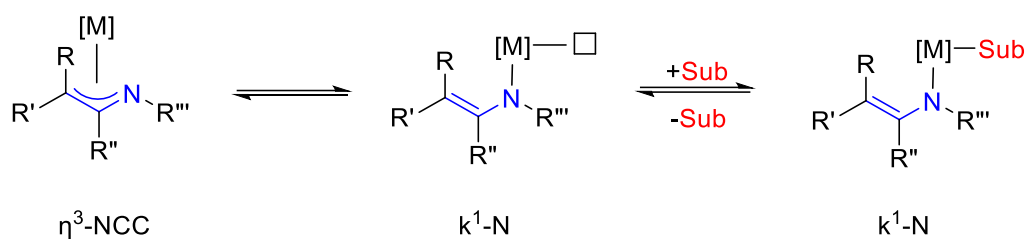
Scheme 1.7. Hypothesized mechanism of η^3-NCC to κ^1-N 1-AzA isomerization, which opens a coordination site for substrate binding.

Lappert and coworkers conducted variable temperature (VT) NMR spectroscopy experiments with a Ni(II) 1-AzA complex **P**, where the 1-AzA ligand is coordinated with an η^3-NCC coordination mode (Scheme1.8).[34] The NMR data revealed a dynamic process between complex **P** and isomers **P′**, **P″** , **P‴**, **P⁗**, which is proposed to be an interconversion between η^3-NCC and κ^1-N coordination modes.[34] The interconversion from the η^3-NCC coordination mode to the κ^1-N coordination mode creates a vacant coordination site at the Ni metal centre (complexes **P′** and **P‴**), where substrate coordination could occur.[34]
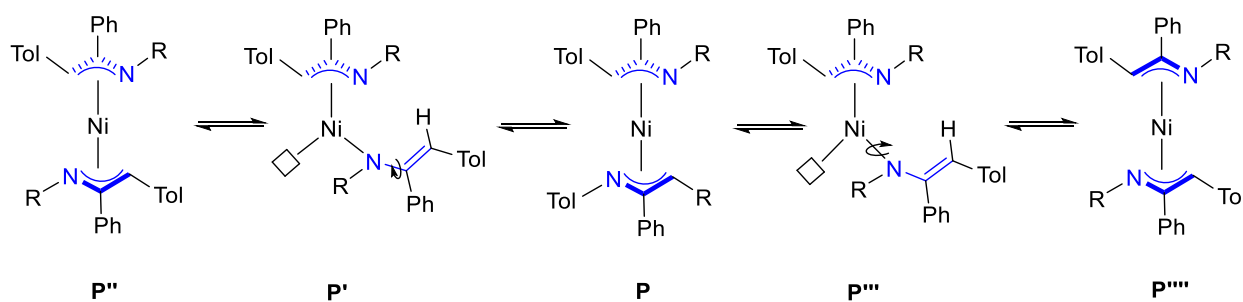
Scheme 1.8. Proposed η^3-NCC to κ^1-N isomerization between isomers of Ni complex **P**. R = Si(CH$_3$)$_3$.[34] The box in structures **P′** and **P‴** represents an open coordination site.

1.6 Phosphine 1-Azaallyl Ligands

In 2017, the Blacquiere group synthesized the first phosphine 1-azaallyl (P^AzA) ligand, **K[L1]** by deprotonation of a phosphine imine (P^I) precursor, **H[L1]** (Scheme 1.9).[40] The P^AzA ligand has a rigid aryl ring between a phosphine donor, that anchors the ligand to the metal centre, and a 1-AzA

moiety. The phosphine donor is statically coordinated to the metal centre and the 1-AzA moiety has the capacity to change coordination modes to induce reactivity at the metal centre.[38,40] Coordination of **L1** to Ru and Pd metal centres was initially conducted to investigate the various coordination modes of the P^AzA ligand at each metal.
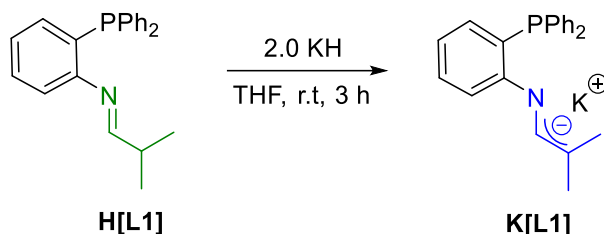
Scheme 1.9. Synthesis of the ligand **K[L1]** from the **H[L1]** precursor.[40]

Coordination of **H[L1]** to [RuCl$_2$(PPh$_3$)$_2$] resulted in the formation of the phosphine imine (P^I) complex **Q**, and subsequent deprotonation by Li[HMDS] in the presence of pyridine afforded Ru P^AzA complex **R**, where the P^AzA ligand is bound with a κ^2-PN coordination mode (Scheme 1.10).[40] Coordinating pyridine to the Ru metal centre provides stability to Ru P^AzA complex **R**, since deprotonation of **Q** with Li[HMDS] in non coordinating solvents was attempted, but a mixture of products was produced.[40] There were no other coordination modes observed of the P^AzA ligand in this complex besides the κ^2-PN coordination mode.[40]
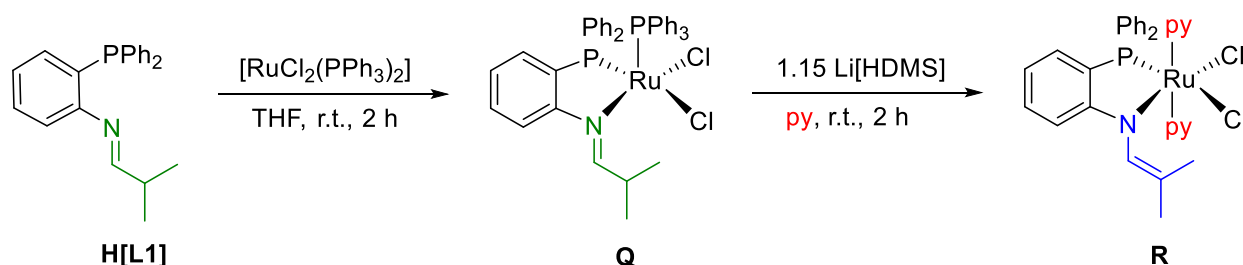
Scheme 1.10. Synthesis of Ru complex **R**, where only a κ^2-PN P^AzA coordination mode was observed.

Coordination of **K[L1]** to [PdCl(CH$_3$)(COD)] resulted in the formation of a Pd(II) P^AzA dimer **S**, with κ^1-P;μ-N coordination of the P^AzA ligand (Scheme 1.11A).[38] Complex **S** readily underwent

a reaction with pyridine, resulting in cleavage of the dimer to afford **T**, accompanied by a change in

P^AzA coordination mode to κ^2-PN (Scheme 12A).[38] Thermolysis of **S** results in reductive elimination

of ethane, to give complexes **U** and **V** with μ-(κ^2-PN;η^2-CC) and κ^2-PN P^AzA coordination modes,

respectively (Scheme 1.11B).[38] The reactivity observed with Pd(II) dimer **S**, demonstrates the dynamic

coordination ability of the 1-AzA moiety in the P^AzA ligand.
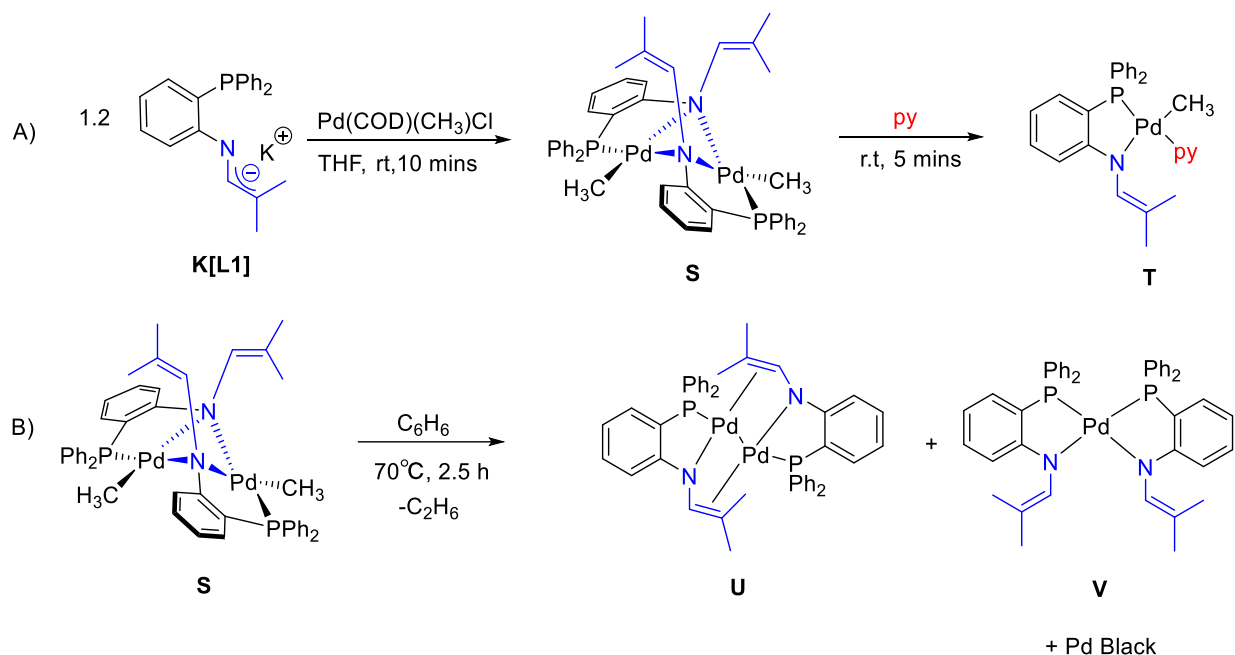
Scheme 1.11. A) Synthesis of the Pd(II) dimer **S** via coordination of ligand **K[L1]** to [PdCl(CH₃)(COD)].

Followed by a reaction with pyridine, forming **T**. B) Reductive elimination of ethane from **S** forming **U** and **V**.[38]

At this point in the investigation the κ^1-P;η^3-NCC coordination mode of the P^AzA ligand had

not been observed with a Pd complex and there had been no demonstration that the P^AzA ligand could

open a coordination site on a monometallic complex. Since Pd complexes usually exist with square

planar coordination geometry, **L1** is likely restricted by bite angle to coordinate in a κ^1-P;η^3-NCC

mode, as it would need to occupy three coordination sites on the Pd metal centre (Figure 1.3). In an

attempt to coordinate **L1** in a κ^1-P;η^3-NCC coordination mode a Ru metal complex precursor,

[RuCl(Cp*)(PPh₃)₂] was explored. Ru(II) complexes usually exist with octahedral geometry and with

this half sandwich precursor, the Cp* ligand would enforce **L1** to coordinate across three coordination sites that are facially disposed, with a smaller angle between them.

κ^1-P;η^3-NCC Coordination
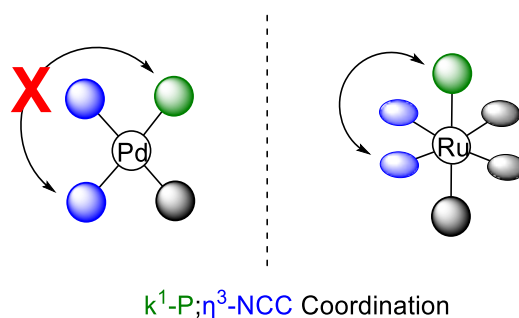
Figure 1.3. Proposed **L1** κ^1-P;η^3-NCC coordination on square planar Pd complexes with *mer* configuration and octahedral half sandwich Ru complexes with *fac* configuration.

Coordination of **H[L1]** to [RuCl(Cp*)(PPh$_3$)$_2$] resulted in the formation of phosphine imine complex **W** (Scheme 1.12A).[41] In the presence of Li[HMDS] and pyridine, the P^I ligand was deprotonated and a κ^2-PN coordination mode of the P^AzA ligand was observed in the Ru complex **X** (Scheme 1.12A).[41] Upon removal of pyridine from complex **X** a Ru P^AzA complex **Y** was isolated without a pyridine donor. The coordination mode of the P^AzA ligand in complex **Y** was indirectly detected through VT NMR spectroscopy, VT UV-Vis experiments, and evaluated through computations, to be an equilibrium between κ^2-PN and κ^1-P;η^3-NCC coordination modes (Scheme 1.12B).[41] This confirms that **L1** is capable of coordinating with a κ^1-P;η^3-NCC coordination mode when not restricted by bite angle and that it can reversibly switch between coordination modes.

A)

H[L1] → [RuCl(Cp*)(PPh₃)₂] / THF, 80 °C, 3 h → **W** → 2.0 Li[HMDS] / 2:1 C₆H₆/py / rt, 1 h → **X**

B)

X → Vac / -py → **Y** ⇌ **Y'**
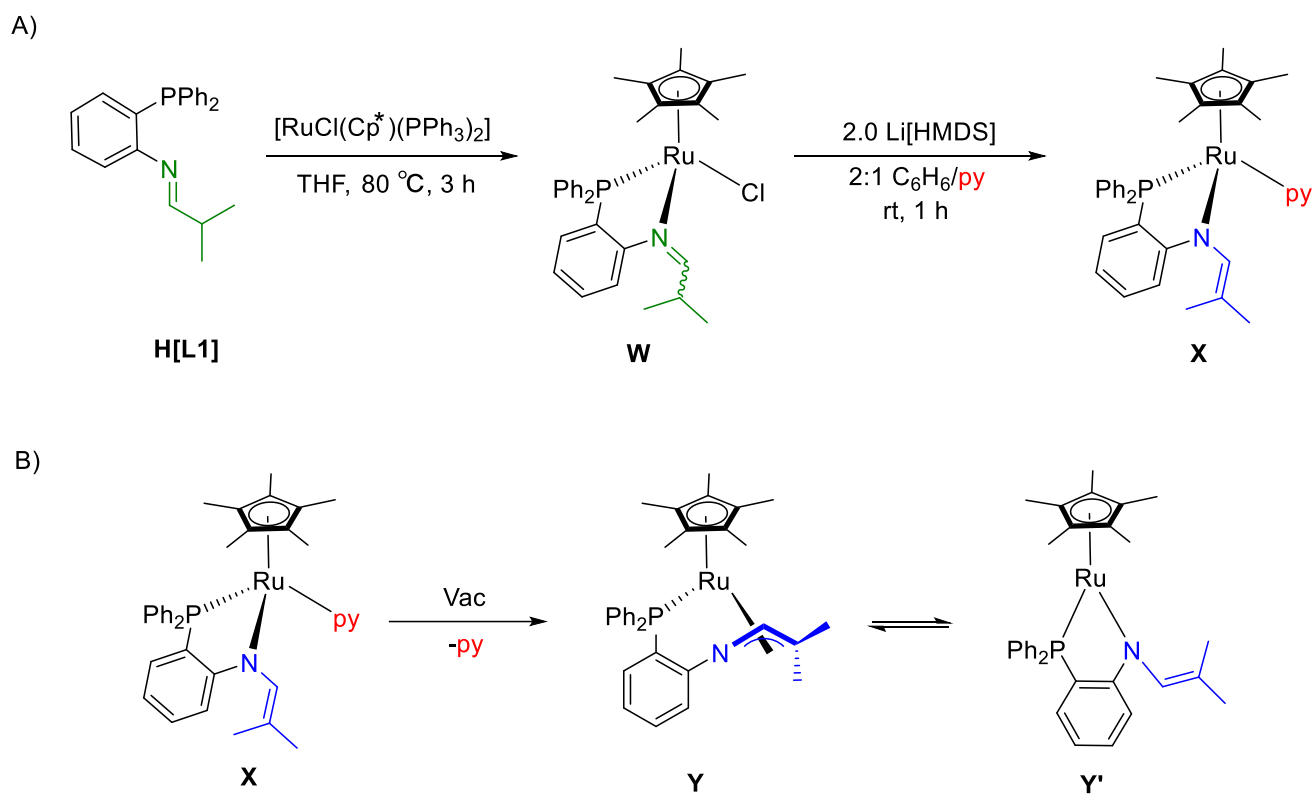
Scheme 1.12. A) Coordination of **H[L1]** to [RuCl(Cp*)(PPh₃)₂] followed by deprotonation of **W** to give pyridine adduct **X**.[41] B) Removal of pyridine to give an equilibrium of Ru complexes **Y** and **Y'**.[41]

1.7 Scope of Thesis

Herein, the synthesis of Pd P^AzA complexes with a new P^AzA ligand **K[L2]** bearing a biaryl backbone will be reported (Figure 1.4). Compared to the 1,2-disubstituted aryl backbone of **K[L1]**, the biaryl backbone increases distance between the heteroatoms, which may increase the P-Pd-N bite angle, potentially resulting in the accessibility and observation of the κ^1-P;η^3-NCC coordination mode.
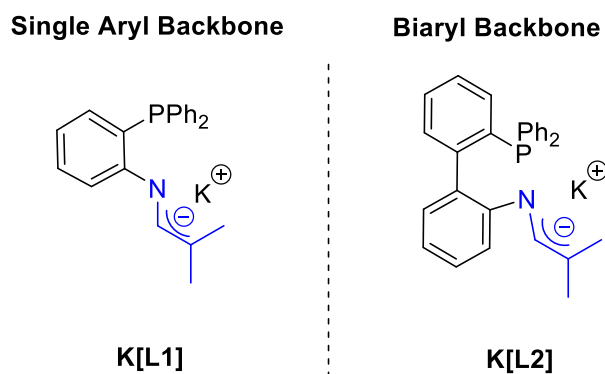
Figure 1.4. P^AzA ligands **K[L1]** and **K[L2]**.

Chapter 2 will cover the synthesis of the biaryl P^I ligand **H[L2]** and the biaryl P^AzA ligand **K[L2]**, as well as the synthesis of Pd complexes bearing either **H[L2]** or **K[L2]**. In a catalytic cycle, the ligand change in coordination mode from κ^1-P;η^3-NCC to κ^2-PN could allow substrate coordination and the ligand change in coordination mode from κ^2-PN to κ^1-P;η^3-NCC could stabilize a low coordinate intermediate, which would create a pathway for catalysis to occur, therefore, Chapter 3 will cover an investigation into the reactivity of the Pd P^AzA complex with a biaryl backbone. Reactivity with pyridine, tertiary phosphines, cyanide, water, carbon monoxide, and methyl acrylate will be investigated, with the hope of inducing a change in **L2** coordination mode on the Pd metal centre. Chapter 4 will cover the preliminary examination of the Pd P^AzA complex as a catalyst for the polymerization, oligomerization, isomerization, cyanation, and carbonylation.

2.0 Synthesis and Characterization of Biaryl Pd Phosphine 1-Azaallyl Complexes

2.1 Ligand Synthesis

The target biaryl P^AzA ligand synthesis was a three-step process that begins with the synthesis of a biaryl phosphine amine precursor and then the synthesis of a biaryl phosphine imine precursor. From here, the target biaryl P^AzA ligand can be synthesized.

2.1.1 Phosphine Amine Synthesis (A[L2])

The synthesis of the known phosphine amine (P^A) precursor **A[L2]** was performed following a literature procedure.[42] Suzuki cross coupling was achieved between 2-bromophenyldiphenylphosphine and 2-aminophenylboronic acid using Pd(dppf)Cl$_2$ as the catalyst (Scheme 2.1). The product was purified by silica gel column chromatography, affording **A[L2]** as a yellow solid with an average yield of 85%. The ^{31}P{^{1}H} NMR spectrum of the product in CDCl$_3$ displayed a singlet at $\delta_P = -13.0$, matching the value reported in the literature.[42] The ^{1}H NMR spectrum of the product in CDCl$_3$ displayed a diagnostic broad singlet at $\delta_H = 3.42$ that integrates to two, which is consistent with the amine protons reported in the literature. All the known aromatic proton signals were also identified in the ^{1}H NMR spectrum which confirmed the formation of **A[L2]**.
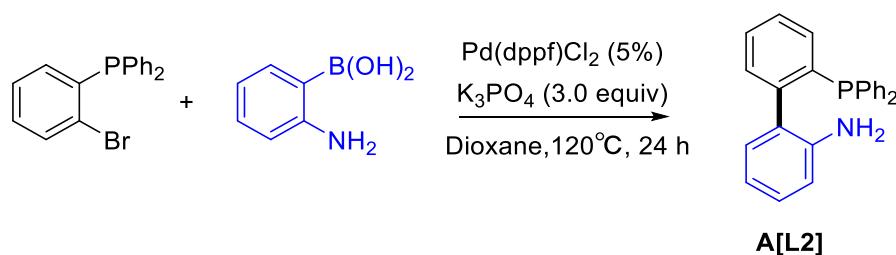
Scheme 2.1. Synthesis of **A[L2]** following literature procedures.[42]

2.1.2 Phosphine Imine Synthesis (H[L2])

The synthesis of the phosphine imine ligand **H[L2]** was performed following a similar procedure to that used for the related phosphine imine ligand **H[L1]**.[38] A condensation reaction between 2'-(diphenylphosphanyl)-[1,1'-biphenyl]-2-amine (**A[L2]**) and isobutyraldehyde was performed to afford **H[L2]**, as a white solid with an average yield of 87% (Scheme 2.2).
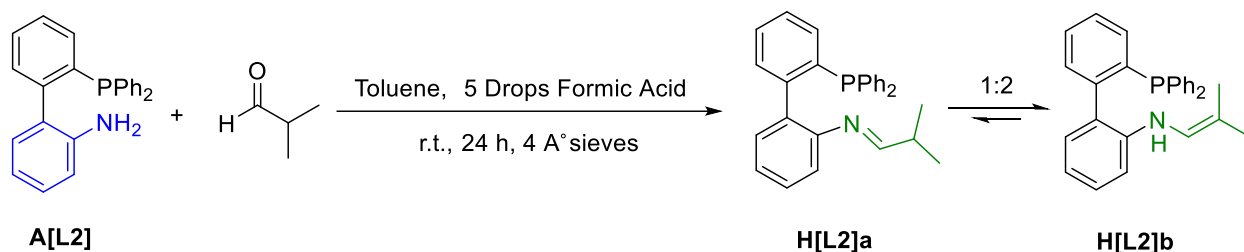
Scheme 2.2. Synthesis of the neutral phosphine 1-azaallyl ligand precursors, **H[L2]**.

The $^{31}P\{^{1}H\}$ NMR spectrum of the isolated product in $CDCl_3$ has two distinct singlets at δ_P = –12.4 and –13.3, in a 1:2 ratio, respectively. There are two sets of signals in the ^{1}H NMR spectrum that were key to assigning the structure of **H[L2]** (Figure 2.1). The first set of signals includes a doublet at δ_H = 7.55, a doublet of septets at δ_H = 2.39, and broad multiplets found in the ranges of δ_H = 7.47 – 7.09, 6.96 – 6.63, and 0.97 – 0.89. The doublet at δ_H = 7.55 integrates to one, which is consistent with an imine proton and the broad multipets found in the range of δ_H = 0.97 – 0.89 integrate to six, and are consistent with two equivalent methyl groups, which is consistent with the target imine structure **H[L2]a**. The second set of signals includes two singlets that each integrate to three at δ_H = 1.69 and 1.36 which suggests inequivalent methyl groups, two doublets that each integrate to one at δ_H = 6.08 and 4.94, and broad multiplets found in the ranges of δ_H = 7.47 – 7.09, and 6.96 – 6.63. The ^{1}H-^{13}C HSQC shows only the proton signal at δ_H = 6.08 is attached to C^1, which established the signal at δ_H = 4.94 as an N-H signal, confirming the structure of the enamine, **H[L2]b**.
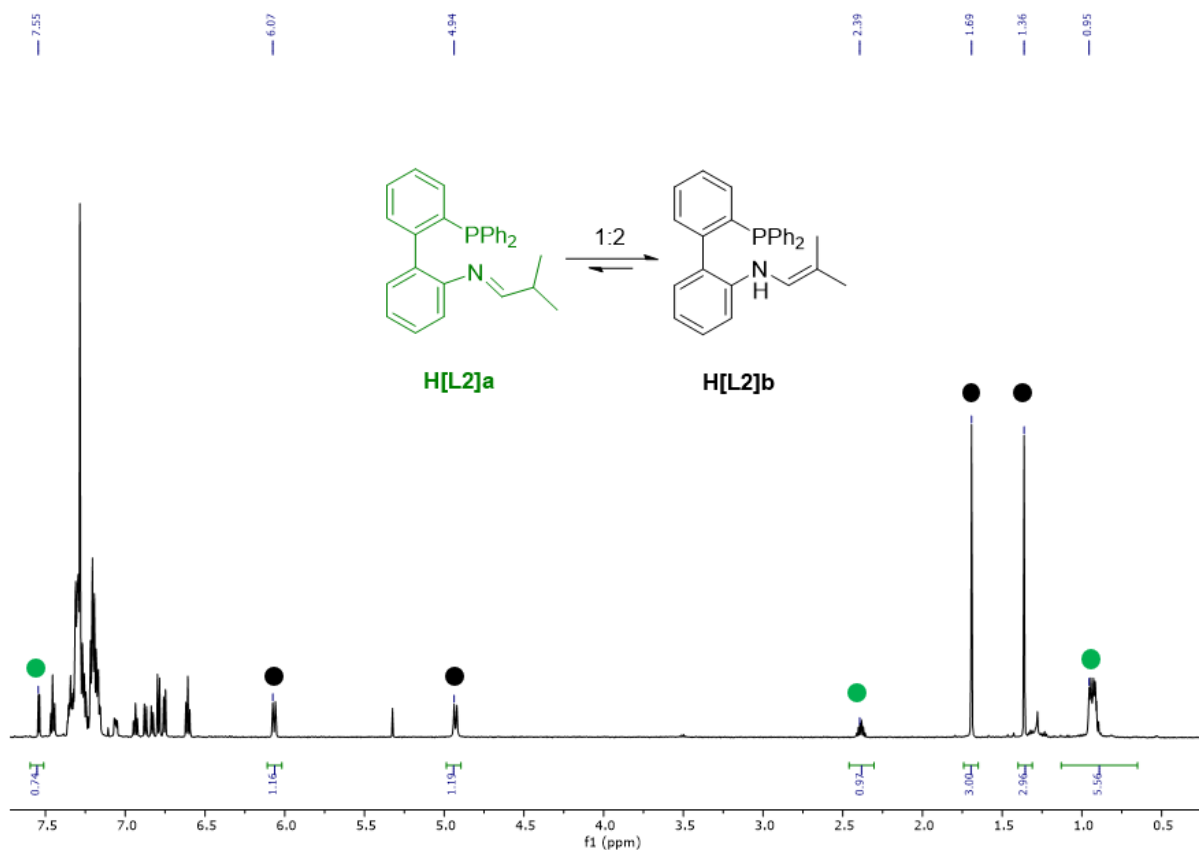
Figure 2.1. ^{1}H NMR spectrum (600 MHz, CDCl$_3$) of **H[L2]** in CDCl$_3$ which, provides spectroscopic evidence for the two tautomers, **H[L2]a** and **H[L2]b**.

For the previous phosphine imine ligand precursor **H[L1]**, only the imine structure was observed and there was no evidence of tautomerization between an imine an enamine structure. This is consistent with typical imine/enamine tautomerization as the imine is usually the favoured tautomer. The two ligands only differ by the ligand backbone, however in **H[L2]**, there is evidence of tautomerization, and the enamine structure is favoured. Since the two ligands only differ by backbone, the biaryl backbone may provide additional stabilization through hydrogen bonding to the enamine tautomer, which drives the equilibrium to favour this tautomer.[43]

2.1.3 Phosphine 1-Azaallyl Synthesis (K[L2])

Deprotonation of **H[L2]** with potassium hydride was performed to afford the phosphine 1-azaallyl ligand **K[L2]**, as an orange solid with an average yield of 60% (Scheme 2.3). The ^{31}P{^{1}H}

NMR spectrum of **K[L2]**, has one signal at $\delta_P = -13.6$, confirming deprotonation of both tautomers to give one species. The deprotonation of **H[L2]** is further confirmed with the ^{1}H NMR spectrum of **K[L2]**, where the loss of the C^2 proton signal from **H[L2]a** and the loss of the N-H proton signal from **H[L2]b** is observed. The proton loss from **H[L2]** confirms deprotonation and the formation of the phosphine 1-azaallyl ligand **K[L2]**.
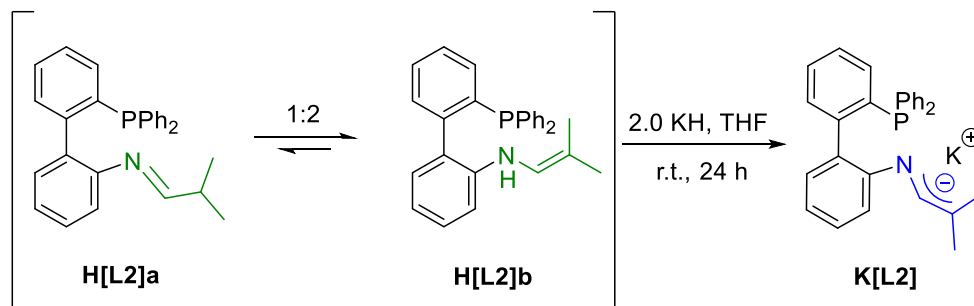
Scheme 2.3. Synthesis of phosphine 1-azaallyl ligand **K[L2]**.

2.2 Pd Complex Synthesis

The target biaryl Pd P^AzA complex synthesis involves either coordination of the neutral **H[L2]** ligand to Pd followed by deprotonation or deprotonation of **H[L2]** to form **K[L2]**, which is then followed by Pd coordination. In this section both synthetic routes will be discussed.

2.2.1 Pd Imine Complex (1) Synthesis

The tautomeric mixture of **H[L2]a** and **H[L2]b** was coordinated to [PdCl(CH$_3$)(COD)] affording complex **1** in 67% isolated yield (Scheme 2.4). The ^{31}P{^{1}H} NMR spectrum shows two distinct species based on two singlets at $\delta_P = 35.4$ and 36.2. The ^{1}H NMR spectrum has a doublet that integrates to one at $\delta_H = 6.32$ consistent with the imine proton on C^1 as well as a doublet of septets that integrates to one $\delta_H = 3.53$, and two doublets that integrate to three at $\delta_H = 1.19$ and 0.68 consistent with the isopropyl group on the target imine complex. The methyl protons at $\delta_H = 1.19$ and 0.68 are likely inequivalent due to hydrogen bonding with the adjacent chloro ligand. A second species is

observed by a doublet that integrates to one at $\delta_H = 6.32$ consistent with the C^1 proton and three broad

singlets at $\delta_H = 5.90$, 1.65 and 1.47 that integrate to one, three, and three, respectively. These proton

signals correspond to N-H and the methyl protons in **H[L2]b**. The diagnostic doublets for the Pd bound

methyls for the two species are observed at $\delta_H = 0.47$ and 0.61, with coupling constants of $^3J_{HP} = 3.4$

and 3.6 Hz, respectively. The small coupling constants are consistent with *cis* coordination of the

phosphine and methyls for both tautomeric products **1a** and **1b**.[44-46]
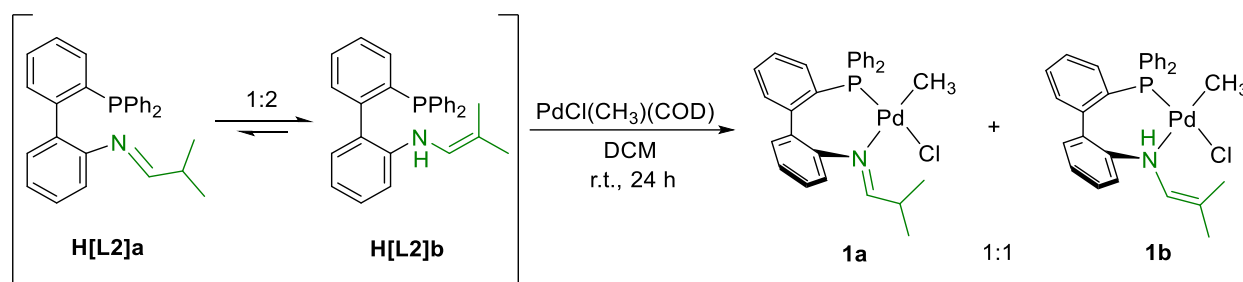
Scheme 2.4. Coordination of **H[L2]** to Pd to form **1a** and **1b**.

Crystals of **1** suitable for X-ray diffraction were grown via slow vapour diffusion of pentane

into a solution of **1** in a 9:1 mixture of toluene and DCM at –20 ˚C (Figure 2.2). X-Ray diffraction

revealed the crystallized structure was only the enamine tautomer **1b**, in which the palladium centre has

square planar geometry, with very minimal distortion according to the τ^4 value of 0.07.[5] The unit cell

included two complexes (A and B) that differed only by rotation of the C-C bond that connects the two

aryl groups in the biaryl backbone, so only the structural parameters of complex A will be discussed.
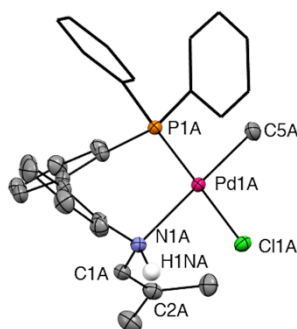
Figure 2.2. Displacement ellipsoid plot of complex **1b**. Ellipsoids are given at 50% probability level, except the phenyl substituents of the phosphine donor that are depicted as wireframe for clarity. H atoms (except H1NA) were omitted for clarity.

The enamine form of the P^AzA ligand is supported by the N(1A)–C(1A) and C(1A)–C(2A) bond lengths of 1.440(2) Å and 1.332(3) Å, respectively, which are characteristic of a C-N single bond and a C-C double bond. The crystal structure also confirms the *cis* orientation of the phosphine and methyl substituents. The P(1A)–Pd–N(1A) bite angle was determined to be 95.18˚(5), which is significantly wider than the angle of 78.48˚ found for the analogous complex with the monoaryl linked phosphine imine ligand **L1**.[38] Therefore, **H[L2]** imparts less conformational strain on the metal centre and may allow for isolation of a Pd phosphine 1-azaallyl species in which **L2** is coordinated in a κ^1-P;η^3-NCC mode.

A Pd phosphine 1-azaallyl complex was initially targeted by deprotonation of the tautomeric mixture of the Pd phosphine imine/enamine complexes **1a/1b**. However, the attempted deprotonation of **1a/1b** with potassium hydride did not result in clean conversion to a Pd phosphine 1-azaallyl complex. The ^{31}P{^{1}H} NMR spectrum had multiple unknown signals, which is indicative of multiple products or decomposition and the ^{1}H NMR spectrum also had many unknown and unexpected product signals. Therefore, the Pd phosphine 1-azaallyl complex was targeted through a different synthetic pathway involving the coordination of the deprotonated P^AzA ligand salt **K[L2]**.

2.2.2 Pd P^AzA Complex (2) Synthesis

K[L2] was coordinated to Pd through a reaction with [PdCl(CH$_3$)(COD)], to afford **2**, as an orange solid in 70% yield (Scheme 2.5). The ^{31}P{^{1}H} NMR spectrum of **2** has one singlet at δ_P = 25.7, which is consistent with ligand coordination to Pd. Due to the P^AzA ligand structure and the favourable square planar geometry for Pd there are two possible products from this reaction: dimeric complex **2′**, with the P^AzA ligand in a κ^1-P;μ-N mode, which is structurally similar to the analogous Pd(II) dimer **S**; or monomeric **2**, which has the P^AzA ligand with a κ^1-P;η^3-NCC coordination mode. Crystal growth was attempted but it is so far unsuccessful.
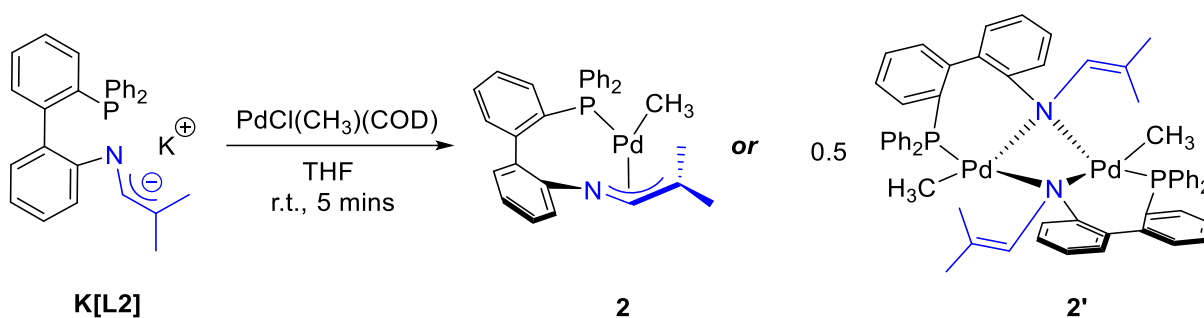
Scheme 2.5. Coordination of phosphine 1-azaallyl ligand **K[L2]** to Palladium to form **2** or **2′**.

A ^{1}H-^{31}P HMBC NMR spectrum of **2** was obtained to provide insight on the coordination mode of the phosphine 1-azaallyl ligand (Figure 2.3). If the P^AzA group is coordinated in the κ^1-P;μ-N mode, the 1-AzA methyl protons would be six bonds away from the phosphine, and no coupling of these protons to the phosphine donor would be expected. If the P^AzA group is coordinated in the κ^1-P;η^3-NCC mode, the 1-AzA methyl protons would be four bonds away from the phosphine, and coupling of these protons to the phosphine donor would be expected. The ^{1}H-^{31}P HMBC NMR spectrum displayed correlation between the 1-AzA methyl protons and the phosphine in **2**, which suggests the P^AzA group is coordinated in the κ^1-P;η^3-NCC mode. By comparison, no analogous correlation was observed in metal complexes that exhibited κ^1-P;μ-N (Pd(II) dimer **S**) or κ^2-PN (pyridine adduct **T**, Pd(II) monomeric **V**) coordination modes, where the 1-AzA methyl protons are six bonds from the

phosphine. However, a correlation was also observed in the Pd(I) dimer **U**, in which each Pd centre is coordinated κ^1-P to the phosphine of one ligand and η^2-CC to the alkene portion of the 1-AzA moiety of another ligand.[6] Thus, for **U** there are four bonds between the coupling methyl protons and phosphine. The observed correlation in the ^{1}H-^{31}P HMBC NMR spectrum of **2** suggests that **L2** is coordinated through an κ^1-P;η^3-NCC coordination mode.
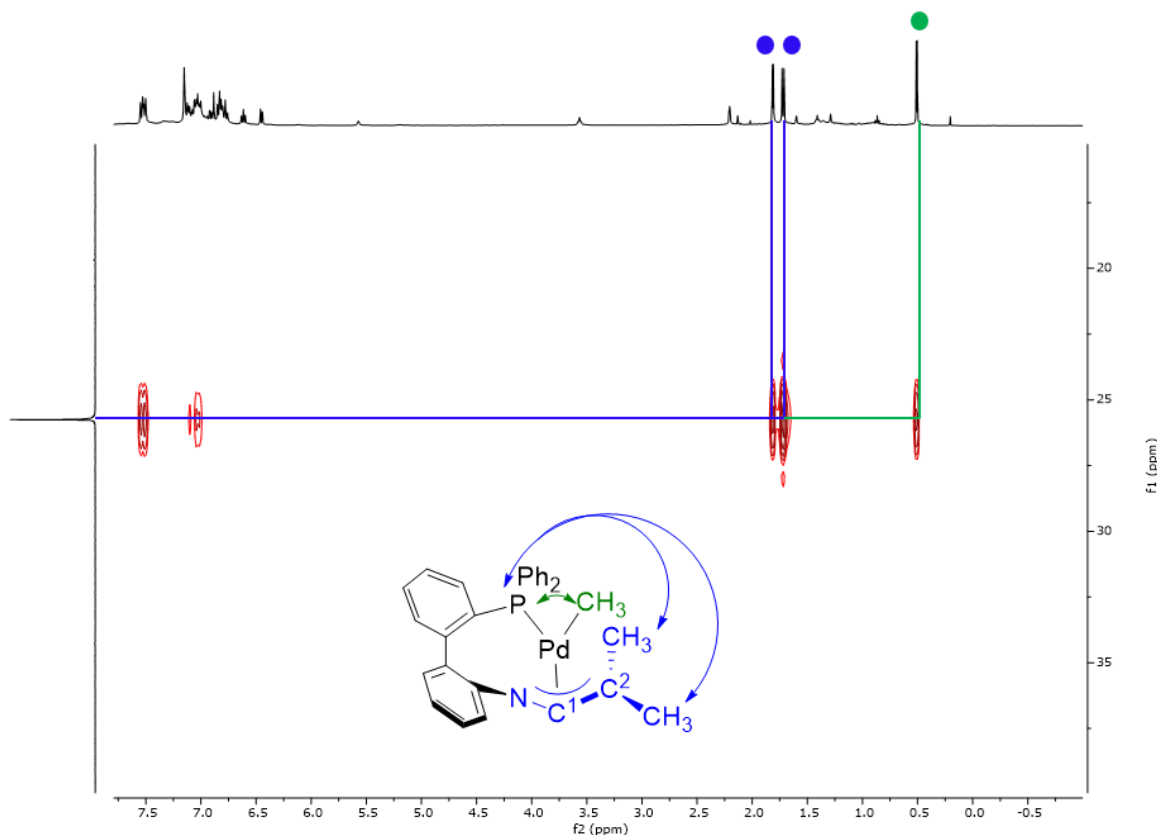
Figure 2.3. ^{1}H-^{31}P HMBC NMR spectrum (600 MHz, C$_6$D$_6$) of **2**.

The coordination mode of the ligand was further analyzed by comparing the chemical shifts of C^1 and C^2 to known η^3-NCC and μ-N 1-AzA complexes. Known η^3-NCC 1-AzA complexes have a C^1 signal within the range of δ_C = 151.9-184.9 and a C^2 signal within the range of δ_C = 42.0-64.5, while the analogous μ-N 1-AzA complex Pd(II) dimer **S** has a C^1 signal at δ_C = 141.5 and a C^2 at δ_C = 117.2.[1] For **2**, C^1 and C^2 are at δ_C = 129.4 and δ = 88.4, respectively, as determined by means of both ^{1}H-^{13}C HSQC and ^{1}H-^{13}C HMBC spectra. These chemical shifts are not consistent with known η^3-NCC or μ-

N 1-AzA complexes. Since Pd dimer **2′** is structurally analogous to Pd(II) dimer **S**, it would be expected that the ^{13}C NMR shifts for C^1 and C^2 would be very similar to those of **S**, however the observed C^1 and C^2 chemical shifts for **2** are both upfield in comparison to **S**. The ^{13}C NMR shift for C^1 is upfield and the ^{13}C NMR shift for C^2 is downfield of the expected range of an η^3-NCC coordination mode, however **L2** is a new ligand and the η^3-NCC range has yet to established for this ligand class. The main difference between **L2** and known η^3-NCC ligands is that **L2** contains a phosphine donor that coordinates to the metal centre along with the 1-AzA moiety. Known η^3-NCC ligands only coordinate to the metal centre through the 1-AzA moiety so the bidentate coordination of the P^AzA ligand **L2** may cause different η^3-NCC carbon shifts outside of the current known range.

In collaboration with the Sham group, a series of XANES and EXAFS experiments were conducted on known compounds Pd(II) dimer **S** and pyridine adduct **T** and unknown compound **2** to provide further insight on the structure and geometry of unknown compound **2**. Three experiments were conducted, Pd K-edge, Pd L$_3$-edge, and P K-edge. In all cases, the **S** and **T** displayed nearly identical features, while compound **2** displayed different features. In both compounds **S** and **T** the 1-AzA moiety coordinates to Pd through the nitrogen atom only, so it makes sense that the geometry around Pd is nearly identical. Specifically, the Pd L$_3$-edge experiment showed that both the whiteline (TEY) (Figure 2.4, Left) and energy threshold (TEY 1st Derivative) (Figure 2.4, Right) of **2** (PdP-E) shifts lower in energy compared to **S** (PdP-C) and **T** (PdP-B), which indicates either a lower oxidation state of Pd or a different coordination geometry of the 1-AzA moiety around Pd. The data suggests that in **2** the 1-AzA moiety is not coordinated solely through the nitrogen atom. It is proposed that **2** exists as a monometallic complex with ligand **L2** coordinated through a κ^1-P;η^3-NCC coordination mode.
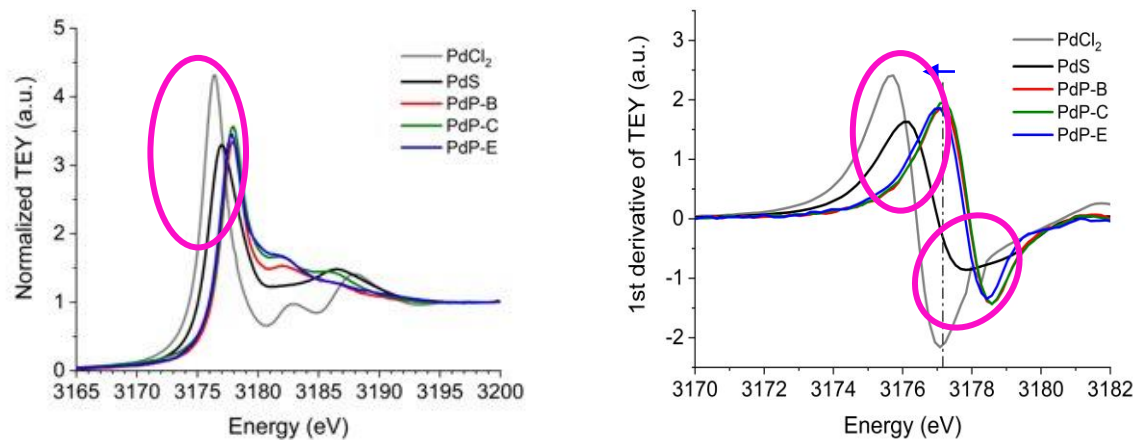
Figure 2.4. Left: XANES Pd L$_3$-edge TEY Plot. Right: XANES Pd L$_3$-edge TEY 1st Derivative Plot. PdCl$_2$ and PdS were included as known standards.

In collaboration with the Staroverov group, a series of DFT calculations were conducted to determine whether Pd complex **2** with **L2** coordinated κ^1-P;η^3-NCC or Pd complex **2′** with **L2** coordinated κ^1-P;μ-N was more energetically favourable. The results indicated that **2** is energetically more favourable than **2′**, and that **2** is predicted to absorb strongly near 400 nm with the HOMO-LUMO pair as the dominant contributor. UV-Vis spectra at various concentrations of **2** in toluene were acquired to determine a λ_{max} at 390 nm and an ε of 1706 M^{-1} cm^{-1} (Figure 2.5). The UV-Vis absorbance of **2** is consistent with the calculated absorbance of the monometallic κ^1-P;η^3-NCC Pd P^AzA complex.
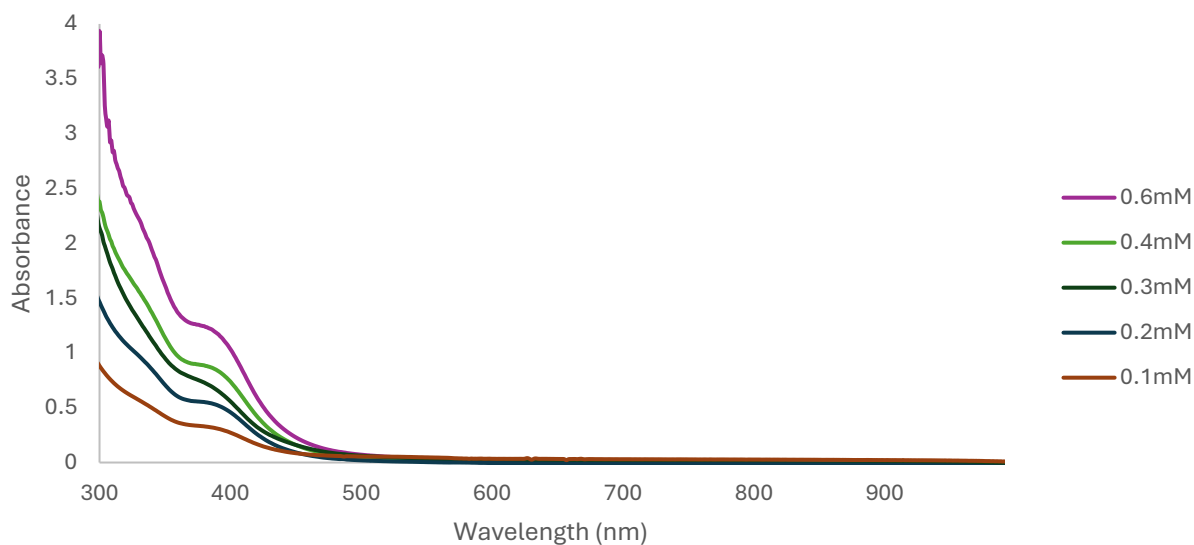
Figure 2.5. UV-Vis spectra of **2** at various concentrations in toluene.

In summary, the target biaryl P^AzA ligand was successfully synthesized and coordinated to Pd, to afford Pd complex **2**. Characterization of complex **2** was completed with a variety of methods including NMR spectroscopy, XANES, EXAFS, calculations, and UV-Vis spectroscopy. The coordination mode of complex **2** was identified with ^{1}H-^{31}P HMBC and ^{1}H-^{13}C HMBC NMR spectroscopy by comparing **2** to previously known palladium P^AzA complexes. The coordination mode of **2** was determined to be κ^1-P;η^3-NCC which supports the monometallic complex **2**. Further comparison experiments were conducted between complex **2** and known palladium P^AzA complexes that did not have κ^1-P;η^3-NCC coordination modes and analyzed with XANES and EXAFS spectroscopy. Complex **2** had very different features compared to the known complexes, which again supports the κ^1-P;η^3-NCC coordination mode. The energies of both complex **2** and complex **2′** were calculated, and complex **2** was energetically more favourable. The UV-Vis spectrum was also consistent with the calculated absorbance of complex **2**. Therefore the structure of complex **2** is the monometallic κ^1-P;η^3-NCC complex.

3.0 Reactivity of Biaryl Pd Phosphine 1-Azaallyl Complexes

3.1 Substitution Reactivity with Lewis Bases

The Blacquiere group previously found that Pd(II) dimer **S** with **L1** coordinated κ^1-P;μ-N readily reacts with pyridine to form a pyridine adduct **T** with **L1** coordinated κ^2-PN, which can be isolated and crystallized (Section 1.6). Similarly, the Blacquiere group found that Ru(II) P^AzA complex **Y**, dynamically interconverts between κ^1-P;η^3-NCC and κ^2-PN coordination modes of **L1** with the addition and removal of Lewis base donors pyridine and PPh3 (Section 1.6). Based on the observed reactivity with previous complexes it was hypothesized that Lewis base donors would bind to complex **2**, and induce a change in **L2** coordination mode from κ^1-P;η^3-NCC to κ^2-PN (Scheme 3.1).

3a: L = py
3b: L = PPh3
3c: L = P(^{t}Bu)3
3d: L = P(NEt2)3
3e: L = PEt3
3f: L = CN$^-$
3g: L = H2O

Proposed Product
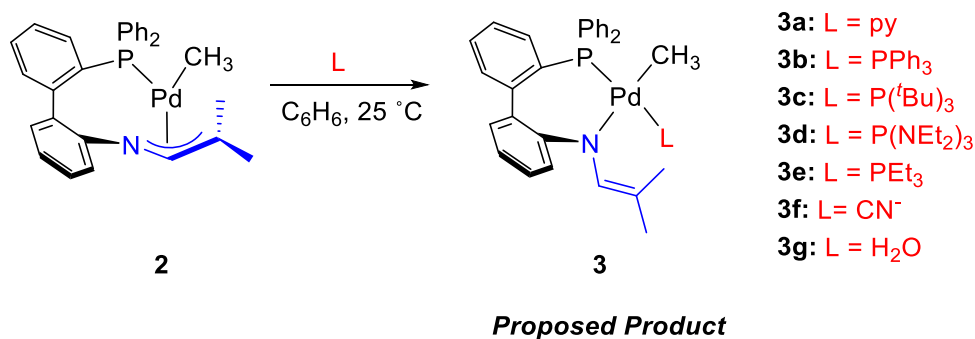
Scheme 3.1. Proposed substitution reactivity of **2** with Lewis base donors (L), which is hypothesized to induce P^AzA isomerization from κ^1-P;η^3-NCC to κ^2-PN to form complex **3**.

3.1.1 Reactivity with Pyridine

Coordination of pyridine to **2** was conducted, with one equivalent of pyridine added to a solution of **2** in C6H6 at room temperature (Scheme 3.2). There was an immediate colour change from the starting orange solution to a red solution. The reaction was analyzed with ^{31}P{^{1}H} NMR spectroscopy, and there was observed signal broadening compared to the spectra of the starting material, and no new signals formed (Figure 3.1). The broadening of the signal for the starting complex suggests that there is a

dynamic equilibrium occurring between **2**, pyridine, and **3a**. The **{2 + L}** labelling represents an unidentified equilibrium mixture between complex **2**, the Lewis base donor **L**, and **3**.
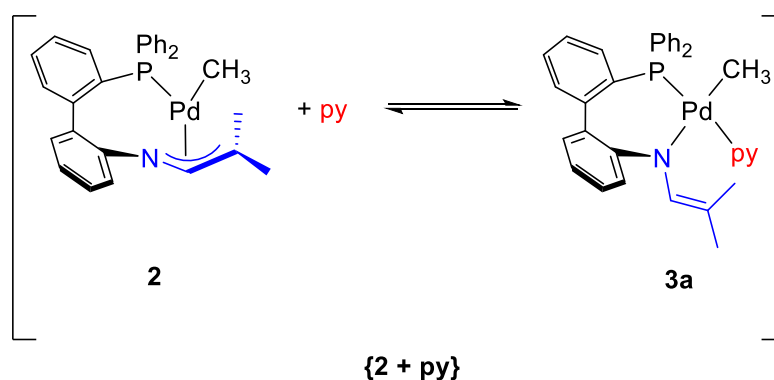
Scheme 3.2. Proposed reactivity with **2** and pyridine.

Since there is an equilibrium present between **2**, pyridine, and **3a** there is no isolable κ^2-PN pyridine adduct, unlike what is observed with the reaction between Pd(II) dimer **S** or Ru complex **W** and pyridine, which both gave stable pyridine adducts. In an attempt to push the proposed equilibrium towards the **3a** pyridine adduct, 1-20 equivalents of pyridine were titrated into a solution of **2** in C_6H_6 at room temperature (Figure 3.1). The only observed change in the $^{31}P\{^1H\}$ NMR spectrum was continued broadening of the signal for starting Pd complex **2**, which completely disappeared after the addition of four pyridine equivalents. This indicates that the proposed dynamic equilibrium between complex **2**, pyridine, and **3a** heavily favours complex **2** and free pyridine, in which the P^AzA ligand is coordinated through a κ^1-P;η^3-NCC coordination mode.
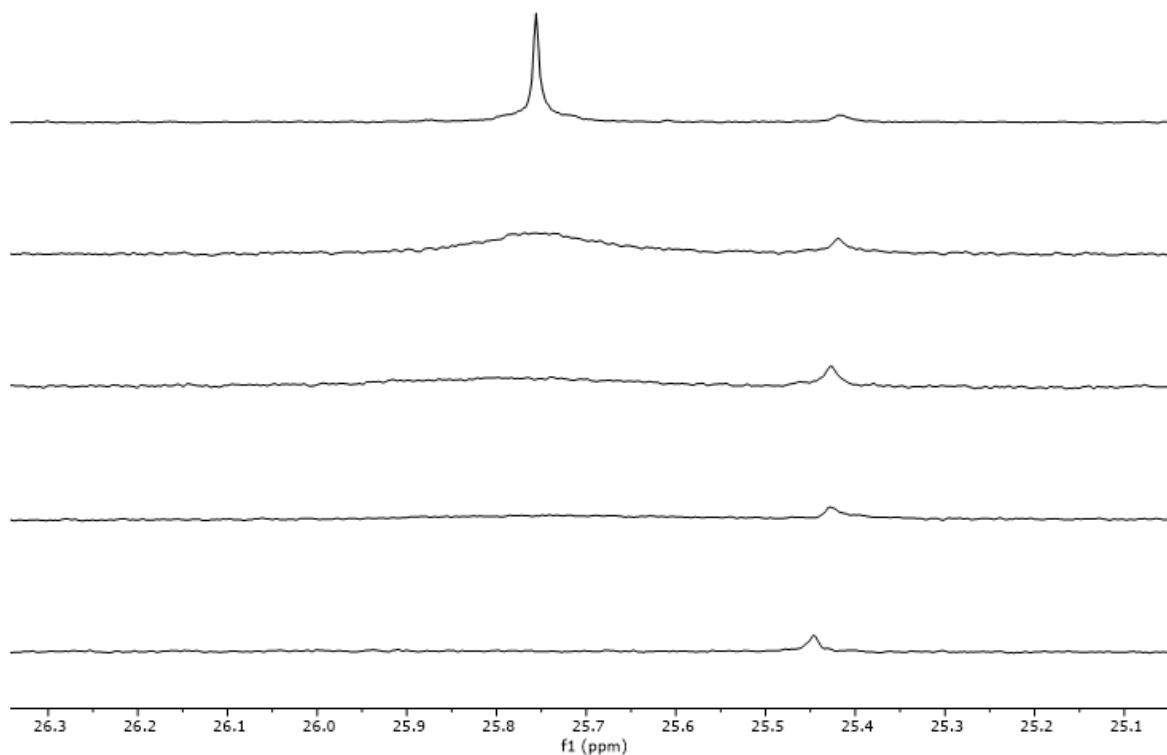
Figure 3.1. $^{31}P\{^1H\}$ NMR spectra (162 MHz, C_6D_6) stack plot of the reaction of **2** with pyridine. From top to bottom: **2**, **2** and one equivalent of pyridine, **2** and two equivalents of pyridine, **2** and four equivalents of pyridine, **2** and 20 equivalents of pyridine. The signal at $\delta_P = 25.4$ is an unidentified impurity.

Variable temperature (VT) NMR spectroscopy was conducted on the solution of complex **2** and 20 equivalents of pyridine to determine if it was feasible to *in situ* characterize the identity of the product **3a**, including the P^AzA coordination mode. *In situ* characterization of the product and the P^AzA coordination mode would be possible if the broad signal observed in the $^{31}P\{^1H\}$ NMR spectrum sharpens into two or more distinct signals at low temperature. The reaction was cooled from 25 ˚C down to –80 ˚C and analyzed at every 10 ˚C change in temperature by $^{31}P\{^1H\}$ NMR spectroscopy. There was no change in the $^{31}P\{^1H\}$ NMR spectroscopy which indicates that *in -situ* characterization of the P^AzA coordination mode is not possible (Figure B.1). Dissolution of **2** in py-d_5 also resulted in signal broadening in the ^1H NMR spectrum, so there was no ability to further characterize the proposed equilibrium products (Figure B.2).

To assess if the observed dynamics represent the proposed equilibrium, a reaction between a mixture of **2** and pyridine, and the Lewis acid $B(C_6F_5)_3$ was conducted to target regeneration of Pd complex **2**, and formation of the $B(C_6F_5)_3$ pyridine adduct (Scheme 3.3).
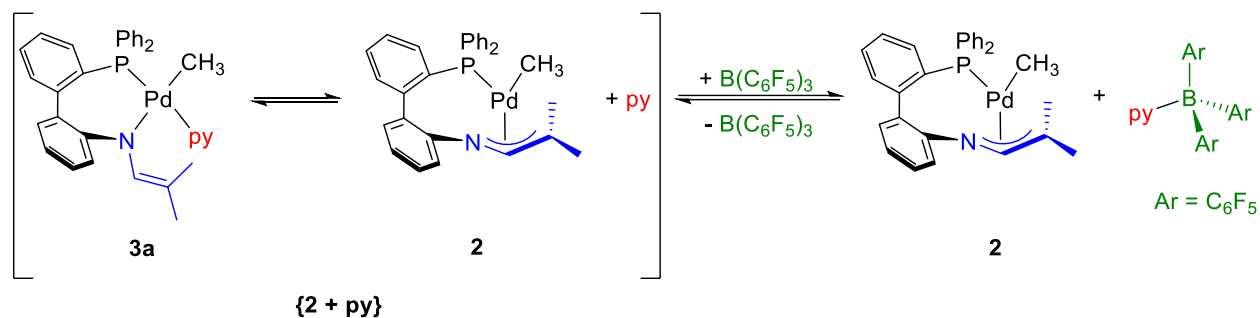
Scheme 3.3. Proposed reactivity with **{2 + py}** and $B(C_6F_5)_3$ to regenerate **2**.

One equivalent of $B(C_6F_5)_3$ was added to a 1:1 solution of **2** and pyridine in C_6D_6 at room temperature and an immediate colour change from the starting red solution to an orange solution, consistent with isolated **2** was observed. The reaction was analyzed by ^1H NMR, $^{31}P\{^1H\}$ NMR, $^{19}F\{^1H\}$ NMR, and ^{11}B NMR spectroscopy. In the ^{11}B NMR spectrum there was a signal observed at $\delta_B = -3.5$, which is consistent with the chemical shift range of four coordinate boron complexes. Additionally, there was disappearance of the three coordinate $B(C_6F_5)_3$ signal at $\delta_B = 60.9$ (Figure 3.2, Left). In the $^{19}F\{^1H\}$ NMR spectrum, a doublet at $\delta_F = -131.5$, and two triplets at $\delta_F = -155.9$ and -163.0 were observed (Figure 3.2, Right). In addition, there was disappearance of the $B(C_6F_5)_3$ singlets at $\delta_F = -128.9$, -141.7, and -160.1. Signal broadening continued to be observed in both the ^1H and $^{31}P\{^1H\}$ NMR spectra, and there was no regeneration of **2** (Figure B.4 and Figure B.5). The results in the NMR spectra suggest that there is formation of a $B(C_6F_5)_3$ pyridine adduct, however because there is no regeneration of **2**, the $B(C_6F_5)_3$ pyridine adduct is likely in equilibrium with **{2 + py}**.
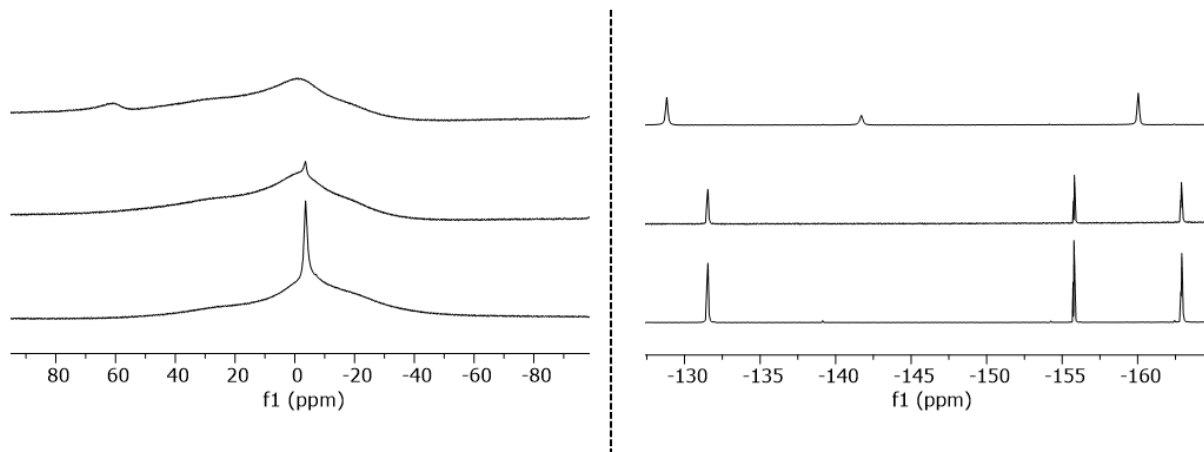
Figure 3.2. Left: ^{11}B NMR spectra (128 MHz, C_6D_6) stack plot of 1:1:1 mixture of **2**, pyridine, and $B(C_6F_5)_3$. Right: $^{19}F\{^1H\}$ NMR spectra (376 MHz, C_6D_6) stack plot of 1:1:1 mixture of **2**, pyridine, and $B(C_6F_5)_3$. In both from top to bottom: $B(C_6F_5)_3$, $B(C_6F_5)_3$ and pyridine, $B(C_6F_5)_3$, **2**, and pyridine.

To fully drive this equilibrium towards the $B(C_6F_5)_3$ pyridine adduct, forty equivalents of $B(C_6F_5)_3$ were added to a 1:1 solution of **2** and pyridine in C_6D_6 at room temperature. Again, there was an immediate colour change from the starting red solution to an orange solution. The reaction was analyzed by ^1H, $^{31}P\{^1H\}$, $^{19}F\{^1H\}$, and ^{11}B NMR spectroscopies. In both the ^{11}B and $^{19}F\{^1H\}$ NMR spectra the signals identified as the $B(C_6F_5)_3$ pyridine adduct continued to be observed along with signals for free $B(C_6F_5)_3$. The ^1H NMR spectrum presented three new signals, a doublet and two triplets at $\delta_H = 8.05$, 6.75, and 6.41, respectively, and complete consumption of free pyridine (Figure 3.3). These results indicate that the equilibrium between {**2** + **py**} and the $B(C_6F_5)_3$ pyridine adduct has been fully pushed to the $B(C_6F_5)_3$ pyridine adduct.
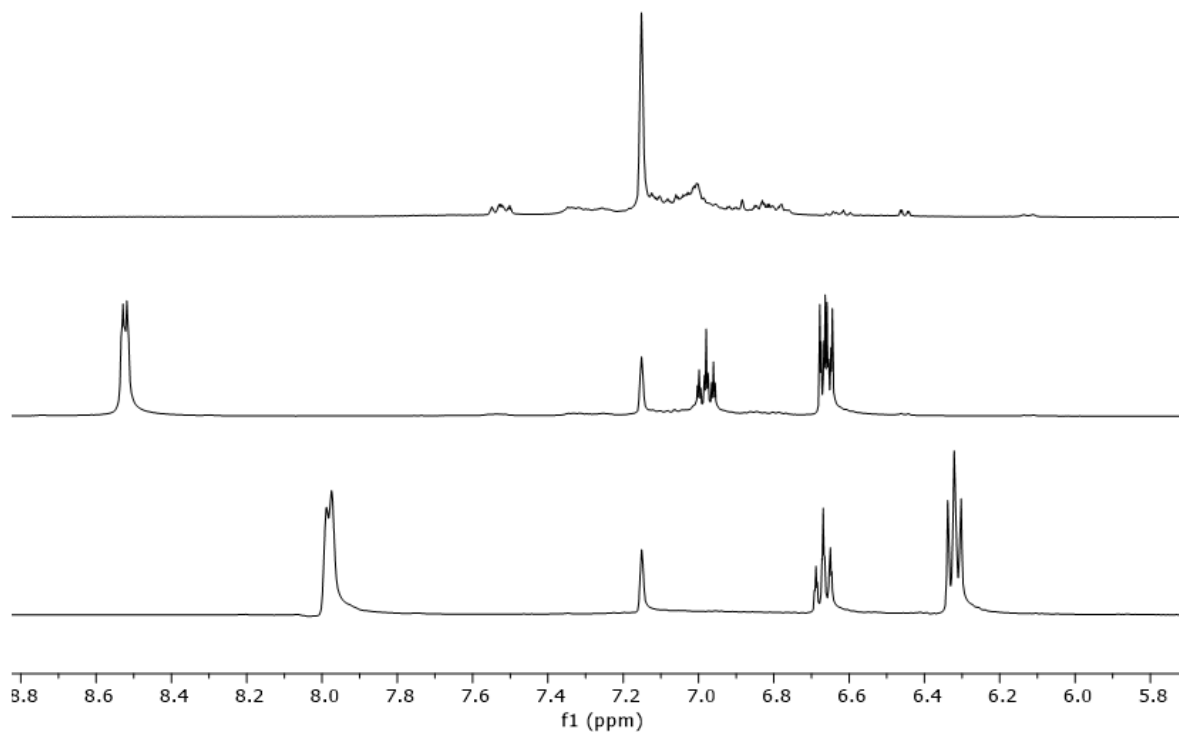
Figure 3.3. ^{1}H NMR spectra (400 MHz, C$_6$D$_6$) stack plot of 1:1:40 mixture of **2**, pyridine, and B(C$_6$F$_5$)$_3$. From top to bottom: **2**; **2** and pyridine; and **2**, pyridine, and B(C$_6$F$_5$)$_3$.

The ^{31}P{^{1}H} NMR spectrum shows a new signal at $\delta_P = 25.6$, which represents regeneration of starting complex **2** upon pyridine abstraction (Figure 3.4). The results indicate that the dynamics observed with pyridine addition to **2** represent an equilibrium involving complex **2** (as hypothesized) as this reaction is reversible once pyridine is sequestered.
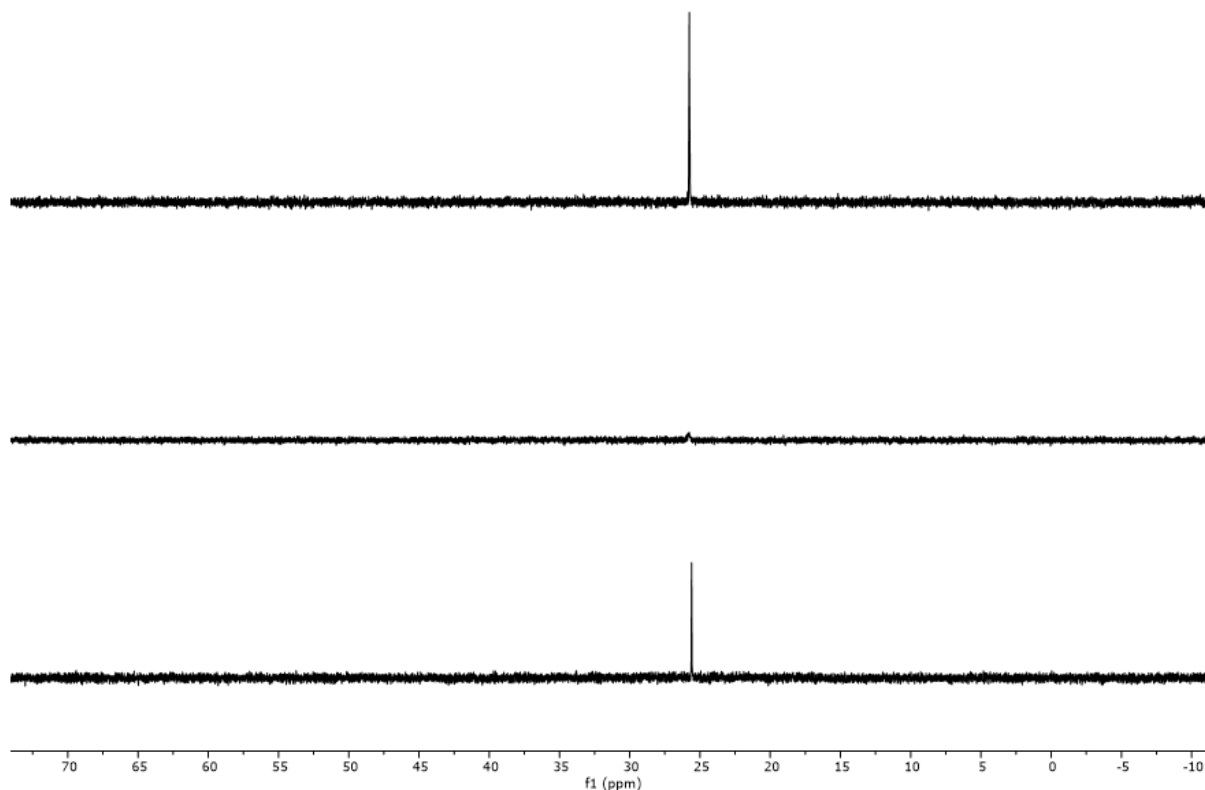
Figure 3.4. ^{31}P{^{1}H} NMR spectra (162 MHz, C$_6$D$_6$) stack plot of 1:1:40 mixture of **2**, pyridine, and B(C$_6$F$_5$)$_3$. From top to bottom: **2**; **2** and pyridine; and **2**, pyridine, and B(C$_6$F$_5$)$_3$.

3.1.2 Reactivity with Tertiary Phosphines

Reactivity of Pd complex **2** with PPh$_3$, P(^{t}Bu)$_3$, and P(NEt$_2$)$_3$ was conducted, because tertiary phosphines readily coordinate to Pd through phosphine σ-donation and Pd π-backbonding interactions. One equivalent of Lewis base was added to a solution of **2** in C$_6$H$_6$ at room temperature and the reactions were analyzed by ^{31}P{^{1}H} NMR spectroscopy (Scheme 3.4).
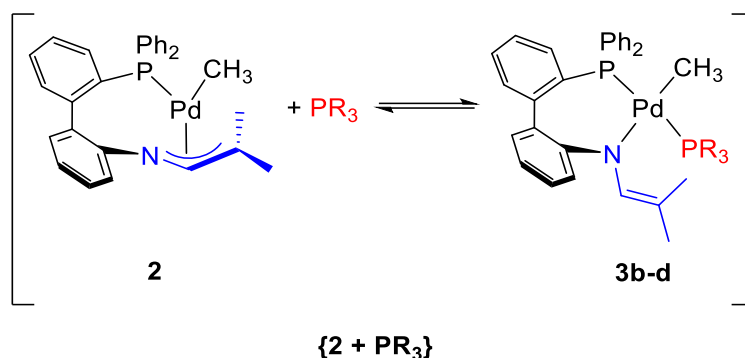
Scheme 3.4. Proposed reactivity of **2** with PR_3, where PR_3 = PPh_3, $P(^tBu)_3$, or $P(NEt_2)_3$.

After the initial addition of each phosphine (PPh_3, $P(^tBu)_3$, or $P(NEt_2)_3$) there was a vibrant colour change, from the starting orange solution to purple, red, and pink, respectively. In all cases the $^{31}P\{^1H\}$ NMR spectra displayed complete consumption of complex **2**, but no new product signals were observed (Figure B.6). The same reactions were conducted with an excess (10 equivalents) of each phosphine, but the same results were observed. In all cases the $^{31}P\{^1H\}$ NMR spectra displayed complete consumption of complex **2**, but no new product signals were observed. This suggests there is likely a dynamic equilibrium occurring between **2**, PR_3, and **3b-d**. Since there is an equilibrium present between **2**, PR_3, and **3b-d** there is no isolable κ^2-PN phosphine adduct, unlike what is observed with the reaction between Ru complex **W** and PPh_3.

As noted above, there were vibrant colour changes observed upon each phosphine addition, so a titration of $P(^tBu)_3$ was conducted and monitored by UV-Vis spectroscopy to determine if it was feasible to characterize an *in situ* change in P^AzA coordination mode between the equilibrium products **{2 + PR₃}**. An *in situ* change in P^AzA coordination mode could be represented by a new absorbance band at a different wavelength than 390 nm, where complex **2** absorbs. A 0.4 mM solution of **2** dissolved in toluene was prepared and a UV-Vis spectrum was collected at 25 °C (Figure 3.5). $P(^tBu)_3$ was added to the solution in 0.2 equivalent increments and a UV-Vis spectrum was collected after each addition. An additional UV-Vis spectrum was collected for a solution that had 10 equivalents of $P(^tBu)_3$. After 0.2 equivalents of $P(^tBu)_3$ was added, there was a reduction in the absorption at 390 nm for **2**. Over the

course of the titration, there was a new absorbance shoulder observed at 360 nm. When two absorbance bands intersect at one specific wavelength it is known as an isobestic point, which is often indicative of a clean one-to-one reaction. In this reaction there was formation of an imperfect isobestic point at 387 nm, which means the absorbance bands do not intersect at one specific wavelength, and the reaction is not a clean one-to-one conversion. Since the observed isobestic point was not perfect, titrations were also conducted at –80 °C and 60 °C to try to overcome a possible two-step reaction barrier that would involve a change in **L2** ligand coordination mode. A similar imperfect isobestic point was observed at both temperatures. This suggests that there is not a clean one-to-one reaction upon P(^{t}Bu)$_3$ addition, which is further evidence that there is a dynamic equilibrium between **2**, PR$_3$, and **3b-d**.
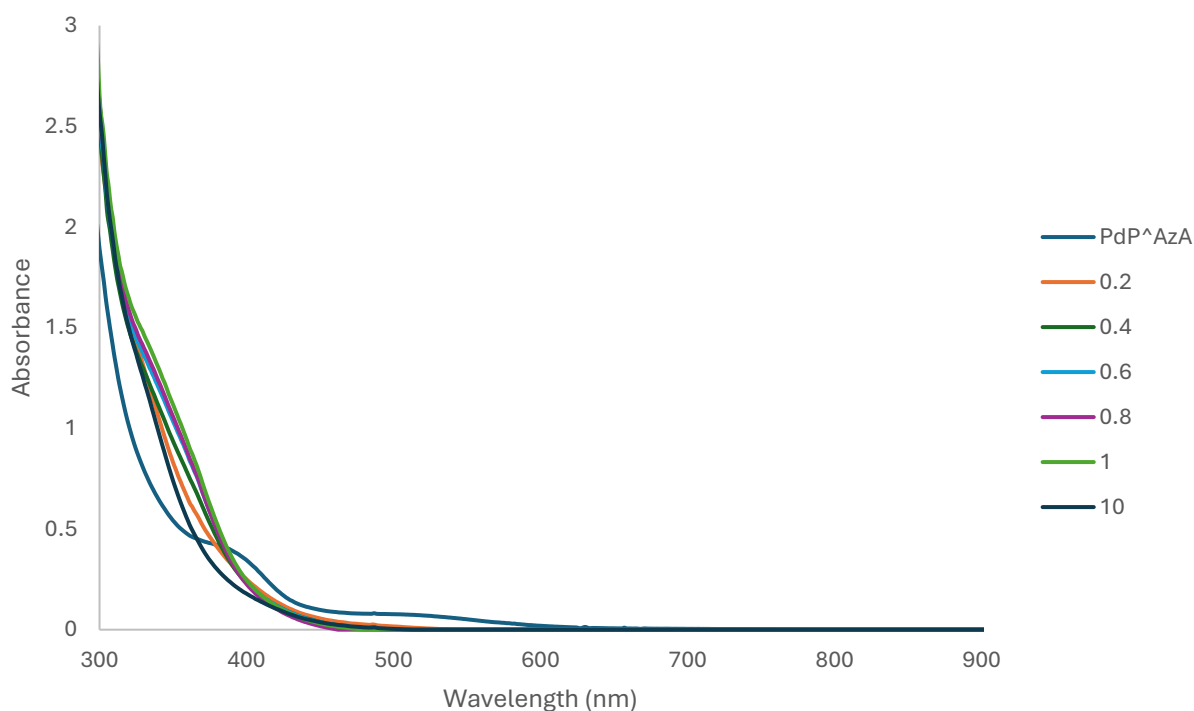
Figure 3.5. UV-Vis spectra of P(^{t}Bu)$_3$ titration at 25 °C in toluene. Concentrations of P(^{t}Bu)$_3$ include: 0.2 mM, 0.4 mM, 0.6 mM. 0.8 mM, 1.0 mM, and 10 mM.

Since the addition of P(^{t}Bu)$_3$ to complex **2** does not proceed through a clean-one-to-one reaction, the substitution pathway is likely two-steps, with an intermediate. If the substitution occurred through

an associative pathway, the association of P(^{t}Bu)$_3$ would give a 5-coordinate intermediate **3c-5**, where

P^AzA isomerization from κ^1-P;η^3-NCC to κ^2-P,N would then give complex **3c** (Scheme 3.5).

Alternatively, if the substitution occurred through a dissociative pathway, P^AzA isomerization would

occur first, to give a 3-coordinate intermediate **2-3**, and P(^{t}Bu)$_3$ coordination would follow to give

complex **3c**.
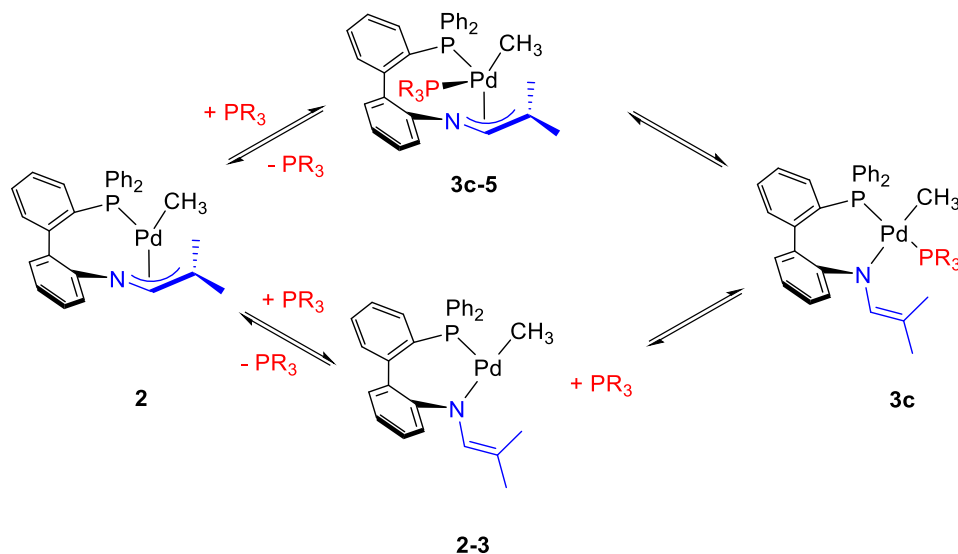
Scheme 3.5. Proposed two-step reaction pathway for P(^{t}Bu)$_3$ substitution. PR$_3$ = P(^{t}Bu)$_3$.

Since the rate of an associative pathway would be dependent on phosphine coordination,

analyzing the rate of the reaction with respect to phosphine concentration would provide insight on

what intermediate the reaction proceeds through. If the rate increased with increased phosphine

concentration the reaction likely proceeds through the 5-coordinate intermediate **3c-5**, and if the rate

does not change with increased phosphine concentration the reaction likely proceeds through the 3-

coordinate intermediate **2-3**. Time analysis of the addition of one equivalent of P(^{t}Bu)$_3$ to a solution of

2 dissolved in toluene was conducted to determine if the reaction occurs on a timescale where rate

analysis would be possible. The reaction was monitored by UV-Vis spectroscopy at –80 °C, with a new

spectrum acquired every 30 seconds (Appendix Figure B.13). Unfortunately, the reaction was complete

after 30 seconds, so a rate analysis was not possible.

The initial PR_3 ligands investigated were all sterically bulky, so it was hypothesized that a less sterically hindered PR_3 ligand may coordinate to Pd more effectively. Reactivity with PEt_3 was explored, where one equivalent of PEt_3 was added to a solution of **2** in C_6H_6 at room temperature and the reaction was analyzed by $^{31}P\{^1H\}$ NMR spectroscopy (Scheme 3.6).
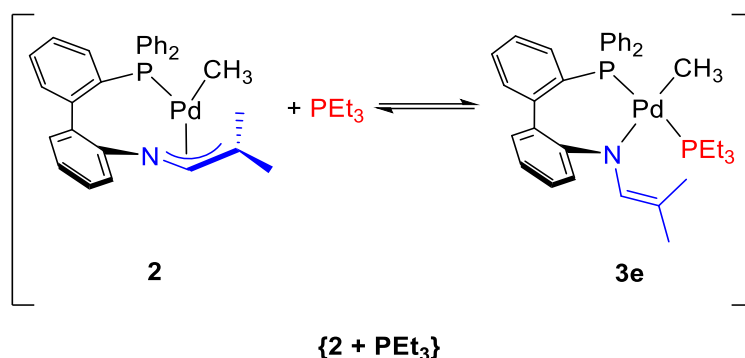
Scheme 3.6. Proposed reactivity of **2** with PEt_3.

After the initial addition of one equivalent of PEt_3 there was a vibrant colour change, from the starting orange solution to red. The $^{31}P\{^1H\}$ NMR spectrum displayed signals that indicate complete consumption of complex **2**, free PEt_3 ligand, and the formation of several new signals in the range of $\delta_P = 10.3 - 27.7$ (Figure 3.6). Overall, the vibrant colour change and the new $^{31}P\{^1H\}$ NMR spectroscopy signals observed with PEt_3 indicate there is reactivity between complex **2** and PEt_3, however, the multiple signals in the $^{31}P\{^1H\}$ NMR spectrum suggest that either a mixture of products possibly containing the κ^2-PN product or an equilibrium between **2**, PEt_3, and **3e**, where there would be no isolable κ^2-PN product. The same reaction was conducted and monitored by variable temperature NMR spectroscopy with the goal of slowing down reactivity to observe a single product by $^{31}P\{^1H\}$ NMR spectroscopy. The reaction was cooled from 25 ˚C down to –50 ˚C and analyzed at every 10 ˚C change in temperature by $^{31}P\{^1H\}$ NMR spectroscopy (Appendix Figure B.15). There was no change in the $^{31}P\{^1H\}$ NMR spectroscopy product distribution, which suggests that a change in temperature does not lead to an isolable κ^2-PN phosphine adduct.
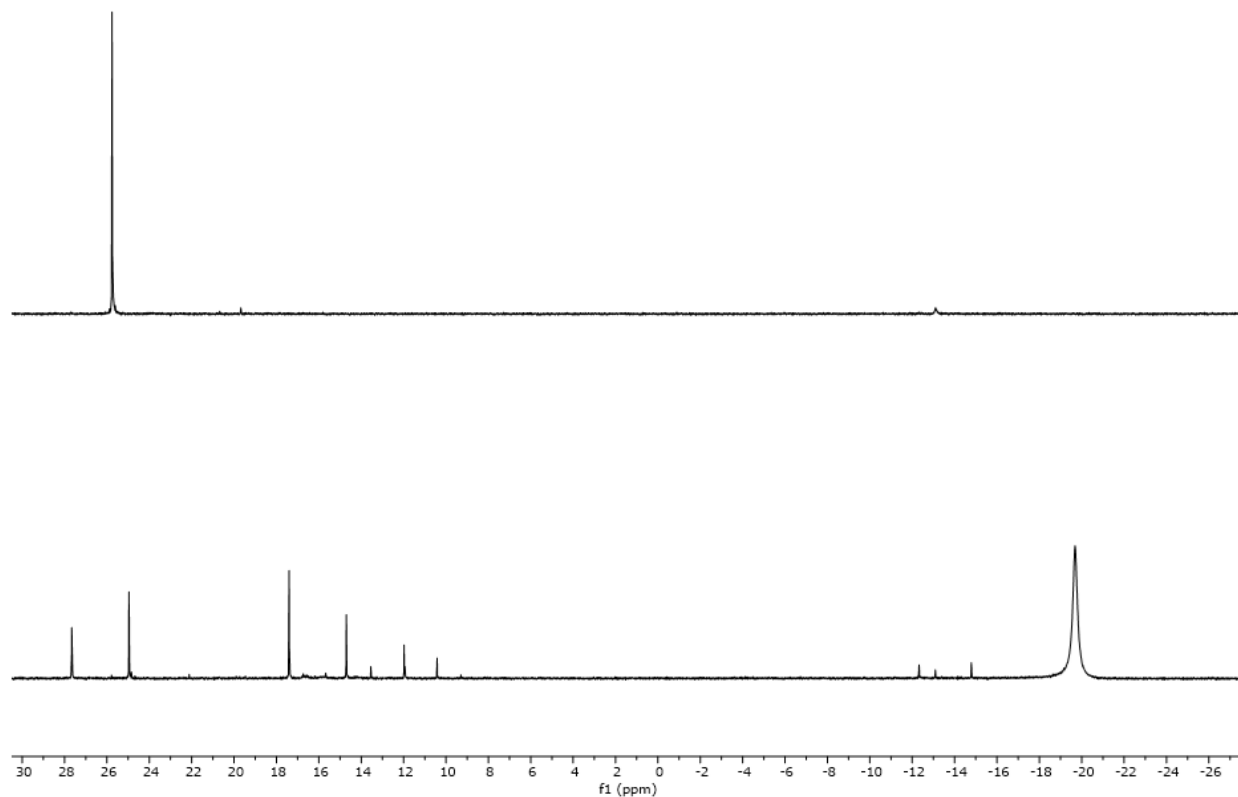
Figure 3.6. ^{31}P{^{1}H} NMR spectra (162 MHz, C$_6$H$_6$) stack plot of the reaction of **2** and PEt$_3$. From top to bottom: **2**, **2** and PEt$_3$. The peak at $\delta_P = -19.8$ is free PEt$_3$.

3.1.3 Reactivity with CN$^-$

The reactivity of Pd complex **2** with CN$^-$ was evaluated, because this anion generally coordinates strongly to Pd(II). One equivalent of tetrabutylammonium bromide (TBABr) was added to a heterogenous solution of Zn(CN)$_2$ in DMF at room temperature. TBABr was added to the Zn(CN)$_2$ solution, to increase solubility of the cyanide salt, through salt metathesis to form a soluble, charge separated [TBA]CN, cyanide source.[47] Complex **2** was dissolved in DMF and added to the TBACN solution at room temperature (Scheme 3.7). The reaction was analyzed by ^{31}P{^{1}H} NMR spectroscopy, and there was complete consumption of complex **2**, but no new product signals were observed (Appendix Figure B.16). This suggests that there may be a dynamic equilibrium occurring between **2**, CN$^-$, and **3f**.
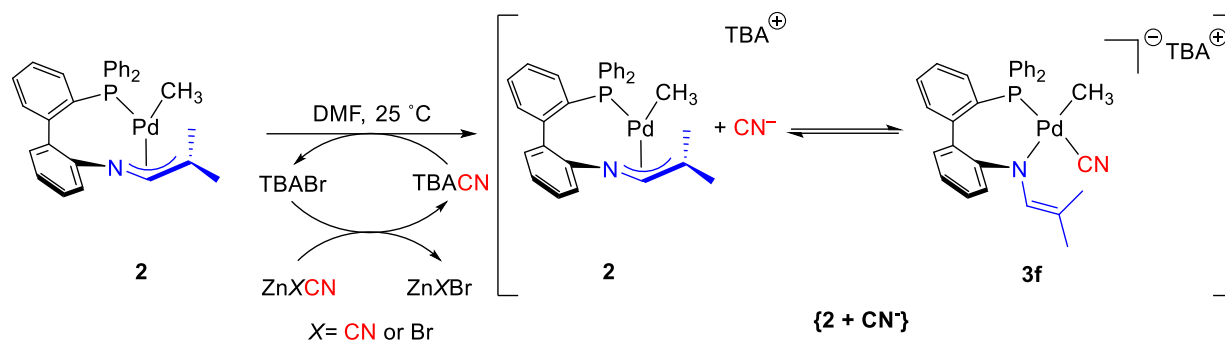
Scheme 3.7. Proposed reactivity with **2** and TBACN.

When complex **2** was added to the TBACN solution there was an immediate colour change from the starting orange solution to a colourless solution. This lack of colour is consistent with a Pd(0) complex, which indicates that reductive elimination of acetonitrile may have occurred, to produce a Pd(0) complex (Scheme 3.8).
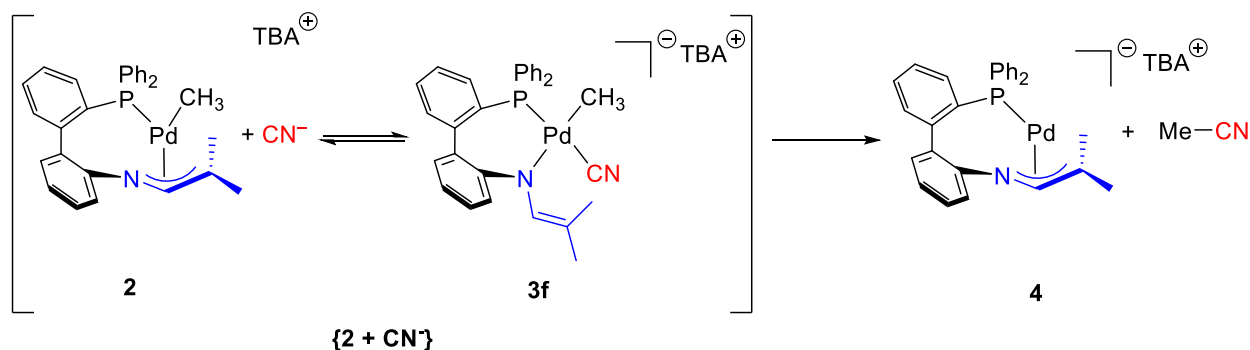
Scheme 3.8. Proposed reactivity with **2** and TBACN, followed by reductive elimination of acetonitrile to produce Pd(0) complex **4**.

Excess maleic anhydride (MAH) was added to the proposed Pd(0) complex **4** solution in an effort to trap the Pd(0) complex (Scheme 3.9). After addition of MAH, there was an immediate colour change in solution from colourless to orange. Over the course of 24 h the colour of the solution continued to change to a dark orange/brown solution. The reaction was analyzed by $^{31}P\{^{1}H\}$ NMR spectroscopy, but there were still no signals observed (Appendix Figure B.16). This suggests that there

is likely a dynamic equilibrium occurring between **4**, MAH, and the MAH adduct **5**, which means that the potential Pd(0) complex could not be trapped with MAH. The results indicate that substitution with CN^- does not lead to an isolable κ^2-PN Pd complex.
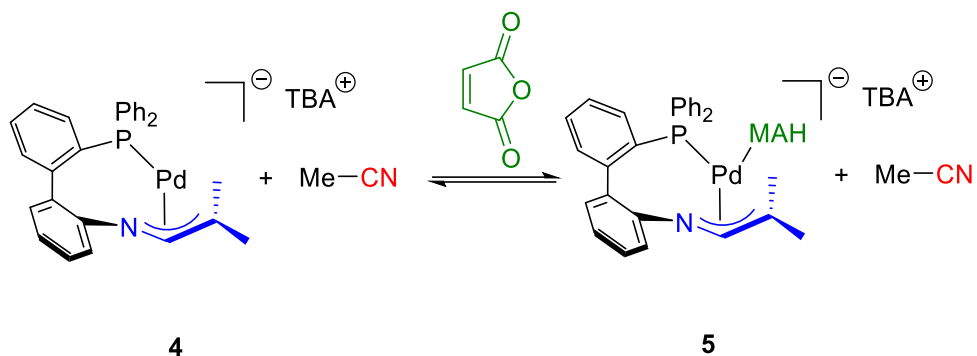
Scheme 3.9. Proposed reactivity with *in situ* generated **4** and MAH.

3.1.4 Reactivity with Water

The reactivity of Pd complex **2** with water was explored to determine if the addition of water would result in hydroxide substitution onto **2** with the release of methane gas (Scheme 3.10), or if protonation of the 1-AzA ligand would occur (Scheme 3.11). One drop of degassed water was added to a solution of **2** in C_6D_6 at room temperature and there was a colour change from the starting orange solution to a yellow solution. Additionally, there was formation of white, yellow, and black precipitates that accumulated over 24 h. This was consistent with the same reaction conducted with Pd(II) dimer **S**.[48]
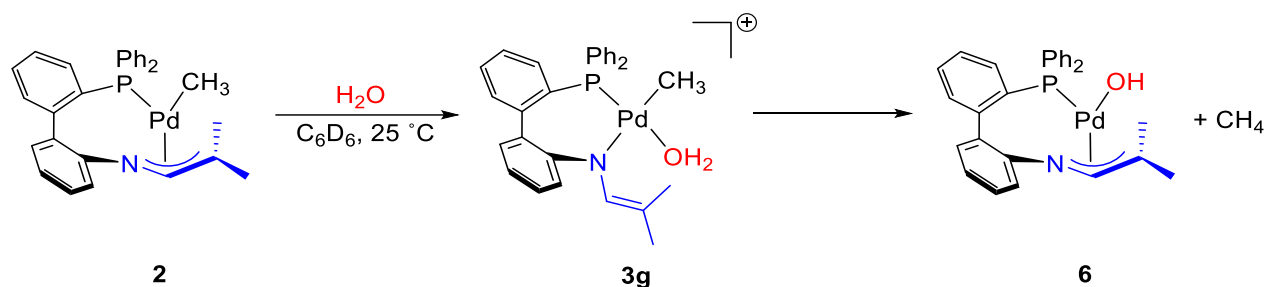
Scheme 3.10. Proposed reactivity with **2** and water.

The reaction was analyzed by both $^{31}P\{^1H\}$ and ^1H NMR spectroscopy. In the $^{31}P\{^1H\}$ NMR spectrum there was complete consumption of complex **2** and the formation of two new signals at δ_P = 36.2 and 35.4 in a 1:10 ratio (Appendix Figure B.18). The product mixture was dissolved and analyzed in both THF and DMSO as well as C_6D_6 and in each case the ratio of the products changed, which suggests that the products are in equilibrium (Appendix Figure B.19). The signals are consistent with Pd bound imine/enamine (**H[L2]**) complexes, which suggests that the water is protonating the coordinated 1-AzA moiety in **2**, however the black precipitate is consistent with Pd black. The ^1H NMR spectroscopy was too broad to identify distinctive signals, and the identity of these signals was not further investigated. Based on the $^{31}P\{^1H\}$ NMR spectroscopy, the reaction likely proceeds through Pd imine/enamine intermediate before decomposing into Pd black, which indicates that complex **2** is not stable upon water addition (Scheme 3.11).
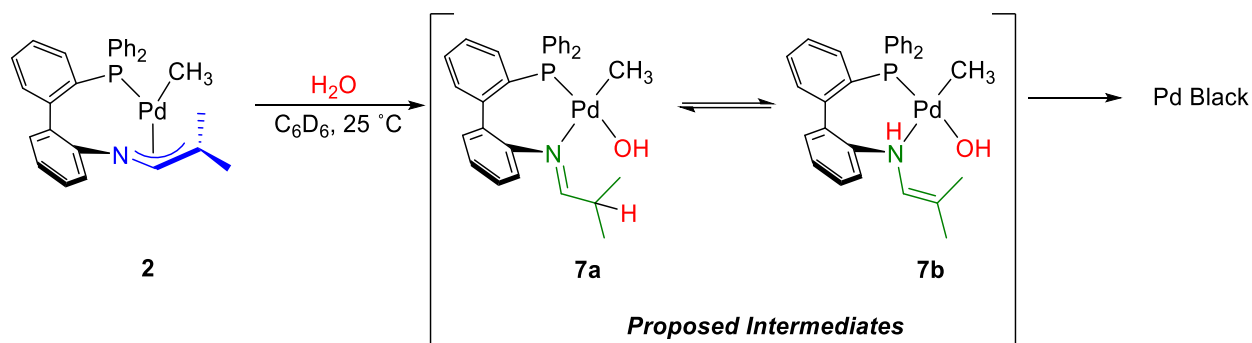
Scheme 3.11. Proposed decomposition pathway of **2** through a Pd imine/enamine intermediate.

3.2 Insertion Reactivity

Since complex **2** has a Pd methyl bond, it was hypothesized that insertion into the Pd methyl bond could occur with CO and/or methyl acrylate.

3.2.1 Reactivity with CO

Reactivity with Pd complex **2** and CO was conducted to assess if CO could coordinate to Pd directly or through insertion into the Pd methyl bond (Scheme 3.12).
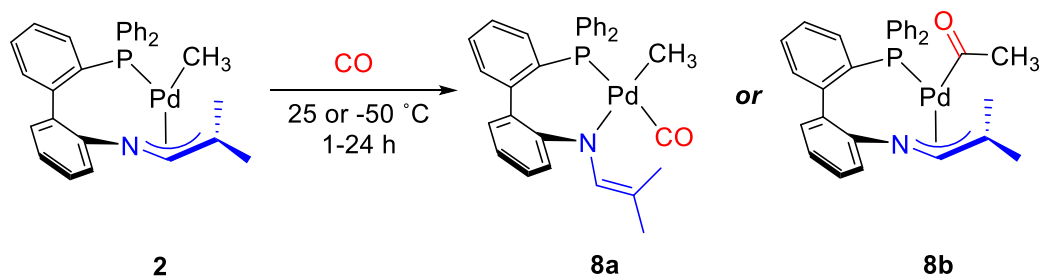
Scheme 3.12. Proposed reactivity of **2** with CO, to form products **8**.

CO was bubbled into to a solution of **2** in C_6D_6 at room temperature and the reaction was monitored over 24 h by ^1H and $^{31}P\{^1H\}$ NMR spectroscopy. There was an observed solution colour change after CO was bubbled into the solution from a light orange to dark orange. After 10 min the $^{31}P\{^1H\}$ NMR spectrum displayed partial consumption of **2** and the formation of multiple new signals between the range of $\delta_P = 18.0 - 40.0$. After six hours **2** was completely consumed, and the new signals

all persisted in greater ratios than the initial 10 min observation. The combination of the colour changes and multiple new ^{31}P{^{1}H} NMR spectroscopy signals suggest that a reaction occurs, but multiple products are formed at room temperature, and currently no products have been isolated. Since there are different possible products for this reaction, CO coordination and insertion products could potentially be in a dynamic equilibrium, where the multiple observed ^{31}P{^{1}H} NMR spectroscopy signals may represent multiple products in equilibrium with each other (Scheme 3.13).
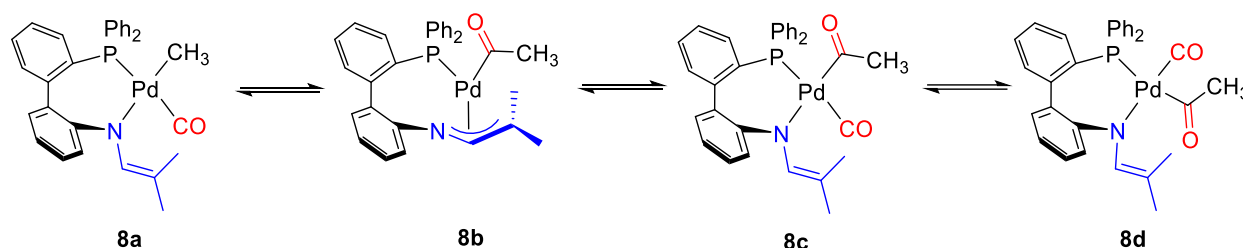
Scheme 3.13. Proposed equilibrium products following CO coordination or insertion with **2**.

The same reaction with CO bubbled into a solution of **2** in toluene-d_8 was conducted in a –50 ˚C cold bath with the objective of slowing down reactivity to potentially isolate or characterize one of the new ^{31}P{^{1}H} NMR spectroscopy signals. Multiple ^{31}P{^{1}H} NMR spectroscopy signals between the range of $\delta_P = 18.0 - 40.0$ were still observed, however there were significantly fewer signals observed at –50 ˚C which indicates that cooling the reaction may provide method to product isolation or characterization (Figure 3.7). Complex **2** does react with CO, but the mechanism of how CO reacts with **2** is still unknown. Future experiments could be conducted try an isolate the products and determine how CO reacts with **2**.
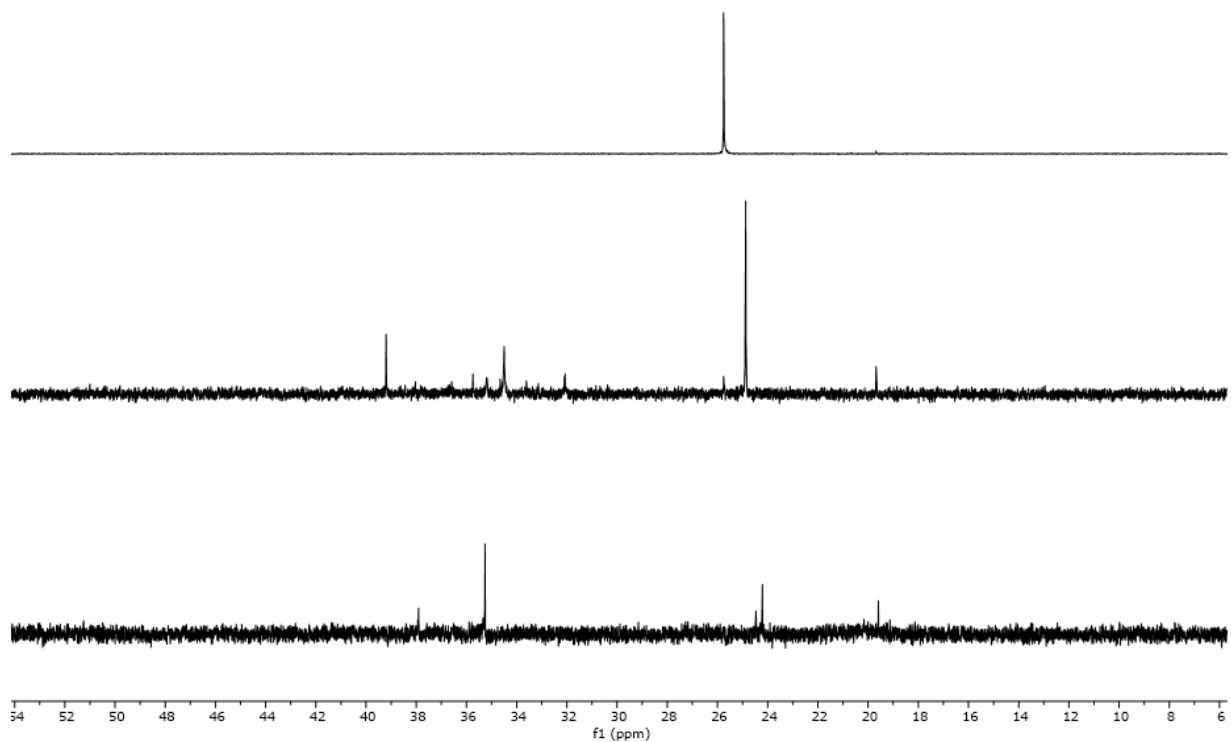
Figure 3.7. $^{31}P\{^1H\}$ NMR spectra (162 MHz, toluene-d_8) stack plot of the reaction of **2** and CO. From top to bottom: **2**, **2** and CO bubbled in at room temperature, **2** and CO bubbled in at –50 ˚C.

3.2.2 Reactivity with Methyl Acrylate

Reactivity with Pd complex **2** and methyl acrylate (MA) was evaluated to assess if MA could coordinate to Pd through either insertion into the Pd methyl bond, polar functional group binding, or alkene binding (Scheme 3.14).
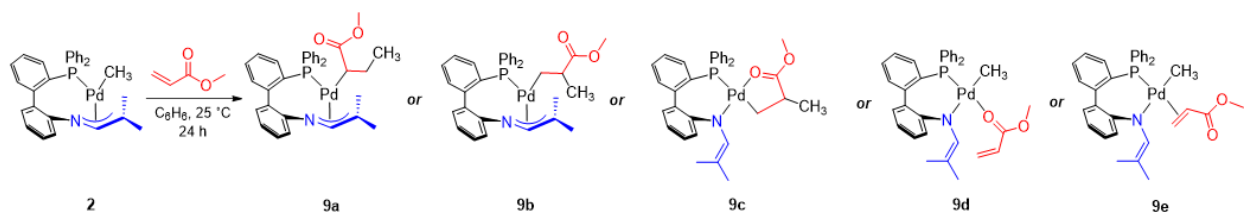
Scheme 3.14. Proposed reactivity of **2** with MA, to form possible products **9a-e**.

One equivalent of MA was added to a solution of **2** in C_6H_6 at room temperature and the reaction was monitored over 24 h by $^{31}P\{^1H\}$ NMR spectroscopy. After 6 h the $^{31}P\{^1H\}$ NMR spectrum

displayed complete consumption of complex **2** and the formation of two new signals with a 2:3 ratio at

δ_P = 19.4 and 23.2, respectively (Appendix Figure B.22). To examine the stability of the products, the

solvent was removed, and the compounds were redissolved in C_6H_6. The $^{31}P\{^1H\}$ NMR spectrum of

the redissolved products displayed the same two signals at δ_P = 19.4 and 23.2 in the same ratio, which

indicates the products persist on solvent removal and redissolution. The product distribution remained

the same when this reaction was conducted in toluene-d_8 or THF. This reaction was then conducted in

a –50 ˚C cold bath, where one equivalent of MA was added to a solution of **2** in toluene-d_8 at –50 ˚C

and the reaction was monitored over time by $^{31}P\{^1H\}$ NMR spectroscopy (Appendix Figure B.24). The

purpose of the low temperature addition was to slow the reaction down, to provide a possible pathway

to product isolation or characterization for one of the new products observed in the $^{31}P\{^1H\}$ NMR

spectroscopy. After 3 h, the $^{31}P\{^1H\}$ NMR spectrum displayed an abundance of new signals between

the range of δ_P = 18.0 – 40.0, which indicates that cooling the reaction either slows down reactivity

allowing multiple intermediates to be observed or that cooling does not provide method to product

isolation or characterization. The ^1H NMR spectrum was too complex to identify specific products,

however there was no evidence of alkene proton signals in the ^1H NMR spectrum, which suggests the

product is likely an insertion product and not complex **9d** or **9e**. Complex **2** does react with MA,

however the mechanism of how MA reacts with **2** is still unknown. Future experiments could be

conducted to try an isolate the products and determine how MA reacts with **2**.

     In Summary, the substitution reactivity of both pyridine and tertiary phosphines with Pd

complex **2** resulted in a reversible dynamic equilibrium mixture between **2**, the Lewis base, and complex

3, which was completely different than the previous observed results with Pd(II) dimer **S** and Ru

complex **W**, where pyridine or phosphine coordinated to Pd or Ru and the P^AzA κ^2-PN product was

isolated and crystallized. The substitution reactivity of cyanide with **2**, provided evidence towards the

formation of a Pd(0) intermediate, following the reductive elimination of acetonitrile. The substitution

reactivity of water with **2**, was consistent with Pd(II) dimer **S**. In both cases the 1-AzA ligand fragment was protonated upon water substitution to form Pd imine/enamine intermediates before proceeding down a decomposition pathway to Pd black. The insertion reactivity with both CO and MA suggested that there was evidence towards insertion into the Pd methyl bond, however no insertion products were isolated or characterized. Pd complex **2**, exhibits unique fast and dynamic reactivity that could be exploited towards catalysis.

4.0 Attempted Catalysis with Biaryl Pd Phosphine 1-Azaallyl Complexes

Preliminary examination of **2** as a catalyst for polymerization, oligomerization, isomerization, cyanation, and carbonylation was evaluated based on the interesting reactivity observed in Chapter 3.

4.1 Attempted Ethylene Homopolymerization

Cationic phosphine phosphonic amide Pd(II) complexes bearing hemilabile bidentate P,O or P,N ligands have been successful ethylene polymerization catalysts.[49] This led to the hypothesis that Pd complex **2** could catalyze ethylene polymerization since it is structurally related to successful ethylene polymerization catalysts. Polymerization of ethylene was attempted with Pd complex **2** (Scheme 4.1). A solution of **2** in toluene was added to a Parr Reactor with pressurized ethylene and heated at 80 ˚C. After 24 h, MeOH was added to the solution to try and precipitate any formed polymers, however upon filtration no solids were observed, which suggests there is no formation of long chain polymers. The solvents were then removed to afford a white solid with an average mass of 11 mg, this white solid was also observed with the control reaction containing no catalyst. The white solid possibly represents the formation of short chain oligomers, however as this isolated product is observed in the control reaction, it appears product formation does not require Pd, and the yield is so small that the result does not warrant follow-up.
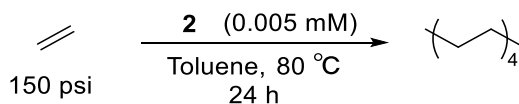
Scheme 4.1. Proposed synthesis of polyethylene catalyzed by **2**.

Nonetheless, the spectroscopic data of the solids was analyzed, and the ^{1}H NMR spectrum of the isolated product from the reaction with **2** and the control reaction both had signals at δ_H = 1.40, 1.28, and 0.88. These signals are consistent with reported polyethylene ^{1}H NMR spectra where the signals at δ_H = 1.40 and 1.28 represent methylene protons and the signal at δ_H = 0.88 represents methyl

protons of polyethylene.[50] The chain length of the products was determined using end group analysis and the chain in both products was found to have of four repeating units, which is consistent with short chain polyethylene oligomers. The ^{1}H NMR spectroscopy signals for the isolated product were very sharp singlets and the ^{1}H NMR spectroscopy signals for the control reaction were very broad. This suggests that Pd complex **2** is not required for ethylene oligomerization but may play a role in product selectivity. To determine if Pd complex **2** could catalyze ethylene oligomerization, a series of optimization reactions were conducted to assess the influence of catalyst, time, and solvent volume on product chain length (Table 1).

Table 1. Optimization reactions for ethylene homopolymerization with varying times, solvent volumes, and catalyst conditions.

Entry	Catalyst Loading (mM)	Temperature (˚C)	Time (h)	Solvent Volume (mL)	Mass (mg)	Repeating Units
1	0	80	24	15	5	4
2	0.005	80	24	15	11	4
3	0.005	80	6	15	10	4
4	0.005	80	3	15	10	4
5	0.005	80	3	8	7	4
6[b]	0.005	80	24	15	6	4
7[b]	0.005	80	6	15	7	4
8[b]	0.005	80	3	15	8	3
9[b]	0.005	80	3	8	5	3

[a] all reactions conducted in toluene with 150 psi of ethylene. [b] with four equivalents of pyridine added to the solution of **2** in toluene.

Reaction time, the first condition examined (Entries 2-4), was decreased from 24 h to six hours, and then three hours, and no changes in product chain length or yield were observed. Toluene volume was then decreased from 15 mL to 8 mL (Entries 4-5), and no changes in product chain length were observed. Four equivalents of pyridine were then added to the solution of **2** in toluene with the hypothesis that the addition of a Lewis base would induce a change in P^AzA coordination mode from κ^1-P;η^3-NCC to κ^2-PN. Accessing a κ^2-PN coordination mode with pyridine coordinated to the metal centre could provide an easier pathway for ethylene coordination. Ethylene substitution onto Pd would then be able to occur through dissociation of the neutral pyridine ligand instead of through dissociation of the anionic 1-AzA ligand. However, there were no observed changes in product chain length, which suggests that reaction time, solvent volume, and the addition of pyridine do not influence the chain length of the solid oligomer products isolated from the MeOH solution. This suggests that **2** is not an effective polymerization catalyst under the given conditions.

4.2 Attempted 1-Octene Oligomerization

Oligomerization of 1-octene was attempted with Pd complex **2** (Scheme 4.2) to evaluate if oligomers were being formed, since the expected oligomeric products should be non-volatile, whereas the potential oligomers formed from the reaction with ethylene would be volatile, and therefore nearly impossible to identify. 1-Octene was added to a solution of **2** in toluene-d_8 and the reaction was monitored by ^{1}H NMR spectroscopy over 24 hours. There were no changes observed in the ^{1}H NMR spectrum, which indicates no oligomerization occurred. This reaction was then conducted at 80 ˚C and monitored over 24 h to investigate if catalysis would occur under more forcing conditions. There were no changes observed in the ^{1}H NMR spectrum, which indicates no oligomerization occurred.
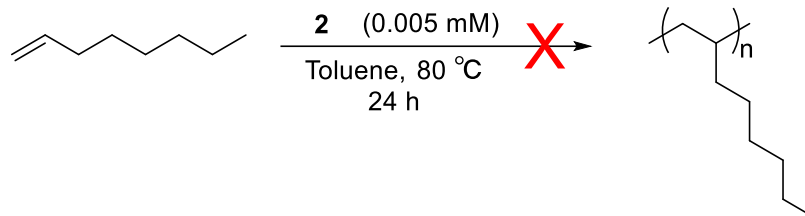
Scheme 4.2. Attempted 1-octene oligomerization with Pd complex **2**.

4.3 Attempted Allyl Benzene Isomerization

Cationic and sterically hindered palladium-diimine polymerization catalysts have also been known to act as catalysts for α-olefin isomerization.[51] This led to the hypothesis that Pd complex **2** could act as an olefin isomerization catalyst, so the potential of **2** to catalyze allyl benzene isomerization was explored. Allyl benzene was added to a solution of **2** in C_6D_6 at room temperature and the reaction was monitored by ^1H NMR spectroscopy over 24 h (Scheme 4.3). A new methyl proton signal at $\delta_H =$ 1.70 or 1.92 would indicate isomerization to the E or Z isomer, respectively.[40] There were no changes observed in the ^1H NMR spectrum, which indicates no isomerization occurred. This reaction was then conducted at 80 °C and monitored over 24 h to investigate if catalysis would occur under more forcing conditions. There were no changes observed in the ^1H NMR spectrum, which indicates no isomerization occurred. The results suggest that **2** is not an effective olefin isomerization catalyst.
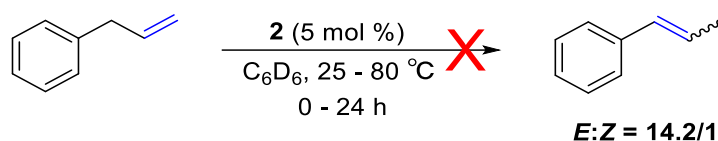
Scheme 4.3. Attempted allyl benzene isomerization with Pd complex **2**.

4.4 Attempted Cyanation of 3-Bromopyridine

Traditionally, Pd(II) catalyzed cyanation of aryl bromides has been unsuccessful due to catalyst decomposition.[51] In a catalytic cycle, when Pd(II) is exposed to strongly binding CN⁻ anions, an inactive

Pd-CN species is formed, and this Pd species cannot be reduced to Pd(0), which ultimately leads to a dead end in the catalytic cycle and catalyst decomposition.[52] The dynamic equilibrium observed with Pd complex **2** with Lewis base donors (Section 3.1) led to the hypothesis that Pd catalyzed cyanation of heteroaryl bromides with **2** could be successful without forming a stable Pd-CN species that would ultimately lead to catalyst deactivation.

Cyanation of 3-bromopyridine with zinc cyanide and catalytic tetrabutylammonium bromide was attempted with **2** following a literature procedure (Scheme 4.4).[53] A solution of one equivalent of 3-bromopyridine, 0.6 equivalents of zinc cyanide, 0.25 equivalents of tetrabutylammonium bromide, and 5 mol% of Pd complex **2** in DMF was stirred at 65 ˚C for 20 h.[53] The reaction was analyzed by $^{13}C\{^1H\}$ NMR spectroscopy where an additional signal at $\delta_C = 110.3$ would be indicative of the nitrile carbon of the proposed cyanation product. The $^{13}C\{^1H\}$ NMR spectrum displayed no additional carbon signal, which indicates that the cyanation catalysis with Pd complex **2** was unsuccessful.
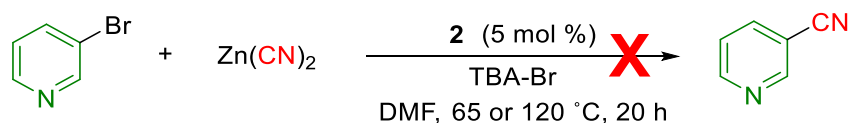
Scheme 4.4. Attempted cyanation of 3-bromopyridine with Pd complex **2**.[53]

In this reaction, oxidative addition of 3-bromopyridine is likely the rate determining step with the highest energy barrier. One way to overcome this energy barrier is to increase the reaction temperature, so catalysis under the same conditions was attempted at 120 ˚C and the reaction was analyzed by $^{13}C\{^1H\}$ NMR spectroscopy. The $^{13}C\{^1H\}$ NMR spectrum displayed no additional carbon signal, which indicates that the cyanation catalysis with **2** was unsuccessful. If catalysis were to occur, the proposed catalytic cycle for this reaction with **2** would initially involve coordination of CN^- to Pd, followed by the reductive elimination of acetonitrile to form a Pd(0) intermediate complex (Scheme

4.5).
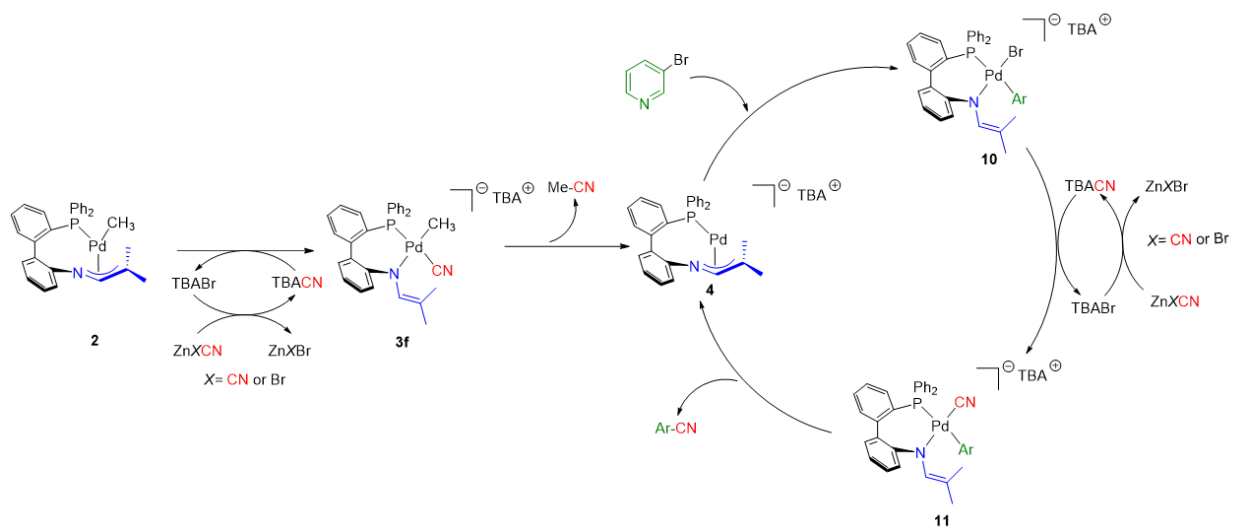
Scheme 4.5. Proposed catalytic cycle for cyanation of 3-bromopyridine with Pd complex **2**.

To confirm if the Pd(0) intermediate complex would be stable, an independent synthesis of a Pd(0) complex with **L2** coordinated was attempted. The tautomeric mixture of **H[L2]a** and **H[L2]b** was coordinated to [^{DMP}DAB-Pd-MAH] affording complexes **12a** and **12b** (Scheme 4.6). The ^{31}P{^{1}H} NMR spectrum displayed two singlets at δ_P = 28.8 and 25.5.
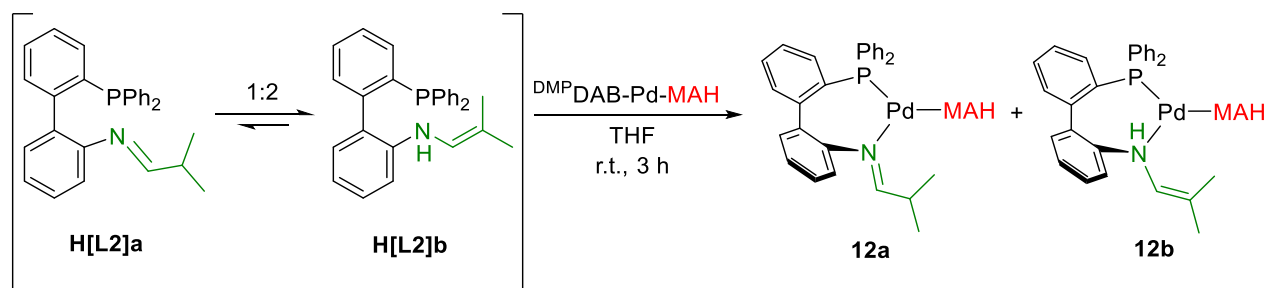
Scheme 4.6. Coordination of **H[L2]** to Pd to form **12a** and **12b**.

Deprotonation of **H[L2]** on complex **12a/b** with potassium hydride was performed to generate the proposed P^AzA Pd(0) complex **7**. The ^{31}P{^{1}H} NMR spectrum displayed two different singlets at δ_P = 33.2 and 29.1, which may imply that there is an equilibrium between the complex **5** and **4** (Scheme 4.7). Only preliminary characterization was conducted on **5**, but the results suggest that a Pd(0)

intermediate could be stable, which implies that oxidative addition is likely the limiting step to successful catalysis with **2** under the given conditions.
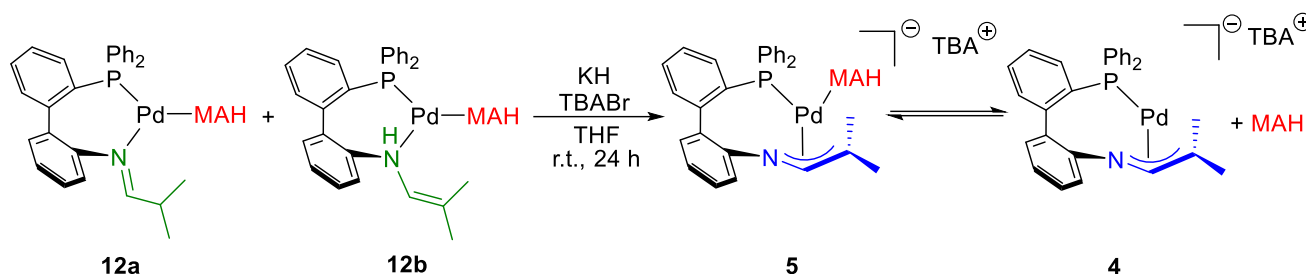
Scheme 4.7. Deprotonation of **12a** and **12b** to form the proposed Pd(0) intermediate **5**.

4.5 Attempted Carbonylation of Aryl Triflates to Aroyl-DMAP Salts

The reactivity observed with CO and Pd complex **2** led to the hypothesis that CO could insert into the Pd alkyl bond which would enable Pd catalyzed carbonylation of phenyl triflate with Pd complex **2**. Carbonylation of phenyl triflate to aroyl-DMAP salts was attempted with **2** following a literature procedure (Scheme 4.8).[54] A solution of phenyl triflate, DMAP, and 5 mol% **2** in toluene was prepared. An immediate colour change from colourless to bright red was observed upon the addition of **2** to the solution of phenyl triflate and DMAP. The red colour is consistent with the colour observed when pyridine was added to a solution of **2**. CO was bubbled into the Strauss flask and the reaction was stirred at 60 ˚C for 24 h. After 24 h there was visible Pd black formation and no visible white solid indicative of the product.
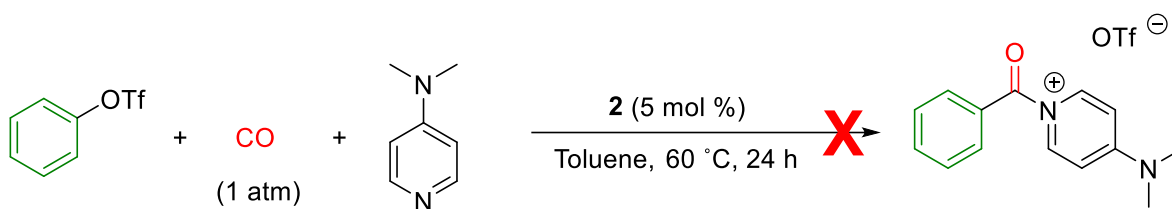
Scheme 4.8. Attempted carbonylation of phenyl triflate with Pd complex **2**.[54]

The reaction was analyzed by ^{1}H, ^{19}F{^{1}H}, and ^{13}C{^{1}H}, and NMR spectroscopy. In the ^{1}H NMR spectrum only signals of the starting material DMAP and PhOTf were observed. In the ^{19}F{^{1}H} NMR spectrum the only signal observed was for the starting material phenyl triflate. In the ^{13}C{^{1}H} NMR spectrum there was no evidence of a new carbon signal indicative of a carbonyl. The NMR spectra indicates that the Pd catalyzed carbonylation of phenyl triflate was unsuccessful with **2**. The Pd black observed during the reaction represents decomposition of Pd complex **2**. To determine if heating the reaction led to catalyst decomposition, the reaction was conducted under the same conditions at room temperature. After 24 h Pd black was again observed and there was no evidence of new product formation in the NMR spectra.

If catalysis were to occur, the proposed catalytic cycle for this reaction with **2** would initially involve CO insertion into the Pd methyl bond, followed by the rapid reductive elimination of the acyl group followed by subsequent DMAP salt formation to form a Pd(0) intermediate (Scheme 4.9). Previous reactivity with **2** suggests that these steps are all possible, which would indicate that the oxidative addition of phenyl triflate is preventing catalysis from occurring. To overcome the potential oxidative addition energy barrier, the carbonylation of p-tolyl triflate was attempted at 120 ˚C. After 24 h both the ^{19}F{^{1}H} NMR spectrum and the ^{13}C{^{1}H} NMR spectrum displayed only signals for starting material. Additionally, Pd black was again observed, which is indicative of catalyst decomposition. The results suggest that **2** is not an effective carbonylation catalyst under the given conditions.
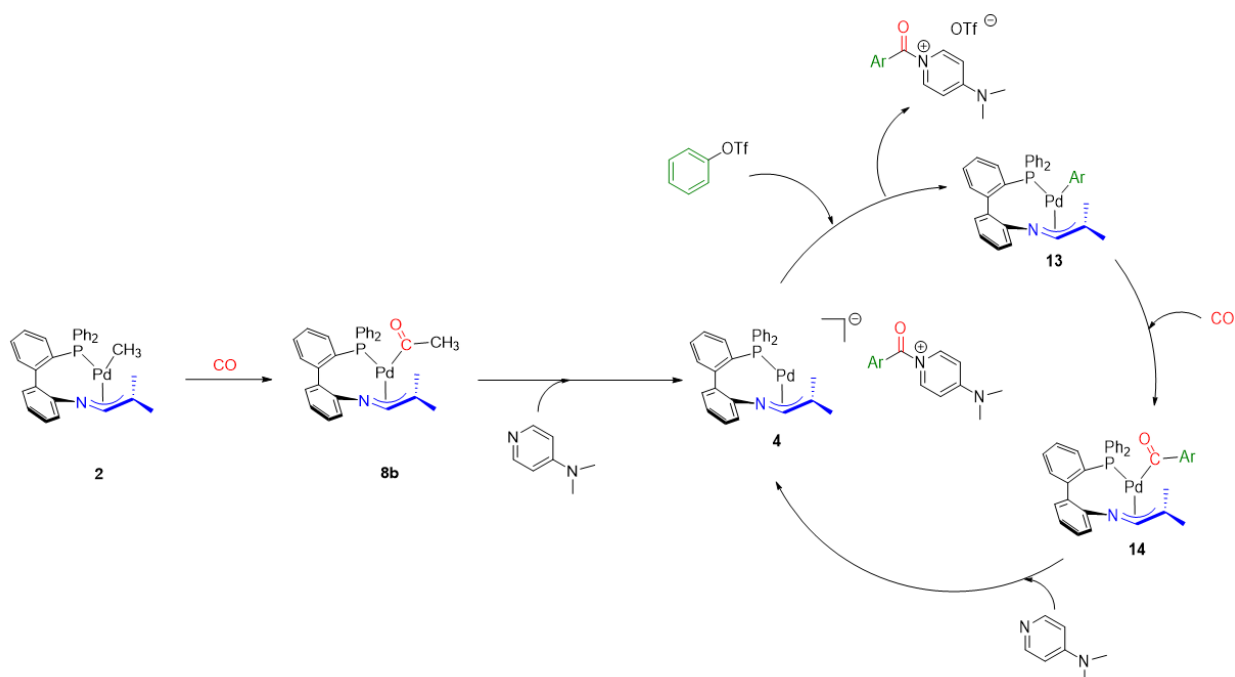
Scheme 4.9. Proposed catalytic cycle for carbonylation of phenyl triflate with Pd complex **2**. In cycle one Ar = Me.

In summary, the promising insertion reactivity with Pd complex **2** and MA, led to the hypothesis that **2** could catalyze ethylene polymerization, however under the tested catalytic conditions **2** was an unsuccessful polymerization catalyst. The ability of **2** to catalyze 1-octene oligomerization and allyl benzene isomerization was also assessed, but again under the tested catalytic conditions **2** was an unsuccessful catalyst. Cyanation catalysis with **2** was attempted because of the unique reactivity observed with **2** and cyanide indicated that an inactive Pd-CN complex would likely not form, and result in a decomposition pathway. The attempted cyanation catalysis with **2** was unsuccessful under the tested conditions. Since, there was evidence that Pd(0) intermediate bearing **L2** would be a stable complex through a catalytic cycle, oxidation addition was likely the barrier to successful catalysis. This was seen again with the attempted carbonylation catalysis where oxidative addition was proposed to be the limiting step towards successful catalysis.

5.0 Conclusions and Future Work

5.1 Summary and Conclusion

Modifying the P^AzA ligand backbone from a single aryl ring to a biaryl backbone led to the isolation of the rare κ^1-P;η^3-NCC coordination mode on a Pd complex and demonstrated how structural variation of the P^AzA ligand can allow for new coordination chemistry and reactivity to occur. The new P^AzA ligand **K[L2]**, with a biaryl backbone was synthesized in three steps. First, the biaryl P^A precursor **A[L2]** was synthesized by a Suzuki cross coupling reaction between 2-bromophenyldiphenylphosphine and 2-aminophenylboronic acid, catalyzed by Pd(dppf)Cl$_2$. **A[L2]** then underwent a condensation reaction with isobutyraldehyde to afford the biaryl P^I precursor **H[L2]**. **H[L2]** was determined to be a tautomeric mixture of both the imine and enamine biaryl precursors. Deprotonation of the **H[L2]** tautomers with potassium hydride led to the formation of the biaryl phosphine 1-azaallyl ligand, **K[L2]**. **K[L2]** was coordinated to [PdCl(CH$_3$)(COD)], to afford Pd complex **2**. The κ^1-P;η^3-NCC coordination mode of complex **2** was characterized by a series of NMR spectroscopy, EXAFS spectroscopy, energy computations, and UV-Vis spectroscopy experiments. Correlation between the 1-AzA protons and the phosphine in ^{1}H-^{31}P HMBC NMR spectrum and the chemical shift of the 1-AzA C^1 and C^2 carbons in ^{13}C{^{1}H} NMR spectrum supported a κ^1-P;η^3-NCC coordination mode. A comparison of unknown complex **2** to known complexes **S** and **T** in the Pd L$_3$-edge experiment indicated that **2** has either a lower oxidation state of Pd or a different coordination geometry of the 1-AzA moiety around Pd. DFT calculations were conducted to determine if the κ^1-P;η^3-NCC coordination mode of **L2** was more favourable than the κ^1-P;μ-N coordination mode, which would have been consistent with known complex **S**. The κ^1-P;η^3-NCC was determined to be more energetically favourable and **2** had absorbance at 390 nm, which was also consistent with a κ^1-P;η^3-NCC coordination mode. Therefore, increasing the P-Pd-N bite angle successfully led to the rare and previously inaccessible κ^1-P;η^3-NCC P^AzA coordination mode on a Pd complex.

The reactivity of **2** with Lewis bases was explored and the Lewis bases tested included pyridine, tertiary phosphines, cyanide, and water. The observed results with both pyridine and phosphine addition to Pd complex **2** were completely different than the previous observed results with Pd(II) dimer **S** and Ru complex **W**, where pyridine or phosphine coordinated to Pd or Ru and the P^AzA κ^2-PN product was isolated and crystallized. Unlike the Ru(II) P^AzA complex **Y**, there was also no formal detection of isomerization between κ^1-P;η^3-NCC and κ^2-PN coordination modes with the addition and removal of Lewis base donors. However, the observed colour changes and changes in NMR spectra suggest that there was a very fast and dynamic equilibrium that occurred with Lewis base addition to complex **2**. This dynamic equilibrium was confirmed to be reversible when Lewis acid $B(C_6F_5)_3$ was added to the equilibrium mixture of **{2 + py}** and complex **2** was regenerated once pyridine was sequestered. The reversible dynamic equilibrium observed with Lewis base substitution could potentially be advantageous for catalysis as it could allow for both substrate coordination and stabilization of a low coordinate intermediate. The observed results with CN^- addition to **2**, suggest that the dynamic **{2 + CN^-}** equilibrium mixture can undergo the reductive elimination of acetonitrile to form a stable Pd(0) intermediate complex **4**. Several Pd catalytic cycles proceed through a Pd(0) active catalyst, as it allows for substrate coordination at two coordination sites, so the ability to generate a stable Pd(0) complex would be extremely valuable for a diverse range of Pd catalyzed reactions. The observed results with water addition to **2**, are consistent with Pd(II) dimer **S**. In both cases the 1-AzA ligand fragment was protonated upon water addition to form Pd imine/enamine intermediates before proceeding down a decomposition pathway to Pd black. The P^AzA ligand is anionic, so it makes sense that the addition of a proton source led to ligand protonation. Since Pd complex **2** had a Pd methyl bond, insertion reactivity with CO and MA was also tested. In both cases there was preliminary evidence that insertion into the Pd methyl bond was possible, however no insertion products were isolated or characterized *in situ*. For this type of insertion to occur, an open coordination site must be generated on the Pd metal

centre to allow for CO or MA to coordinate before insertion can occur. This suggests that **L2** was dynamically adapting different coordination modes to facilitate insertion into the Pd methyl bond. Overall, the unique, fast, and dynamic reactivity observed with Pd complex **2**, and a diverse range of small molecules could be exploited towards several catalytic processes.

The promising insertion reactivity observed with Pd complex **2** and MA, led to the hypothesis that **2** could catalyze ethylene polymerization, 1-octene oligomerization, and allyl benzene isomerization as each mechanism would initially involve the coordination of an alkene to Pd followed by insertion into a Pd alkyl bond. There was preliminary evidence that **L2** could enable this transformation, however under the tested catalytic conditions **2** was an unsuccessful catalyst. The promising reactivity observed with Pd complex **2** and cyanide, led to the hypothesis that **2** could catalyze the cyanation 3-bromopyridine. The most common deactivation pathway for Pd catalyzed cyanation is the formation of an inactive Pd-CN species, which terminates the catalytic cycle. When **2** underwent a reaction with cyanide a dynamic equilibrium mixture between **2**, CN⁻, and **3f** was produced, which indicates that an inactive Pd-CN complex does not form. Furthermore, there is evidence that this **{2 + CN⁻}** equilibrium mixture can undergo the reductive elimination of acetonitrile to form a stable Pd(0) intermediate complex **4**, which would be the active catalyst in the cyanation of 3-bromopyridine. The attempted cyanation catalysis with **2** was unsuccessful under the tested conditions, which suggests that the oxidative addition of 3-bromopyridine onto **4** was likely the barrier to successful catalysis. The promising insertion reactivity observed with Pd complex **2** and CO, led to the hypothesis that **2** could catalyze the carbonylation of aryl triflates. All the Pd complexes that would be generated in the catalytic cycle for this reaction should be stable and possible to form, however the attempted carbonylation catalysis with **2** was unsuccessful under the tested conditions. It was again proposed that the oxidative addition of the aryl triflate onto the Pd(0) active catalyst **4**,was the limiting step towards successful catalysis.

5.2 Future Work

Since Pd complex **2** reacts with both CO and MA further experimentation should be conducted to try to isolate and characterize the various insertion products. Characterization of the insertion products would provide a way to establish the mechanism of how CO and MA insert into the Pd methyl bond, which could then be useful to apply towards catalytic reactions.

When cyanide was substituted onto Pd complex **2** to form **3f**, there was evidence that the complex underwent reductive elimination of acetonitrile to form a Pd(0) intermediate **4**. Similarly, when **H[L2]** was coordinated to a Pd(0) precursor and then subsequently deprotonated, there was again evidence that **4** was formed in an equilibrium mixture. It would be beneficial to develop a conclusive synthesis pathway towards **4**, because the reduction of a Pd(II) intermediate to a Pd(0) complex is fundamental step in a vast number of Pd-catalyzed processes, including cross-coupling or C-H activation.[55] Ligand **L2** has the capacity to alter its coordination mode from κ^1-P;η^3-NCC to κ^2-PN, which could open a second coordination site at Pd in **4**, to allow for substrate coordination and oxidative addition from Pd(0) to Pd(II) (Scheme 5.1). As seen with the tested cyanation and carbonylation catalysis reactions, the barrier to successful catalysis was proposed to be oxidative addition, so a thorough substrate scope towards Pd(0) to Pd(II) oxidative addition should be examined, to determine how best to exploit complex **4** towards successful catalytic reactions.
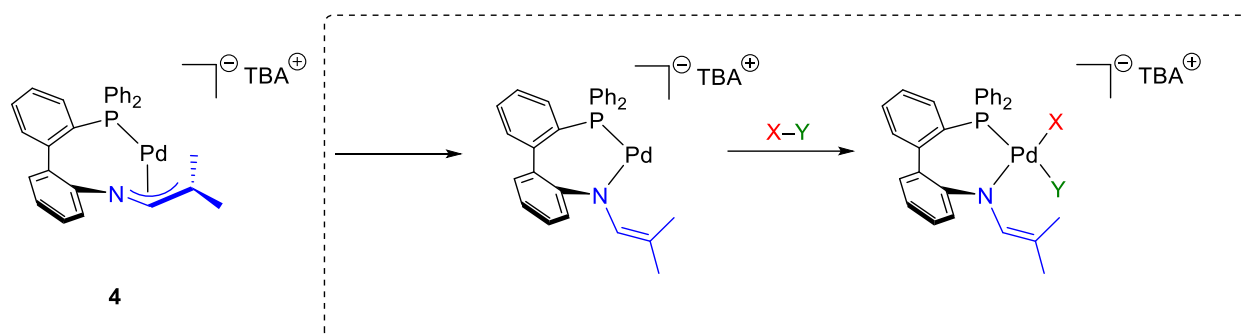
Scheme 5.1. Proposed oxidative addition from Pd(0) to Pd(II).

Synthesizing an analogous Pd complex to complex **2**, with a chloro ligand bound to Pd instead of a methyl ligand bound to Pd could be intriguing, because of the potential to generate two open coordination sites on the Pd metal centre. The two open coordination sites could potentially be generated with a change in **L2** coordination mode along with chloride abstraction. Preliminary work has gone into synthesizing this proposed Pd chloro complex. There is promising evidence that this biaryl Pd choro complex with **L2** coordinated κ^1-P;η^3-NCC can be synthesized by the coordination of **H[L2]** to [PdCl$_2$(COD)] (Scheme 5.2A), followed by deprotonation with potassium hydride (Scheme 5.2B). Developing a reproducible synthetic route and characterizing this proposed Pd chloro complex should be targeted. This Pd complex could potentially have the ability generate two open coordination sites, which would be immensely valuable for oxidative addition, a fundamental step in several Pd-catalyzed processes.
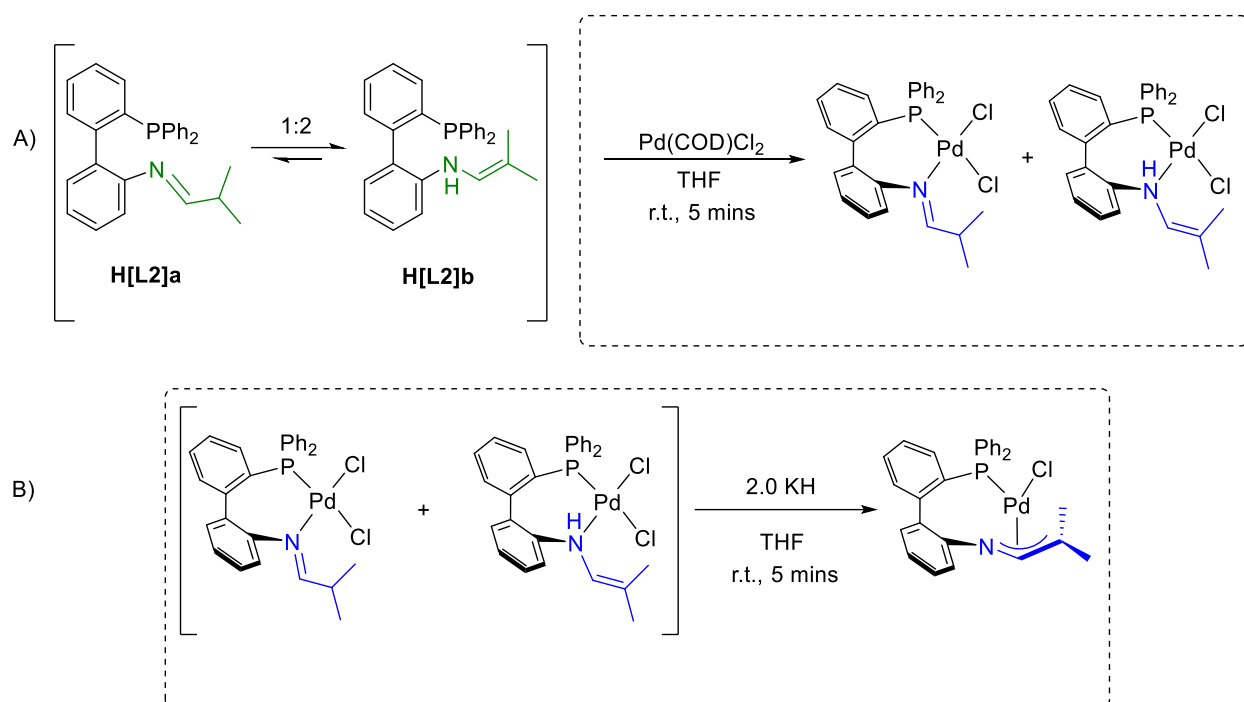
Scheme 5.2. A) Proposed coordination of **H[L2]** to Pd to form a Pd chloro imine complex. B) Proposed deprotonation of the Pd chloro imine complex to form a Pd chloro P^AzA complex.

The reactivity of the proposed Pd chloro complex should also be assessed. It would be useful to investigate the reactivity of the proposed Pd chloro complex towards Lewis base substitution with parallel experiments to those that were conducted with **2**. This would determine if similar reactivity is observed with the proposed Pd chloro complex, or if reaction products with the proposed Pd chloro complex can be isolated or characterized *in situ*. Isolation or *in situ* characterization of these reaction products would provide direct evidence towards the expected change in **L2** ligand coordination mode. Since the proposed Pd chloro complex has a chloride bound to Pd, halide abstraction could be conducted to install a labile Lewis base ligand (L) onto Pd to form a charge separated complex (Scheme 5.3). In the presence of a strong bidentate phosphine donor, L should dissociate, and the phosphine donor should coordinate. This would induce a ligand change in coordination mode from κ^1-P;η^3-NCC to κ^2-PN, to form a complex where the κ^2-PN ligand coordination mode could be characterized, which would show

the dynamic coordination of **L2**. Reduction of the proposed Pd chloro complex to form a Pd(0) complex

may also provide pathway to a direct synthetic route towards Pd(0) complex **4**.
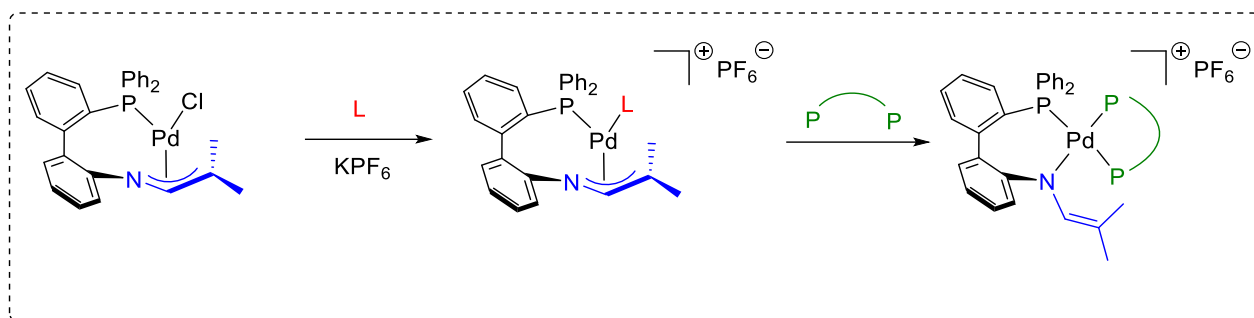
Scheme 5.3. Proposed halide abstraction and bidentate phosphine ligand coordination on the proposed Pd chloro

complex.

6.0 Experimental

## 6.1 General Experimental Procedure

All reactions were conducted in a nitrogen atmosphere glovebox or using standard Schlenk line techniques under an argon atmosphere, unless explicitly stated otherwise. All glassware was oven dried at 150 ˚C for at least three hours and cooled under nitrogen atmosphere prior to use, unless otherwise stated. All reagents used were obtained from commercially available sources and used without further purification, unless otherwise indicated. Potassium hydride was purchased from Alfa Aesar as a 30% w/w suspension in mineral oil and was purified by filtration through a fritted funnel. The solid KH was then washed with dry hexanes and diethyl ether (20 mL/g KH) and dried under vacuum inside a nitrogen atmosphere glovebox for use. The following materials were prepared following literature procedures: **A[L2]**[42], [PdCl(CH$_3$)(COD)][56] and [^{DMP}DAB-Pd-MAH][57]**.** All reaction solvents were obtained from an Innovative Technology 400-5 Solvent Purification system and stored over 4 Å molecular sieves unless otherwise stated. Pyridine was dried over CaH$_2$, distilled under dynamic vacuum, and stored in an inert atmosphere over activated 4 Å molecular sieves. Deuterated solvents were obtained from commercially available sources and stored over 4 Å molecular sieves in an inert atmosphere unless otherwise stated. Acetone-*d$_6$* and toluene-*d$_8$* were purchased in glass ampoules and used as received.

All NMR spectra were obtained using either a 600 or 400 MHz Bruker, or 600 MHz Varian NMR spectrometer at 25 ˚C unless otherwise indicated. ^{1}H and ^{13}C{^{1}H} spectra were referenced internally to TMS at 0 ppm as follows: benzene-*d$_6$* (^{1}H, 7.16 ppm; ^{13}C{^{1}H}, 128.1 ppm), CDCl$_3$ (^{1}H, 7.26 ppm; ^{13}C{^{1}H} 77.2 ppm), toluene-*d$_8$* (^{1}H, 2.08 ppm, ^{13}C{^{1}H}, 20.4 ppm), acetone-*d$_6$* (^{1}H, 2.05 ppm; ^{13}C{^{1}H}, 205.9 ppm).^{31}P{^{1}H} spectra obtained in deuterated solvents were referenced internally to H$_3$PO$_4$ at 0.0 ppm, whereas spectra acquired in non-deuterated solvents were referenced externally to a sample of 85% H$_3$PO$_4$. Multiplicities are identified as: s (singlet), d (doublet), t (triplet), sept (septet), m (multiplet) or, br (broad). Chemical shift assignments were obtained using 1D NMR

spectroscopy and 2D heteronuclear and homonuclear NMR spectroscopy (i.e. ^{1}H-^{1}H COSY, ^{1}H-^{13}C HSQC, ^{1}H-^{13}C/^{31}P/^{15}N HMBC). X-ray diffraction measurements were made on a Bruker Kappa Axis Apex2 diffractometer at a temperature of 110 K. Further details are provided in Appendix A. UV-Vis spectra were collected using an Agilent Technologies Cary 8454 UV-Vis spectrometer, fitted with a Unisoko CoolspeK UV USP-203-A cryostat for low temperature analyses. Infrared spectra were collected on solid samples using a Bruker ALPHA II FTIR spectrometer. Charge-transfer Matrix Assisted Laser Desorption/Ionization (MALDI) mass spectrometry data were collected on an AB Sciex 5800 TOF/TOF mass spectrometer using pyrene as the matrix in a 20:1 molar ratio to complex. Solutions were prepared in C_6H_6 and spotted on a sample plate under an inert atmosphere and transferred to the instrument in a sealed Ziplock® bag. The instrument is equipped with a 349 nm OptiBeam On-Axis laser. The laser pulse rate was 400 Hz and data were collected in reflectron positive mode unless otherwise indicated. Reflectron mode was externally calibrated at 50 ppm mass tolerance. Each mass spectrum was collected as a sum of 500 shots. The acquired data sets were plotted in Microsoft Excel, and simulations for 130 peaks of interest were simulated from envipat.eawag.ch[58] and plotted in Microsoft Excel.

6.2 Ligand Synthesis
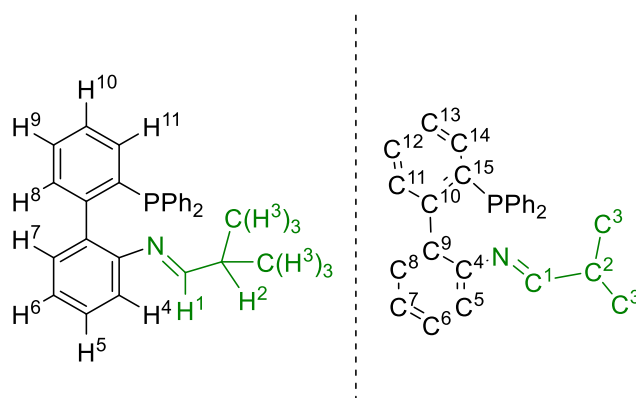
Figure 6.1. General labelling scheme for the phosphine imine ligand **H[L2]**. This scheme will be used consistently for all compounds throughout the experimental. In cases where H³ and C³ atoms are not equivalent H³ and H³', C³ and C³' are used to distinguish between the two sites.

### 6.2.1 Phosphine Imine Synthesis (H[L2])
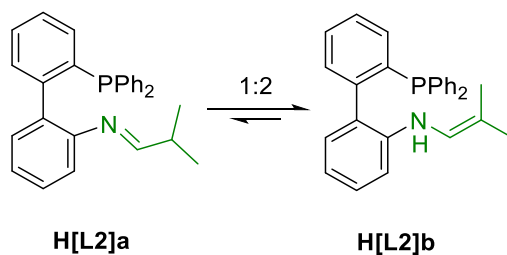
Figure 6.2. Phosphine imine ligand **H[L2]**.

In a glovebox, 2'-(diphenylphosphanyl)-[1,1'-biphenyl]-2-amine (237 mg, 0.671 mmol) was dissolved in toluene (20 mL) and added to a 100 mL Schlenk flask containing a magnetic stir bar and 4 Å molecular sieves. The Schlenk flask was then removed from the glovebox and attached to the Schlenk line. Isobutyraldehyde (0.080 mL, 0.874 mmol) and five drops of formic acid were individually added to the Schlenk flask by a plastic syringe through a septum, and the flask was left to stir for 24 h at room temperature. After 24 h, the solution was filtered through a pad of Celite in a fritted funnel via cannula. The original flask was washed with degassed toluene (3 × 10 mL) and the washings were filtered through Celite. The solvent of the combined filtrates was removed under vacuum at 60 ˚C to afford a

yellow oil. The Schlenk flask was brought into the glovebox and DCM (2 mL) was added to dissolve the yellow oil. The yellow solution was transferred to a 20 mL vial, the Schlenk flask was rinsed with DCM (3 × 1 mL), transferred to the sample vial, and the combined solvent was then reduced under vacuum to afford 2'-(diphenylphosphanyl)-[1,1'-biphenyl]-2-imine **H[L2]** as a white/yellow solid. **H[L2]** is a mixture of two tautomers **H[L2]a** the imine and **H[L2]b** the enamine in a 1:2 ratio, respectively. Yield: 240 mg, 0.589 mmol (88%).

^{1}H NMR (600 MHz, CDCl$_3$): **H[L2]a**: δ = 7.55 (d, $^3J_{HH}$ = 4.7 Hz, 1H, H^1), 7.47 – 7.04 (m, 15H, C$_{12}$H$_8$ and P(C$_6$H$_5$)), 6.96 – 6.59 (m, 3H, C$_{12}$H$_8$), 2.39 (sept. of d, $^3J_{HH}$ = 4.7 Hz, 1.7 Hz, 1H, H^2), 0.97–0.89 (m, 6H, H^3). **H[L2]b**: δ = 7.47 – 7.04 (m, 15H, C$_{12}$H$_8$, P(C$_6$H$_5$)), 6.96 – 6.59 (m, 3H, C$_{12}$H$_8$), 6.08 (d, $^3J_{HH}$ = 10.1 Hz, 1H, H^1), 4.94 (d, $^3J_{HH}$ = 10.1 Hz, 1H, N-H), 1.69 (s, 3H, H^3), 1.36 (s, 3H, $H^{3'}$). ^{31}P{^{1}H} NMR (162 MHz (CDCl$_3$): **H[L2]a**: δ = –12.4 (s, PPh$_2$). **H[L2]b**: δ = –13.3 (s, PPh$_2$). ^{13}C{^{1}H} NMR (151 MHz, CDCl$_3$): **H[L2]a**: δ =171.2 (s, C^1) 150.7 (s, C_{12}H$_8$), 145.9 (d, J_{CP} = 30.6 Hz, C$_{12}$H$_8$), 138.8 (d, J_{CP}= 13.6 Hz, C$_{12}$H$_8$), 137.3 (d, J_{CP} = 6.9 Hz, P(C$_6$H$_5$)), 133.9 (d, J_{CP} = 5.2 Hz, C$_{12}$H$_8$), 133.4 (s, C$_{12}$H$_8$) 131.3 (d, J_{CP} = 4.2 Hz, P(C$_6$H$_5$)), 130.9 (d, J_{CP} = 5.3 Hz, C$_{12}$H$_8$), 128.6 (s, C$_{12}$H$_8$), 128.5 (s, C$_{12}$H$_8$), 128.4 (s, P(C$_6$H$_5$)), 128.3 (s, C$_{12}$H$_8$), 128.2 (s, P(C$_6$H$_5$)) 127.3, (s, C$_{12}$H$_8$), 123.8 (s, C$_{12}$H$_8$), 119.6 (s, C$_{12}$H$_8$), 34.6 (s, C^2), 18.0 (s, C^3). **H[L2]b**: δ = 144.2 (d, J_{CP} = 30.5 Hz, C$_{12}$H$_8$) 141.3 (s, C$_{12}$H$_8$), 137.4 (d, J_{CP} = 7.8 Hz, C$_{12}$H$_8$), 137.0 (d, J_{CP} = 11.7 Hz, P(C$_6$H$_5$)), 134.3 (s, C$_{12}$H$_8$), 134.0 (d, J_{CP} = 5.9 Hz, C$_{12}$H$_8$), 131.0 (d, J_{CP} = 3.4 Hz, P(C$_6$H$_5$)), 130.8 (d, J_{CP} = 4.5 Hz, C$_{12}$H$_8$), 129.8 (d, J_{CP} = 6.9 Hz, P(C$_6$H$_5$)), 129.6 (s, C$_{12}$H$_8$), 129.1 (s, C$_{12}$H$_8$), 128.4 (s, C$_{12}$H$_8$), 128.3 (s, P(C$_6$H$_5$)), 126.7 (d, J_{CP} = 6.9 Hz, C$_{12}$H$_8$), 121.3 (s, C^1), 117.3 (s, C$_{12}$H$_8$), 110.7 (s, C$_{12}$H$_8$), 109.7 (s, C^2) 22.5 (s, C^3), 16.1 (s, $C^{3'}$). ATR-FTIR (cm^{-1}): ν 3067 (C$_{sp}$^{3} –H, w), 1680 (C=N). ESI MS: m/z found: 408.1865, calc: **[H[L2]]**$^+$ 408.1881.

6.2.2 Phosphine 1-Azaallyl Synthesis (K[L2])
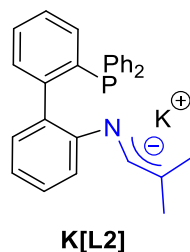

Figure 6.3. Phosphine 1-azaallyl ligand **K[L2]**.

In a glovebox, **H[L2]** (112 mg, 0.270 mmol) was dissolved in THF (2 mL) and added to a suspension of KH (44 mg, 1.09 mmol) in THF (2 mL) in a 20 mL vial. The **H[L2]** solution was added to the KH vial with vigorous stirring, and immediately the solution changed colour from pale yellow to light orange/red. The reaction solution was left to stir for 24 h at room temperature, during which the solution became a dark orange/red. The solution was passed through a pad of Celite to remove any unreacted KH. The solvent of the filtrate was then reduced to 1 mL under vacuum and cold pentane (3 mL) was added to the vial to precipitate an orange powder. The precipitate was washed with cold pentane (3 × 1 mL), and the solvent from each wash was removed by pipette. The resulting solid was dried under vacuum to produce **K[L2]** as an orange powder. NOTE: **K[L2]** is thermally unstable and was stored in the freezer (–20 °C). Yield: 73 mg, 0.16 mmol (60%).

^{1}H NMR (600 MHz, (CD$_3$)$_2$CO): δ = 7.53 – 7.49 (m, 1H, C$_{12}$$H_8$), 7.43 – 7.37 (m, 8H, C$_{12}$$H_8$, P(C$_6$$H_5$)), 7.20 – 7.09 (m, 6H, C$_{12}$$H_8$, P(C$_6$$H_5$)), 6.82 (d, $^3J_{HH}$ = 8.4 Hz, 1H, C$_{12}$$H_8$), 6.71 (d, $^3J_{HH}$ = 7.2 Hz, 1H, C$_{12}$$H_8$), 6.56 – 6.50 (m, 1H, C$_{12}$$H_8$), 6.15 (s, 1H, H^1), 1.66 (s, 3H, H^3), 1.32 (s, 3H, $H^{3'}$). ^{31}P{^{1}H} NMR (243 MHz, (CD$_3$)$_2$CO): δ = –13.6 (s, PPh$_2$). ^{13}C{^{1}H} NMR (151 MHz, (CD$_3$)$_2$CO)): δ = 145.0 (d, J_{CP} = 31.5, C$_{12}$$H_8$),142.0 (s, C$_{12}$$H_8$), 139.2 (d, J_{CP} = 13.9 Hz, C$_{12}$$H_8$), 138.2 (d, J_{CP} = 3.3 Hz, P(C$_6$$H_5$)), 134.9 (s, C$_{12}$$H_8$), 134.4 (d, J_{CP} = 9.8 Hz, P(C$_6$$H_5$)), 134.3 (s, C$_{12}$$H_8$), 134.2 (s, C$_{12}$$H_8$), 131.5 (d, J_{CP} = 5.3 Hz, C$_{12}$$H_8$), 131.4 (d, J_{CP} = 3.0 Hz, C$_{12}$$H_8$), 130.5 (s, C$_{12}$$H_8$), 129.6 (s, C$_{12}$$H_8$), 129.3 (d, J_{CP} = 10.6 Hz, P(C$_6$$H_5$)), 129.1 (d J_{CP} = 6.04 Hz, P(C$_6$$H_5$)), 122.0 (s, C^1), 117.9 (s, C$_{12}$$H_8$), 111.3 (s, C$_{12}$$H_8$), 109.1

(s, C^2), 22.4 (s, C^3) 15.9 (s, $C^{3'}$). ATR-FTIR (cm^{-1}): ν 3049 ($C_{sp}{}^3$ –H, w), 1090 (P–Ar, m). MALDI MS (pyrene) collected in negative ion mode m/z found: 406.2, calc. [**L2**]$^{\cdot-}$: 406.2.

6.3 Pd Complex Synthesis

6.3.1 Pd Imine Complex (1) Synthesis
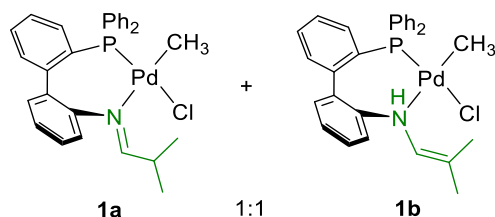

Figure 6.4. Pd imine complex **1**.

H[L2] (65 mg, 0.16 mmol) was dissolved in DCM (2 mL) and added to a solution of [PdCl(CH$_3$)(COD)] (38 mg, 0.15 mmol) and stirred for 24 h. The reaction volume was reduced to 0.5 mL and placed in a freezer at –20 ˚C for 10 min. Cold pentane (6 mL) was added to produce a white precipitate. The solvent was decanted via pipette and the white solid was washed with cold pentane (3 × 4 mL) and dried under vacuum to yield **1** as a white powder. Yield: 55 mg, 67%.

^{1}H NMR (600 MHz, CDCl$_3$): **1a**: δ =7.39 – 7.34 (m, 4H, $C_{12}H_4$, P(C_6H_5)), 7.26 – 7.15 (m, 11H, $C_{12}H_4$, P(C_6H_5)), 6.94 – 6.87 (m, 1H, $C_{12}H_8$), 6.83 – 6.75 (m, 1H, $C_{12}H_8$), 6.32 (d, $^3J_{HH}$ = 7.7 Hz, 1H, $C_{12}H_4$), 3.53 (d of sept, $^3J_{HH}$ = 1.0 Hz, 6.6 Hz, 1H, H^2), 1.19 (d, $^3J_{HH}$ = 6.6 Hz, 3H, H^3), 0.68 (d, $^3J_{HH}$ = 6.6 Hz, 3H, $H^{3'}$), 0.47 (d, $^3J_{HP}$ = 3.4 Hz, 3H, Pd-CH_3). **1b**: 7.63 – 7.52 (m, 4H, $C_{12}H_8$, P(C_6H_5)), 7.52 – 7.40 (m, 8H, P(C_6H_5)), 7.33 – 7.26 (m. 2H, $C_{12}H_8$), 7.10 – 7.03 (m, 1H, $C_{12}H_8$), 7.01 – 6.95 (m, 1H, $C_{12}H_8$), 6.64 – 6.52 (m, 1H, $C_{12}H_8$), 6.13 (dd, $^3J_{HH}$ = 1.4 Hz, 7.6 Hz, 1H, $C_{12}H_8$), 5.90 (br, 1H, N-H), 1.65 (br, 3H, H^3), 1.47 (s, 3H, $H^{3'}$), 0.60 (d, $^3J_{HP}$ = 3.6 Hz, 3H, Pd-CH_3). ^{31}P{^{1}H} NMR (243 MHz, CDCl$_3$): **1a**: δ = 35.4 (s, PPh$_2$). **1b**: 36.2 (s, PPh$_2$). ^{13}C{^{1}H} NMR (151 MHz, CDCl$_3$): **1a**: δ = 179.5 (s, C^1), 148.6 (s, $C_{12}H_8$), 35.3 (s, C^2), 19.0 (s, C^3) 18.5 (s, $C^{3'}$) 0.76 (d, J_{CP} = 2.9 Hz, Pd-CH_3). **1b**: δ = 121.4 (s, C^1), 119.7 (s, C^2), 22.5 (s, C^3), 22.5 (s, $C^{3'}$), 1.26 (d, J_{CP} = 2.7 Hz, Pd-CH_3). The following signals

cannot be assigned specifically to **1a** or **1b**. 136.0 (d, J_{CP} = 14.0 Hz, $C_{12}H_8$), 134.2 (d, J = 12.5 Hz, $C_{12}H_8$) 132.5 (s, P(C_6H_5)), 132.4 (s, P(C_6H_5)), 132.3 (s, $C_{12}H_8$), 132.3 (s, $C_{12}H_8$), 132.3 (s, $C_{12}H_8$), 132.3 (s, $C_{12}H_8$), 132.2 (s, $C_{12}H_8$), 132.2 (s, $C_{12}H_8$,), 131.6 (s, $C_{12}H_8$), 131.0 (s, $C_{12}H_8$), 130.9 (d, J_{CP} = 2.3 Hz, $C_{12}H_8$), 130.8 (d, J_{CP} = 2.3 Hz, $C_{12}H_8$), 129.8 (s, $C_{12}H_8$), 129.4 (s, $C_{12}H_8$), 129.1 (s, $C_{12}H_8$), 129.0 (s, $C_{12}H_8$), 128.8 (s, $C_{12}H_8$), 128.8 (s, $C_{12}H_8$), 128.7 (s, $C_{12}H_8$), 128.6 (s, $C_{12}H_8$), 128.5 (s, P(C_6H_5)), 128.4 (s, P(C_6H_5)), 128.4 (s, P(C_6H_5)), 128.3 (s, P(C_6H_5)), 127.4 (d, J_{CP} = 8.2 Hz, $C_{12}H_8$), 126.4 (s, $C_{12}H_8$), 125.4 (s, $C_{12}H_8$), 124.0 (s, $C_{12}H_8$), 122.5 (s, $C_{12}H_8$). ATR-FTIR (cm^{-1}): ν 3306 (N-H, w), 1671 (C=N, m). MALDI MS (pyrene) m/z found: 337.1, calc: $[H[L2]-C_4H_8N]^{\bullet+}$ 337.1, found: 347.0, calc: $[1-CH_3]^{\bullet+}$ 347.0.

6.3.2 Pd P^AzA Complex (2) Synthesis

2
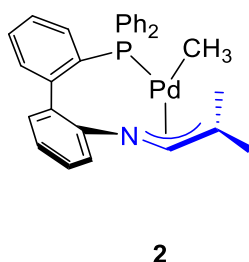
Figure 6.5. Pd P^AzA complex **2**.

Prior to initiation of the reaction, all reagents were stored in the glovebox freezer (–20 °C) for at least 30 min. In a glovebox, separate solutions of **K[L2]** (50 mg, 0.112 mmol) and [PdCl(CH$_3$)(COD)] (23 mg, 0.094 mmol) were prepared in cold THF (2 mL each) in two separate 20 mL vials. The **K[L2]** solution was added dropwise to the stirring solution of [PdCl(CH$_3$)(COD)] resulting in an immediate colour change from white to orange. The orange solution was stirred for five minutes and was filtered through a pad of Celite into a 20 mL vial. The reaction vial was rinsed with THF (0.5 mL) passed through the filter until the rinses were no longer yellow. The rinses were filtered again through a pad of Celite, and the filtrates were combined. The solvent of the filtrate was removed under vacuum to give

an orange solid. NOTE: **2** is thermally unstable and it was stored in the freezer (–20 ˚C). Yield: 35 mg, 0.066 mmol (70%).

^{1}H NMR (400 MHz, C$_6$D$_6$): δ = 7.57 – 7.50 (m, 5H, C$_{12}$H$_8$), 7.09 – 6.95 (m, 10H, P(C$_6$H$_5$)), 6.88 (s, 1H, *H*^{1}), 6.80 – 6.76 (m, 1H, C$_{12}$H$_8$), 6.65 – 6.60 (m, 1H, C$_{12}$H$_8$), 6.46 (d, 3 $^3J_{HH}$ = 7.3Hz, 1H, C$_{12}$H$_8$), 1.82 (d, $^3J_{HH}$ = 3.8 Hz, 3H, *H*^{3}), 1.72 (d, $^3J_{HH}$ = 6.9 Hz, 3H, *H*$^{3'}$), 0.52 (d, $^3J_{HP}$ = 3.6 Hz, 3H, Pd-C*H*$_3$). ^{31}P{^{1}H} NMR (162 MHz, C$_6$D$_6$): δ = 25.8 (s, *P*Ph$_2$). ^{13}C{^{1}H} NMR (151 MHz, C$_6$D$_6$): δ = 153.1 (s, *C*$_{12}$H$_8$), 148.1 (s, *C*$_{12}$H$_8$), 136.2 (d, J_{CP} = 14.1 Hz, *C*$_{12}$H$_8$), 135.4 (d, J_{CP} = 12.2 Hz, *C*$_{12}$H$_8$), 134.7 (d, J_{CP} = 7.0 Hz, P(*C*$_6$H$_5$)), 133.0 (s, *C*$_{12}$H$_8$), 132.7 (s, *C*$_{12}$H$_8$), 131.1 (s, *C*$_{12}$H$_8$), 131.0 (d, J_{CP} = 7.6 Hz, P(*C*$_6$H$_5$)), 130.6 (d, J_{CP} = 18.0 Hz, *C*$_{12}$H$_8$), 129.7 (d, J_{CP} = 4.7 Hz, *C*^{1}), 128.8 (s, *C*$_{12}$H$_8$), 128.7 (d, J_{CP} = 10.1 Hz, P(*C*$_6$H$_5$)), 128.4 (s, *C*$_{12}$H$_8$), 126.6 (d, J_{CP} = 7.0 Hz, P(*C*$_6$H$_5$)), 121.9 (s, *C*$_{12}$H$_8$), 113.9 (s, *C*$_{12}$H$_8$), 88.7 (d, $^2J_{CP}$ = 28.2 Hz, *C*^{2}), 22.2 (s, *C*^{3}), 21.2 (s, *C*^{3}), –1.3 (d, J_{CP} = 11.8 Hz, Pd-*C*H$_3$). ATR-FTIR (cm^{-1}): ν 2957 (C$_{sp}^2$ –H, w), 1098 (P– Aryl, m). MALDI MS (pyrene) m/z found: 406.1, calc: [**L2**]$^{•+}$ 406.2, found: 512.1, calc: [**2**- CH$_3$]$^{•+}$ 512.1.

6.3.3 Pd(0) Imine MAH Complex (12) Preliminary Synthesis
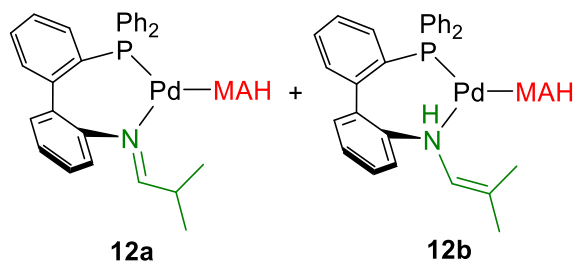
Figure 6.6. Pd(0) imine MAH complex **12**.

In a glovebox, separate solutions of **H[L2]** (21 mg, 0.05 mmol) and [^{DMP}DAB-Pd-MAH] (20 mg, 0.04 mmol) were prepared in cold THF (1 mL each) in two separate 20 mL vials. The **H[L2]** solution was added to the stirring solution of [^{DMP}DAB-Pd-MAH] resulting in an immediate colour change from dark red to dark yellow. The yellow solution was stirred for 3 h and then it was filtered through a pad of Celite into a 20 mL vial. The reaction volume was reduced to 0.5 mL. Cold pentane (6

mL) was added to produce a yellow precipitate, and the suspension was placed in a freezer at –20 ˚C for 1 h. The solvent was decanted via pipette and the yellow solid was washed with cold pentane (3 × 4 mL) and dried under vacuum to yield **12** as a yellow powder. Yield = 20 mg, 0.03 mmol (95%)

$^{31}P\{^{1}H\}$ NMR (162 MHz, C_6D_6): δ = 28.8 (s, PPh_2), 25.5 (s, PPh_2).

6.3.4 Pd(0) P^AzA MAH Complex (5) Preliminary Synthesis
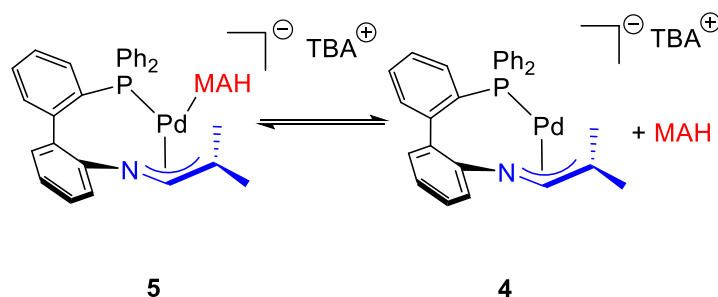
Figure 6.7. Pd(0) P^AzA MAH complex **5**.

In a glovebox, **12** (20 mg, 0.03 mmol) was dissolved in THF (1 mL) and added to a suspension of KH (10 mg, 0.25 mmol) and TBABr (10 mg, 0.07 mmol) in THF (2 mL) in a 20 mL vial. The solution of **12** was added to the KH/TBABr vial with vigorous stirring, and immediately the solution changed colour from yellow to dark red. The reaction solution was left to stir for 24 h at room temperature. The solution was passed through a pad of Celite to remove any unreacted KH. The solvent of the filtrate was then reduced to 1 mL under vacuum and cold pentane (3 mL) was added to the vial to precipitate a red powder. The red powder was stored in a –20 ˚C freezer overnight. The precipitate was washed with cold pentane (3 × 1 mL) and the solvent was removed by pipette. The solid was dried under vacuum to produce **5** as a red powder.

$^{31}P\{^{1}H\}$ NMR (162 MHz, C_6D_6): δ = 33.2 (s, PPh_2), 29.1 (s, PPh_2).

6.4 General Procedure for Substitution Reactivity with Lewis Bases

6.4.1 General Procedure for Pyridine Reactivity

In a glovebox, a solution of **2** (10 mg, 0.020 mmol) dissolved in C_6H_6 (1 mL) was prepared in a 4 mL vial. One equivalent of pyridine was added, and the solution was transferred to an NMR tube, where it was monitored by $^{31}P\{^1H\}$ NMR spectroscopy. This procedure was repeated for the pyridine titrations where a subsequent equivalent of pyridine was added from 1 – 5 equivalents, 10, and 20 equivalents. In a separate experiment, complex **2** was dissolved in a solution of py-d_5 and it was analyzed by ^1H and $^{31}P\{^1H\}$ NMR spectroscopy.

6.4.1.1 Procedure For $B(C_6F_5)_3$ Addition

In a glovebox, a 0.375 mM stock solution of pyridine in C_6D_6 was prepared in a 4 mL vial. In a separate 4 mL vial, a solution of **2** (10 mg, 0.020 mmol) dissolved in the pyridine/C_6D_6 stock solution (1 mL) was prepared. 40 equivalents of $B(C_6F_5)_3$ (100 mg, 0.76 mmol) were dissolved in the solution of **2**, pyridine, and C_6D_6. The solution was transferred to an NMR tube, where it was analyzed by ^1H, $^{31}P\{^1H\}$, $^{19}F\{^1H\}$, and ^{11}B NMR spectroscopies.

$B(C_6F_5)_3$ Pyridine Adduct: ^1H NMR (400 MHz, C_6D_6): δ = 8.05 (d), 6.75 (t), 6.41 (t). $^{19}F\{^1H\}$ NMR (376 MHz, C_6D_6): δ = –131.5 (d), –155.9 (t), –163.0 (t). ^{11}B NMR (128 MHz, C_6D_6): δ = –3.5(s).

Regenerated Complex **2**: $^{31}P\{^1H\}$ NMR (162 MHz, C_6D_6): δ = 25.6 (s, PPh$_2$).

6.4.2 General Procedure for Phosphine Reactivity

In a glovebox, a solution of **2** (10 mg, 0.020 mmol) dissolved in C_6H_6 (1 mL) was prepared in a 4 mL vial. One equivalent of PR$_3$ was added, and the solution was transferred to an NMR tube, where it was analyzed by $^{31}P\{^1H\}$ NMR spectroscopy. This procedure was conducted separately for the following phosphines: PPh$_3$, P(tBu)$_3$, P(NEt$_2$)$_3$, and PEt$_3$.

6.4.3 General Procedure for CN⁻ Reactivity

In a glovebox, a solution of **2** (10 mg, 0.020 mmol) dissolved in DMF (1 mL) was prepared in a 4 mL vial. In a separate 4 mL vial equipped with a stir bar, one equivalent of TBABr (0.020 mmol) was added to a solution of one equivalent of $Zn(CN)_2$ (0.020 mmol) in DMF (1 mL). The solution of **2** in DMF was transferred to the 4 mL vial containing TBACN solution. The reaction mixture was stirred for five minutes and there was an immediate colour change from orange to colourless. The solution was then transferred to an NMR tube, where it was analyzed by $^{31}P\{^1H\}$ NMR spectroscopy.

6.4.4 General Procedure for Water Reactivity

In a glovebox, a solution of **2** (10 mg, 0.020 mmol) dissolved in C_6D_6 (0.6 mL) was prepared in a 4 mL vial and the solution was transferred to an NMR tube with a septum cap. One drop of degassed water was added to the NMR tube using a syringe, and the NMR tube was then inverted three times. The reaction was analyzed by ^1H and $^{31}P\{^1H\}$ NMR spectroscopy.

$^{31}P\{^1H\}$ NMR (162 MHz, C_6D_6): δ = 36.2 (s, PPh$_2$), 35.4 (s, PPh$_2$).

6.5 General Procedure for UV-Vis Spectroscopy

All UV-Vis spectra were obtained using the Agilent Technologies Cary 8454 UV-Vis spectrometer at 25 ˚C unless otherwise indicated. A solvent blank was run before each set of samples to calibrate the instrument to the selected solvent. All data was plotted using Microsoft Excel.

6.5.1 UV-Vis Procedure for Complex 2 Characterization

A stock solution of **2** dissolved in toluene was prepared in a 4 mL vial. Solutions with concentrations of 0.1 mM, 0.2 mM, 0.3 mM, 0.4 mM, and 0.6 mM of **2** were prepared in separate 4 mL vials and added to a cuvette equipped with a septum cap. UV-Vis spectra were collected for each concentration. The λ_{max} was found at 390 nm and an ε value of 1706 $M^{-1}\,cm^{-1}$ was determined.

6.5.2 UV-Vis Procedure for P(^{t}Bu)$_3$ Titration

A 0.4 mM solution of **2** dissolved in toluene was prepared in a 4 mL vial. The solution (3 mL) was added to a cuvette equipped with a stir bar and septum cap. The solution was cooled to -80 °C, heated to 60 °C, or run at 25 °C in the spectrometer and a UV-Vis spectrum was collected. Using a gas tight syringe, 0.2 equivalents of P(^{t}Bu)$_3$ were added to the cuvette with stirring and a UV-Vis spectrum was collected after a 30 second equilibration period. This procedure was repeated with 0.2 equivalent P(^{t}Bu)$_3$ additions until the solution had one equivalent of P(^{t}Bu)$_3$ added. From here P(^{t}Bu)$_3$ was added via syringe until the solution had 10 equivalents of P(^{t}Bu)$_3$. Spectra were collected with each addition of P(^{t}Bu)$_3$ at –80 °C, 60 °C, or 25 °C.

6.6 General Procedure for CO Reactivity

In a glovebox, a solution of **2** (10 mg, 0.020 mmol) dissolved in C$_6$D$_6$ (1 mL) or toluene-d_8 (1 mL) was prepared in a 4 mL vial. The solution was transferred to a J Young NMR tube and the NMR tube was sealed and removed from the glovebox. The J Young NMR tube was connected to a Schlenk line under a carbon monoxide atmosphere (prepared by evacuating and filling with CO 3 times). Either at room temperature or submerged in a –50 °C dry ice/acetone bath the tube was degassed by three cycles of a freeze/pump/thaw procedure using dry ice/acetone and backfilled at room temperature with CO. The reaction was analyzed by ^{1}H and ^{31}P{^{1}H} NMR spectroscopy.

6.7 General Procedure for Methyl Acrylate Reactivity

In a glovebox, a solution of **2** (10 mg, 0.020 mmol) dissolved in C$_6$D$_6$ (1 mL) was prepared in a 4 mL vial. One equivalent of MA was added, and the solution was transferred to an NMR tube, where it was analyzed by ^{1}H and ^{31}P{^{1}H} NMR spectroscopy. The ^{1}H and ^{31}P{^{1}H} NMR spectroscopy was also analyzed with a scan delay of 5 s.

^{31}P{^{1}H} NMR (162 MHz, C$_6$D$_6$): δ = 23.2 (s), 19.4 (s).

6.8 General Procedure for Attempted Catalytic Ethylene Homopolymerization

A 25 mL Parr Reactor fitted with a glass insert was brought into the glovebox. In the glovebox, a 58 mM solution of the catalyst **2** (52 mg, 0.098 mmol) dissolved in benzene (1.7 mL) was prepared in a 20 mL vial. A portion of the catalyst **2** stock solution (86 μL, 0.005 mmol) and toluene (14.914 mL) were added to the Parr Reactor to give 15 mL of a 0.005 mM solution of **2**. The Parr Reactor was sealed and then removed from the glovebox and stirring was initiated. The Parr Reactor was pressurized with 150 psi of ethylene, and the reactor pressure line was closed. The reactor was heated to 80 ˚C, and left to stir for 24 h, after which, the reactor was cooled to room temperature, pressure was released, and the solution was open to air. The solution was transferred from the reactor into a 250 mL round bottom flask, MeOH (60 mL) was added to the flask submerged in dry ice and acetone to precipitate the generated polymer. No visible precipitate was observed. The solvent was removed via rotary evaporation and a white precipitate with an average mass of 11 mg was observed.

Product formed with **2** as a catalyst: ^{1}H NMR (400 MHz, CDCl$_3$): δ = 7.00 (s, 2H), 5.03 (s, 1H), 2.29 (s, 2H) 1.40 (s), 1.28 (s), 0.88 (br, 3H).

6.9 General Procedure for Attempted Catalytic 1-Octene Oligomerization

In a glovebox a solution of **2** (10 mg, 0.020 mmol) dissolved in toluene-d_8 was prepared and 1 mL of the stock solution was added to four separate 4 mL vials (A-D). In vial A, one equivalent of 1-octene (0.020 mmol) was added, and the solution was transferred to an NMR tube, where it was analyzed after 24 hours at room temperature by ^{1}H NMR spectroscopy. In vial B, 50 equivalents of 1-octene (1.000 mmol) were added, and the solution was transferred to an NMR tube, where it was analyzed after 24 hours at room temperature by ^{1}H NMR spectroscopy. In vial C, one equivalent of 1-octene (0.020 mmol) was added, and the solution was transferred to an NMR tube, where it was heated to 80 ˚C for 24 hours and analyzed by ^{1}H NMR spectroscopy. In vial D, 50 equivalents of 1-octene (1.000 mmol) were added, and the solution was transferred to an NMR tube, where it was heated to 80

°C for 24 hours and analyzed by ^{1}H NMR spectroscopy. After 24 hours there were no changes observed in any of the four reactions.

6.10 General Procedure for Attempted Catalytic Allyl Benzene Isomerization

In a glovebox, two solutions of **2** (10 mg, 0.020 mmol) dissolved in C_6D_6 (1 mL each) were prepared in 4 mL vials. In vial one, allyl benzene (0.190 mmol) was added, and the solution was transferred to an NMR tube, where it was monitored for 24 hours at room temperature by ^{1}H NMR spectroscopy (Timepoints: 10 min, 1 h, 6 h, 24 h). In vial two, allyl benzene (0.190 mmol) was added, and the solution was transferred to an NMR tube, where it was heated to 80 °C for 24 hours and monitored by ^{1}H NMR spectroscopy (Timepoints: 10 min, 1 h, 6 h, 24 h). Over 24 hours there were no changes observed in either of the two reactions.

6.11 General Procedure for Attempted Catalytic Cyanation of 3-Bromopyridine

A 4 mL vial equipped with a stir bar was charged with $Zn(CN)_2$ (40 mg, 0.34 mmol, 0.60 equiv) and TBABr (22 mg, 0.10 mmol, 0.25 equiv), and brought into a glovebox. In the glovebox, a solution of Pd complex **2** (15 mg, 0.03 mmol, 0.05 equiv), DMF (3.0 mL), and 3-bromopyridine (148 μL, 0.57 mmol, 1.0 equiv) was added to the vial that contained $Zn(CN)_2$ and TBABr. The 4 mL vial was capped, and the cap was secured with electrical tape. The reaction mixture was stirred outside the glovebox in a heating block at either 65 °C or 120 °C, for 20 h. After 20 h, the reaction was cooled to ambient temperature, diluted with EtOAc (10 mL), filtered through Celite and washed with 10 wt% LiCl(aq) (3 x 5 mL). The organic layer was dried ($MgSO_4$), filtered through a frit, and the filtrate was concentrated *in vacuo*. The crude residue was analyzed by $^{13}C\{^{1}H\}$ NMR spectroscopy, however there was no indication of product formation.

6.12 General Procedure for Attempted Carbonylation of Aryl Triflates to Aroyl-DMAP Salts

In a glovebox, a 25 mL thick-walled Strauss flask with a side arm was equipped with a stir bar and charged with 4-dimethylaminopyridine (DMAP) (73 mg, 0.60 mmol) and phenyl triflate (113 mg,

0.50 mmol) or *p*-tolyl triflate (120 mg, 0.50 mmol). In a separate 4 mL vial Pd complex **2** (15 mg, 0.03 mmol, 5 mol%), was dissolved in 2 mL of toluene, and transferred to the reaction vessel containing DMAP and the aryl triflate. The Strauss flask was sealed and removed from the glovebox. The Strauss flask was connected to a Schlenk line under a carbon monoxide atmosphere (prepared by evacuating and filling with CO 3 times). The Strauss flask was degassed by three cycles of a freeze/pump/thaw procedure using liquid nitrogen and backfilled at room temperature with CO. The reaction was then stirred at 60 ˚C or 120 ˚C for 24 h. After 24 h, the CO was removed in vacuo by freeze/thaw cycles with liquid nitrogen, and the Strauss flask was brought back into the glovebox. The solution was washed with an excess of toluene and pentane, filtered through a frit packed with Celite, and transferred to an NMR tube. The filtrate was analyzed by $^{13}C\{^{1}H\}$ NMR spectroscopy, however there was no indication of product formation.

7.0 References

[1] van Leeuwen, P. W. N. M. *Reference Module in Chemistry, Molecular Sciences and Chemical Engineering*; Elsevier, 2016.

[2] Shelke, Y. G.; Yashmeen, A.; Gholap, A. V. A.; Gharpure, S. J.; Kapdi, A. R. *Chem. Asian J.* **2018**, 13 (20), 2991–3013.

[3] Foscato, M.; Jensen, V. R. *ACS Catal*. **2020**, 10 (3), 2354–2377.

[4] dos Passos Gomes, G.; Pollice, R.; Aspuru-Guzik, A. Chemrxiv.org. (accessed 2024-08-07).

[5] Fadhel, A. Z.; Pollet, P.; Liotta, C. L.; Eckert, C. A. *Molecules* **2010**, *15* (11), 8400–8424.

[6] Lundgren, R. J.; Stradiotto, M. *Ligand Design in Metal Chemistry*. Wiley September 23, 2016, pp 1–14.

[7] Engle, K. M.; Yu, J.-Q. *J. Org. Chem*. **2013**, *78* (18), 8927–8955.

[8] Durand, D. J.; Fey, N. *Chem. Rev*. **2019**, *119* (11), 6561–6594.

[9] Matsuoka, W.; Harabuchi, Y.; Maeda, S. *ACS Catal*. **2023**, *13* (8), 5697–5711.

[10] Wang, W.; Hammond, G. B.; Xu, B. *J. Am. Chem. Soc*. **2012**, *134* (12), 5697–5705.

[11] Macyk, W.; Franke, A.; Stochel, G. *Coord. Chem. Rev*. **2005**, *249* (21–22), 2437–2457.

[12] Wang, Q.; Brooks, S. H.; Liu, T.; Tomson, N. C. *Chem. Commun*. **2021**, *57* (23), 2839–2853.

[13] Maurya, Y.; Singh, A.; Kumar, V.; Ul Nisa, M.; Chatterjee, S. *Tetrahedron Lett*. **2024**, *142* (155066), 155066.

[14] Taylor, L. J.; Kays, D. L. *Dalton Trans*. **2019**, *48* (33), 12365–12381.

[15] Roesky, P. W.; Fout, A. R. *Inorg. Chem*. **2021**, *60* (18), 13757–13758.

[16] Stucke, N.; Flöser, B. M.; Weyrich, T.; Tuczek, F. *Eur. J. Inorg. Chem*. **2018**, *2018* (12), 1337–1355.

[17] Zeng, Q.; Lewis, F. W.; Harwood, L. M.; Hartl, F. *Coord. Chem. Rev*. **2015**, *304–305*, 88–101.

[18] Itoh, S. *Acc. Chem. Res*. **2015**, *48* (7), 2066–2074.

[19] Hetterscheid, D. G. H.; Reek, J. N. H. *Angew. Chem. Int. Ed Engl*. **2012**, *51* (39), 9740–9747.

[20] Slone, C. S.; Weinberger, D. A.; Mirkin, C. A. *Progress in Inorganic Chemistry*. Wiley January 1999, pp 233–350.

[21] Blacquiere, J. M. *ACS Catal*. **2021**, *11* (9), 5416–5437.

[22] Adams, G. M.; Weller, A. S. *Coord. Chem. Rev*. **2018**, *355*, 150–172.

[23] Braunstein, P.; Naud, F. *Angew. Chem. Int. Ed*. **2001**, *40* (4), 680–699.

[24] Orrell, K. G.; Osborne, A. G.; Šik, V.; da Silva, M. W. *Polyhedron* **1995**, *14* (19), 2797–2802.

[25] Dulebohn, J. I.; Haefner, S. C.; Berglund, K. R. *Chem. Mater*. **1992**, *4* (3), 506–508.

[26] Bae, J.; Cho, E. J. *ACS Catal*. **2023**, *13* (20), 13540–13560.

[27] Carroll, M. P.; Guiry, P. J. *Chem. Soc. Rev*. **2014**, *43* (3), 819–833.

[28] Margalef, J.; Biosca, M.; de la Cruz Sánchez, P.; Faiges, J.; Pàmies, O.; Diéguez, M. *Coord. Chem. Rev*. **2021**, *446* (214120), 214120.

[29] Mecking, S.; Keim, W. *Organometallics* **1996**, *15* (11), 2650–2656.

[30] Wei, C.; Zhang, L.; Xia, Z. *Org. Lett*. **2023**, *25* (37), 6808–6812.

[31] Hashmi, A. S. K. *Chem. Rev*. **2007**, *107* (7), 3180–3211.

[32] Gorin, D. J.; Toste, F. D. *Nature* **2007**, *446* (7134), 395–403.

[33] Fensterbank, L.; Malacria, M. *Acc. Chem. Res*. **2014**, *47* (3), 953–965.

[34] Avent, A. G.; Hitchcock, P. B.; Lappert, M. F.; Sablong, R.; Severn, J. R. *Organometallics* **2004**, *23* (11), 2591-2600.

[35] Xing, J.; Sun, H.; Xue, B.; Li, X.; Fuhr, O.; Fenske, D. *Organometallics* **2017,** *36* (5), 975–980.

[36] Jackman, K. M. K.; Fogh, A. A.; Stubbs, J. M.; Blacquiere, J. M. J. *Organomet. Chem*. **2019**, *880*, 56–61.

[37] Caro, C. F.; Lappert, M F..; Merle, P. G. *Coord. Chem. Rev*. **2001**, *219–221*, 605–663.

[38] Jackman,K. M. K.; Bridge, B. J.; Sauvé, E. R.; Rowley, C. N.; Zheng, C. H. M.; Stubbs, J. M.; Boyle, P. D.; Blacquiere, J. M. *Organometallics* **2019**, *38* (8), 1677–1681.

[39] Hitchcock, P. B.; Lappert, M. F.; Layh, A. M. Z. *Anorg. Allg. Chem*. **2000**, *626* (5), 1081–1086.

[40] Stubbs, J. M.; Firth, K. F.; Bridge, B. J.; Berger, K. J.; Hazlehurst, R. J.; Boyle, P. D.; Blacquiere, J. M., *Dalton Trans*. 2017, *46*, 647-650.

[41] Kindervater, M. B.; Staroverov, V. N.; Jackman, K. M. K.; Fogh, A. A.; Kelley, L. S. G.; Lim, L.; Sirohey, S. A.; Boyle, P. D.; Blacquiere, J. M. *Dalton Trans*. **2023**.

[42] Li, X. G..; Zhou, Q. L. *Adv. Synth. Catal*. **2021**, *363*, 3471-3475.

[43] Essential Organic Chemistry, 3rd Edition Published by Pearson. Essential Organic Chemistry **2016**.

[44] Zhou, X.; Lau, K.-C.; Petro, B. J.; Jordan, R. F., *Organometallics*. **2014**, *33*, 7209-7214.

[45] Contrella, N. D.; Sampson, J. R.; Jordan, R. F., *Organometallics*. **2014**, *33*, 3546-3555.

[46] Kochi, T.; Noda, S.; Yoshimura, K.; Nozaki, K., *J. Am. Chem. Soc*. **2007**, *129*, 8948- 8949.

[47] Duran-Camacho, G.; Hethcox, J. C. *Org. Lett*. **2022**, *24*, 8397-8400.

[48] Kindervater, Meagan, "Coordination and Reactivity of a Structurally Responsive Phosphine-1-Azallyl Ligand" (2020). *Electronic Thesis and Dissertation Repository*. 7504.

[49] Sui, X.; Dai, S.; Chen, C. *ACS Catal.* **2015**, *5* (10), 5932–5937.

[50] Allen, K. E.; Campos, J.; Daugulis, O.; Brookhart, M. *ACS Catal*. **2015**, *5* (1), 456-464.

[51] Kocen, A. L.; Klimovica, K.; Brookhart, M.; Daugulis, O. *Organometallics* **2017**, *36*, 787–790.

[52] Anbarasan, P.; Schareina, T.; Beller, M. *Chem. Soc. Rev*. **2011**, *40* (10), 5049.

[53] Duran-Camacho, G.; Hethcox, J. C. *Org. Lett*. **2022**, *24*, 8397-8400.

[54] Lagueux-Tremblay, P.-L.; Augereau, C.; Nair, P.; Tam, K. M.; Arndtsen, B. A. *ACS Catal*. **2022**, *12* (21), 13394–13399.

[55] Johansson Seechurn, C. C. C.; Sperger, T.; Scrase, T. G.; Schoenebeck, F.; Colacot, T. J. *J. Am. Chem. Soc.* **2017**, *139* (14), 5194–5200.

[56] Salo, E. V.; Guan, Z. *Organometallics* **2003**, *22* (24), 5033-5046.

[57] Huang, J.; Isaac, M.; Watt, R.; Becica, J.; Dennis, E.; Saidaminov, M. I.; Sabbers, W. A.; Leitch, D. C. *ACS Catal*. **2021**, *11* (9), 5636–5646.

[58] Loos, M.; Gerber, C. enviPat: Isotope Pattern, Profile and Centroid Calculation for Mass Spectrometry. https://www.envipat.eawag.ch/.

[59] Bruker-AXS, SAINT version 2013.8, **2013**, Bruker-AXS, Madison, WI 53711, USA.

[60] Bruker-AXS, SADABS version 2012.1, **2012**, Bruker-AXS, Madison, WI 53711, USA.

[61] Sheldrick, G. M., *Acta Cryst*. **2015**, *A71*, 3-8.

[62] Macrae, C. F.; Bruno, I. J.; Chisholm, J. A.; Edington, P. R.; McCabe, P.; Pidcock, E.; Rodriguez-Monge, L.; Taylor, R.; van de Streek, J. and Wood, P. A. J. *Appl. Cryst*., **2008**, *41*, 466-470.

8.0 Appendix

8.1 Appendix A: Supplementary Information for Chapter 2
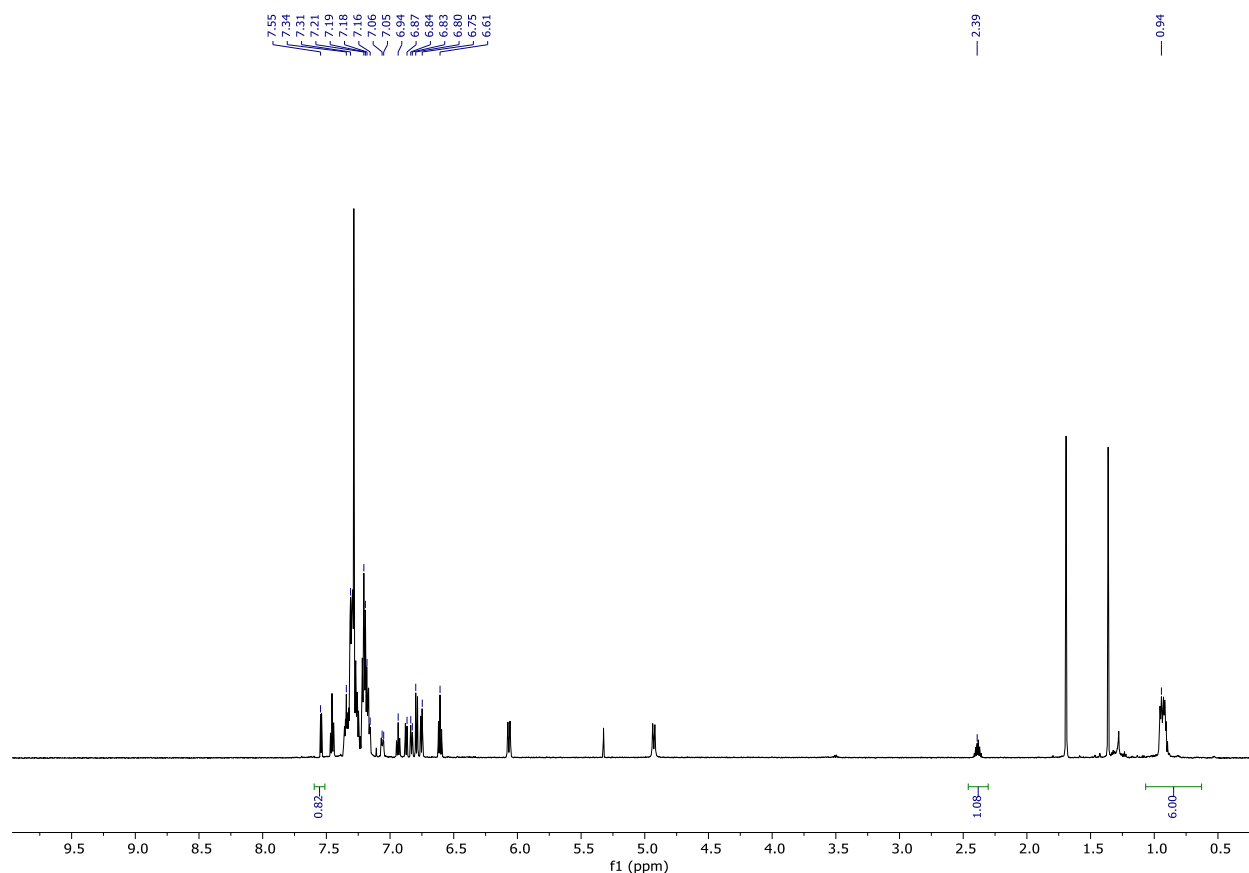
Figure A.1. ^{1}H NMR spectrum (CDCl$_3$, 600 MHz) of Ph$_2$P(o-C$_6$H$_4$)(o-C$_6$H$_4$)N(3-Methyl-1-butene), **H[L2]a** and Ph$_2$P(o-C$_6$H$_4$)(o-C$_6$H$_4$)NH(2-Methyl-2-butene), **H[L2]b**. Signals identified are for **H[L2]a**.

H[L2]a   1:2   H[L2]b
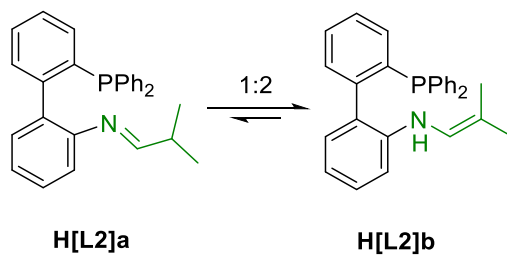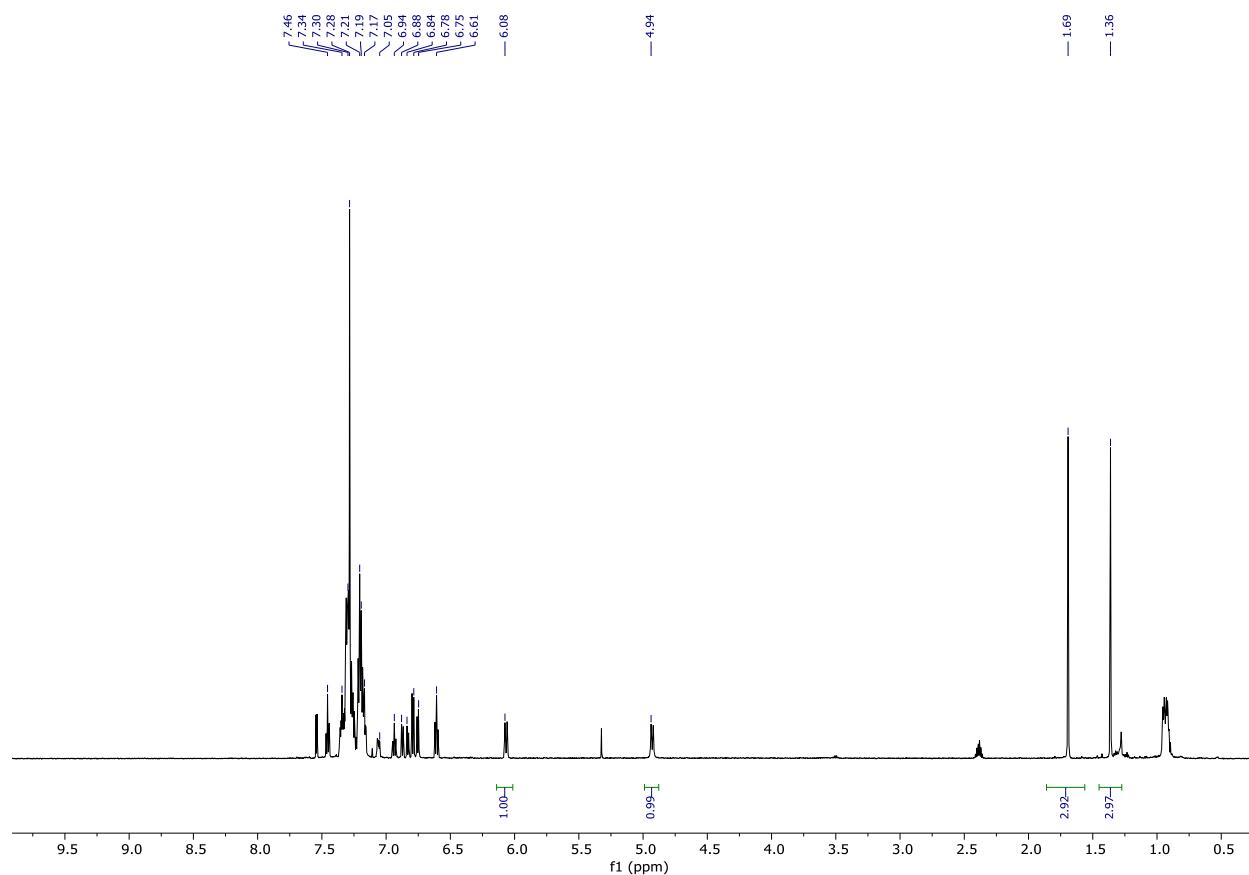
Figure A.2. ^{1}H NMR spectrum (CDCl$_3$, 600 MHz) of Ph$_2$P(o-C$_6$H$_4$)(o-C$_6$H$_4$)N(3-Methyl-1-butene), **H[L2]a** and Ph$_2$P(o-C$_6$H$_4$)(o-C$_6$H$_4$)NH(2-Methyl-2-butene), **H[L2]b**. Signals identified are for **H[L2]b**.

H[L2]a   1:2   H[L2]b
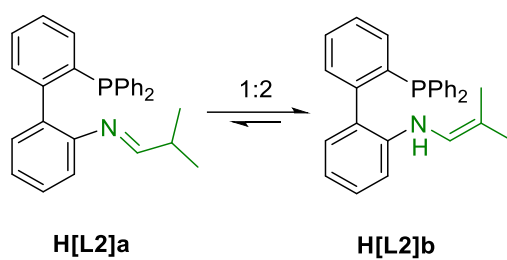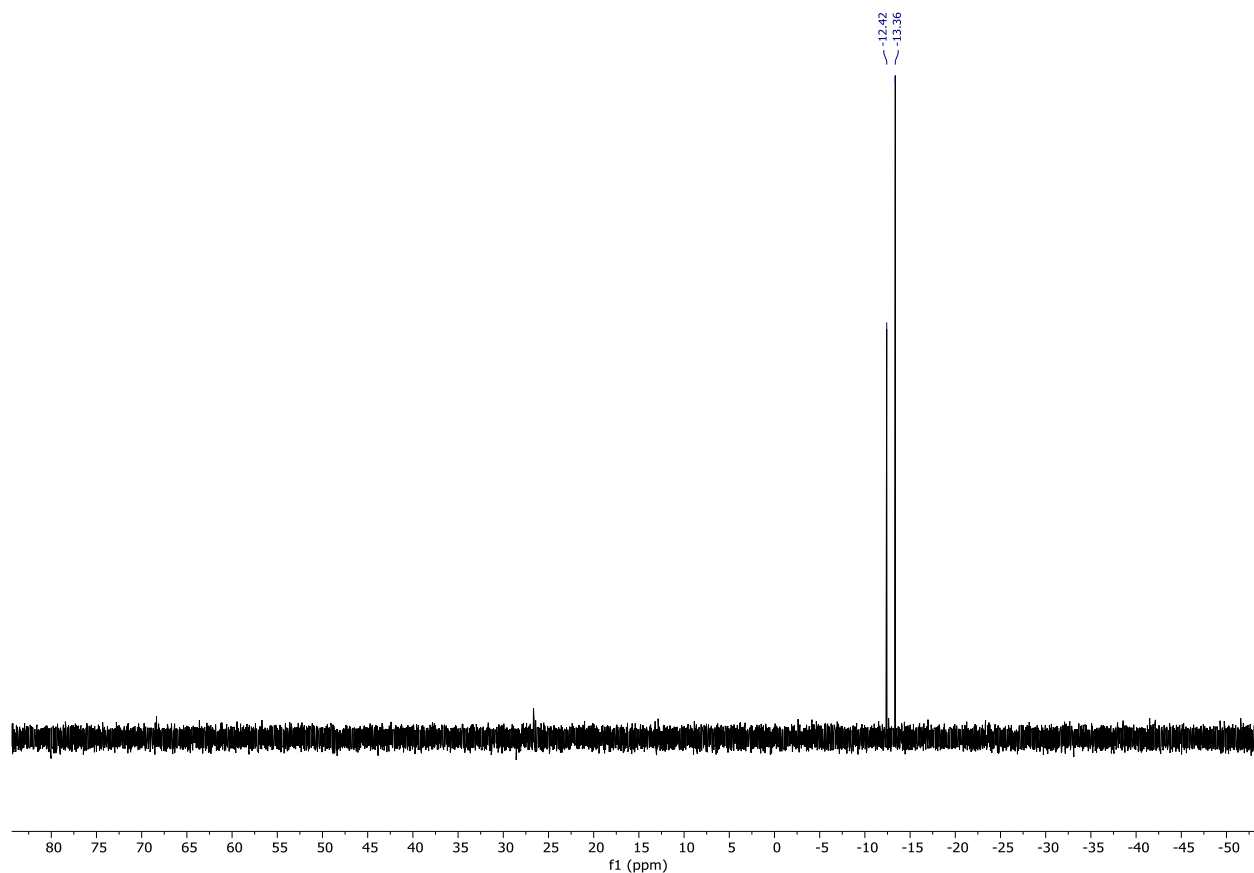
Figure A.3. $^{31}P\{^1H\}$ NMR spectrum (CDCl$_3$, 243 MHz) of Ph$_2$P(o-C$_6$H$_4$)(o-C$_6$H$_4$)N(3-Methyl-1-butene), **H[L2]a** and Ph$_2$P(o-C$_6$H$_4$)(o-C$_6$H$_4$)NH(2-Methyl-2-butene), **H[L2]b**.
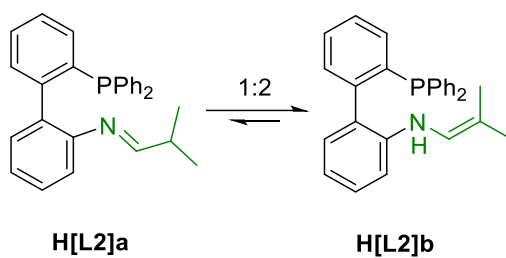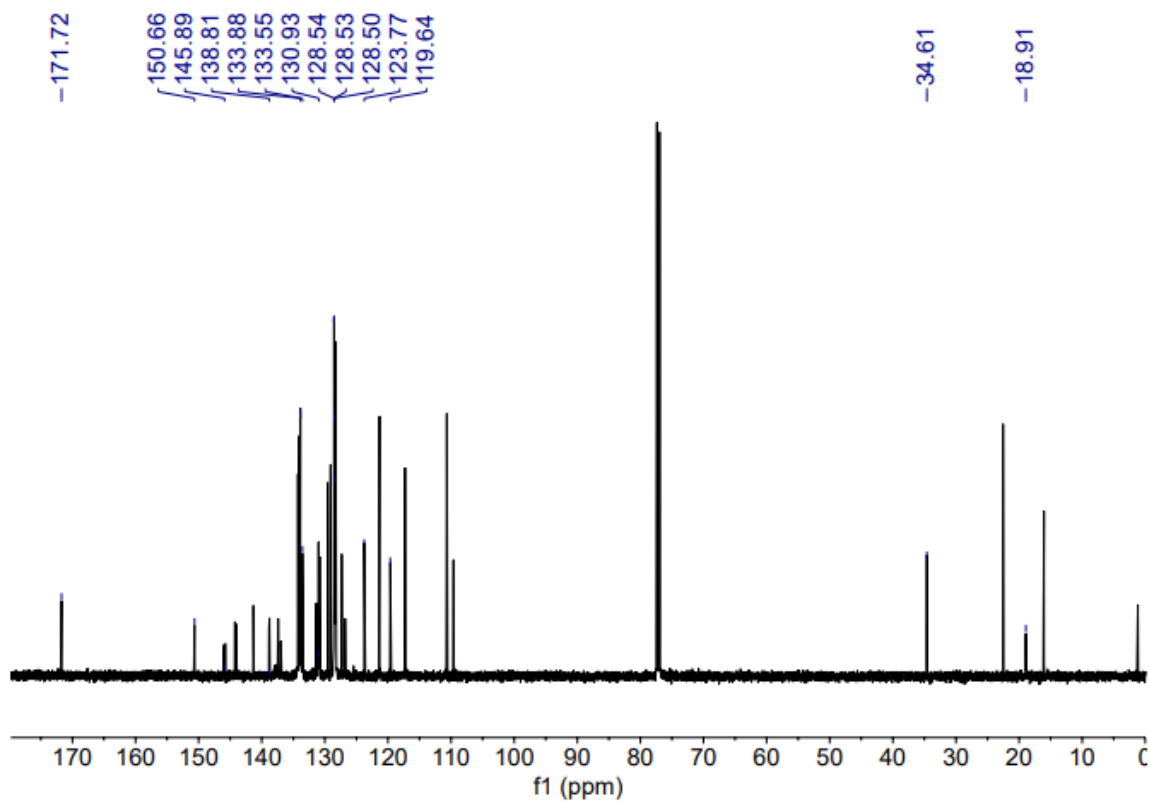
Figure A.4. $^{13}C\{^1H\}$ NMR spectrum (CDCl$_3$, 151 MHz) of Ph$_2$P(o-C$_6$H$_4$)(o-C$_6$H$_4$)N(3-Methyl-1-butene), **H[L2]a** and Ph$_2$P(o-C$_6$H$_4$)(o-C$_6$H$_4$)NH(2-Methyl-2-butene), **H[L2]b**. Signals identified are for **H[L2]a**.

H[L2]a   1:2   H[L2]b
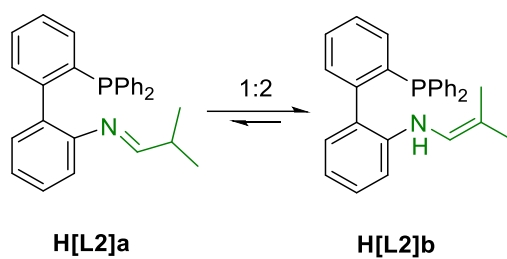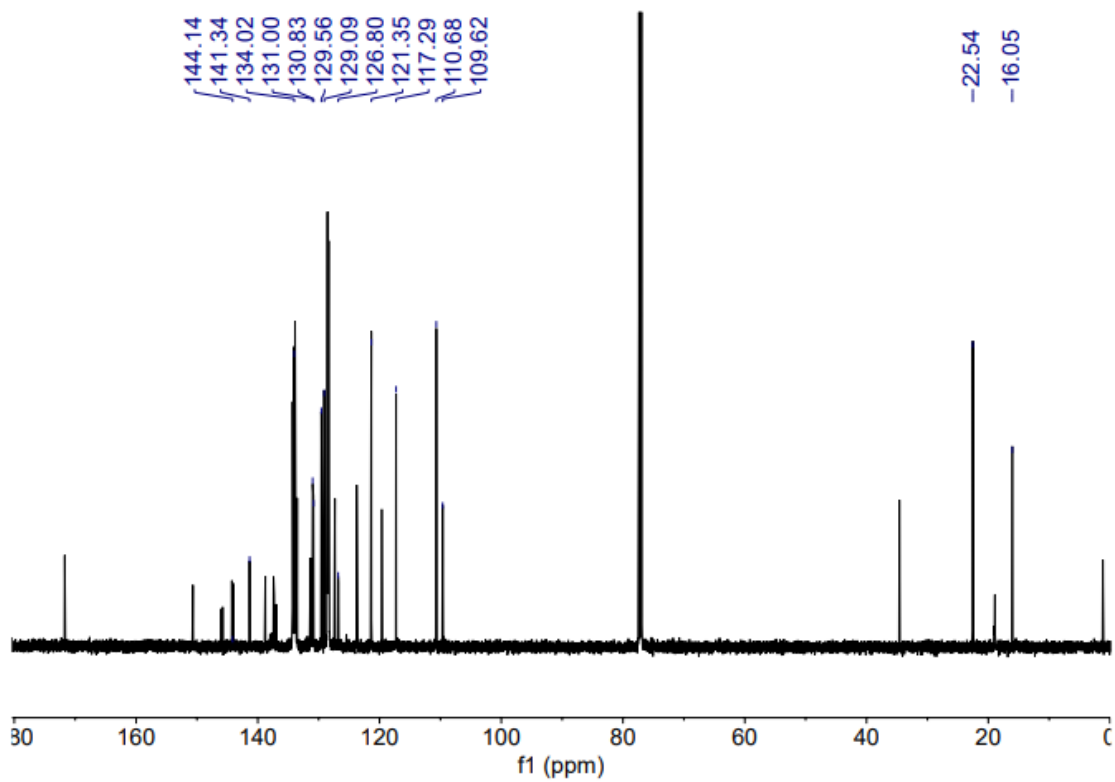
Figure A.5. $^{13}C\{^1H\}$ NMR spectrum (CDCl$_3$, 151 MHz) of Ph$_2$P(o-C$_6$H$_4$)(o-C$_6$H$_4$)N(3-Methyl-1-butene), **H[L2]a** and Ph$_2$P(o-C$_6$H$_4$)(o-C$_6$H$_4$)NH(2-Methyl-2-butene), **H[L2]b**. Signals identified are for **H[L2]b**.

H[L2]a   1:2   H[L2]b
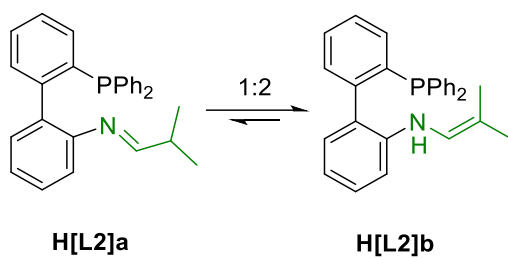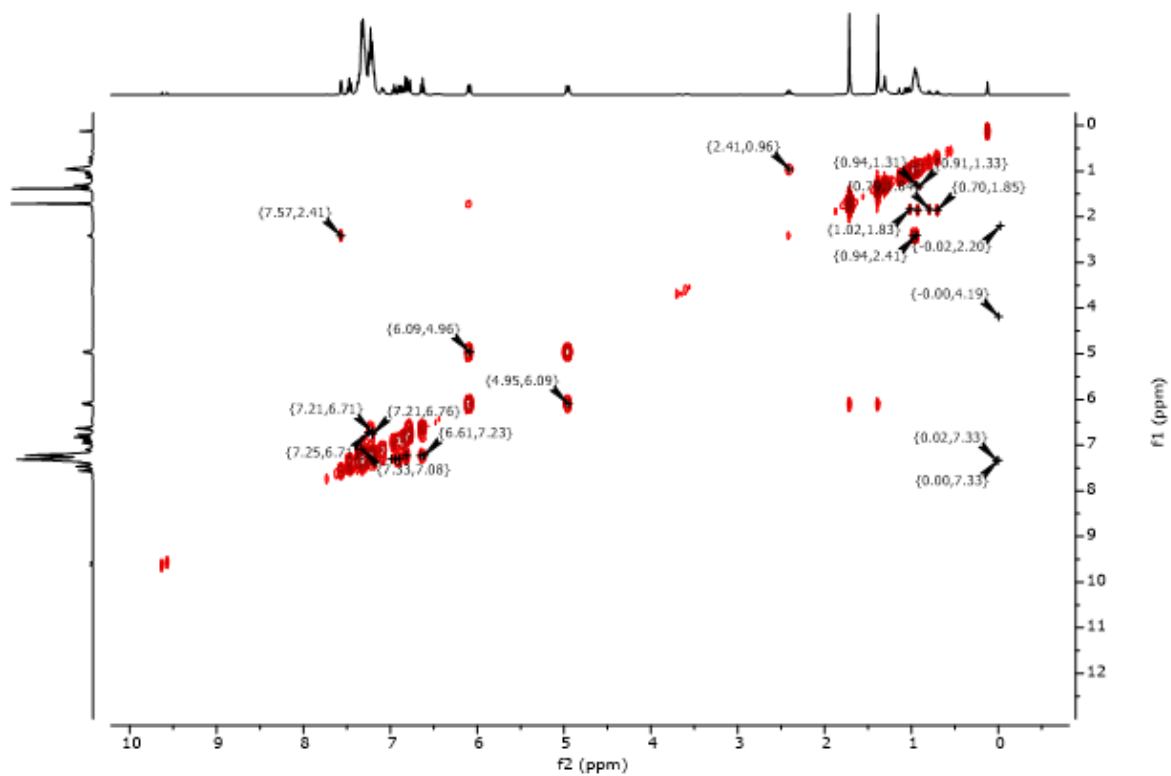
Figure A.6. ^{1}H-^{1}H COSY NMR spectrum (400 MHz, CDCl$_3$) of Ph$_2$P(o-C$_6$H$_4$)(o-C$_6$H$_4$)N(3-Methyl-1-butene), **H[L2]a** and Ph$_2$P(o-C$_6$H$_4$)(o-C$_6$H$_4$)NH(2-Methyl-2-butene), **H[L2]b**.
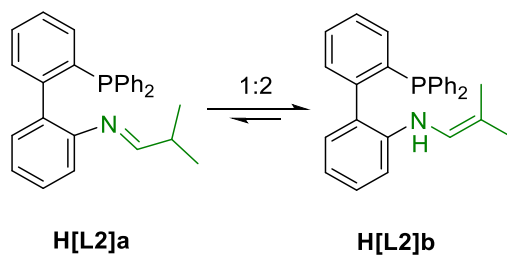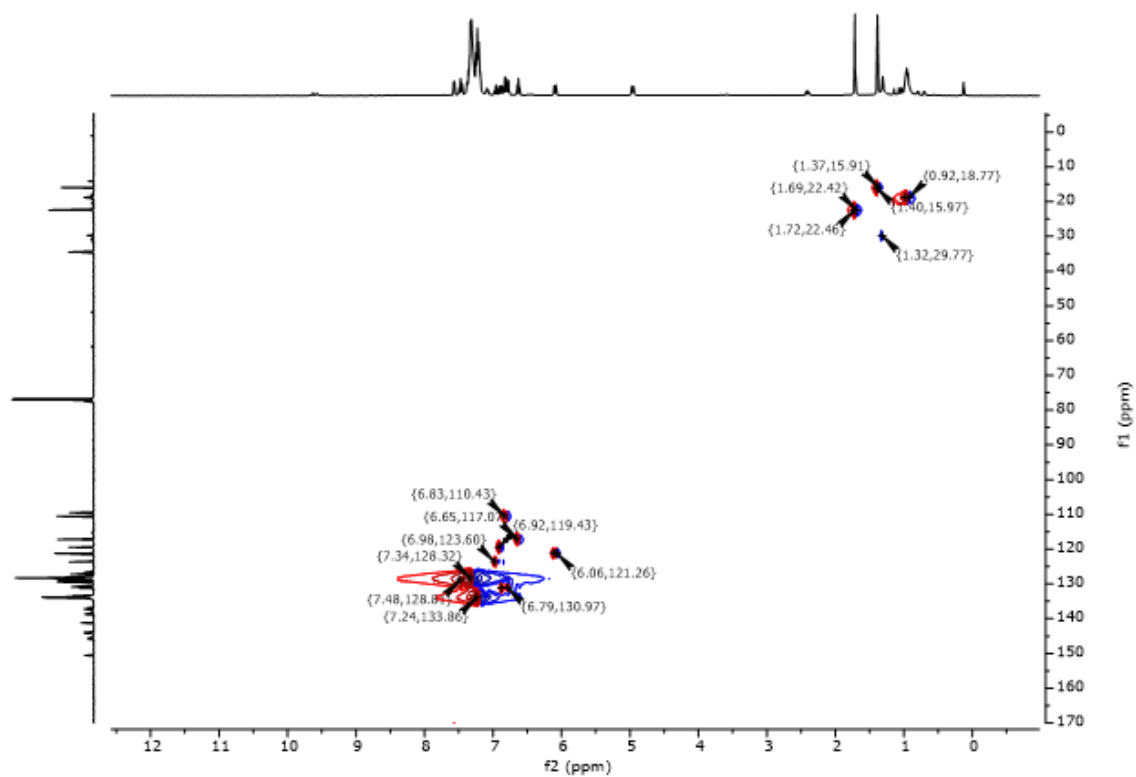
Figure A.7. ^{1}H-^{13}C HSQC NMR spectrum (400 MHz, CDCl$_3$) of Ph$_2$P(o-C$_6$H$_4$)(o-C$_6$H$_4$)N(3-Methyl-1-butene), **H[L2]a** and Ph$_2$P(o-C$_6$H$_4$)(o-C$_6$H$_4$)NH(2-Methyl-2-butene), **H[L2]b**.

H[L2]a   H[L2]b

87
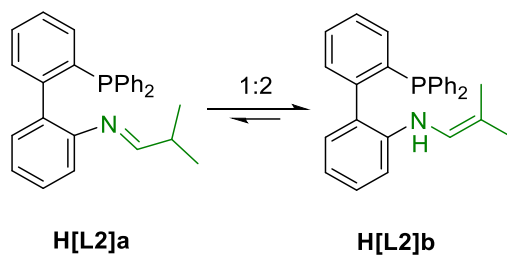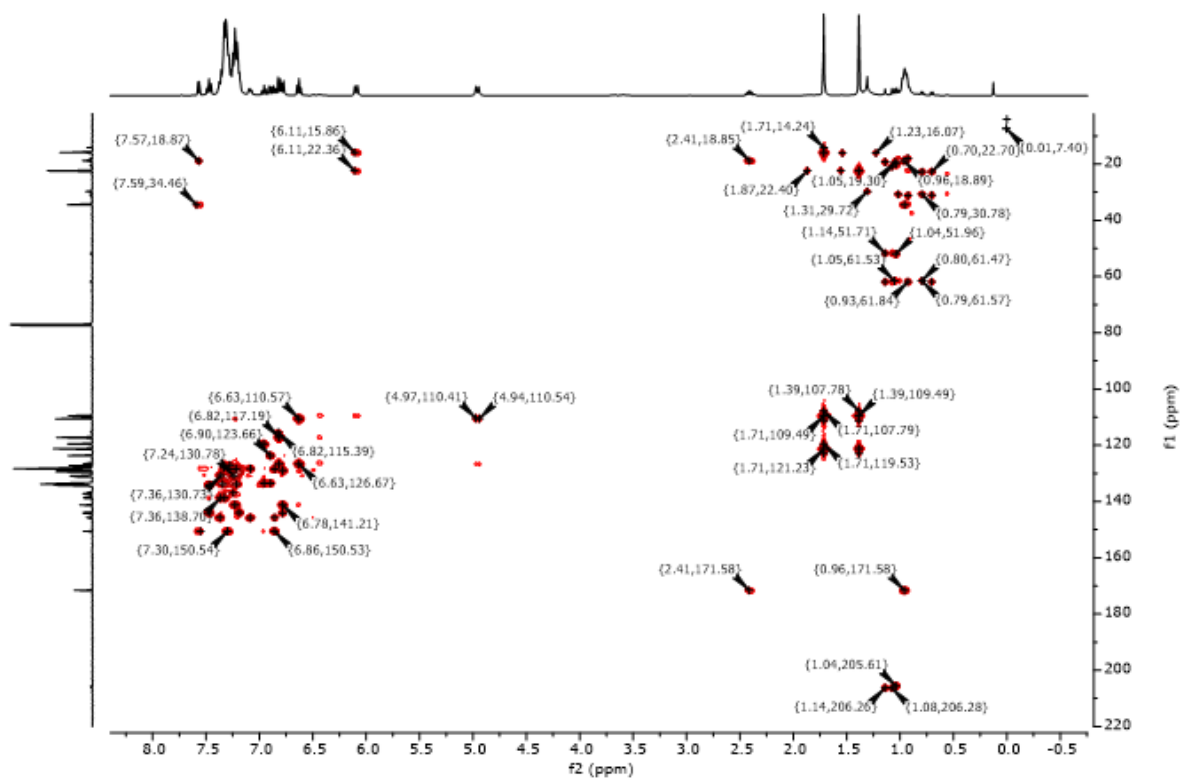
Figure A.8. ^{1}H-^{13}C HMBC NMR spectrum (400 MHz, CDCl$_3$) of Ph$_2$P(o-C$_6$H$_4$)(o-C$_6$H$_4$)N(3-Methyl-1-butene), **H[L2]a** and Ph$_2$P(o-C$_6$H$_4$)(o-C$_6$H$_4$)NH(2-Methyl-2-butene), **H[L2]b**.

H[L2]a   H[L2]b
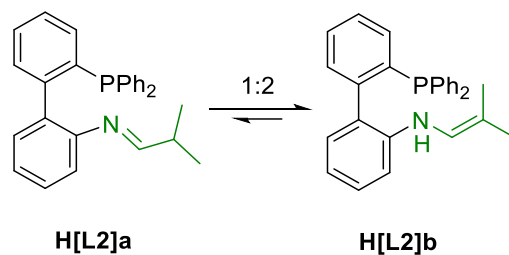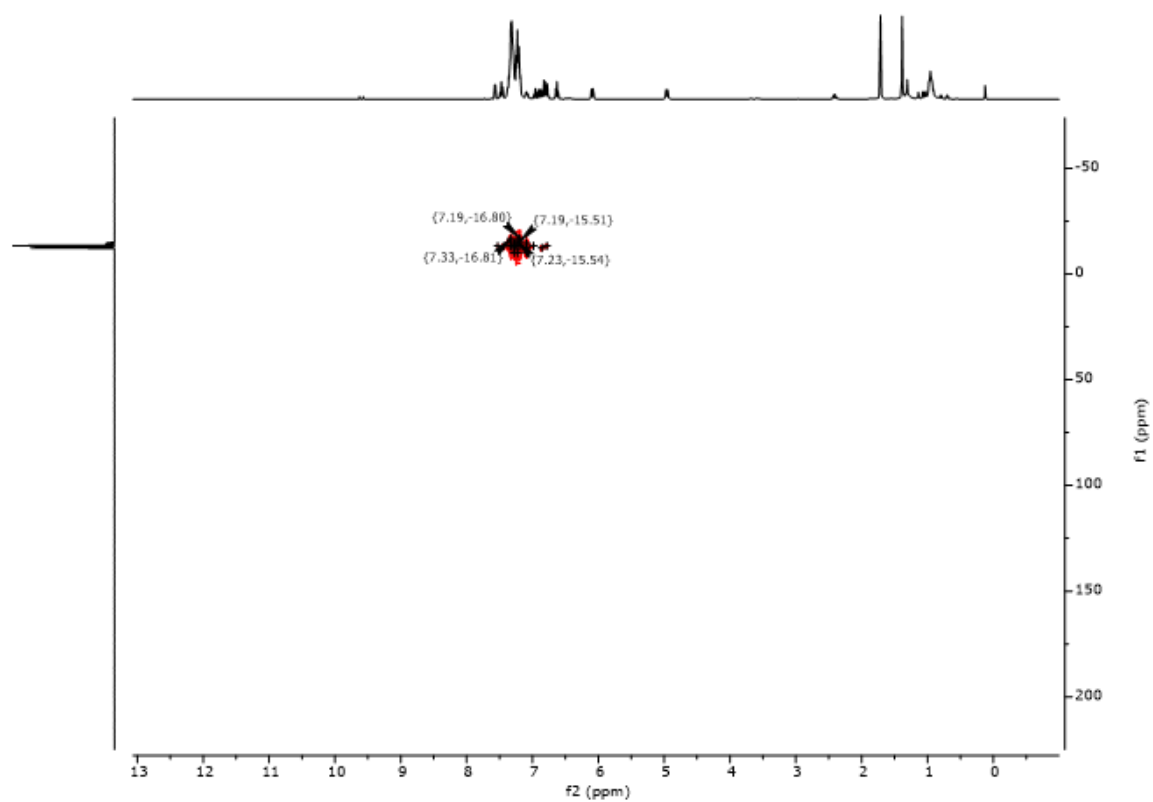
Figure A.9. ^{1}H-^{31}P HMBC NMR spectrum (400 MHz, CDCl$_3$) of Ph$_2$P(o-C$_6$H$_4$)(o-C$_6$H$_4$)N(3-Methyl-1-butene), **H[L2]a** and Ph$_2$P(o-C$_6$H$_4$)(o-C$_6$H$_4$)NH(2-Methyl-2-butene), **H[L2]b**.

H[L2]a   H[L2]b
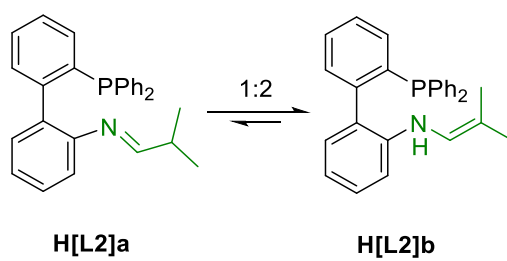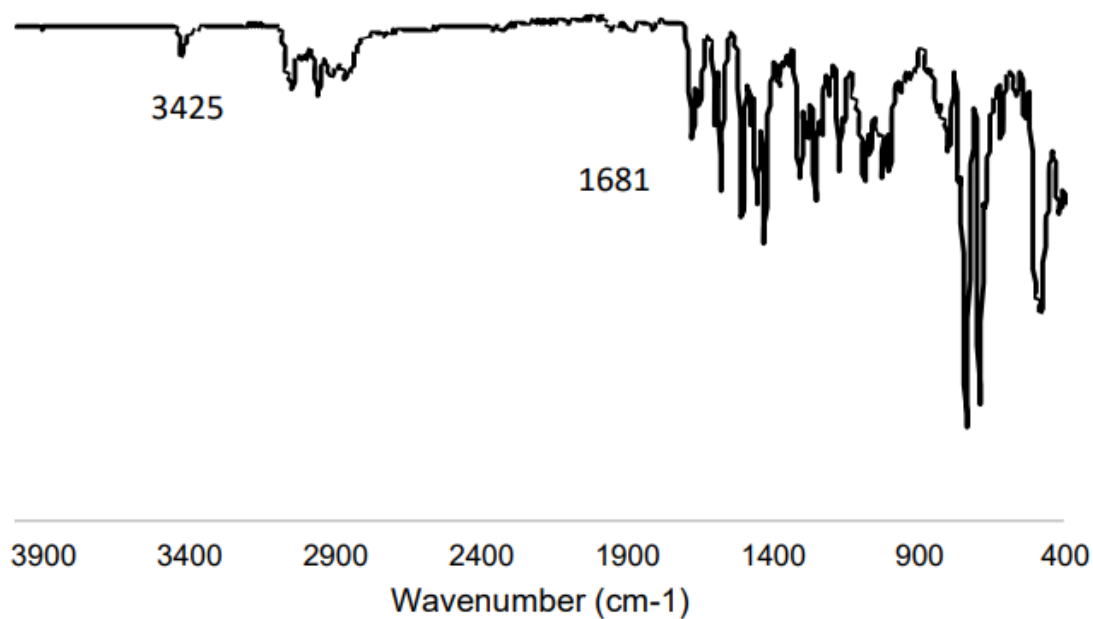
Figure A.10. ATR-FTIR of solid Ph$_2$P(o-C$_6$H$_4$)(o-C$_6$H$_4$)N(3-Methyl-1-butene), **H[L2]a** and Ph$_2$P(o-C$_6$H$_4$)(o-C$_6$H$_4$)NH(2-Methyl-2-butene), **H[L2]b**. Data acquired using Bruker Alpha II ATR-FTIR and plotted using Microsoft Excel.
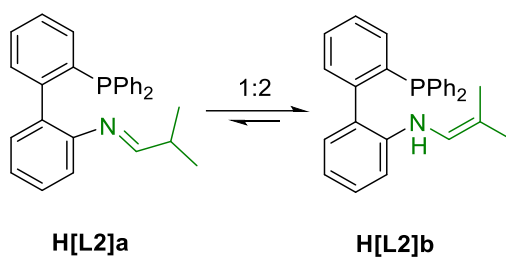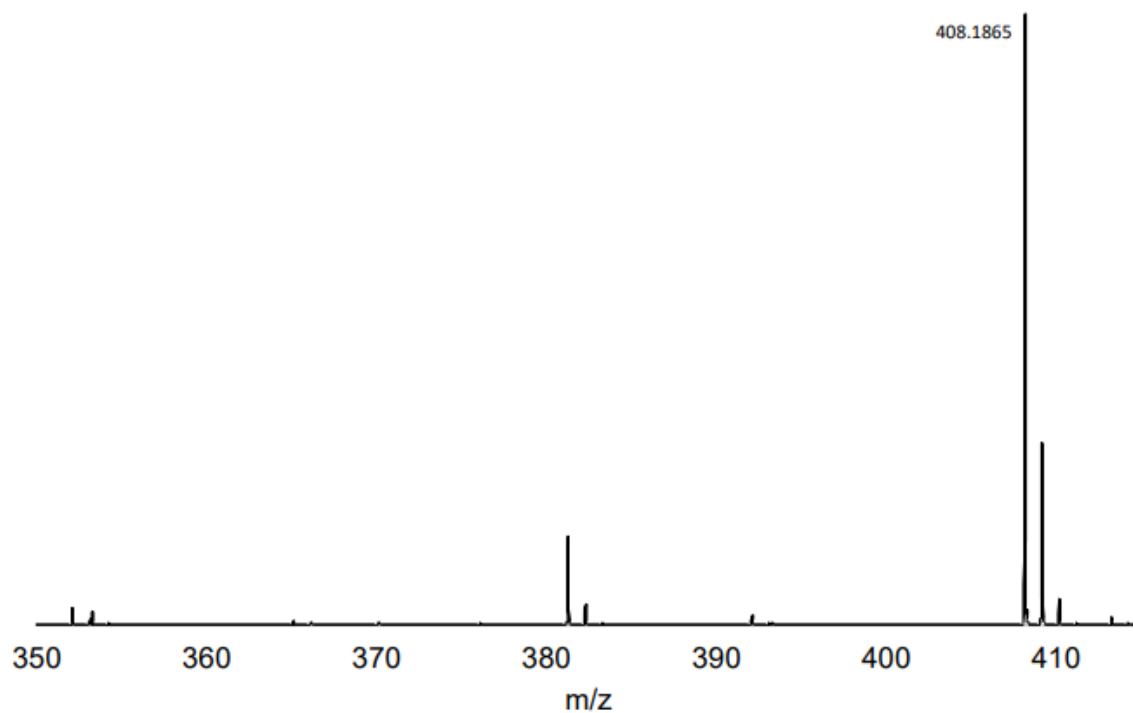
Figure A.11. ESI Mass spectrum of Ph$_2$P(o-C$_6$H$_4$)(o-C$_6$H$_4$)N(3-Methyl-1-butene), **H[L2]a** and Ph$_2$P(o-C$_6$H$_4$)(o-C$_6$H$_4$)NH(2-Methyl-2-butene), **H[L2]b**. m/z found: 408.1865, calc: [**H[L2]**]$^+$ 408.1881. Data plotted with Microsoft Excel.

H[L2]a   H[L2]b
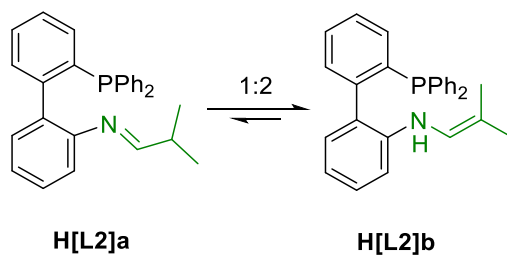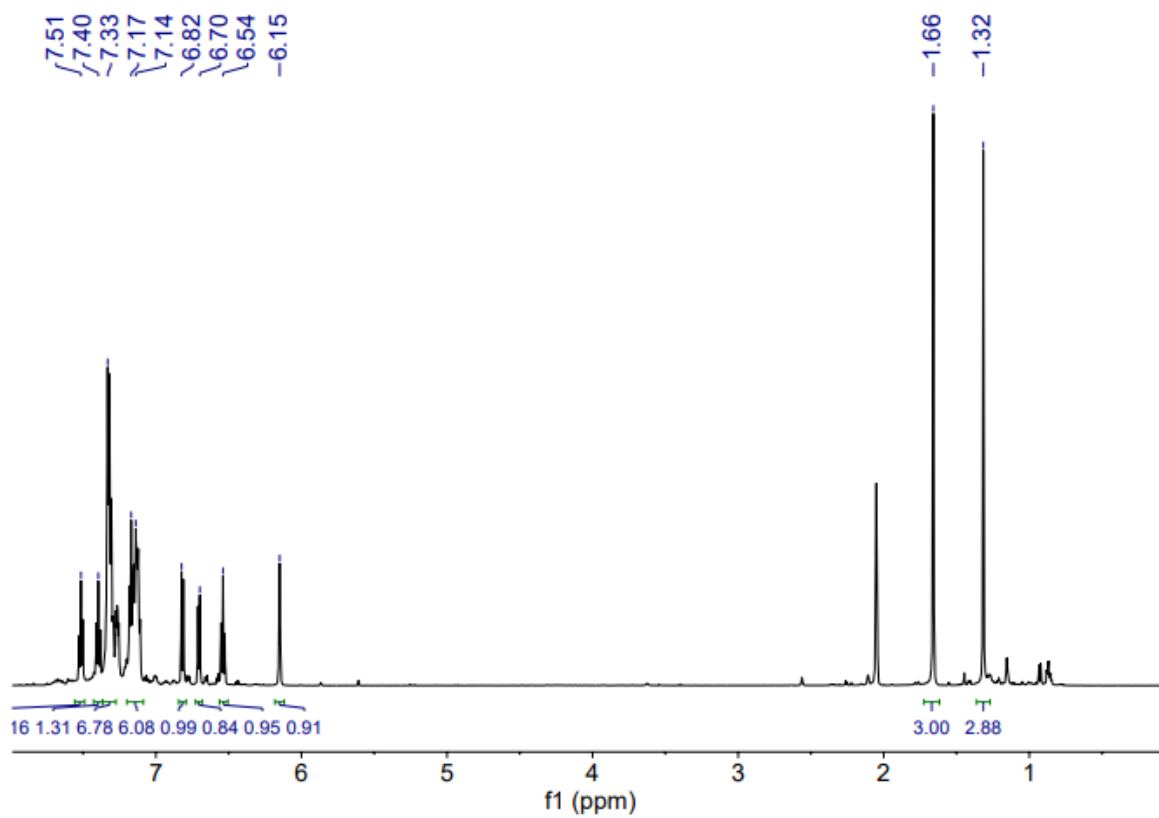
Figure A.12. ^{1}H NMR spectrum ((CD$_3$)$_2$CO, 600 MHz) of [Ph$_2$P(o-C$_6$H$_4$)(o-C$_6$H$_4$)N(2-Methyl-2-butene)]K, **K[L2]**.

K[L2]
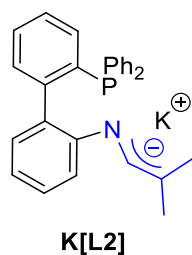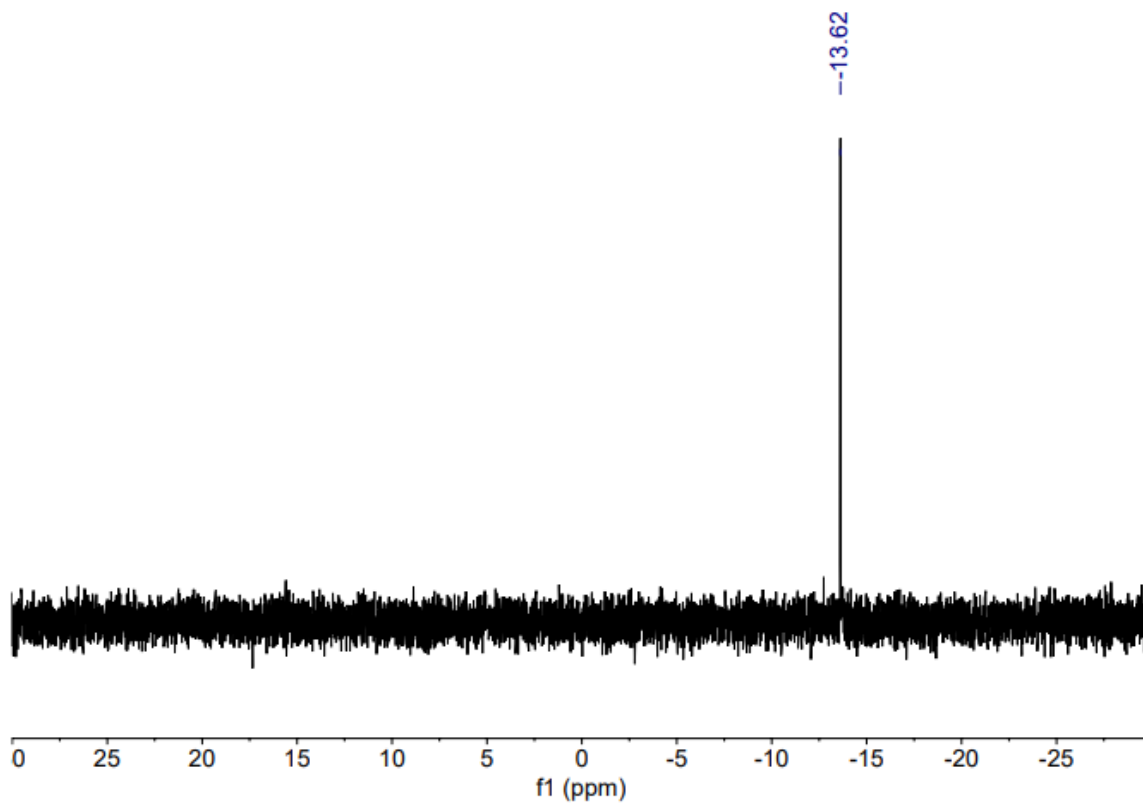
Figure A.13. $^{31}P\{^1H\}$ NMR spectrum ($(CD_3)_2CO$, 243 MHz) of $[Ph_2P(o\text{-}C_6H_4)(o\text{-}C_6H_4)N(2\text{-Methyl-2-butene})]K$, **K[L2]**.

K[L2]
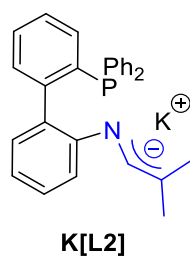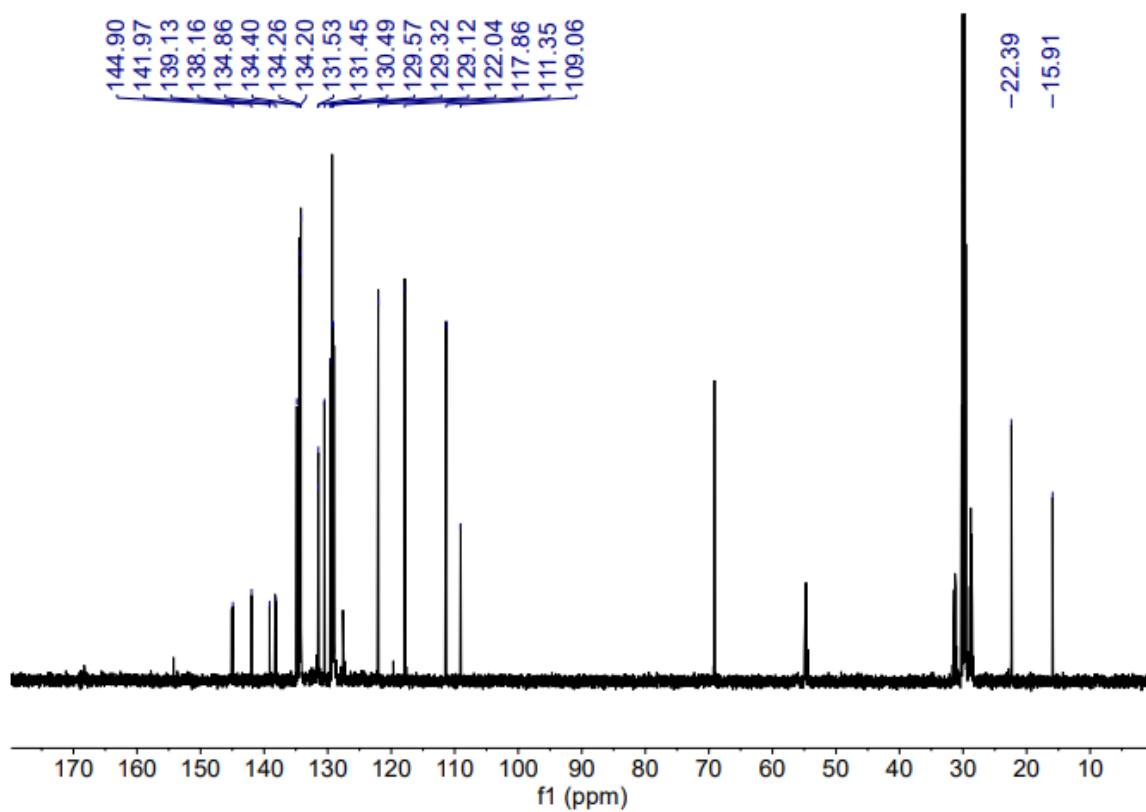
Figure A.14. $^{13}C\{^{1}H\}$ NMR spectrum ((CD$_3$)$_2$CO, 151 MHz) of [Ph$_2$P(o-C$_6$H$_4$)(o-C$_6$H$_4$)N(2-Methyl-2-butene)]K, **K[L2]**.

K[L2]
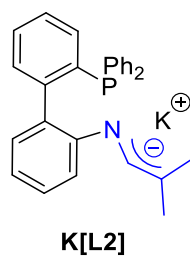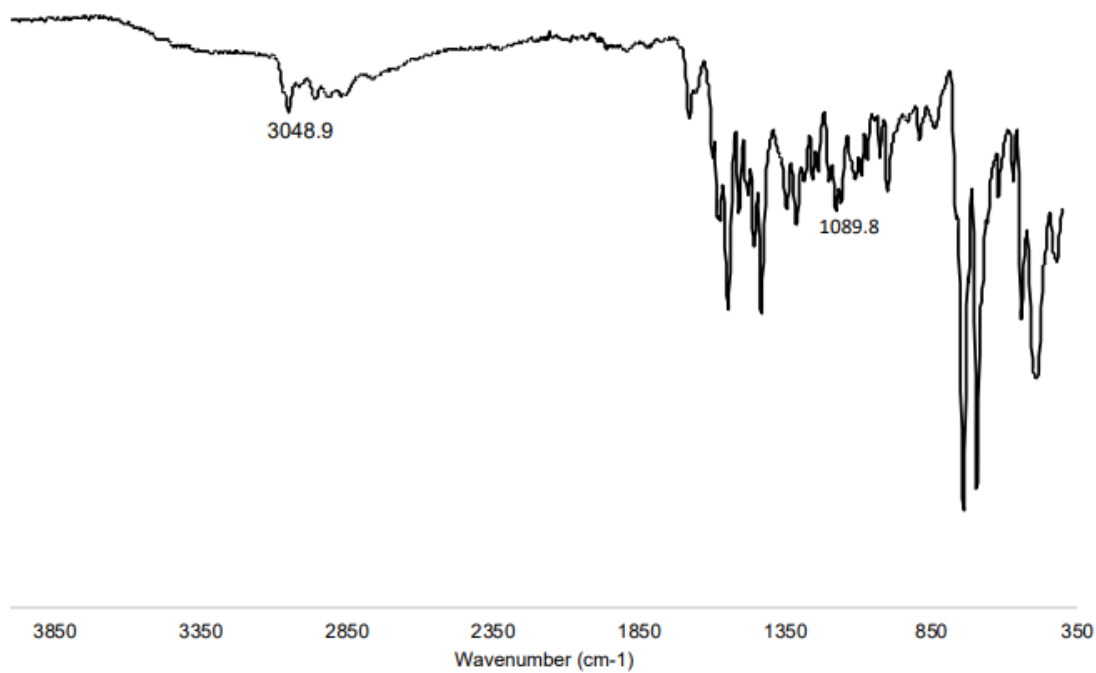
Figure A.15. ATR-FTIR of solid [Ph$_2$P(o-C$_6$H$_4$)(o-C$_6$H$_4$)N(2-Methyl-2-butene)]K, **K[L2]**. Data acquired using Bruker Alpha II ATR-FTIR and plotted using Microsoft Excel.
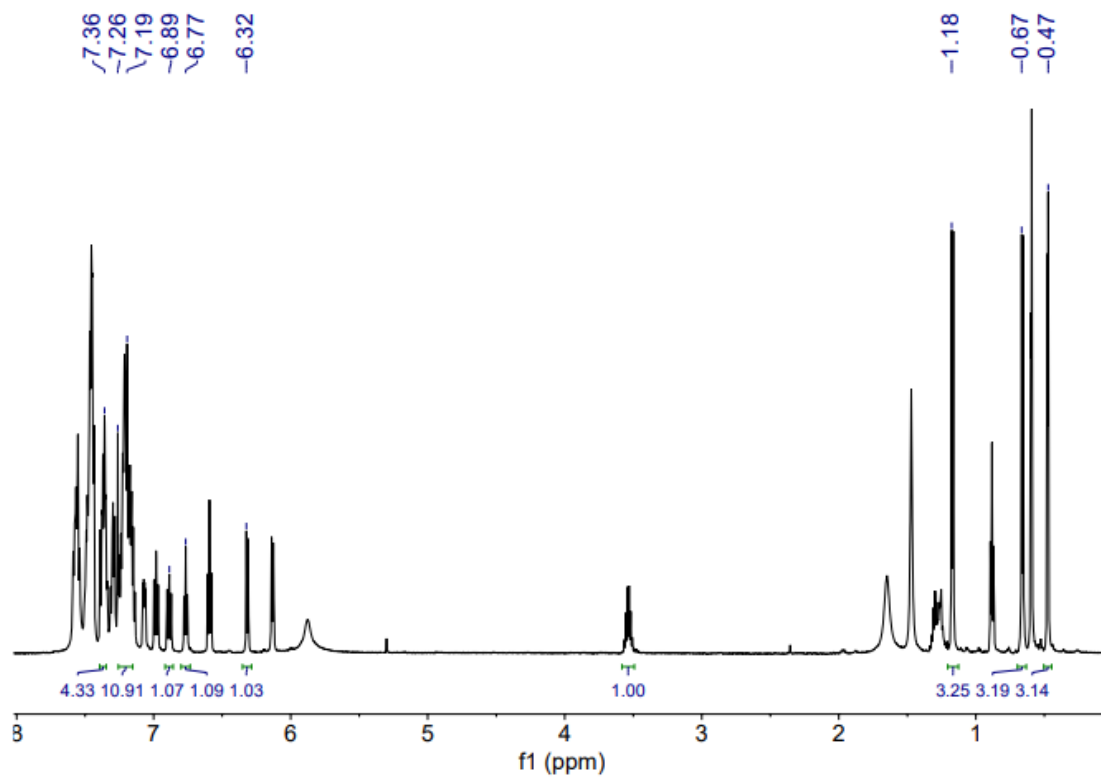

K[L2]
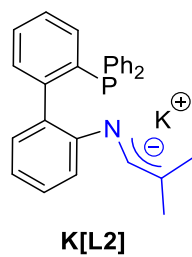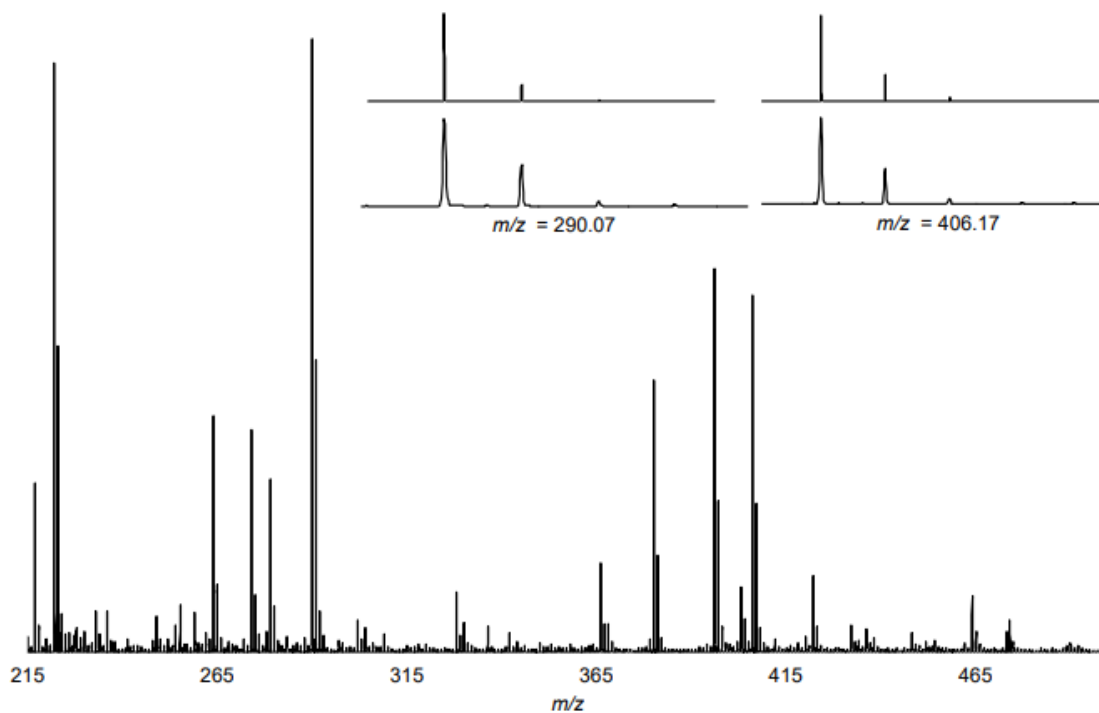
Figure A.16. MALDI mass spectrum collected in negative ion mode of $[Ph_2P(o\text{-}C_6H_4)(o\text{-}C_6H_4)N(2\text{-Methyl-2-}$ butene)]K, **K[L2]** with pyrene as the matrix. Left inset: simulated[3] isotope pattern (top) for $[(PhP=O)(C_{12}H_8)N]^{\cdot-}$ and observed signal (bottom) at m/z = 290.1. Right inset: simulated[3] isotope pattern (top) for $[\mathbf{L2}]^{\cdot-}$ and observed signal (bottom) at m/z = 406.2.
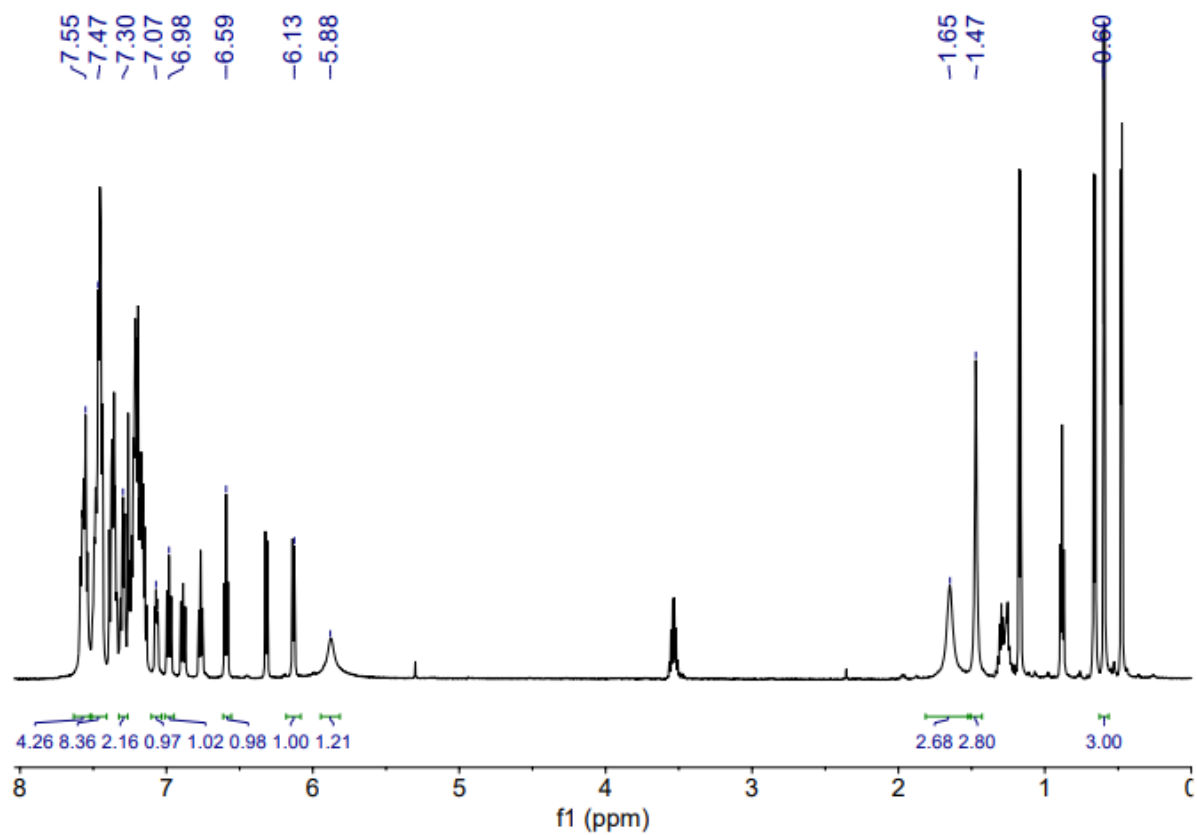

K[L2]
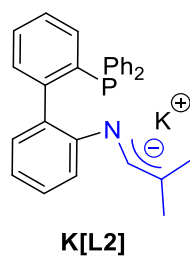
Figure A.17. ^{1}H NMR spectrum (CDCl$_3$, 600 MHz) of [PdCl(CH$_3$)(**H[L2]a**)], **1a**, and [PdCl(CH$_3$)(**H[L2]b**)], **1b**. Signals shown are for **1a**.
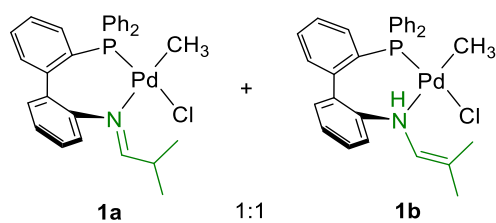
Figure A.18. ^{1}H NMR spectrum (CDCl$_3$, 600 MHz) of [PdCl(CH$_3$)(**H[L2]a**)], **1a**, and [PdCl(CH$_3$)(**H[L2]b**)], **1b**. Signals shown are for **1b**.
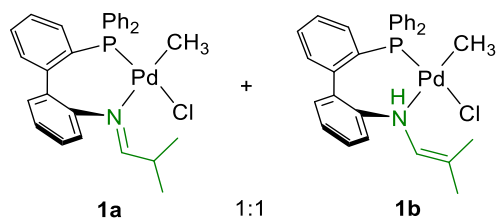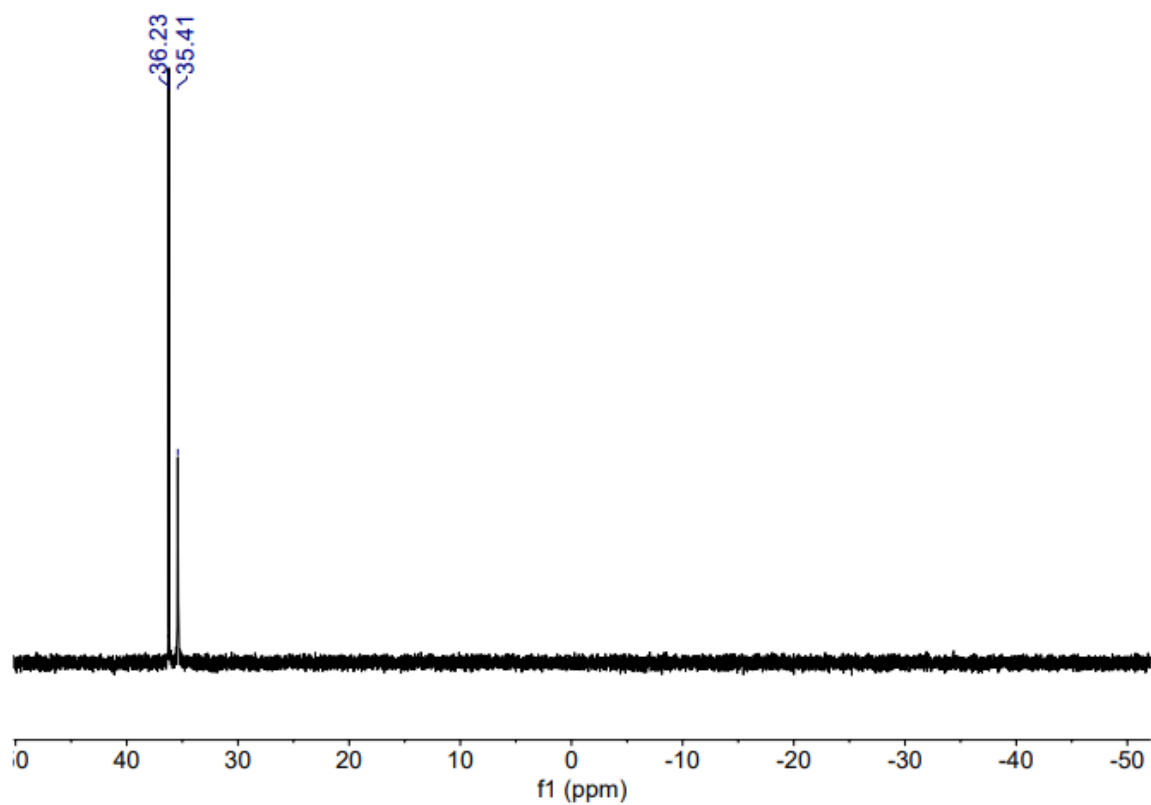
Figure A.19. $^{31}P\{^1H\}$ NMR spectrum (CDCl$_3$, 243 MHz) of [PdCl(CH$_3$)(**H[L2]a**)], **1a**, and [PdCl(CH$_3$)(**H[L2]b**)], **1b**.

Figure A.20. ¹³C{¹H} NMR spectrum (CDCl₃, 151 MHz) of [PdCl(CH₃)(**H[L2]a**)], **1a**, and [PdCl(CH₃)(**H[L2]b**)], **1b**. Signals shown are for **1a**.
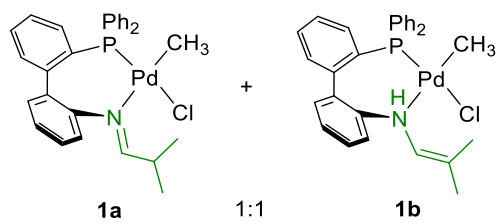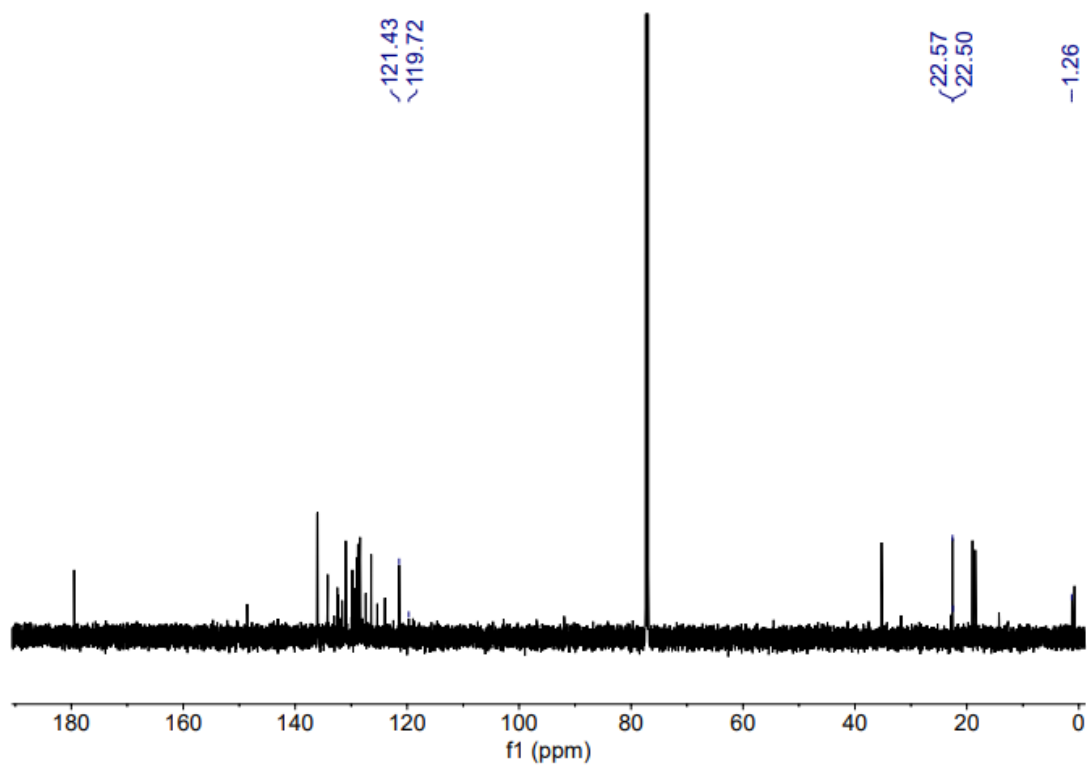
Figure A.21. $^{13}C\{^1H\}$ NMR spectrum (CDCl$_3$, 151 MHz) of [PdCl(CH$_3$)(**H[L2]a**)], **1a**, and [PdCl(CH$_3$)(**H[L2]b**)], **1b**. Signals shown are for **1b**.
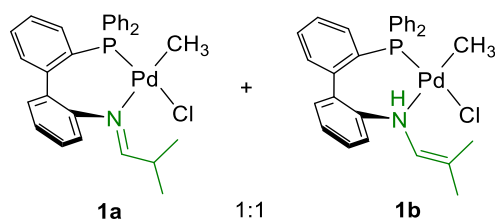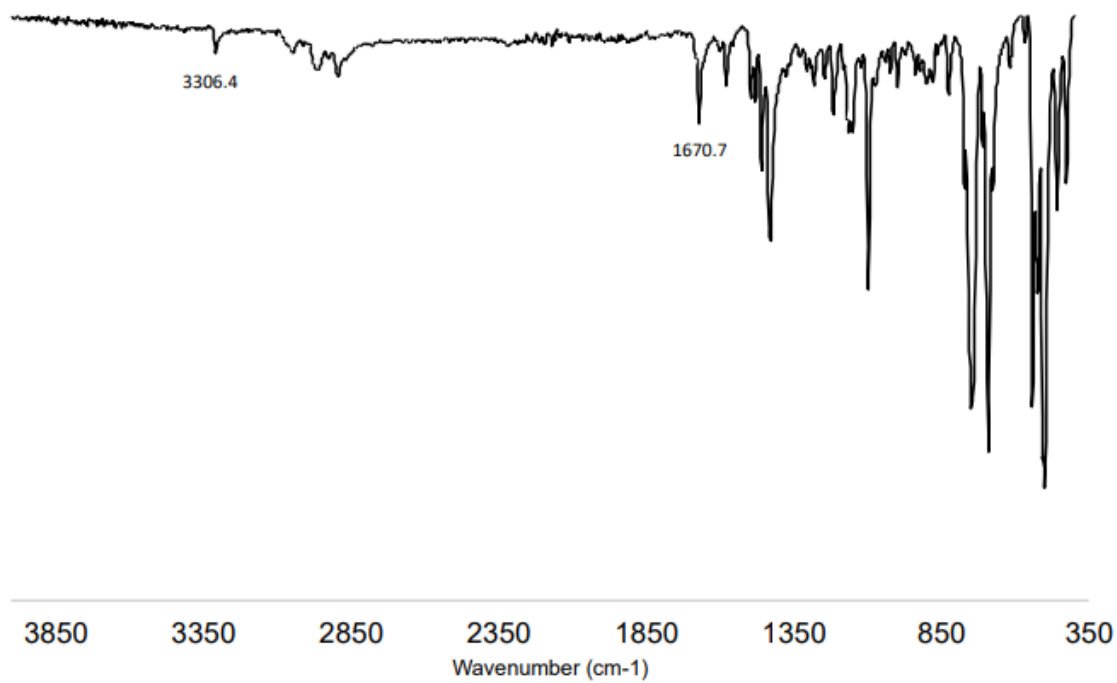
Figure A.22. ATR-FTIR of solid [PdCl(CH$_3$)(**H[L2]a**)], **1a**, and [PdCl(CH$_3$)(**H[L2]b**)], **1b**. Data acquired using Bruker Alpha II ATR-FTIR and plotted using Microsoft Excel.
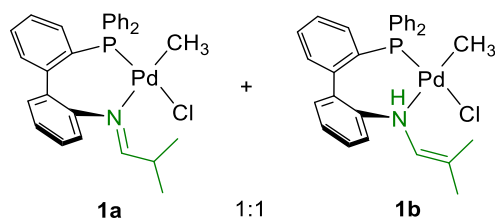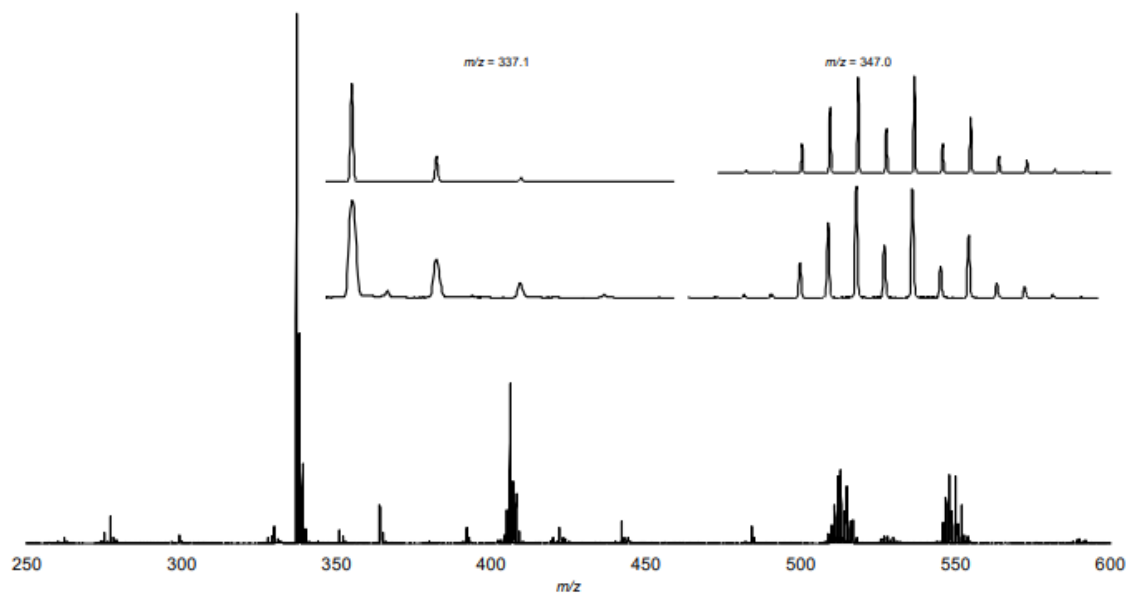
Figure A.23. MALDI mass spectrum mode of [PdCl(CH$_3$)(**H[L2]a**)], **1a**, and [PdCl(CH$_3$)(**H[L2]b**)], **1b** with pyrene as the matrix. Left inset: simulated[3] isotope pattern (top) for [**H[L2]**-C$_4$H$_8$N]$^{\bullet+}$ and observed signal (bottom) at m/z = 337.1. Right inset: simulated[3] isotope pattern (top) for [**1**-CH$_3$]$^{\bullet+}$ and observed signal (bottom) at m/z = 347.0.
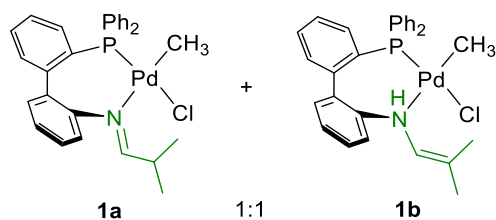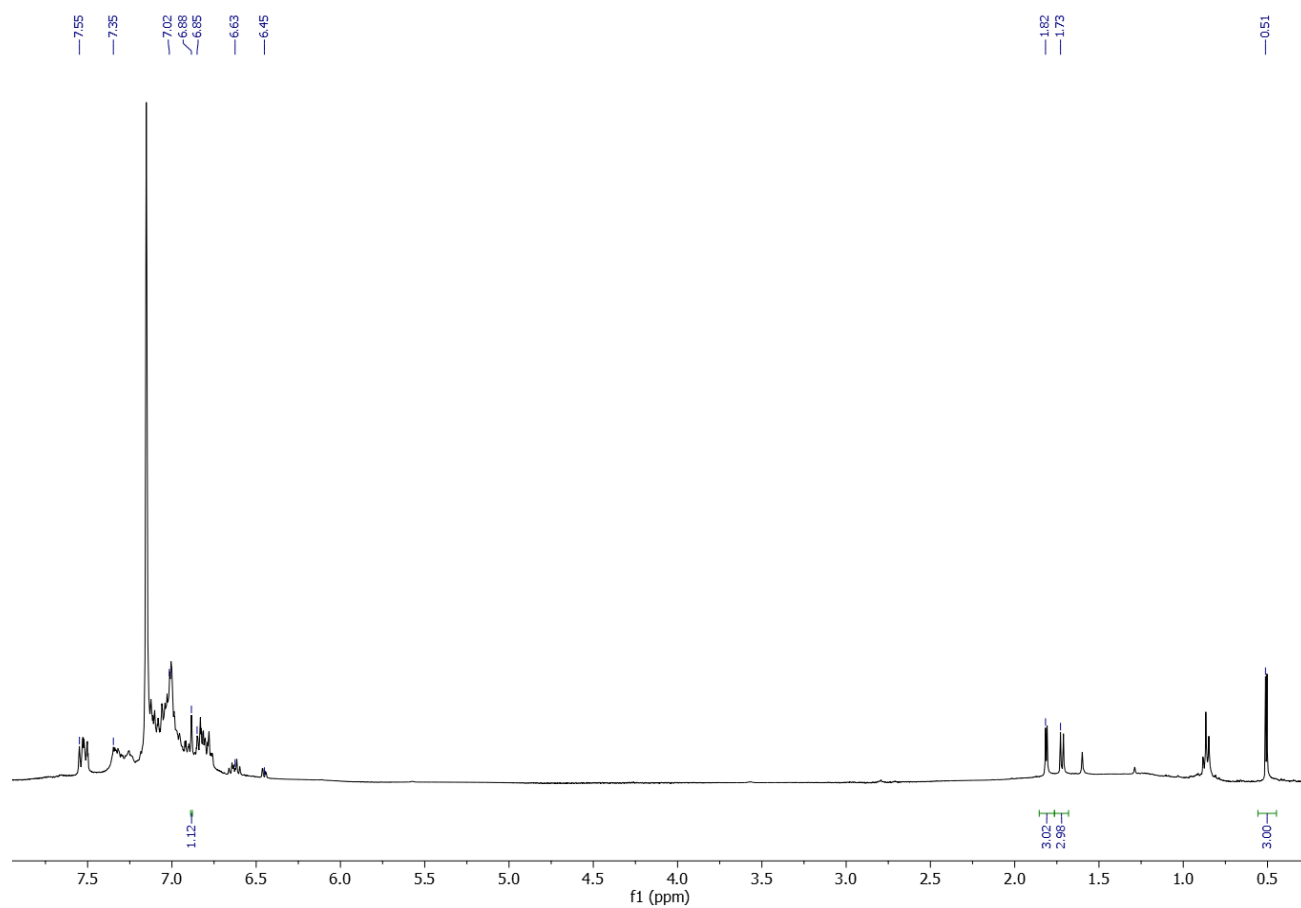
Figure A.24. ^{1}H NMR spectrum (C$_6$D$_6$, 600 MHz) of [Pd(CH$_3$)([**L2**])], **2**.
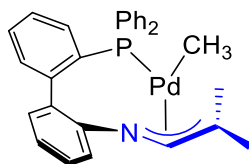
2
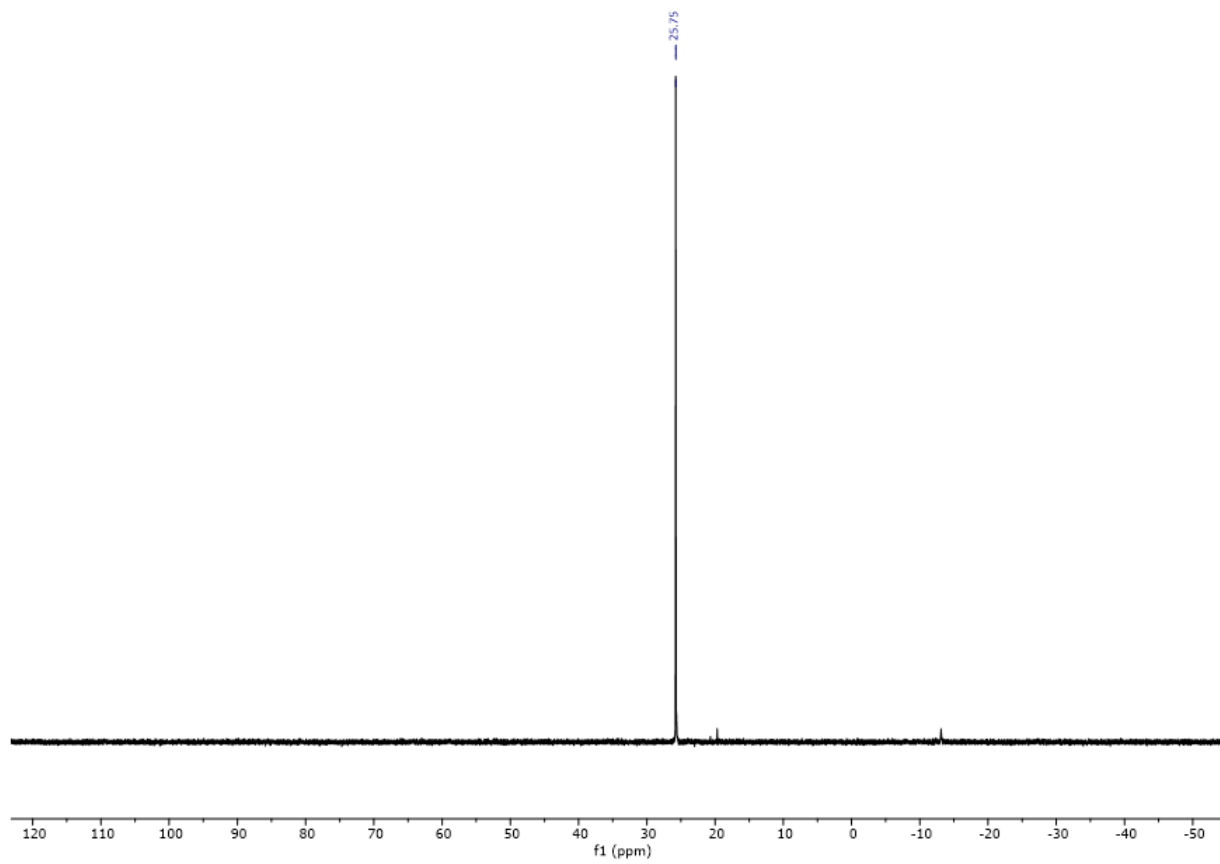
Figure A.25. $^{31}P\{^1H\}$ NMR spectrum (C_6D_6, 243 MHz) of [Pd(CH$_3$)([**L2**])], **2**.
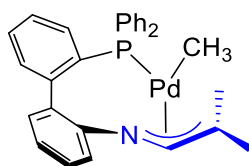
2
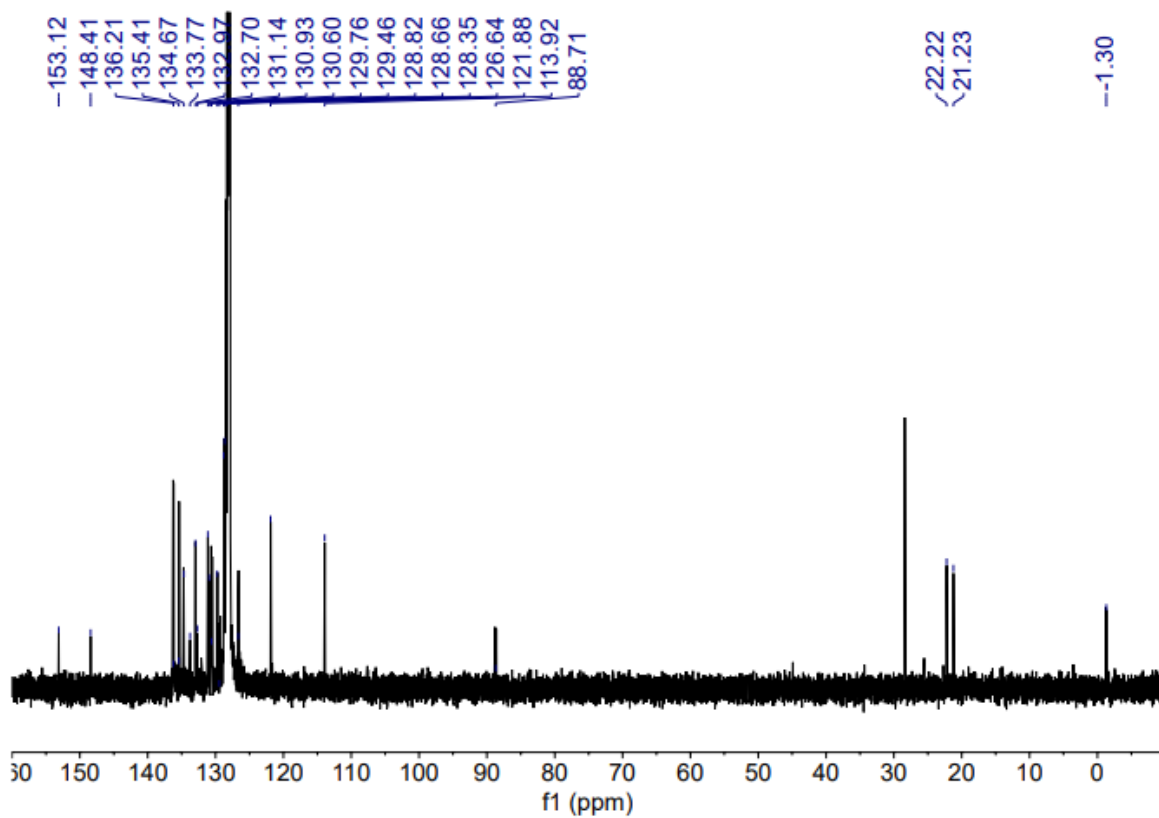
Figure A.26. $^{13}C\{^1H\}$ NMR spectrum (C_6D_6, 151 MHz) of [Pd(CH$_3$)([**L2**])], **2**.
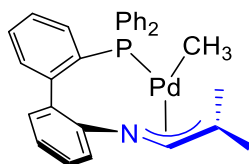
2
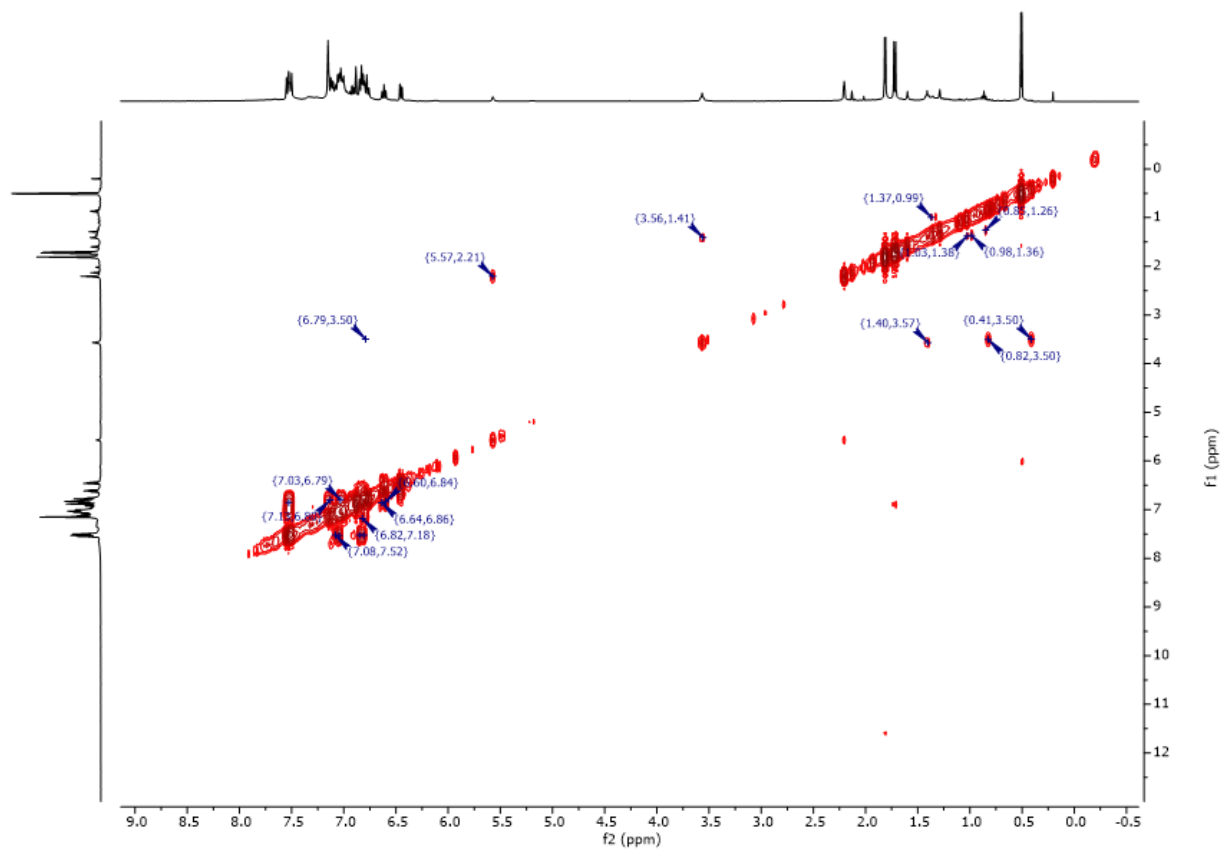
Figure A.27. ^{1}H-^{1}H COSY NMR spectrum (600 MHz, C$_6$D$_6$) of [Pd(CH$_3$)(**[L2]**)], **2**.
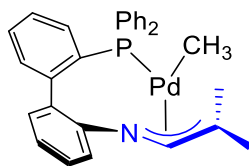
2
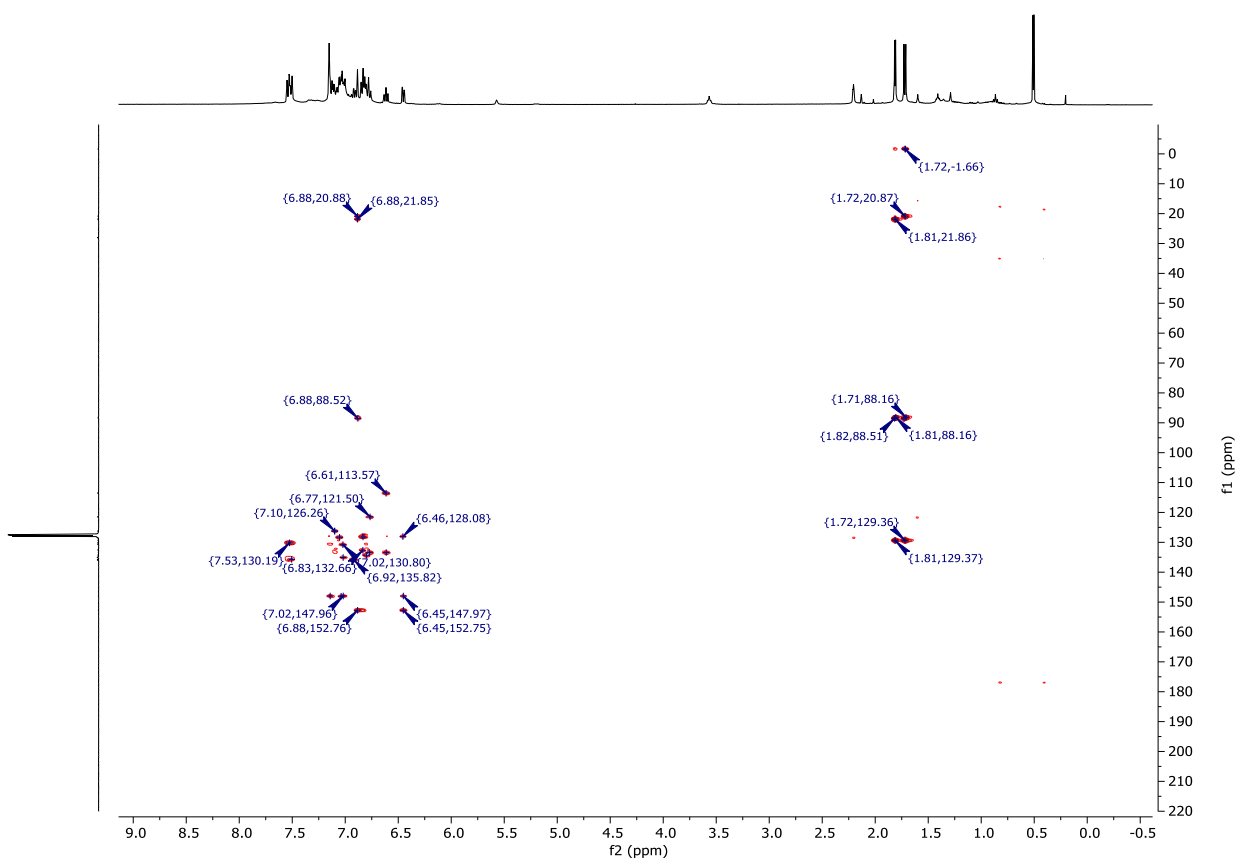
Figure A.28. ^{1}H-^{13}C HMBC NMR spectrum (600 MHz, C$_6$D$_6$) of [Pd(CH$_3$)(**[L2]**)], **2**.
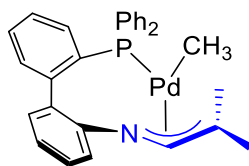
2
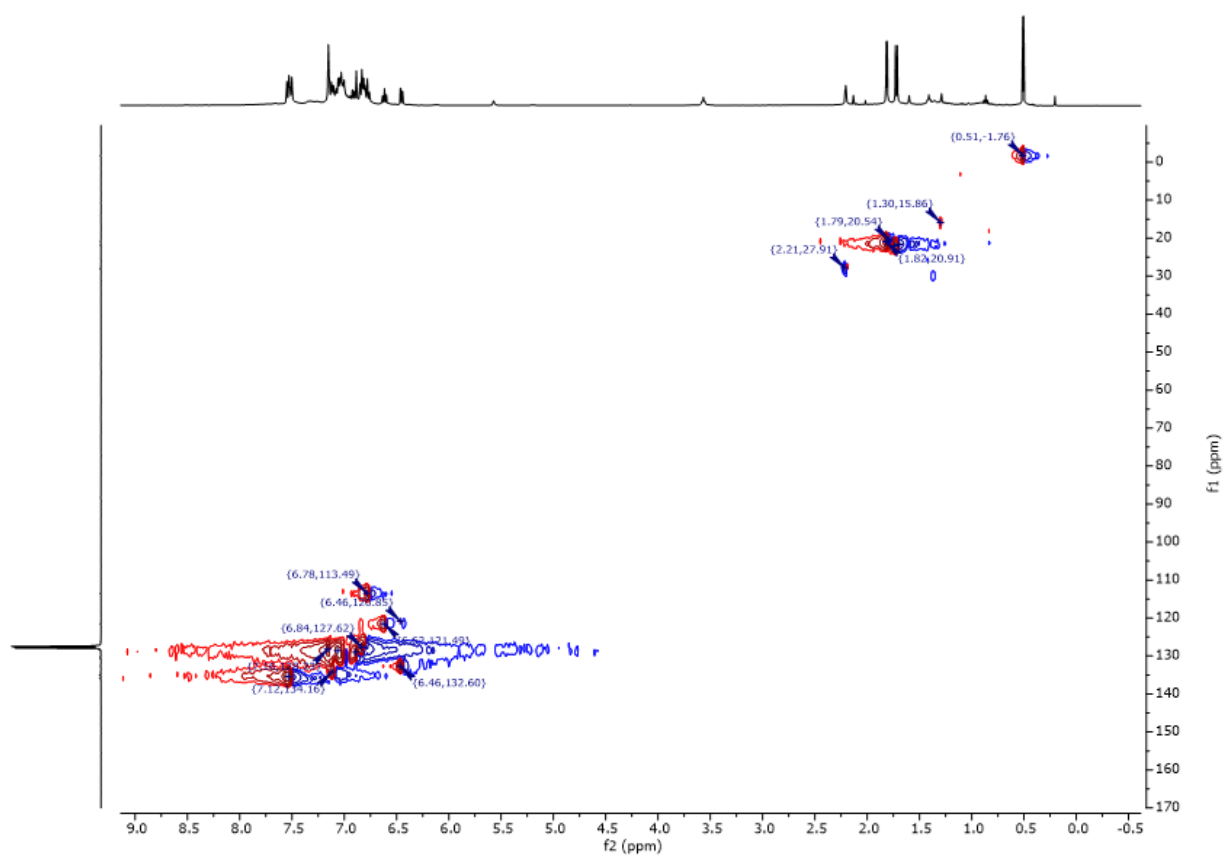
Figure A.29. ^{1}H-^{13}C HSQC NMR spectrum (600 MHz, C$_6$D$_6$) of [Pd(CH$_3$)(**[L2]**)], **2**.
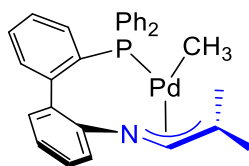
2
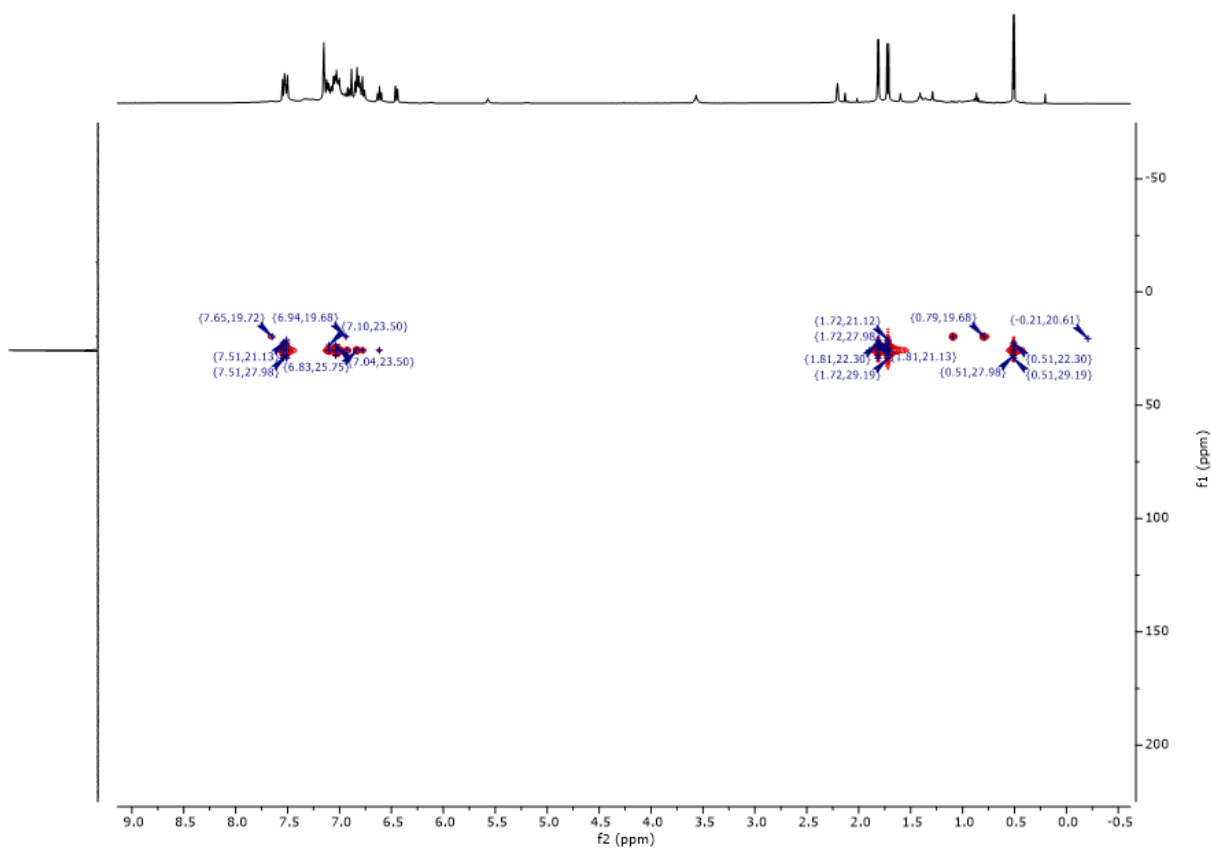
Figure A.30. ^{1}H-^{31}P HMBC NMR spectrum (600 MHz, C$_6$D$_6$) of [Pd(CH$_3$)(**[L2]**)], **2**.
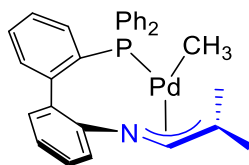
2
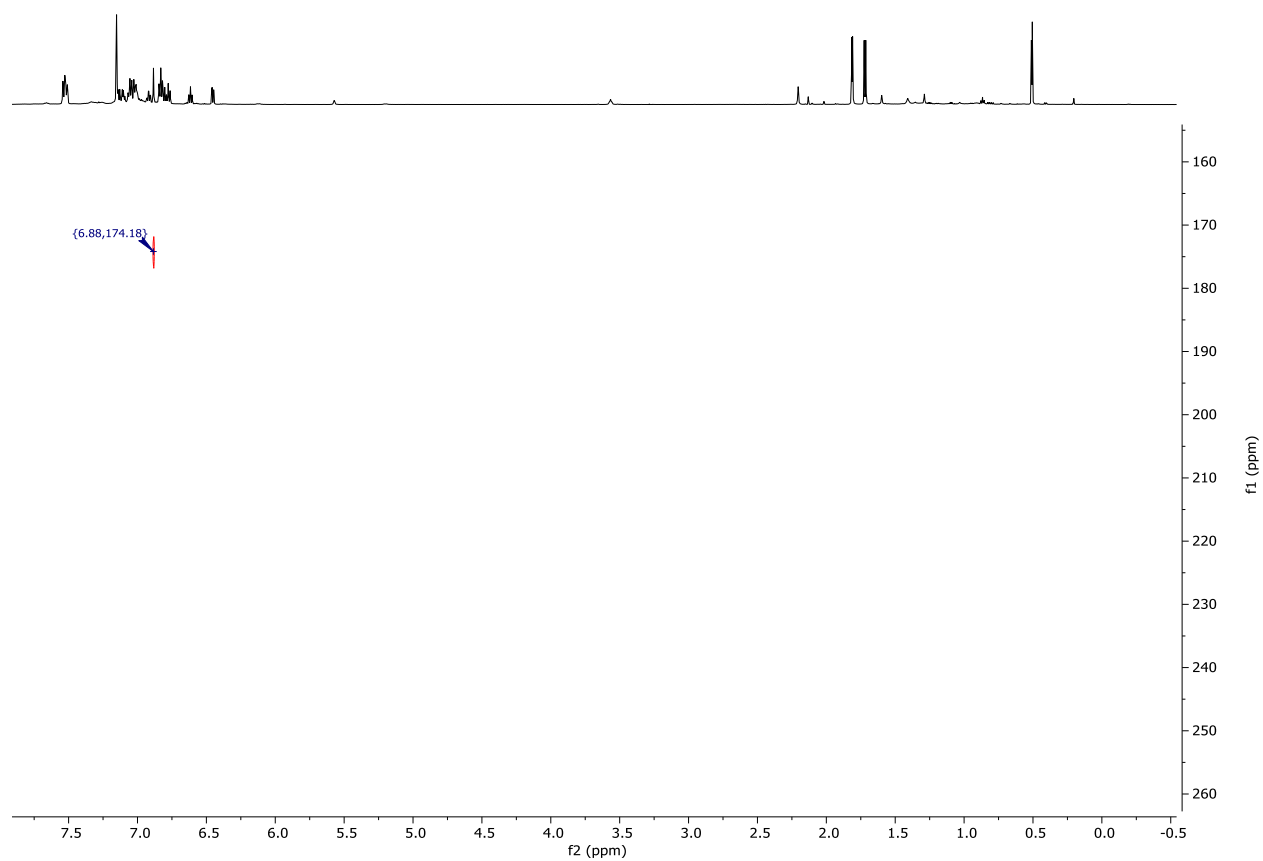
Figure A.31. ^{1}H-^{15}N HMBC NMR spectrum (600 MHz, C_6D_6) of [Pd(CH$_3$)([**L2**])], **2**.
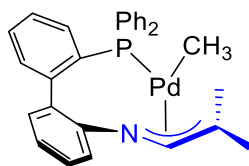
2
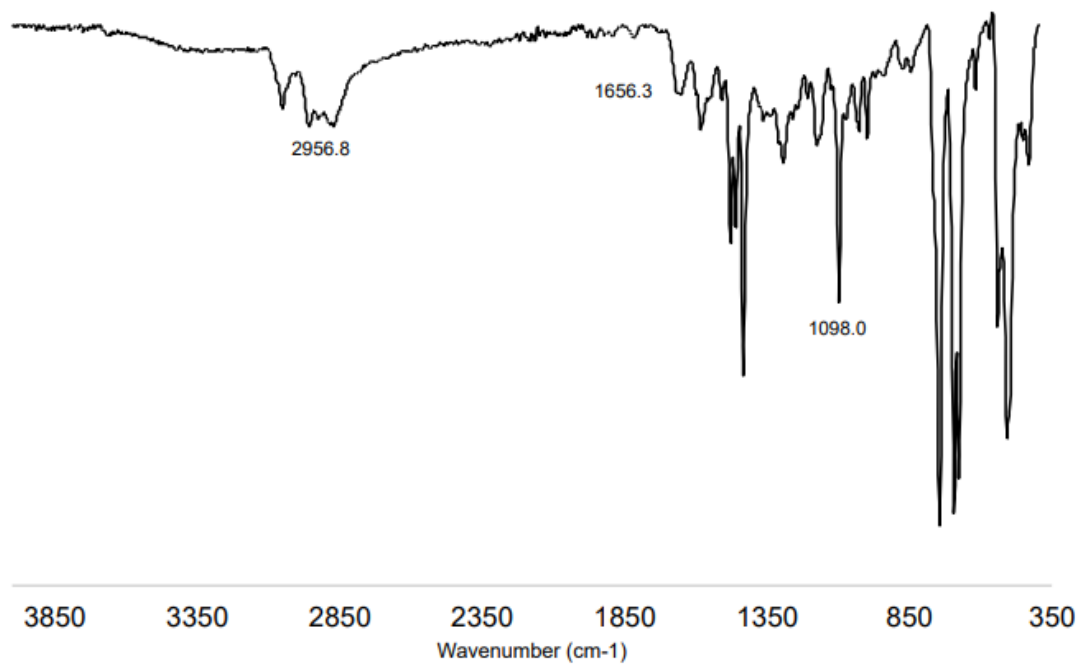
Figure A.32. ATR-FTIR of solid [Pd(CH₃)([**L2**])], **2**. Data acquired using Bruker Alpha II ATRFTIR and plotted using Microsoft Excel.
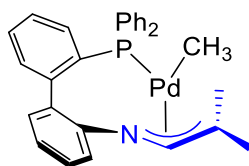
2
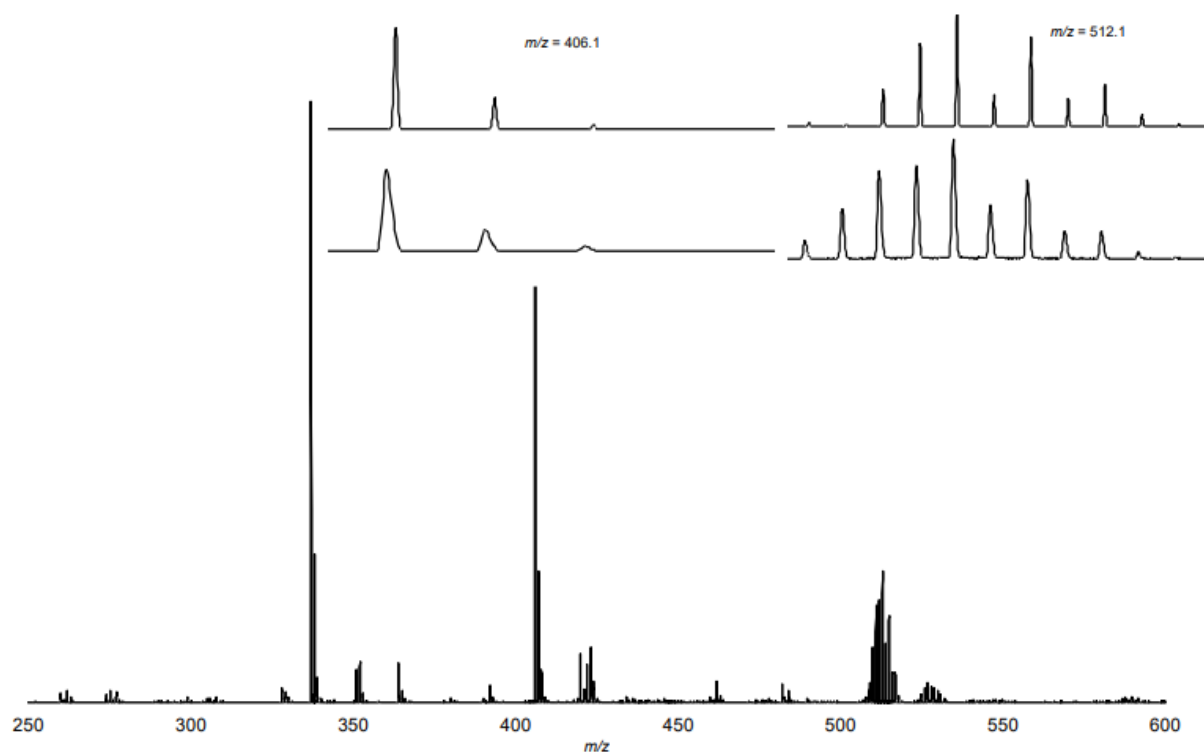
Figure A.33. MALDI mass spectrum mode of [Pd(CH$_3$)([**L2**])], **2** with pyrene as the matrix. Left inset: simulated[3] isotope pattern (top) for [**L2**]$^{\bullet+}$ and observed signal (bottom) at m/z = 406.1. Right inset: simulated[3] isotope pattern (top) for [**2**-CH$_3$]$^{\bullet+}$ and observed signal (bottom) at m/z = 512.1.

2

B $C_{29}H_{28}NPPd$ **A** $C_{58}H_{56}N_2P_2Pd_2$

Reaction in benzene: 2 **B** → **A**

$\Delta E_e = 217$ kJ/mol
$\Delta G°_{298} = 272$ kJ/mol
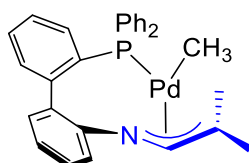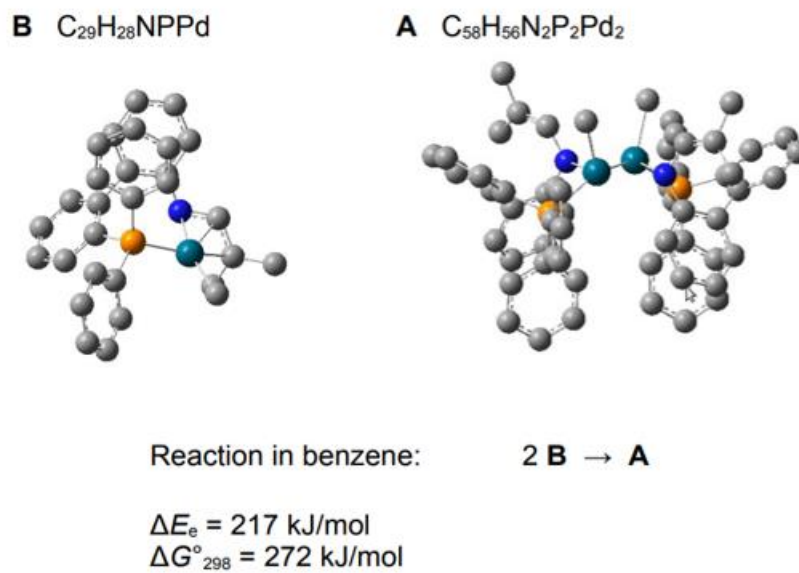
Figure A.34. DFT calculations for [Pd(CH$_3$)([**L2**])], **2** and [Pd$_2$(CH$_3$)$_2$([**L2**])$_2$], **2′**. Computations were calculated by Dr. Staroverov.
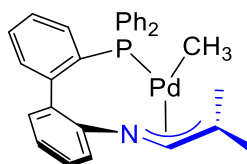
2
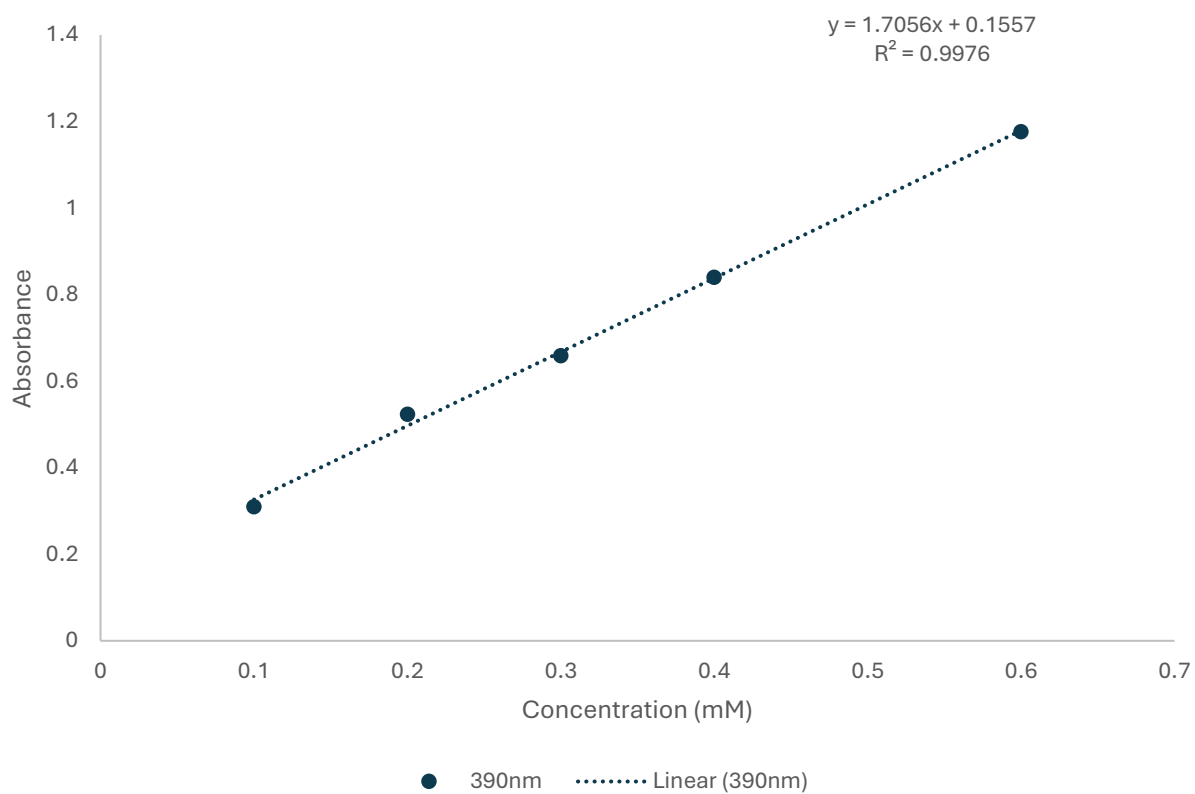
Figure A.35. Calibration curve for UV-Vis spectra of [Pd(CH$_3$)([**L2**]), **2** in toluene. Concentrations include 0.1 mM, 0.2 mM, 0.3 mM, 0.4 mM, and 0.6 mM.
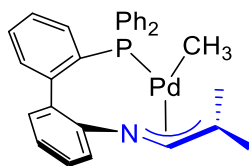
2
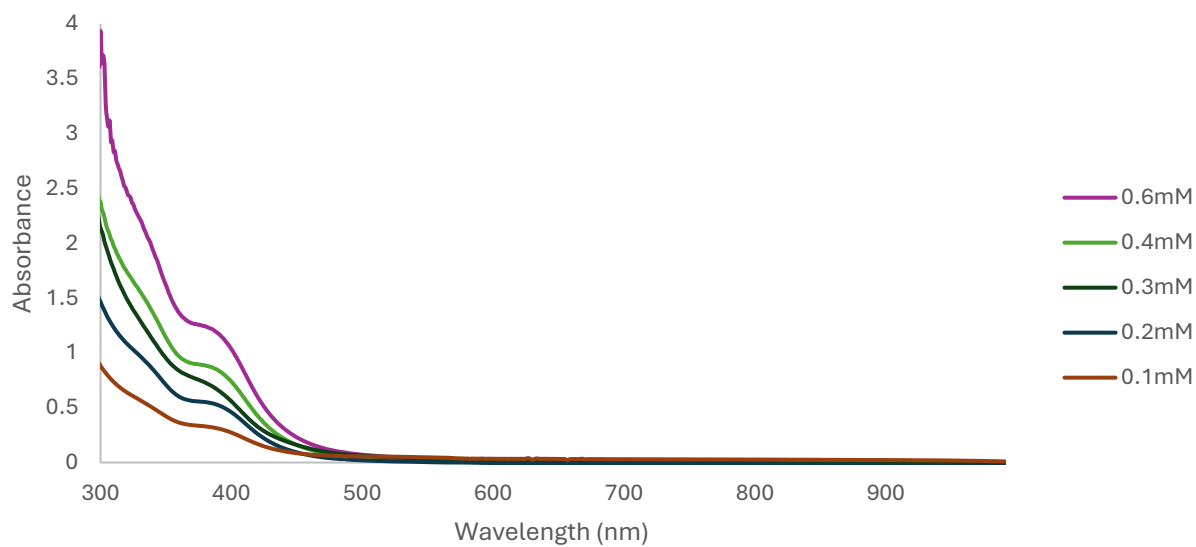
Figure A.36. UV-Vis spectra of [Pd(CH$_3$)(**[L2]**)], **2** in toluene.
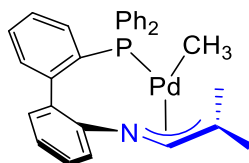
2
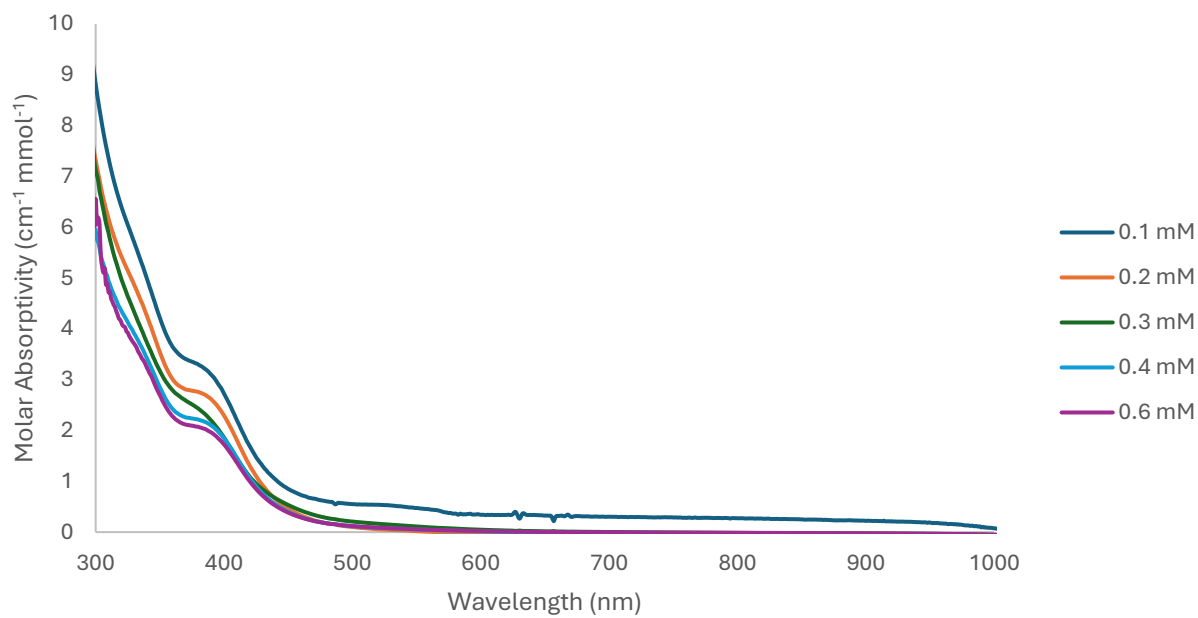
Figure A.37. Plot of molar absorptivity vs wavelength of [Pd(CH$_3$)([**L2**])], **2** in toluene. Concentrations include 0.1 mM, 0.2 mM, 0.3 mM, 0.4 mM, and 0.6 mM.
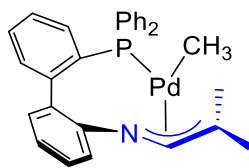
2

X-Ray Experimental for C$_{29.50}$H$_{30}$Cl$_2$NPPd (1b)

Data Collection and Processing. The sample **1b** was submitted by Kyle Jackman of the Blacquiere research group at the University of Western Ontario. The sample was mounted on a Mitegen polyimide micromount with a small amount of Paratone N oil. All X-ray measurements were made on a Bruker Kappa Axis Apex2 diffractometer at a temperature of 110 K. The unit cell dimensions were determined from a symmetry constrained fit of 9246 reflections with 5.06° < 2θ < 64.12°. The data collection strategy was a number of ω and φ scans which collected data up to 72.702° (2θ). The frame integration was performed using SAINT.[59] The resulting raw data was scaled, and absorption corrected using a multi-scan averaging of symmetry equivalent data using SADABS.[60]

Structure Solution and Refinement. The structure was solved by using a dual space methodology using the SHELXT program.[61] All non-hydrogen atoms were obtained from the initial solution. The asymmetric unit contained two symmetry independent Pd complexes, designated **A** and **B** and one CH$_2$Cl$_2$ molecule of solvation. The hydrogen atoms were introduced at idealized positions and were allowed to ride on the parent atom. The structural model was fit to the data using full matrix least-squares based on F^2. The calculated structure factors included corrections for anomalous dispersion from the usual tabulation. The structure was refined using the SHELXL program from the SHELX suite of crystallographic software.[61] Graphic plots were produced using the Mercury program.[62] Additional information and other relevant literature references can be found in the reference section of this website (http://xray.chem.uwo.ca).
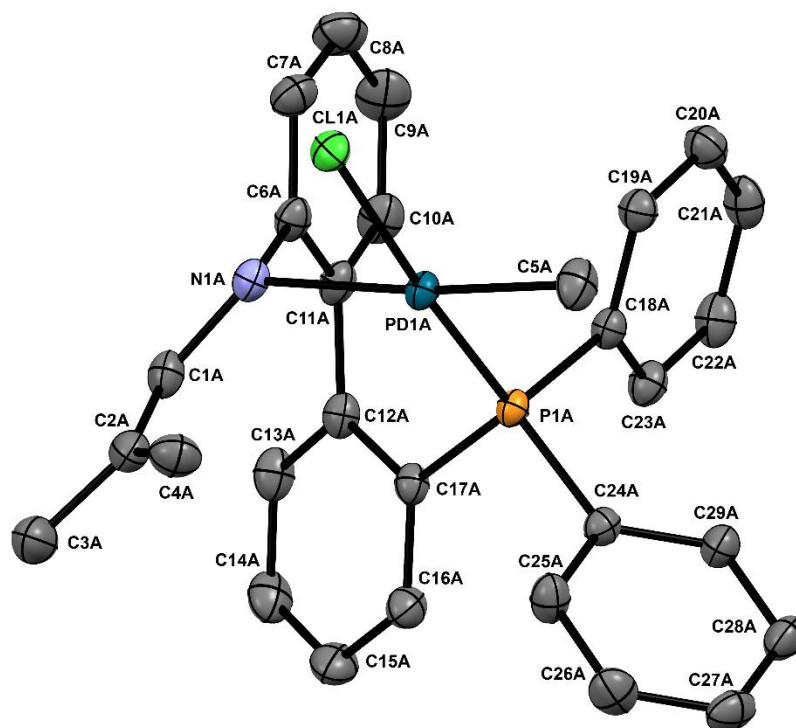
Figure A.38. ORTEP drawing of **1b** *molecule A* showing naming and numbering scheme. Ellipsoids are at the 50% probability level and hydrogen atoms were omitted for clarity.
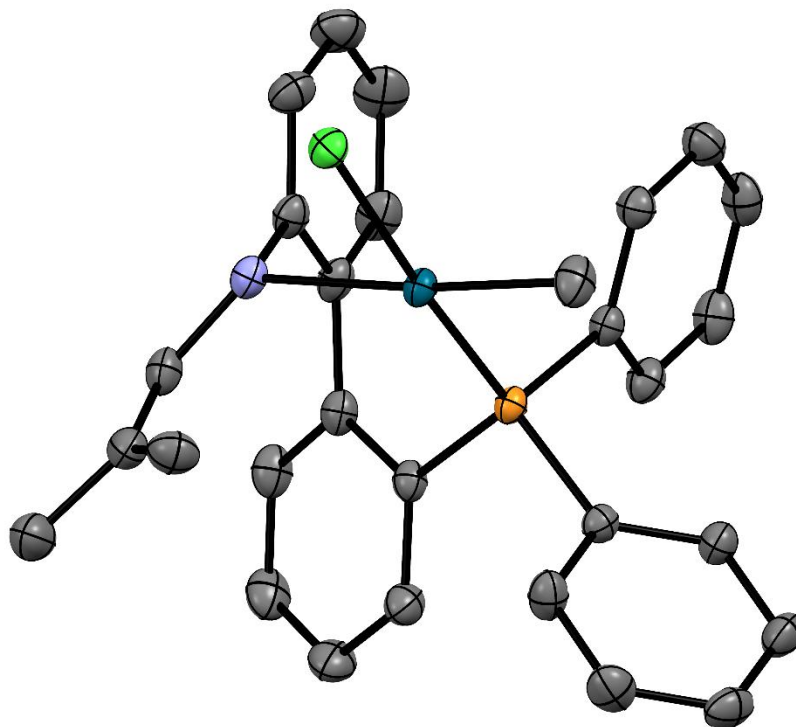
Figure A.39. ORTEP drawing of **1b** *molecule A*. Ellipsoids are at the 50% probability level and hydrogen atoms were omitted for clarity.
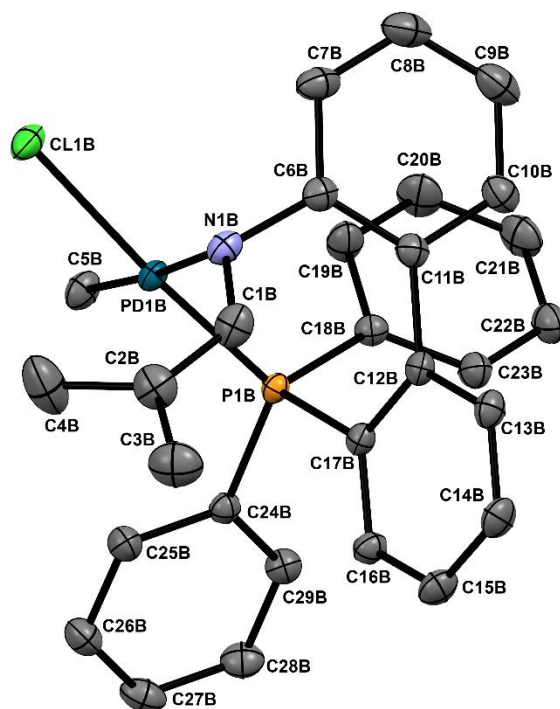
Figure A.40. ORTEP drawing of **1b** *molecule B* showing naming and numbering scheme. Ellipsoids are at the 50% probability level and hydrogen atoms were omitted for clarity.
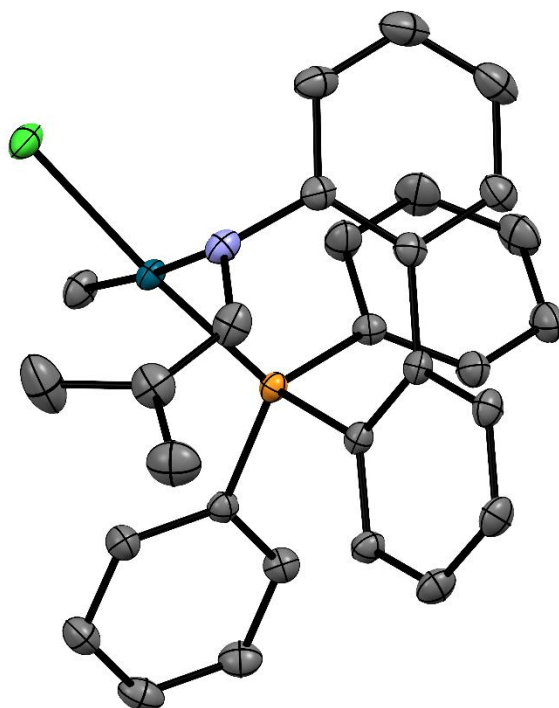
Figure A.41. ORTEP drawing of **1b** *molecule B*. Ellipsoids are at the 50% probability level and hydrogen atoms were omitted for clarity.

Table A.1. Summary of Crystal Data for 1b

Formula	$C_{29.50}H_{30}Cl_2NPPd$
Formula Weight (*g/mol*)	606.81
Crystal Dimensions (*mm*)	0.372 × 0.214 × 0.094
Crystal Color and Habit	colourless prism
Crystal System	triclinic
Space Group	P -1
Temperature, K	110
a, Å	10.701(5)
b, Å	14.209(6)
c, Å	18.491(8)
a,°	100.258(10)
b,°	94.936(14)
g,°	94.487(14)
V, Å^3	2744(2)
Number of reflections to determine final unit cell	9246
Min and Max 2q for cell determination, °	5.06, 64.12
Z	4
F(000)	1236
r (*g/cm*)	1.469
l, Å, (MoKa)	0.71073
m, (*cm^{-1}*)	0.948
Diffractometer Type	Bruker Kappa Axis Apex2
Scan Type(s)	phi and omega scans
Max 2q for data collection, °	72.702
Measured fraction of data	0.999
Number of reflections measured	219806
Unique reflections measured	26623
R$_{merge}$	0.0583
Number of reflections included in refinement	26623
Cut off Threshold Expression	I > 2sigma(I)
Structure refined using	full matrix least-squares using F^2

Weighting Scheme	$w=1/[\text{sigma}^2(F_o^2)+(0.0393P)^2+0.9644P]$ where $P=(F_o^2+2F_c^2)/3$

Number of parameters in least-squares	628
R_1	0.0362
wR_2	0.0813
R_1 (all data)	0.0544
wR_2 (all data)	0.0880
GOF	1.026
Maximum shift/error	0.005
Min & Max peak heights on final DF Map ($e^-/Å$)	-0.905, 0.950

Where:

$$R_1 = S\,|\,|F_o| - |F_c|\,|\,/\,S\,F_o$$

$$wR_2 = [\,S(\,w(\,F_o^2 - F_c^2\,)^2\,)\,/\,S(w\,F_o^4\,)\,]^{\frac{1}{2}}$$

$$GOF = [\,S(\,w(\,F_o^2 - F_c^2\,)^2\,)\,/\,(\text{No. of reflns. - No. of params.}\,)\,]^{\frac{1}{2}}$$

Table A.2. Atomic Coordinates for 1b

Atom	x	y	z	$U_{iso/equiv}$
Pd1A	0.57803(2)	0.27874(2)	1.04200(2)	0.01652(3)
Cl1A	0.43336(4)	0.29250(3)	1.13380(2)	0.02127(7)
P1A	0.70983(4)	0.25423(3)	0.95646(2)	0.01614(7)
N1A	0.72678(13)	0.29432(10)	1.13803(7)	0.0197(2)
C1A	0.82435(16)	0.37208(13)	1.16194(9)	0.0235(3)
C2A	0.80978(17)	0.46509(13)	1.16645(9)	0.0250(3)
C3A	0.9192(2)	0.53808(15)	1.19680(11)	0.0352(4)
C4A	0.68970(18)	0.50410(13)	1.14389(11)	0.0296(4)
C5A	0.43501(15)	0.25610(15)	0.95906(10)	0.0276(3)
C6A	0.76633(15)	0.19824(12)	1.12574(9)	0.0213(3)
C7A	0.70233(17)	0.12817(13)	1.15615(10)	0.0271(3)
C8A	0.7329(2)	0.03378(14)	1.14188(12)	0.0340(4)
C9A	0.8287(2)	0.00935(14)	1.09851(12)	0.0349(4)
C10A	0.89334(18)	0.07971(13)	1.06897(10)	0.0278(3)
C11A	0.86281(15)	0.17455(12)	1.08084(9)	0.0213(3)

C12A	0.93340(14)	0.24588(12)	1.04546(9)	0.0201(3)
C13A	1.06249(16)	0.26748(13)	1.06571(10)	0.0262(3)
C14A	1.13230(16)	0.33576(15)	1.03700(10)	0.0300(4)
C15A	1.07412(17)	0.38328(15)	0.98691(11)	0.0302(4)
C16A	0.94621(15)	0.36000(13)	0.96305(9)	0.0244(3)
C17A	0.87512(14)	0.29121(11)	0.99107(8)	0.0185(3)
C18A	0.71612(14)	0.12796(11)	0.91828(8)	0.0185(3)
C19A	0.62557(15)	0.05956(12)	0.93200(9)	0.0217(3)
C20A	0.63436(17)	-0.03769(13)	0.90638(10)	0.0269(3)
C21A	0.73380(17)	-0.06630(13)	0.86714(10)	0.0273(3)
C22A	0.82441(17)	0.00138(13)	0.85297(10)	0.0271(3)
C23A	0.81680(16)	0.09823(13)	0.87858(9)	0.0234(3)
C24A	0.68143(14)	0.31429(11)	0.87844(8)	0.0185(3)
C25A	0.66676(17)	0.41231(12)	0.89322(10)	0.0259(3)
C26A	0.64695(18)	0.46238(13)	0.83598(11)	0.0301(4)
C27A	0.63809(17)	0.41393(14)	0.76326(10)	0.0289(4)
C28A	0.64765(17)	0.31658(14)	0.74811(10)	0.0276(3)
C29A	0.67082(16)	0.26626(12)	0.80552(9)	0.0230(3)
Pd1B	0.38073(2)	0.25125(2)	0.55623(2)	0.01525(3)
Cl1B	0.53329(3)	0.14052(3)	0.57152(2)	0.02312(7)
P1B	0.24226(3)	0.35152(3)	0.53102(2)	0.01397(6)
N1B	0.23860(12)	0.13416(10)	0.57240(8)	0.0196(2)
C1B	0.15731(16)	0.13997(13)	0.63127(10)	0.0248(3)
C2B	0.19583(18)	0.16945(14)	0.70258(10)	0.0289(3)
C3B	0.1013(2)	0.17156(16)	0.75822(12)	0.0374(4)
C4B	0.3296(2)	0.20248(19)	0.73218(12)	0.0444(5)
C5B	0.51850(14)	0.35001(12)	0.53972(10)	0.0221(3)
C6B	0.17906(14)	0.10688(11)	0.49808(9)	0.0190(3)
C7B	0.22819(16)	0.03562(12)	0.44961(10)	0.0257(3)
C8B	0.17845(18)	0.01147(14)	0.37648(11)	0.0317(4)
C9B	0.07899(19)	0.05734(14)	0.35105(10)	0.0318(4)
C10B	0.02900(16)	0.12790(12)	0.39891(9)	0.0240(3)

C11B	0.07829(14)	0.15419(11)	0.47298(9)	0.0183(3)
C12B	0.02010(13)	0.22963(11)	0.52241(8)	0.0163(2)
C13B	-0.10384(14)	0.20925(12)	0.53731(9)	0.0205(3)
C14B	-0.16243(14)	0.27465(13)	0.58501(10)	0.0239(3)
C15B	-0.09858(15)	0.36189(13)	0.61808(10)	0.0237(3)
C16B	0.02396(14)	0.38468(11)	0.60216(9)	0.0188(3)
C17B	0.08397(13)	0.31985(11)	0.55439(8)	0.0156(2)
C18B	0.21367(14)	0.35535(11)	0.43288(8)	0.0170(3)
C19B	0.30442(16)	0.32982(14)	0.38533(9)	0.0257(3)
C20B	0.28081(19)	0.32987(16)	0.30993(10)	0.0325(4)
C21B	0.16645(19)	0.35363(14)	0.28175(10)	0.0301(4)
C22B	0.07365(17)	0.37710(13)	0.32834(9)	0.0261(3)
C23B	0.09720(15)	0.37830(12)	0.40351(9)	0.0214(3)
C24B	0.27865(13)	0.47526(10)	0.57940(8)	0.0161(2)
C25B	0.35035(15)	0.49091(12)	0.64780(9)	0.0209(3)
C26B	0.37775(17)	0.58353(12)	0.68877(9)	0.0249(3)
C27B	0.33183(17)	0.66073(12)	0.66147(10)	0.0257(3)
C28B	0.26068(17)	0.64564(12)	0.59381(10)	0.0246(3)
C29B	0.23458(15)	0.55322(11)	0.55213(9)	0.0198(3)
C1M	0.47360(18)	-0.08899(15)	0.62509(11)	0.0313(4)
Cl1M	0.31157(4)	-0.07731(4)	0.63201(3)	0.03695(11)
Cl2M	0.55330(5)	-0.08880(6)	0.71174(3)	0.05402(17)
H1NA	0.677242	0.296027	1.181626	0.024
H1A	0.906253	0.355603	1.175679	0.028
H3A1	0.994969	0.505208	1.204798	0.053
H3A2	0.901061	0.575784	1.243825	0.053
H3A3	0.933109	0.580933	1.161585	0.053
H4A1	0.627896	0.450999	1.119406	0.044
H4A2	0.705805	0.548017	1.109733	0.044
H4A3	0.656668	0.538855	1.187744	0.044
H5A1	0.410183	0.318055	0.949522	0.041
H5A2	0.362788	0.219580	0.973531	0.041

H5A3	0.463171	0.219772	0.914200	0.041
H7A	0.637569	0.144879	1.186772	0.033
H8A	0.687772	-0.014081	1.161956	0.041
H9A	0.850140	-0.055027	1.089020	0.042
H10A	0.960056	0.062846	1.039926	0.033
H13A	1.103493	0.234591	1.099989	0.031
H14A	1.219992	0.349683	1.051860	0.036
H15A	1.120900	0.431933	0.968545	0.036
H16A	0.907248	0.391569	0.927186	0.029
H19A	0.557452	0.079225	0.958942	0.026
H20A	0.572308	-0.084342	0.915773	0.032
H21A	0.739927	-0.132698	0.849850	0.033
H22A	0.891882	-0.018731	0.825623	0.033
H23A	0.879516	0.144497	0.869342	0.028
H25A	0.670374	0.445094	0.942943	0.031
H26A	0.639472	0.529509	0.846480	0.036
H27A	0.625413	0.448101	0.723918	0.035
H28A	0.638445	0.283355	0.698321	0.033
H29A	0.679313	0.199293	0.794707	0.028
H1NB	0.289748	0.079818	0.579162	0.024
H1B	0.069963	0.121369	0.618014	0.030
H3B1	0.016076	0.159047	0.732493	0.056
H3B2	0.110324	0.234875	0.790507	0.056
H3B3	0.115976	0.122130	0.787969	0.056
H4B1	0.377586	0.216095	0.691825	0.067
H4B2	0.366649	0.152060	0.754380	0.067
H4B3	0.332064	0.260913	0.769738	0.067
H5B1	0.480078	0.402113	0.520450	0.033
H5B2	0.572410	0.319238	0.504087	0.033
H5B3	0.569347	0.376237	0.586667	0.033
H7B	0.296123	0.003546	0.466922	0.031
H8B	0.212721	-0.036774	0.343643	0.038

H9B	0.044886	0.040546	0.300803	0.038
H10B	-0.039723	0.158826	0.381115	0.029
H13B	-0.148854	0.149611	0.514427	0.025
H14B	-0.246526	0.259298	0.594875	0.029
H15B	-0.137858	0.406199	0.651497	0.028
H16B	0.067172	0.445308	0.624226	0.023
H19B	0.382837	0.312277	0.404291	0.031
H20B	0.343748	0.313482	0.277910	0.039
H21B	0.150976	0.353973	0.230440	0.036
H22B	-0.005696	0.392270	0.308727	0.031
H23B	0.033942	0.394801	0.435279	0.026
H25B	0.380705	0.438015	0.666572	0.025
H26B	0.427485	0.593992	0.735082	0.030
H27B	0.349503	0.723980	0.689482	0.031
H28B	0.229337	0.698573	0.575559	0.029
H29B	0.186839	0.543355	0.505212	0.024
H1M1	0.483601	-0.149709	0.591308	0.038
H1M2	0.510828	-0.035144	0.604062	0.038

Table A.3. Anisotropic Displacement Parameters for 1b

Atom	u^{11}	u^{22}	u^{33}	u^{12}	u^{13}	u^{23}
Pd1A	0.01529(5)	0.01958(5)	0.01475(5)	0.00421(4)	0.00194(4)	0.00206(4)
Cl1A	0.02084(16)	0.02268(17)	0.02041(16)	0.00376(13)	0.00635(13)	0.00158(13)
P1A	0.01513(15)	0.01916(17)	0.01418(16)	0.00336(13)	0.00123(12)	0.00263(13)
N1A	0.0208(6)	0.0224(6)	0.0164(6)	0.0056(5)	0.0019(5)	0.0030(5)
C1A	0.0219(7)	0.0297(8)	0.0174(7)	0.0042(6)	-0.0007(5)	0.0012(6)
C2A	0.0269(8)	0.0282(8)	0.0197(7)	0.0003(6)	0.0023(6)	0.0047(6)
C3A	0.0382(10)	0.0355(10)	0.0308(9)	-0.0044(8)	-0.0037(8)	0.0098(8)
C4A	0.0300(9)	0.0245(8)	0.0361(10)	0.0038(7)	0.0035(7)	0.0102(7)
C5A	0.0176(7)	0.0405(10)	0.0240(8)	0.0052(6)	-0.0007(6)	0.0039(7)
C6A	0.0237(7)	0.0232(7)	0.0176(7)	0.0062(6)	-0.0008(5)	0.0048(5)
C7A	0.0287(8)	0.0307(9)	0.0244(8)	0.0043(7)	0.0026(6)	0.0112(7)

C8A	0.0390(10)	0.0291(9)	0.0374(10)	0.0035(8)	0.0008(8)	0.0165(8)
C9A	0.0433(11)	0.0252(9)	0.0390(10)	0.0136(8)	0.0004(8)	0.0113(8)
C10A	0.0309(9)	0.0273(8)	0.0268(8)	0.0115(7)	0.0013(7)	0.0061(7)
C11A	0.0217(7)	0.0251(7)	0.0179(7)	0.0072(6)	-0.0005(5)	0.0054(6)
C12A	0.0185(6)	0.0235(7)	0.0179(6)	0.0068(5)	0.0005(5)	0.0015(5)
C13A	0.0201(7)	0.0333(9)	0.0243(8)	0.0088(6)	-0.0017(6)	0.0025(7)
C14A	0.0167(7)	0.0416(10)	0.0294(9)	0.0010(7)	0.0000(6)	0.0028(7)
C15A	0.0210(7)	0.0384(10)	0.0309(9)	-0.0045(7)	0.0035(6)	0.0085(7)
C16A	0.0191(7)	0.0316(8)	0.0225(7)	0.0000(6)	0.0005(6)	0.0067(6)
C17A	0.0154(6)	0.0224(7)	0.0170(6)	0.0030(5)	0.0007(5)	0.0016(5)
C18A	0.0190(6)	0.0206(7)	0.0159(6)	0.0045(5)	0.0010(5)	0.0027(5)
C19A	0.0224(7)	0.0214(7)	0.0211(7)	0.0038(6)	0.0030(6)	0.0024(6)
C20A	0.0293(8)	0.0214(8)	0.0288(8)	0.0004(6)	0.0002(7)	0.0040(6)
C21A	0.0316(9)	0.0220(8)	0.0265(8)	0.0085(6)	-0.0034(7)	-0.0002(6)
C22A	0.0260(8)	0.0306(9)	0.0239(8)	0.0113(7)	0.0023(6)	-0.0010(6)
C23A	0.0224(7)	0.0281(8)	0.0200(7)	0.0055(6)	0.0034(6)	0.0033(6)
C24A	0.0164(6)	0.0210(7)	0.0184(6)	0.0026(5)	0.0009(5)	0.0051(5)
C25A	0.0302(8)	0.0232(8)	0.0231(8)	0.0074(6)	-0.0029(6)	0.0021(6)
C26A	0.0322(9)	0.0239(8)	0.0348(9)	0.0050(7)	-0.0045(7)	0.0095(7)
C27A	0.0255(8)	0.0363(10)	0.0284(9)	0.0024(7)	-0.0013(6)	0.0179(7)
C28A	0.0289(8)	0.0362(9)	0.0187(7)	0.0025(7)	0.0013(6)	0.0085(7)
C29A	0.0252(7)	0.0250(8)	0.0187(7)	0.0032(6)	0.0016(6)	0.0044(6)
Pd1B	0.01205(4)	0.01607(5)	0.01841(5)	0.00225(3)	0.00229(3)	0.00453(4)
Cl1B	0.01628(15)	0.02014(16)	0.0335(2)	0.00537(12)	0.00141(14)	0.00537(14)
P1B	0.01226(14)	0.01534(16)	0.01487(15)	0.00149(12)	0.00211(12)	0.00392(12)
N1B	0.0164(5)	0.0192(6)	0.0246(6)	0.0031(4)	0.0041(5)	0.0062(5)
C1B	0.0220(7)	0.0279(8)	0.0275(8)	0.0019(6)	0.0044(6)	0.0129(6)
C2B	0.0309(9)	0.0296(9)	0.0270(8)	-0.0009(7)	0.0047(7)	0.0085(7)
C3B	0.0459(12)	0.0372(11)	0.0320(10)	0.0050(9)	0.0131(9)	0.0095(8)
C4B	0.0377(11)	0.0621(15)	0.0278(10)	-0.0162(10)	-0.0004(8)	0.0044(9)
C5B	0.0150(6)	0.0238(7)	0.0289(8)	0.0011(5)	0.0046(5)	0.0078(6)
C6B	0.0170(6)	0.0165(6)	0.0235(7)	-0.0009(5)	0.0047(5)	0.0036(5)

C7B	0.0218(7)	0.0194(7)	0.0353(9)	0.0011(6)	0.0102(6)	0.0006(6)
C8B	0.0321(9)	0.0255(8)	0.0341(9)	-0.0022(7)	0.0132(7)	-0.0062(7)
C9B	0.0335(9)	0.0345(10)	0.0224(8)	-0.0077(7)	0.0053(7)	-0.0048(7)
C10B	0.0232(7)	0.0256(8)	0.0210(7)	-0.0027(6)	0.0014(6)	0.0010(6)
C11B	0.0164(6)	0.0171(6)	0.0206(7)	-0.0019(5)	0.0030(5)	0.0023(5)
C12B	0.0142(6)	0.0179(6)	0.0173(6)	0.0017(5)	0.0002(5)	0.0049(5)
C13B	0.0152(6)	0.0220(7)	0.0242(7)	-0.0006(5)	0.0005(5)	0.0056(6)
C14B	0.0132(6)	0.0295(8)	0.0298(8)	0.0013(6)	0.0050(6)	0.0067(6)
C15B	0.0179(7)	0.0269(8)	0.0278(8)	0.0047(6)	0.0081(6)	0.0056(6)
C16B	0.0161(6)	0.0197(7)	0.0208(7)	0.0026(5)	0.0043(5)	0.0029(5)
C17B	0.0133(6)	0.0187(6)	0.0158(6)	0.0026(5)	0.0016(4)	0.0054(5)
C18B	0.0175(6)	0.0172(6)	0.0168(6)	0.0014(5)	0.0034(5)	0.0039(5)
C19B	0.0199(7)	0.0381(9)	0.0201(7)	0.0048(6)	0.0051(6)	0.0057(6)
C20B	0.0327(9)	0.0482(11)	0.0182(7)	0.0062(8)	0.0101(7)	0.0063(7)
C21B	0.0386(10)	0.0354(10)	0.0164(7)	0.0032(8)	0.0019(7)	0.0055(7)
C22B	0.0298(8)	0.0284(8)	0.0194(7)	0.0050(7)	-0.0032(6)	0.0042(6)
C23B	0.0221(7)	0.0235(7)	0.0190(7)	0.0047(6)	0.0006(5)	0.0044(6)
C24B	0.0142(6)	0.0177(6)	0.0167(6)	0.0016(5)	0.0028(5)	0.0033(5)
C25B	0.0209(7)	0.0221(7)	0.0190(7)	0.0024(5)	0.0007(5)	0.0025(5)
C26B	0.0272(8)	0.0251(8)	0.0196(7)	-0.0013(6)	0.0002(6)	-0.0004(6)
C27B	0.0323(8)	0.0192(7)	0.0241(8)	-0.0029(6)	0.0080(6)	0.0000(6)
C28B	0.0295(8)	0.0179(7)	0.0274(8)	0.0023(6)	0.0062(6)	0.0057(6)
C29B	0.0203(7)	0.0193(7)	0.0204(7)	0.0015(5)	0.0032(5)	0.0048(5)
C1M	0.0315(9)	0.0374(10)	0.0277(9)	0.0084(7)	0.0026(7)	0.0118(7)
Cl1M	0.0262(2)	0.0376(2)	0.0499(3)	0.00265(18)	-0.00165(19)	0.0188(2)
Cl2M	0.0294(2)	0.0998(5)	0.0369(3)	-0.0018(3)	-0.0039(2)	0.0305(3)

Table A.4. Bond Lengths for 1b

Pd1A-C5A	2.0351(18)		Pd1B-N1B	2.2429(15)
Pd1A-P1A	2.2085(8)		Pd1B-Cl1B	2.3879(8)
Pd1A-N1A	2.2483(15)		P1B-C24B	1.8209(16)
Pd1A-Cl1A	2.3871(9)		P1B-C18B	1.8253(17)
P1A-C18A	1.8161(17)		P1B-C17B	1.8261(16)
P1A-C24A	1.8181(17)		N1B-C6B	1.437(2)
P1A-C17A	1.8315(17)		N1B-C1B	1.446(2)
N1A-C1A	1.440(2)		N1B-H1NB	1.0000
N1A-C6A	1.446(2)		C1B-C2B	1.329(3)
N1A-H1NA	1.0000		C1B-H1B	0.9500
C1A-C2A	1.332(3)		C2B-C4B	1.495(3)
C1A-H1A	0.9500		C2B-C3B	1.501(3)
C2A-C4A	1.495(3)		C3B-H3B1	0.9800
C2A-C3A	1.501(3)		C3B-H3B2	0.9800
C3A-H3A1	0.9800		C3B-H3B3	0.9800
C3A-H3A2	0.9800		C4B-H4B1	0.9800
C3A-H3A3	0.9800		C4B-H4B2	0.9800
C4A-H4A1	0.9800		C4B-H4B3	0.9800
C4A-H4A2	0.9800		C5B-H5B1	0.9800
C4A-H4A3	0.9800		C5B-H5B2	0.9800
C5A-H5A1	0.9800		C5B-H5B3	0.9800
C5A-H5A2	0.9800		C6B-C7B	1.395(2)
C5A-H5A3	0.9800		C6B-C11B	1.403(2)
C6A-C7A	1.391(2)		C7B-C8B	1.383(3)
C6A-C11A	1.404(2)		C7B-H7B	0.9500
C7A-C8A	1.390(3)		C8B-C9B	1.382(3)
C7A-H7A	0.9500		C8B-H8B	0.9500
C8A-C9A	1.384(3)		C9B-C10B	1.387(3)
C8A-H8A	0.9500		C9B-H9B	0.9500
C9A-C10A	1.388(3)		C10B-C11B	1.399(2)
C9A-H9A	0.9500		C10B-H10B	0.9500

C10A-C11A	1.395(2)	C11B-C12B	1.492(2)
C10A-H10A	0.9500	C12B-C13B	1.397(2)
C11A-C12A	1.493(2)	C12B-C17B	1.408(2)
C12A-C13A	1.395(2)	C13B-C14B	1.389(2)
C12A-C17A	1.415(2)	C13B-H13B	0.9500
C13A-C14A	1.385(3)	C14B-C15B	1.379(2)
C13A-H13A	0.9500	C14B-H14B	0.9500
C14A-C15A	1.375(3)	C15B-C16B	1.395(2)
C14A-H14A	0.9500	C15B-H15B	0.9500
C15A-C16A	1.397(2)	C16B-C17B	1.393(2)
C15A-H15A	0.9500	C16B-H16B	0.9500
C16A-C17A	1.391(2)	C18B-C19B	1.392(2)
C16A-H16A	0.9500	C18B-C23B	1.402(2)
C18A-C19A	1.390(2)	C19B-C20B	1.396(2)
C18A-C23A	1.405(2)	C19B-H19B	0.9500
C19A-C20A	1.392(2)	C20B-C21B	1.379(3)
C19A-H19A	0.9500	C20B-H20B	0.9500
C20A-C21A	1.386(3)	C21B-C22B	1.392(3)
C20A-H20A	0.9500	C21B-H21B	0.9500
C21A-C22A	1.386(3)	C22B-C23B	1.388(2)
C21A-H21A	0.9500	C22B-H22B	0.9500
C22A-C23A	1.384(3)	C23B-H23B	0.9500
C22A-H22A	0.9500	C24B-C25B	1.394(2)
C23A-H23A	0.9500	C24B-C29B	1.394(2)
C24A-C29A	1.389(2)	C25B-C26B	1.392(2)
C24A-C25A	1.395(2)	C25B-H25B	0.9500
C25A-C26A	1.387(3)	C26B-C27B	1.392(3)
C25A-H25A	0.9500	C26B-H26B	0.9500
C26A-C27A	1.389(3)	C27B-C28B	1.381(3)
C26A-H26A	0.9500	C27B-H27B	0.9500
C27A-C28A	1.375(3)	C28B-C29B	1.393(2)
C27A-H27A	0.9500	C28B-H28B	0.9500

C28A-C29A	1.397(2)	C29B-H29B	0.9500
C28A-H28A	0.9500	C1M-Cl2M	1.749(2)
C29A-H29A	0.9500	C1M-Cl1M	1.768(2)
Pd1B-C5B	2.0353(17)	C1M-H1M1	0.9900
Pd1B-P1B	2.2115(8)	C1M-H1M2	0.9900

Table A.5. Bond Angles for 1b

C5A-Pd1A-P1A	87.90(6)	C5B-Pd1B-Cl1B	90.40(6)
C5A-Pd1A-N1A	175.06(7)	P1B-Pd1B-Cl1B	174.651(15)
P1A-Pd1A-N1A	95.18(5)	N1B-Pd1B-Cl1B	85.64(5)
C5A-Pd1A-Cl1A	91.68(6)	C24B-P1B-C18B	106.84(7)
P1A-Pd1A-Cl1A	175.713(15)	C24B-P1B-C17B	103.30(7)
N1A-Pd1A-Cl1A	84.97(5)	C18B-P1B-C17B	102.06(7)
C18A-P1A-C24A	106.61(8)	C24B-P1B-Pd1B	115.28(5)
C18A-P1A-C17A	101.37(7)	C18B-P1B-Pd1B	113.95(5)
C24A-P1A-C17A	104.69(7)	C17B-P1B-Pd1B	114.03(5)
C18A-P1A-Pd1A	113.23(5)	C6B-N1B-C1B	117.01(13)
C24A-P1A-Pd1A	115.65(6)	C6B-N1B-Pd1B	99.35(9)
C17A-P1A-Pd1A	113.93(6)	C1B-N1B-Pd1B	125.66(11)
C1A-N1A-C6A	116.71(13)	C6B-N1B-H1NB	104.2
C1A-N1A-Pd1A	127.03(11)	C1B-N1B-H1NB	104.2
C6A-N1A-Pd1A	99.52(9)	Pd1B-N1B-H1NB	104.2
C1A-N1A-H1NA	103.6	C2B-C1B-N1B	124.79(16)
C6A-N1A-H1NA	103.6	C2B-C1B-H1B	117.6
Pd1A-N1A-H1NA	103.6	N1B-C1B-H1B	117.6
C2A-C1A-N1A	125.67(15)	C1B-C2B-C4B	124.07(18)
C2A-C1A-H1A	117.2	C1B-C2B-C3B	119.37(18)
N1A-C1A-H1A	117.2	C4B-C2B-C3B	116.56(18)
C1A-C2A-C4A	124.64(16)	C2B-C3B-H3B1	109.5
C1A-C2A-C3A	119.31(17)	C2B-C3B-H3B2	109.5
C4A-C2A-C3A	116.05(17)	H3B1-C3B-H3B2	109.5
C2A-C3A-H3A1	109.5	C2B-C3B-H3B3	109.5

C2A-C3A-H3A2	109.5		H3B1-C3B-H3B3	109.5
H3A1-C3A-H3A2	109.5		H3B2-C3B-H3B3	109.5
C2A-C3A-H3A3	109.5		C2B-C4B-H4B1	109.5
H3A1-C3A-H3A3	109.5		C2B-C4B-H4B2	109.5
H3A2-C3A-H3A3	109.5		H4B1-C4B-H4B2	109.5
C2A-C4A-H4A1	109.5		C2B-C4B-H4B3	109.5
C2A-C4A-H4A2	109.5		H4B1-C4B-H4B3	109.5
H4A1-C4A-H4A2	109.5		H4B2-C4B-H4B3	109.5
C2A-C4A-H4A3	109.5		Pd1B-C5B-H5B1	109.5
H4A1-C4A-H4A3	109.5		Pd1B-C5B-H5B2	109.5
H4A2-C4A-H4A3	109.5		H5B1-C5B-H5B2	109.5
Pd1A-C5A-H5A1	109.5		Pd1B-C5B-H5B3	109.5
Pd1A-C5A-H5A2	109.5		H5B1-C5B-H5B3	109.5
H5A1-C5A-H5A2	109.5		H5B2-C5B-H5B3	109.5
Pd1A-C5A-H5A3	109.5		C7B-C6B-C11B	120.15(15)
H5A1-C5A-H5A3	109.5		C7B-C6B-N1B	118.54(15)
H5A2-C5A-H5A3	109.5		C11B-C6B-N1B	121.21(14)
C7A-C6A-C11A	120.42(16)		C8B-C7B-C6B	120.30(17)
C7A-C6A-N1A	118.62(15)		C8B-C7B-H7B	119.9
C11A-C6A-N1A	120.87(15)		C6B-C7B-H7B	119.9
C8A-C7A-C6A	120.19(18)		C9B-C8B-C7B	120.16(17)
C8A-C7A-H7A	119.9		C9B-C8B-H8B	119.9
C6A-C7A-H7A	119.9		C7B-C8B-H8B	119.9
C9A-C8A-C7A	120.18(18)		C8B-C9B-C10B	119.99(17)
C9A-C8A-H8A	119.9		C8B-C9B-H9B	120.0
C7A-C8A-H8A	119.9		C10B-C9B-H9B	120.0
C8A-C9A-C10A	119.43(18)		C9B-C10B-C11B	120.96(17)
C8A-C9A-H9A	120.3		C9B-C10B-H10B	119.5
C10A-C9A-H9A	120.3		C11B-C10B-H10B	119.5
C9A-C10A-C11A	121.69(18)		C10B-C11B-C6B	118.45(15)
C9A-C10A-H10A	119.2		C10B-C11B-C12B	118.87(14)
C11A-C10A-H10A	119.2		C6B-C11B-C12B	122.67(14)

C10A-C11A-C6A	118.05(16)	C13B-C12B-C17B	118.80(14)
C10A-C11A-C12A	118.90(15)	C13B-C12B-C11B	118.00(13)
C6A-C11A-C12A	123.05(15)	C17B-C12B-C11B	123.21(13)
C13A-C12A-C17A	118.56(16)	C14B-C13B-C12B	121.14(15)
C13A-C12A-C11A	118.81(15)	C14B-C13B-H13B	119.4
C17A-C12A-C11A	122.62(14)	C12B-C13B-H13B	119.4
C14A-C13A-C12A	121.56(16)	C15B-C14B-C13B	120.04(15)
C14A-C13A-H13A	119.2	C15B-C14B-H14B	120.0
C12A-C13A-H13A	119.2	C13B-C14B-H14B	120.0
C15A-C14A-C13A	119.72(16)	C14B-C15B-C16B	119.62(15)
C15A-C14A-H14A	120.1	C14B-C15B-H15B	120.2
C13A-C14A-H14A	120.1	C16B-C15B-H15B	120.2
C14A-C15A-C16A	119.97(17)	C17B-C16B-C15B	120.99(15)
C14A-C15A-H15A	120.0	C17B-C16B-H16B	119.5
C16A-C15A-H15A	120.0	C15B-C16B-H16B	119.5
C17A-C16A-C15A	120.90(16)	C16B-C17B-C12B	119.34(13)
C17A-C16A-H16A	119.6	C16B-C17B-P1B	120.91(11)
C15A-C16A-H16A	119.6	C12B-C17B-P1B	119.73(11)
C16A-C17A-C12A	119.14(14)	C19B-C18B-C23B	118.95(15)
C16A-C17A-P1A	121.61(12)	C19B-C18B-P1B	120.41(12)
C12A-C17A-P1A	119.19(12)	C23B-C18B-P1B	120.53(11)
C19A-C18A-C23A	119.53(15)	C18B-C19B-C20B	120.33(16)
C19A-C18A-P1A	120.14(12)	C18B-C19B-H19B	119.8
C23A-C18A-P1A	120.21(12)	C20B-C19B-H19B	119.8
C18A-C19A-C20A	120.20(16)	C21B-C20B-C19B	120.22(17)
C18A-C19A-H19A	119.9	C21B-C20B-H20B	119.9
C20A-C19A-H19A	119.9	C19B-C20B-H20B	119.9
C21A-C20A-C19A	119.85(17)	C20B-C21B-C22B	120.12(16)
C21A-C20A-H20A	120.1	C20B-C21B-H21B	119.9
C19A-C20A-H20A	120.1	C22B-C21B-H21B	119.9
C20A-C21A-C22A	120.39(16)	C23B-C22B-C21B	119.89(16)
C20A-C21A-H21A	119.8	C23B-C22B-H22B	120.1

C22A-C21A-H21A	119.8	C21B-C22B-H22B	120.1
C23A-C22A-C21A	120.15(16)	C22B-C23B-C18B	120.47(15)
C23A-C22A-H22A	119.9	C22B-C23B-H23B	119.8
C21A-C22A-H22A	119.9	C18B-C23B-H23B	119.8
C22A-C23A-C18A	119.87(16)	C25B-C24B-C29B	119.48(14)
C22A-C23A-H23A	120.1	C25B-C24B-P1B	117.60(11)
C18A-C23A-H23A	120.1	C29B-C24B-P1B	122.89(12)
C29A-C24A-C25A	119.19(15)	C26B-C25B-C24B	120.44(15)
C29A-C24A-P1A	122.82(13)	C26B-C25B-H25B	119.8
C25A-C24A-P1A	117.98(12)	C24B-C25B-H25B	119.8
C26A-C25A-C24A	120.62(16)	C27B-C26B-C25B	119.60(16)
C26A-C25A-H25A	119.7	C27B-C26B-H26B	120.2
C24A-C25A-H25A	119.7	C25B-C26B-H26B	120.2
C25A-C26A-C27A	119.70(17)	C28B-C27B-C26B	120.20(16)
C25A-C26A-H26A	120.1	C28B-C27B-H27B	119.9
C27A-C26A-H26A	120.1	C26B-C27B-H27B	119.9
C28A-C27A-C26A	120.12(16)	C27B-C28B-C29B	120.39(16)
C28A-C27A-H27A	119.9	C27B-C28B-H28B	119.8
C26A-C27A-H27A	119.9	C29B-C28B-H28B	119.8
C27A-C28A-C29A	120.39(17)	C28B-C29B-C24B	119.88(15)
C27A-C28A-H28A	119.8	C28B-C29B-H29B	120.1
C29A-C28A-H28A	119.8	C24B-C29B-H29B	120.1
C24A-C29A-C28A	119.92(16)	Cl2M-C1M-Cl1M	110.88(11)
C24A-C29A-H29A	120.0	Cl2M-C1M-H1M1	109.5
C28A-C29A-H29A	120.0	Cl1M-C1M-H1M1	109.5
C5B-Pd1B-P1B	87.84(6)	Cl2M-C1M-H1M2	109.5
C5B-Pd1B-N1B	175.81(6)	Cl1M-C1M-H1M2	109.5
P1B-Pd1B-N1B	95.97(5)	H1M1-C1M-H1M2	108.1

Table A.6. Torsion Angles for 1b

C6A-N1A-C1A-C2A	170.28(16)	C6B-N1B-C1B-C2B	-175.84(17)
Pd1A-N1A-C1A-C2A	42.6(2)	Pd1B-N1B-C1B-C2B	-49.7(2)
N1A-C1A-C2A-C4A	-3.0(3)	N1B-C1B-C2B-C4B	1.0(3)
N1A-C1A-C2A-C3A	176.35(16)	N1B-C1B-C2B-C3B	-179.69(16)
C1A-N1A-C6A-C7A	132.03(16)	C1B-N1B-C6B-C7B	-132.09(16)
Pd1A-N1A-C6A-C7A	-87.81(15)	Pd1B-N1B-C6B-C7B	89.57(14)
C1A-N1A-C6A-C11A	-51.3(2)	C1B-N1B-C6B-C11B	51.6(2)
Pd1A-N1A-C6A-C11A	88.85(15)	Pd1B-N1B-C6B-C11B	-86.79(14)
C11A-C6A-C7A-C8A	-0.5(3)	C11B-C6B-C7B-C8B	0.3(2)
N1A-C6A-C7A-C8A	176.21(16)	N1B-C6B-C7B-C8B	-176.06(15)
C6A-C7A-C8A-C9A	1.3(3)	C6B-C7B-C8B-C9B	-0.5(3)
C7A-C8A-C9A-C10A	-0.5(3)	C7B-C8B-C9B-C10B	0.1(3)
C8A-C9A-C10A-C11A	-1.1(3)	C8B-C9B-C10B-C11B	0.4(3)
C9A-C10A-C11A-C6A	1.8(3)	C9B-C10B-C11B-C6B	-0.5(2)
C9A-C10A-C11A-C12A	-178.06(17)	C9B-C10B-C11B-C12B	-179.24(15)
C7A-C6A-C11A-C10A	-1.1(2)	C7B-C6B-C11B-C10B	0.2(2)
N1A-C6A-C11A-C10A	-177.66(14)	N1B-C6B-C11B-C10B	176.47(14)
C7A-C6A-C11A-C12A	178.84(15)	C7B-C6B-C11B-C12B	178.81(14)
N1A-C6A-C11A-C12A	2.2(2)	N1B-C6B-C11B-C12B	-4.9(2)
C10A-C11A-C12A-C13A	-63.6(2)	C10B-C11B-C12B-C13B	65.5(2)
C6A-C11A-C12A-C13A	116.51(18)	C6B-C11B-C12B-C13B	-113.13(17)
C10A-C11A-C12A-C17A	115.16(18)	C10B-C11B-C12B-C17B	-114.40(17)
C6A-C11A-C12A-C17A	-64.7(2)	C6B-C11B-C12B-C17B	67.0(2)
C17A-C12A-C13A-C14A	3.7(2)	C17B-C12B-C13B-C14B	-2.5(2)
C11A-C12A-C13A-C14A	-177.47(16)	C11B-C12B-C13B-C14B	177.57(15)
C12A-C13A-C14A-C15A	-0.5(3)	C12B-C13B-C14B-C15B	0.6(3)
C13A-C14A-C15A-C16A	-2.5(3)	C13B-C14B-C15B-C16B	1.3(3)
C14A-C15A-C16A-C17A	2.1(3)	C14B-C15B-C16B-C17B	-1.2(2)
C15A-C16A-C17A-C12A	1.2(3)	C15B-C16B-C17B-C12B	-0.7(2)
C15A-C16A-C17A-P1A	-176.17(14)	C15B-C16B-C17B-P1B	177.76(12)
C13A-C12A-C17A-C16A	-4.0(2)	C13B-C12B-C17B-C16B	2.5(2)

C11A-C12A-C17A-C16A	177.24(15)	C11B-C12B-C17B-C16B	-177.58(14)
C13A-C12A-C17A-P1A	173.39(12)	C13B-C12B-C17B-P1B	-175.94(11)
C11A-C12A-C17A-P1A	-5.4(2)	C11B-C12B-C17B-P1B	4.0(2)
C18A-P1A-C17A-C16A	117.30(14)	C24B-P1B-C17B-C16B	-2.59(14)
C24A-P1A-C17A-C16A	6.56(15)	C18B-P1B-C17B-C16B	-113.37(13)
Pd1A-P1A-C17A-C16A	-120.73(13)	Pd1B-P1B-C17B-C16B	123.28(12)
C18A-P1A-C17A-C12A	-60.04(14)	C24B-P1B-C17B-C12B	175.85(12)
C24A-P1A-C17A-C12A	-170.78(12)	C18B-P1B-C17B-C12B	65.06(13)
Pd1A-P1A-C17A-C12A	61.92(13)	Pd1B-P1B-C17B-C12B	-58.28(13)
C24A-P1A-C18A-C19A	-115.41(13)	C24B-P1B-C18B-C19B	104.10(14)
C17A-P1A-C18A-C19A	135.33(13)	C17B-P1B-C18B-C19B	-147.82(14)
Pd1A-P1A-C18A-C19A	12.88(14)	Pd1B-P1B-C18B-C19B	-24.42(15)
C24A-P1A-C18A-C23A	68.54(14)	C24B-P1B-C18B-C23B	-79.83(14)
C17A-P1A-C18A-C23A	-40.72(14)	C17B-P1B-C18B-C23B	28.26(14)
Pd1A-P1A-C18A-C23A	-163.16(11)	Pd1B-P1B-C18B-C23B	151.66(11)
C23A-C18A-C19A-C20A	-0.2(2)	C23B-C18B-C19B-C20B	1.8(3)
P1A-C18A-C19A-C20A	-176.28(13)	P1B-C18B-C19B-C20B	177.97(15)
C18A-C19A-C20A-C21A	0.1(3)	C18B-C19B-C20B-C21B	-1.1(3)
C19A-C20A-C21A-C22A	-0.3(3)	C19B-C20B-C21B-C22B	-0.4(3)
C20A-C21A-C22A-C23A	0.6(3)	C20B-C21B-C22B-C23B	1.2(3)
C21A-C22A-C23A-C18A	-0.8(3)	C21B-C22B-C23B-C18B	-0.5(3)
C19A-C18A-C23A-C22A	0.6(2)	C19B-C18B-C23B-C22B	-1.0(2)
P1A-C18A-C23A-C22A	176.62(13)	P1B-C18B-C23B-C22B	-177.18(13)
C18A-P1A-C24A-C29A	-1.26(15)	C18B-P1B-C24B-C25B	-155.32(12)
C17A-P1A-C24A-C29A	105.65(14)	C17B-P1B-C24B-C25B	97.47(13)
Pd1A-P1A-C24A-C29A	-128.12(13)	Pd1B-P1B-C24B-C25B	-27.59(13)
C18A-P1A-C24A-C25A	177.13(13)	C18B-P1B-C24B-C29B	26.87(14)
C17A-P1A-C24A-C25A	-75.96(14)	C17B-P1B-C24B-C29B	-80.34(14)
Pd1A-P1A-C24A-C25A	50.27(14)	Pd1B-P1B-C24B-C29B	154.61(11)
C29A-C24A-C25A-C26A	-2.6(3)	C29B-C24B-C25B-C26B	0.1(2)
P1A-C24A-C25A-C26A	178.93(14)	P1B-C24B-C25B-C26B	-177.78(13)
C24A-C25A-C26A-C27A	1.8(3)	C24B-C25B-C26B-C27B	0.8(3)

C25A-C26A-C27A-C28A	0.7(3)	C25B-C26B-C27B-C28B	-0.7(3)
C26A-C27A-C28A-C29A	-2.3(3)	C26B-C27B-C28B-C29B	-0.2(3)
C25A-C24A-C29A-C28A	1.0(2)	C27B-C28B-C29B-C24B	1.1(2)
P1A-C24A-C29A-C28A	179.34(13)	C25B-C24B-C29B-C28B	-1.0(2)
C27A-C28A-C29A-C24A	1.5(3)	P1B-C24B-C29B-C28B	176.72(12)

Table A.7. Potential Hydrogen Bonds for 1b

Hydrogen Bond	D—H (Å)	H⋯A (Å)	D⋯A (Å)	D—H⋯A (°)
N1B-H1NB⋯Cl1M	1.00	2.61	3.5002(18)	148.2
C7B-H7B⋯Cl1B[1]	0.95	2.88	3.709(2)	145.8
C1M-H1M2⋯Cl1B	0.99	2.67	3.600(2)	157.0

1. 1-x, -y,1+ -z

8.2 Appendix B: Supplementary Information for Chapter 3
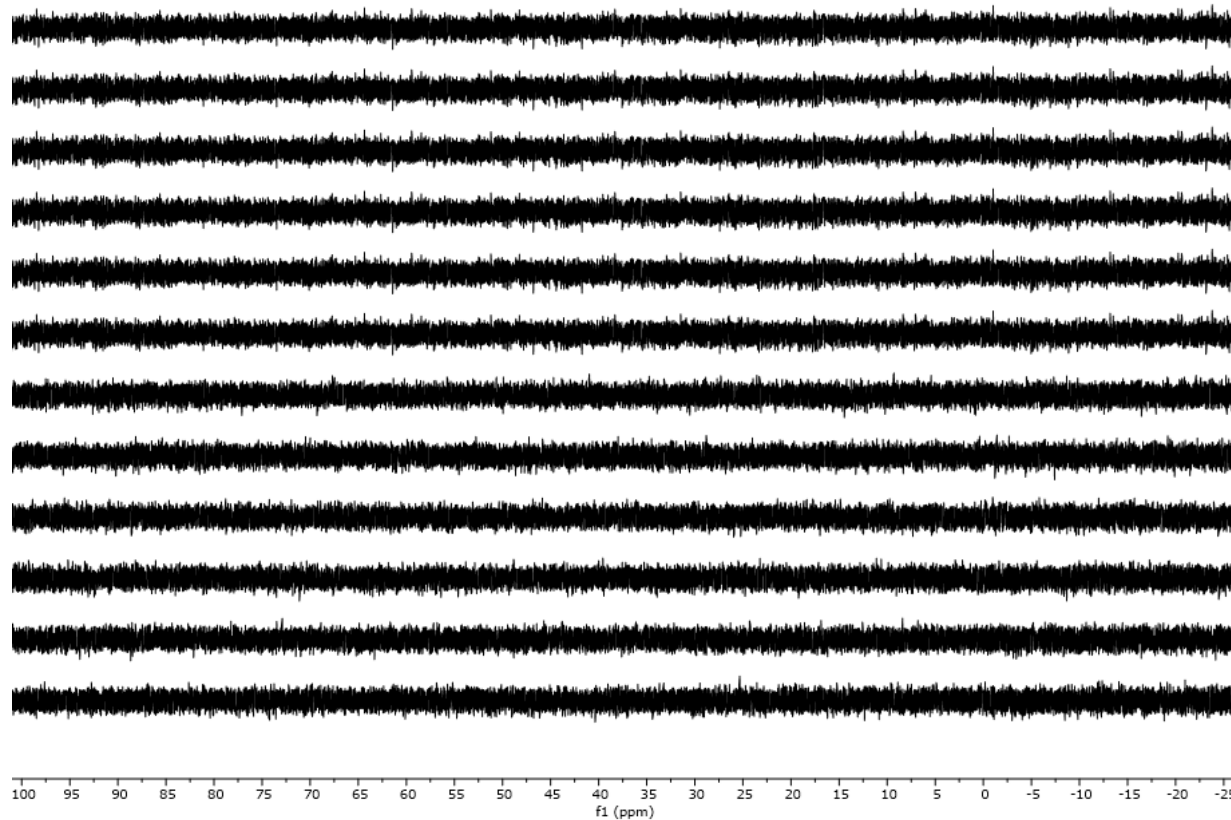
Figure B.1. $^{31}P\{^1H\}$ variable temperature NMR spectra (243 MHz, toluene-d_8) stack plot of the reaction of **2** with one equivalent of pyridine. From top to bottom: 25 °C, 20 °C, –50 °C, 10 °C, 0°C, –10 °C, –20 °C, –30 °C, –40 °C, –60 °C, –70 °C, –80 °C.
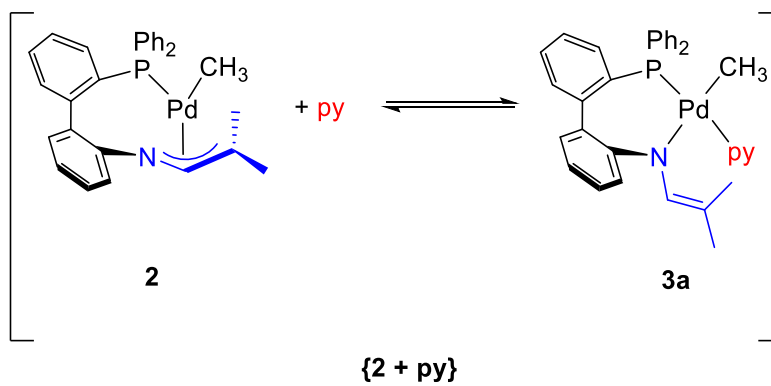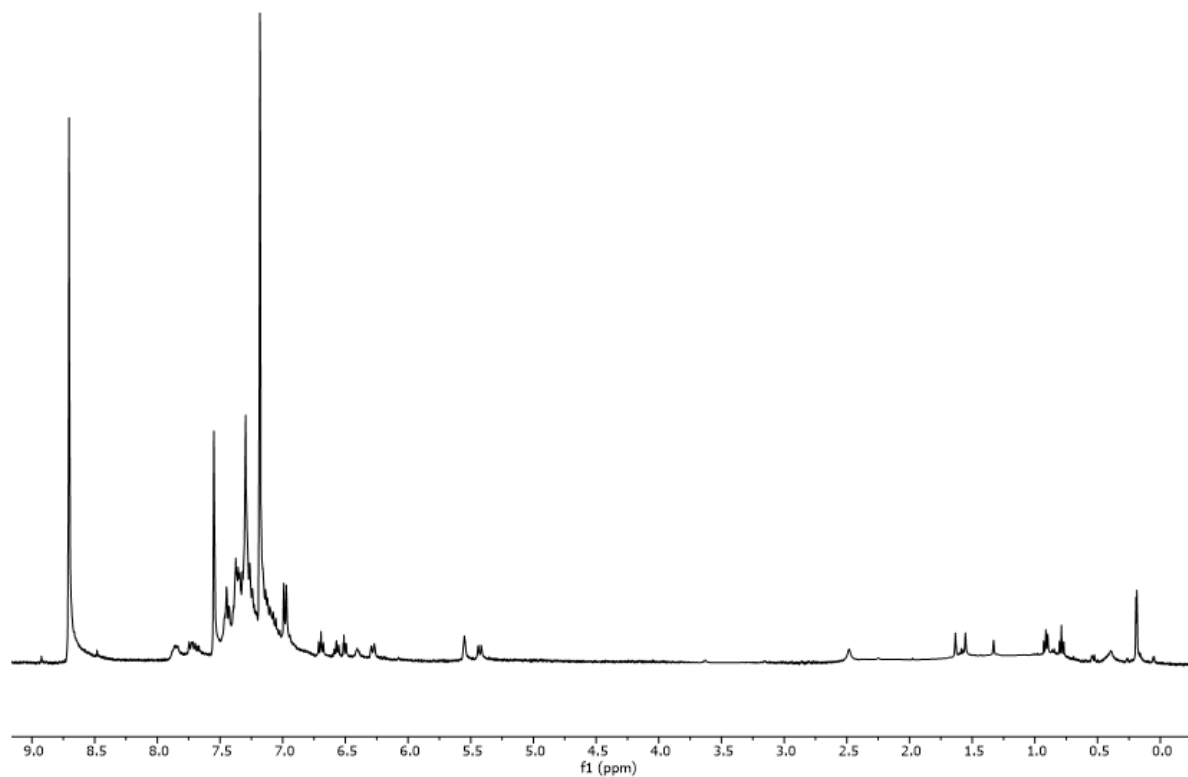
Figure B.2. ^{1}H NMR spectrum (py-d_5), 400 MHz) of [Pd(CH$_3$)([**L2**])], **2** dissolved in pyridine.

{2 + py}
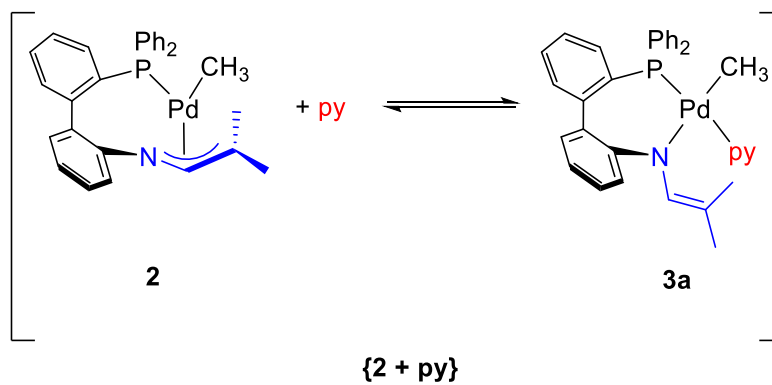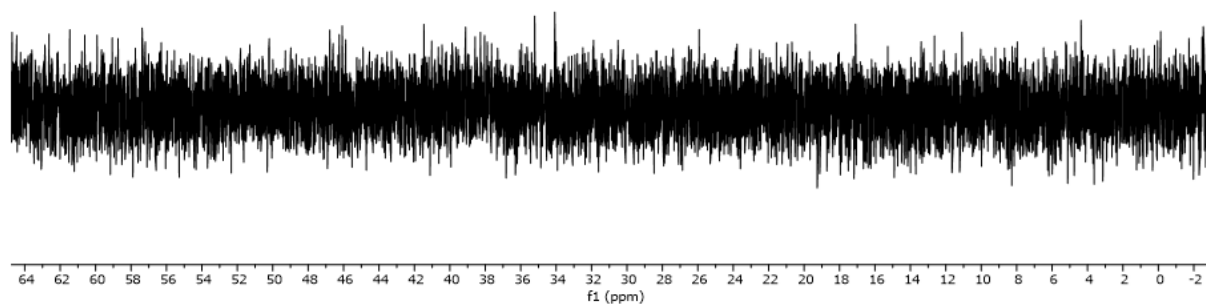
Figure B.3. $^{31}P\{^1H\}$ NMR spectrum (py-d_5, 162 MHz) of [Pd(CH$_3$([**L2**])], **2** dissolved in pyridine.
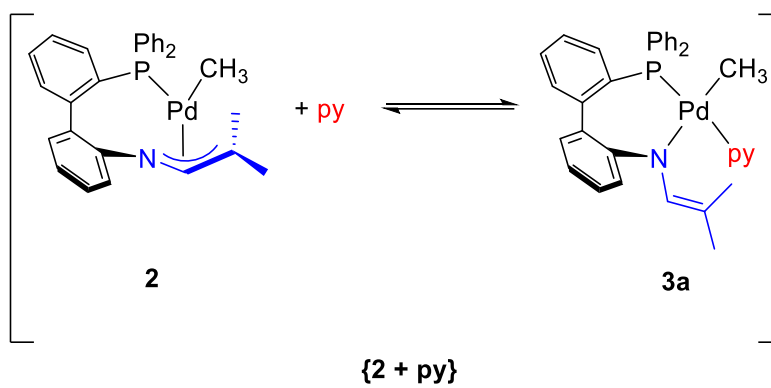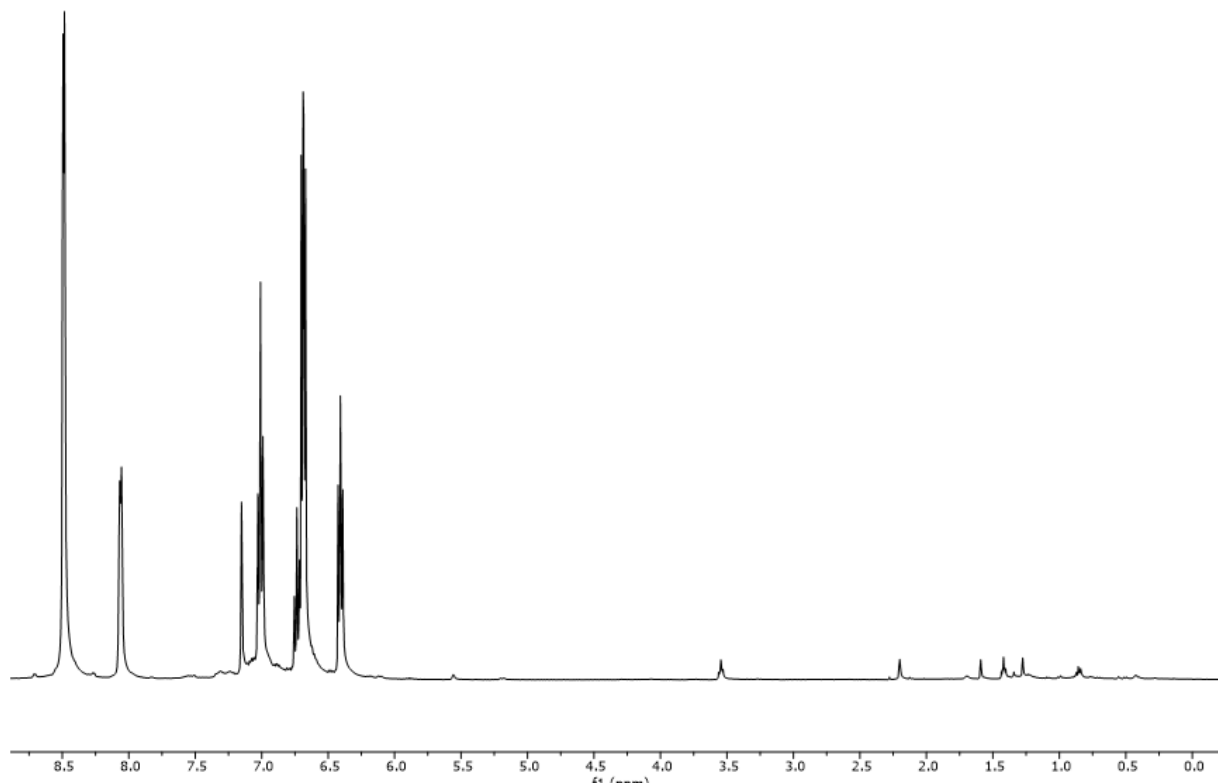
Figure B.4. ^{1}H NMR spectrum (C$_6$D$_6$, 400 MHz) of a 1:1:1 mixture of **2**, pyridine, and B(C$_6$F$_5$)$_3$.
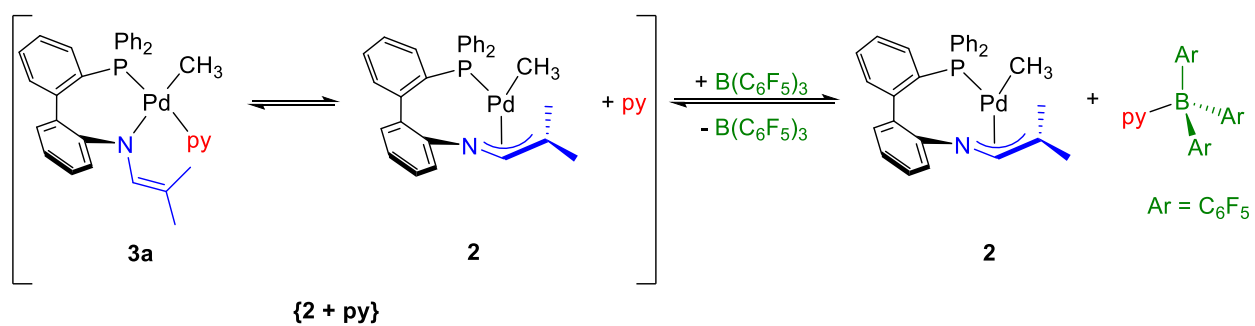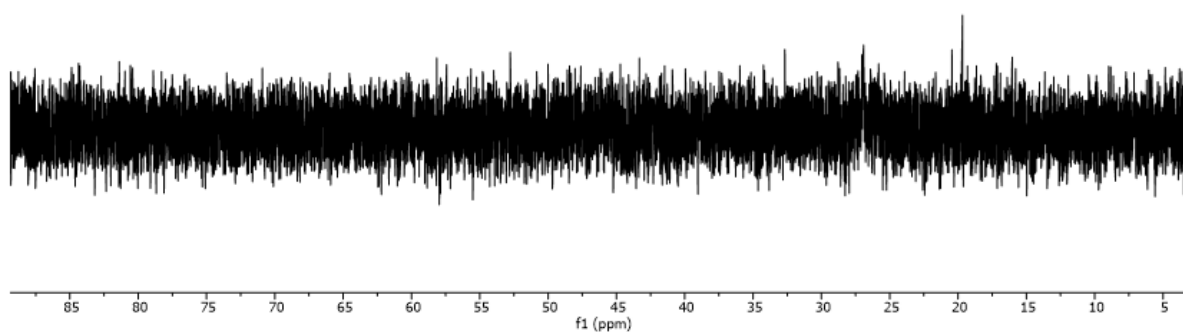
Figure B.5. $^{31}P\{^{1}H\}$ NMR spectrum (C_6D_6, 162 MHz) of a 1:1:1 mixture of **2**, pyridine, and $B(C_6F_5)_3$.
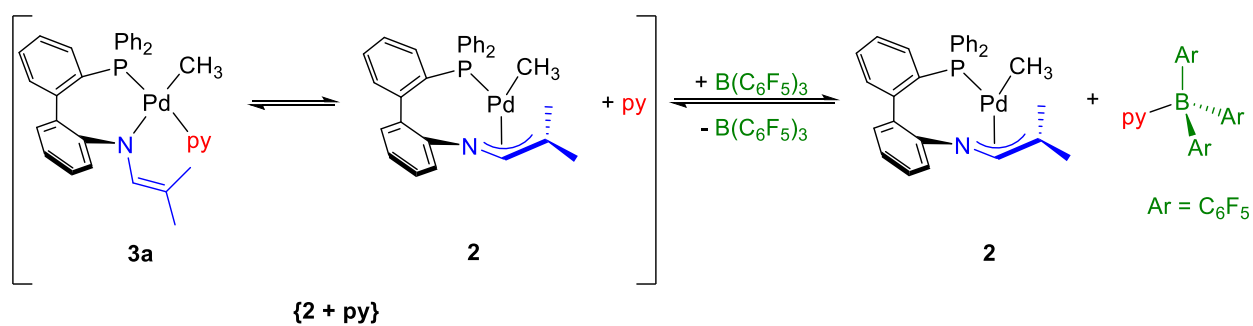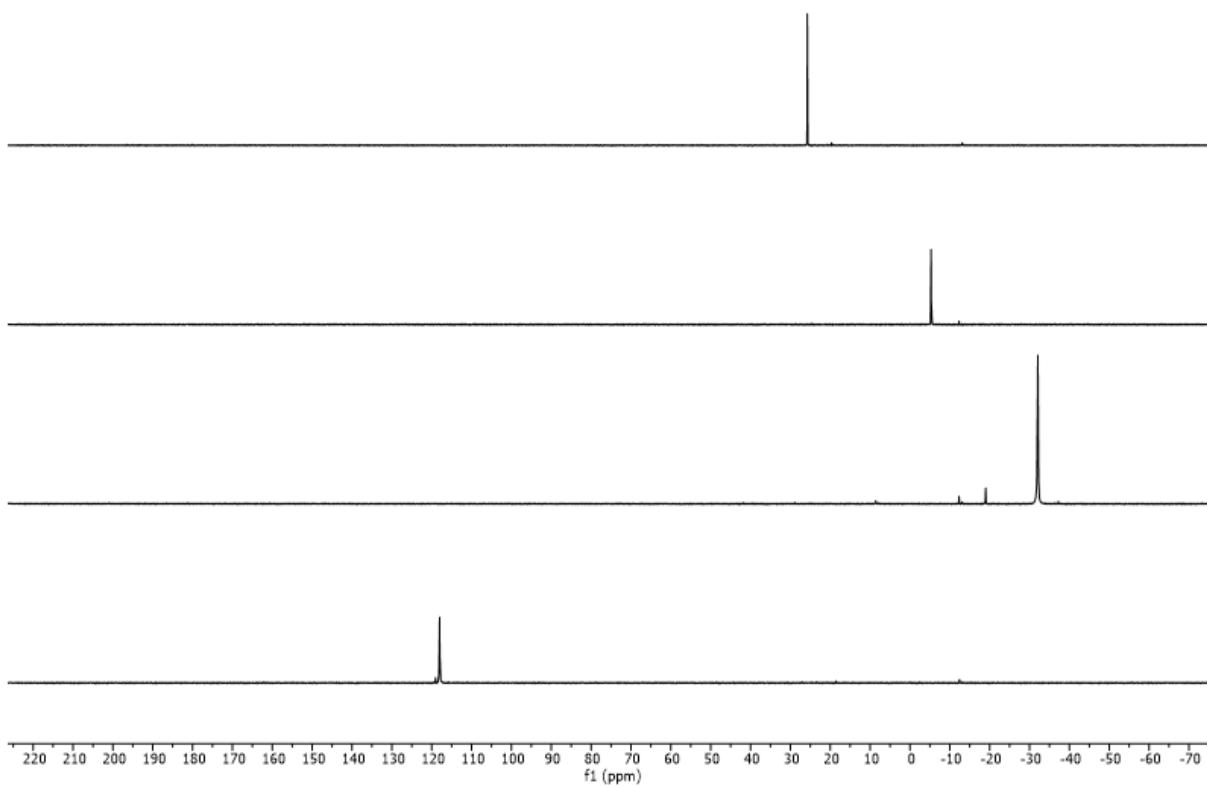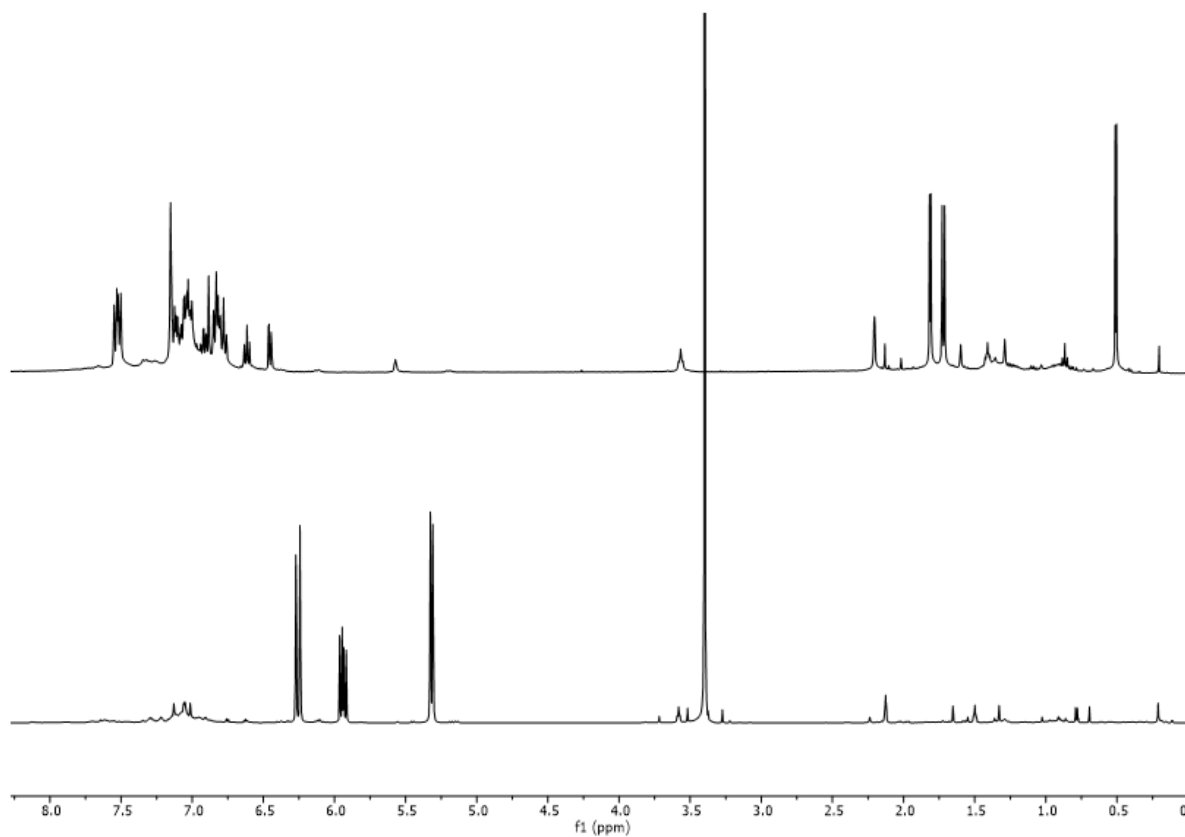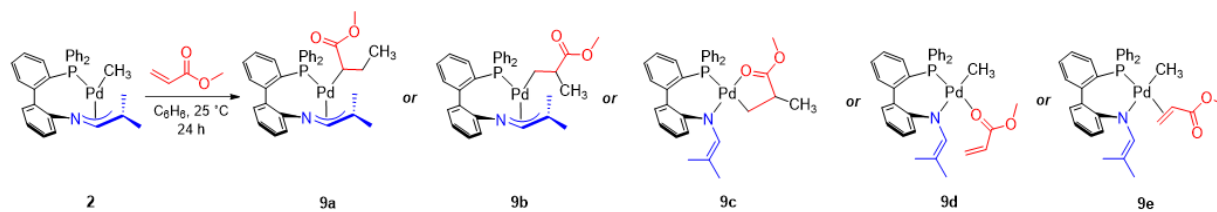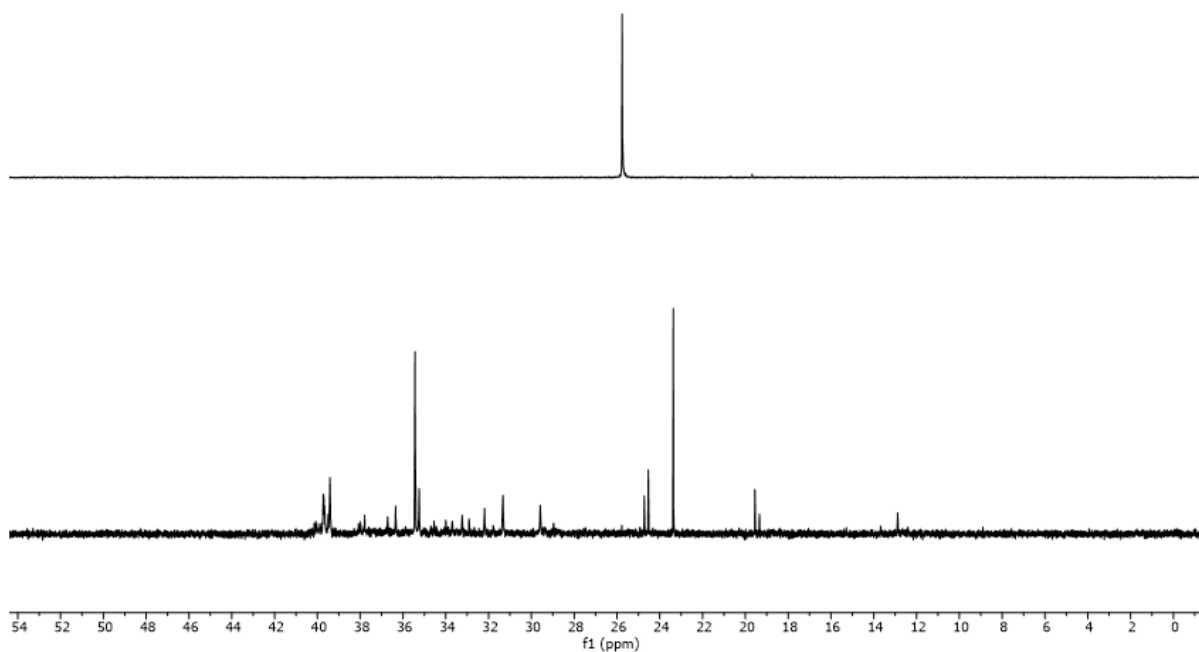
Figure B.6. $^{31}P\{^1H\}$ NMR spectra (C$_6$H$_6$, 162 MHz) stack plot of the reaction of **2** and one equivalent od PR$_3$. From top to bottom: **2**, **2** and PPh$_3$, where the peak at $\delta_P = -5.3$ is free PPh$_3$, **2** and P(^{t}Bu)$_3$, where the peak at $\delta_P = -32.1$ is free P(^{t}Bu)$_3$, **2** and P(NEt$_2$)$_3$, where the peak at $\delta_P = 118.0$ is free P(NEt$_2$)$_3$.

2   + PR$_3$ ⇌   **3b-d**

{2 + PR$_3$}
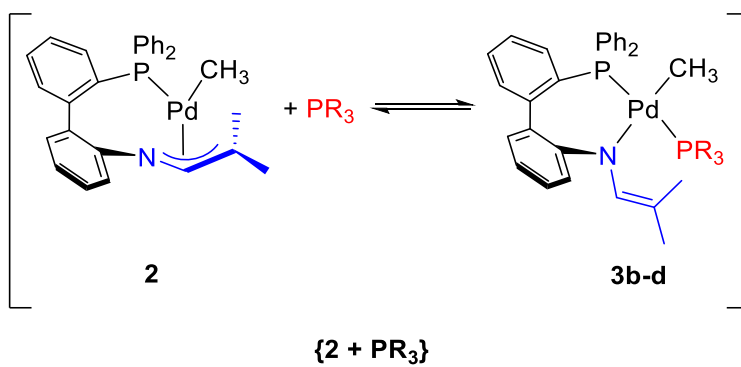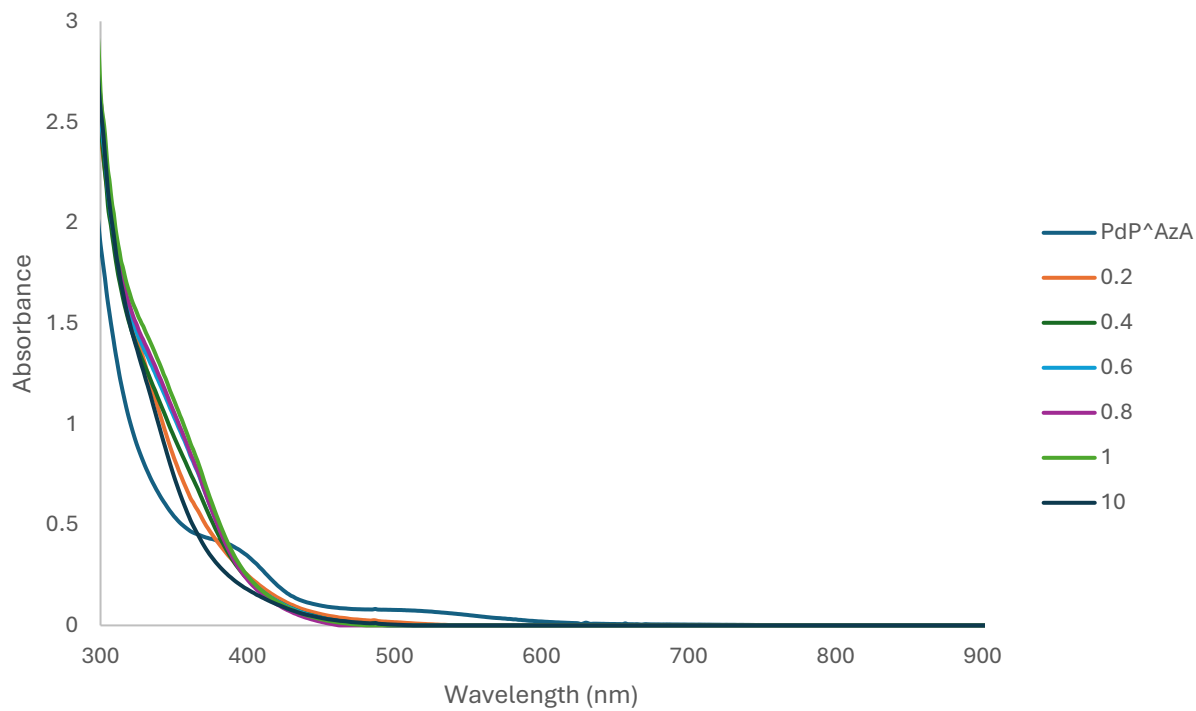
Figure B.7. UV-Vis spectra of P(^{t}Bu)$_3$ titration at 25 °C in toluene. Concentrations of P(^{t}Bu)$_3$ include: 0.2 mM, 0.4 mM, 0.6 mM. 0.8 mM, 1.0 mM, and 10 mM.
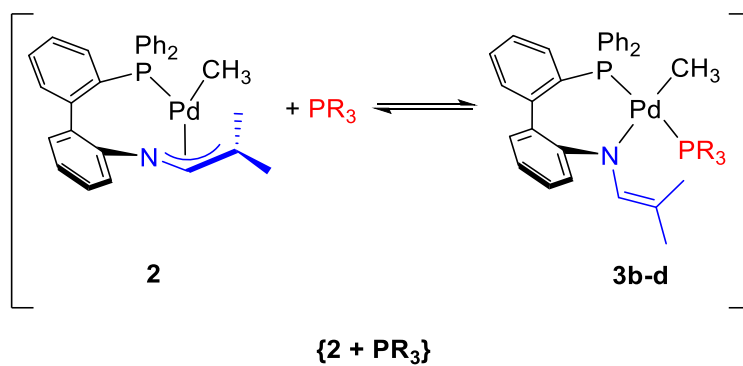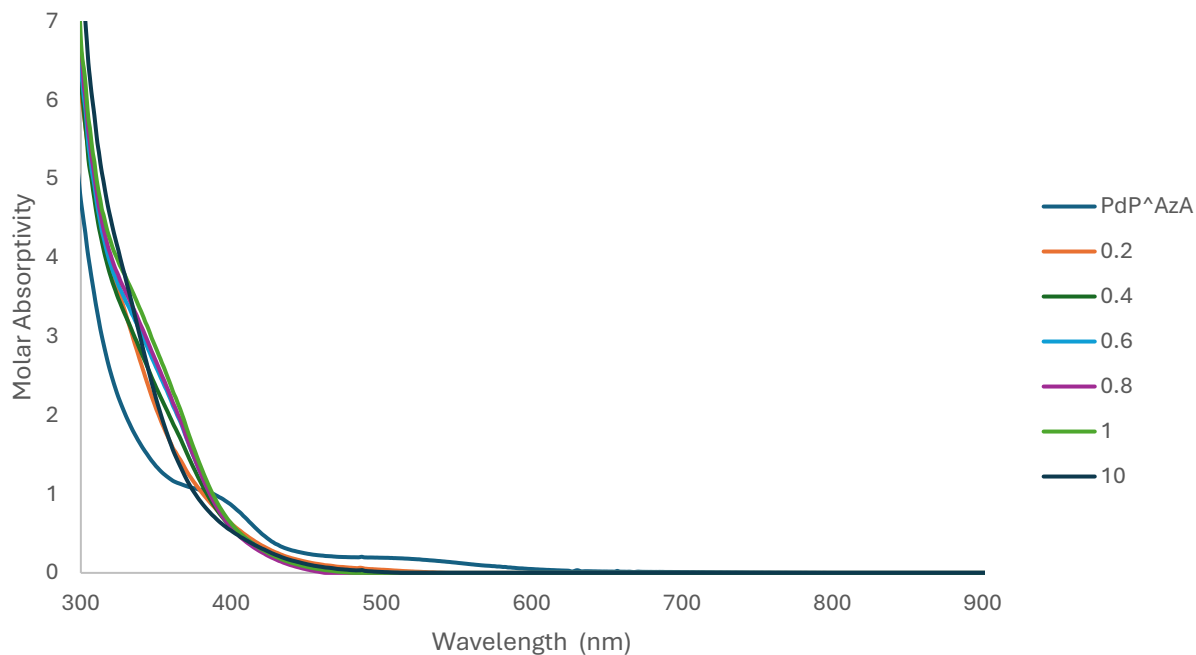
Figure B.8. Plot of molar absorptivity vs wavelength of P(^{t}Bu)$_3$ titration at 25 °C in toluene. Concentrations of P(^{t}Bu)$_3$ include 0.2 mM, 0.4 mM, 0.6 mM. 0.8 mM, 1.0 mM, and 10 mM.
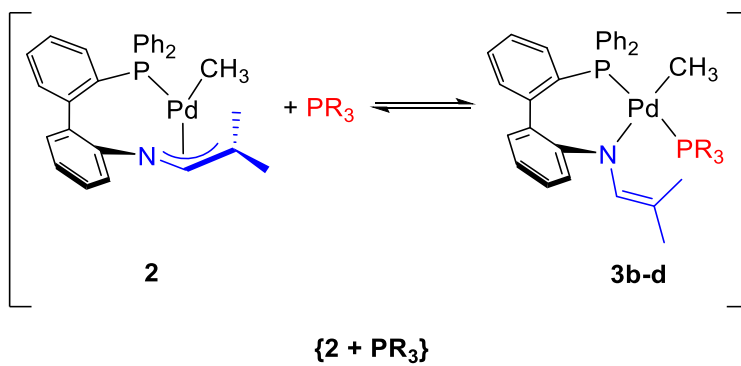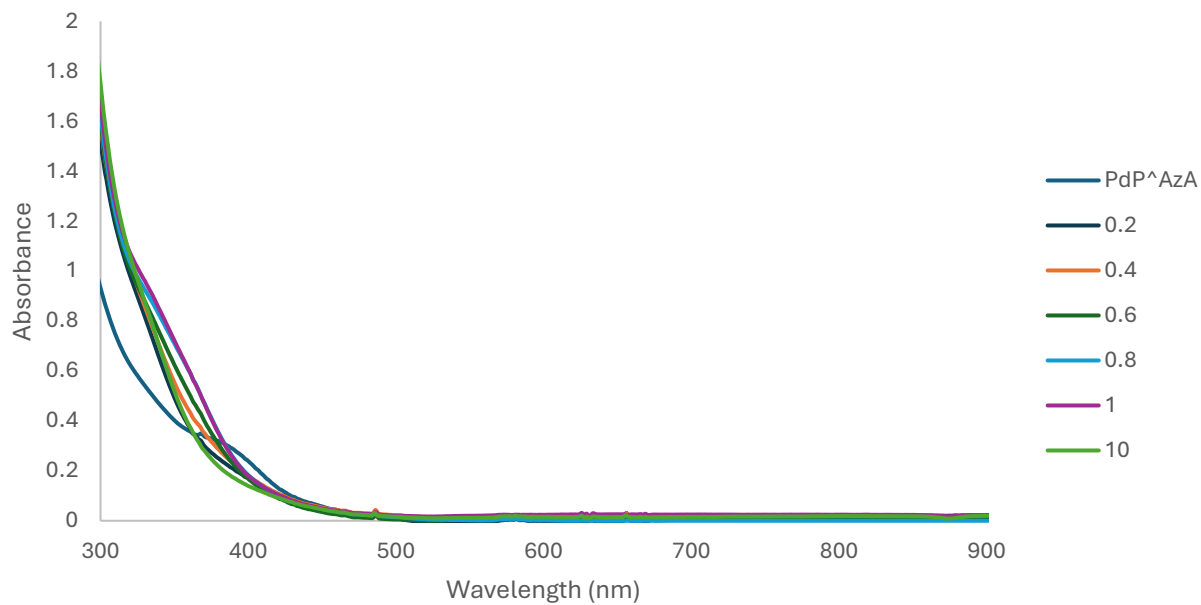
Figure B.9. UV-Vis spectra of P(^{t}Bu)$_3$ titration at –80 °C in toluene. Concentrations of P(^{t}Bu)$_3$ include 0.2 mM, 0.4 mM, 0.6 mM. 0.8 mM, 1.0 mM, and 10 mM.

2   + PR$_3$ ⇌   **3b-d**

{2 + PR$_3$}
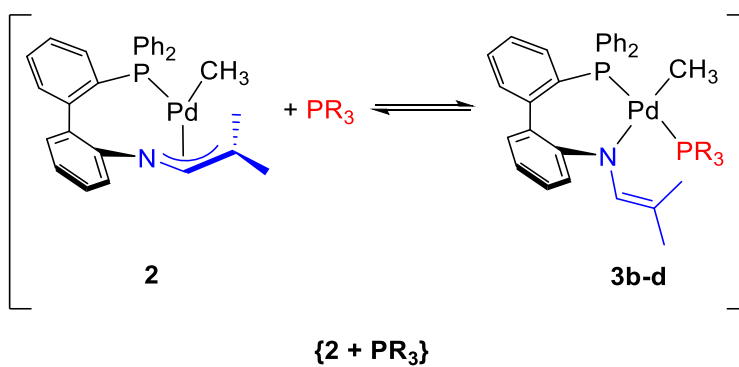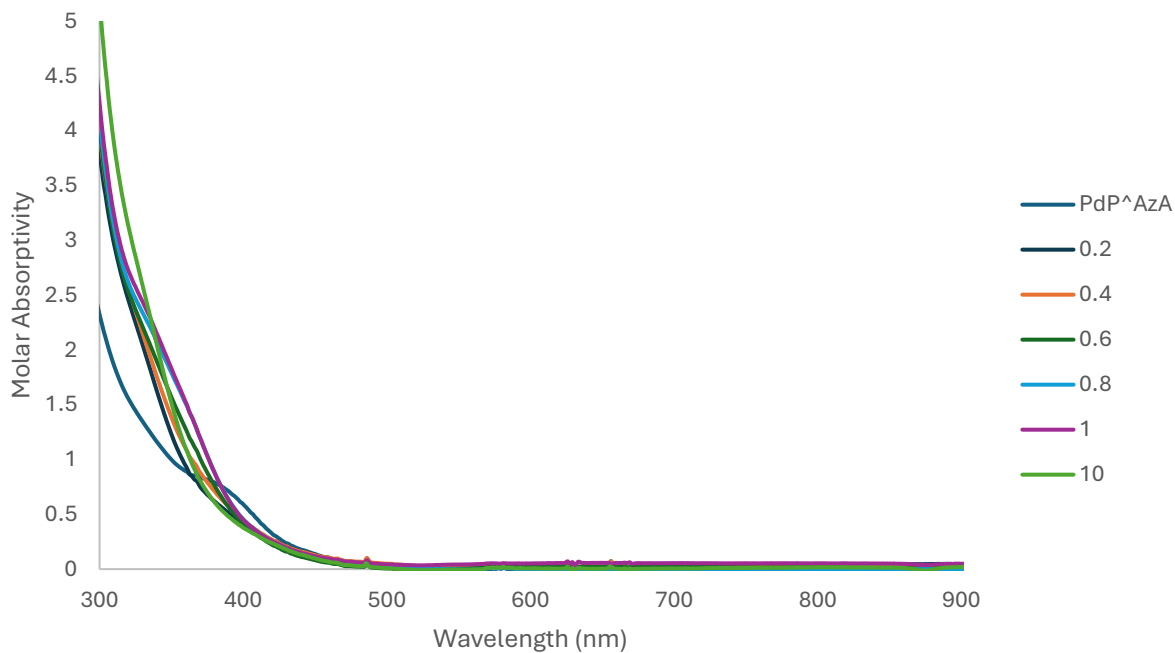
Figure B.10. Plot of molar absorptivity vs wavelength of P(^{t}Bu)$_3$ titration at –80 °C in toluene. Concentrations of P(^{t}Bu)$_3$ include 0.2 mM, 0.4 mM, 0.6 mM. 0.8 mM, 1.0 mM, and 10 mM.
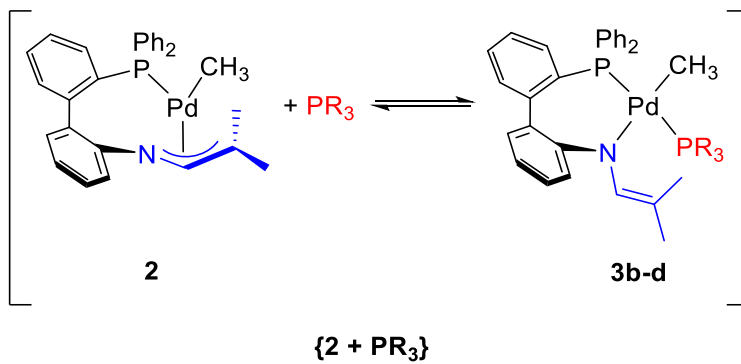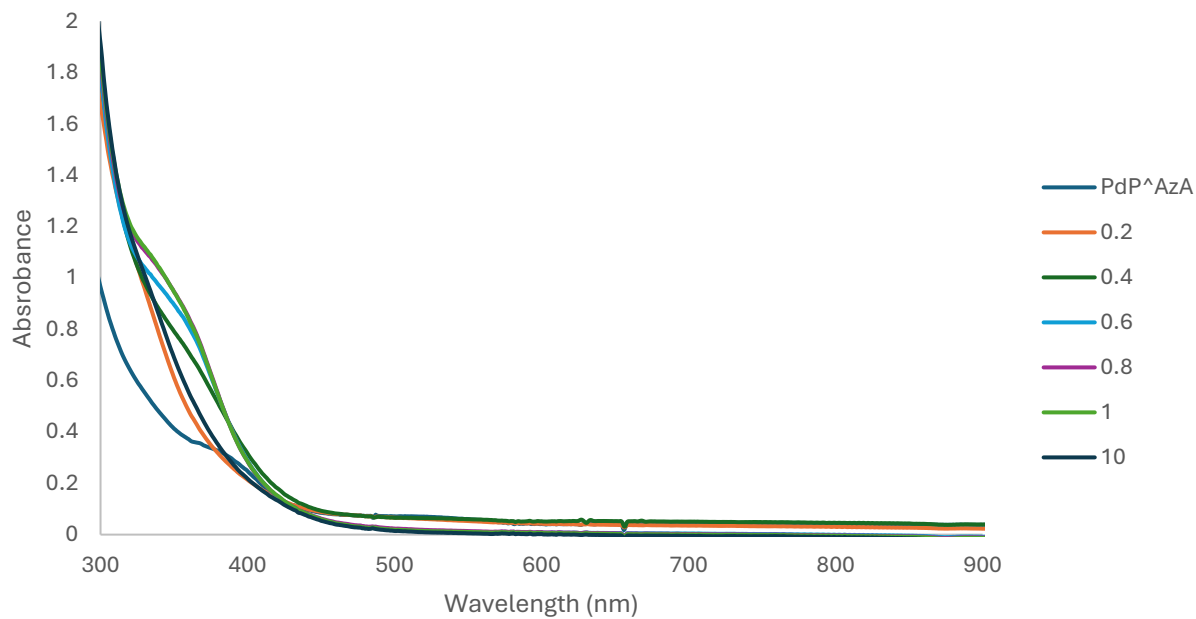
Figure B.11. UV-Vis spectra of P(^{t}Bu)$_3$ titration at 60 °C in toluene. Concentrations of P(^{t}Bu)$_3$ include 0.2 mM, 0.4 mM, 0.6 mM. 0.8 mM, 1.0 mM, and 10 mM.

{2 + PR$_3$}
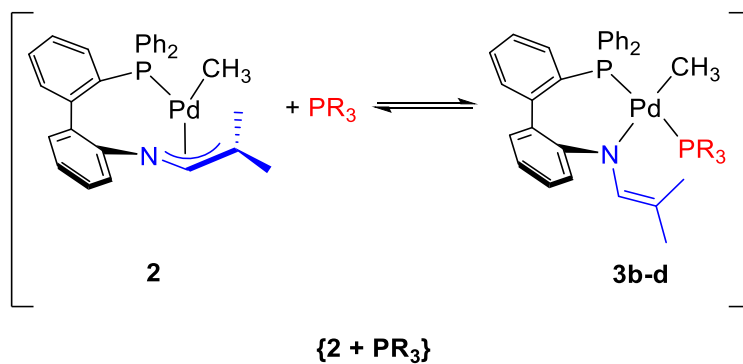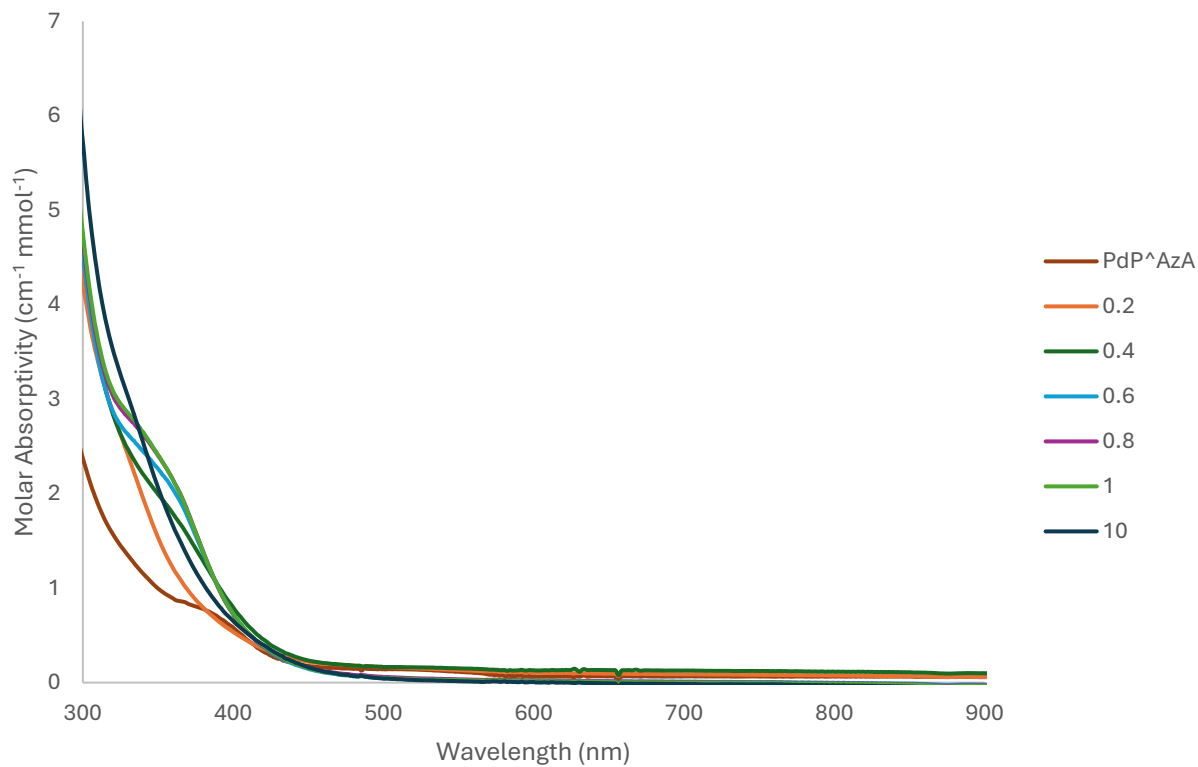
Figure B.12. Plot of molar absorptivity vs wavelength of P(^{t}Bu)$_3$ titration at 60 °C in toluene. Concentrations of P(^{t}Bu)$_3$ include 0.2 mM, 0.4 mM, 0.6 mM. 0.8 mM, 1.0 mM, and 10 mM.
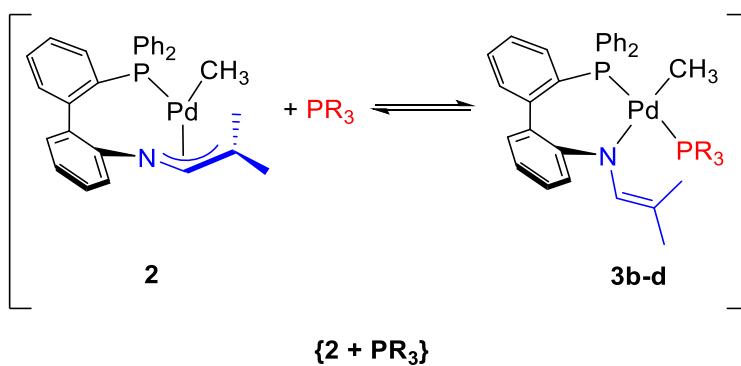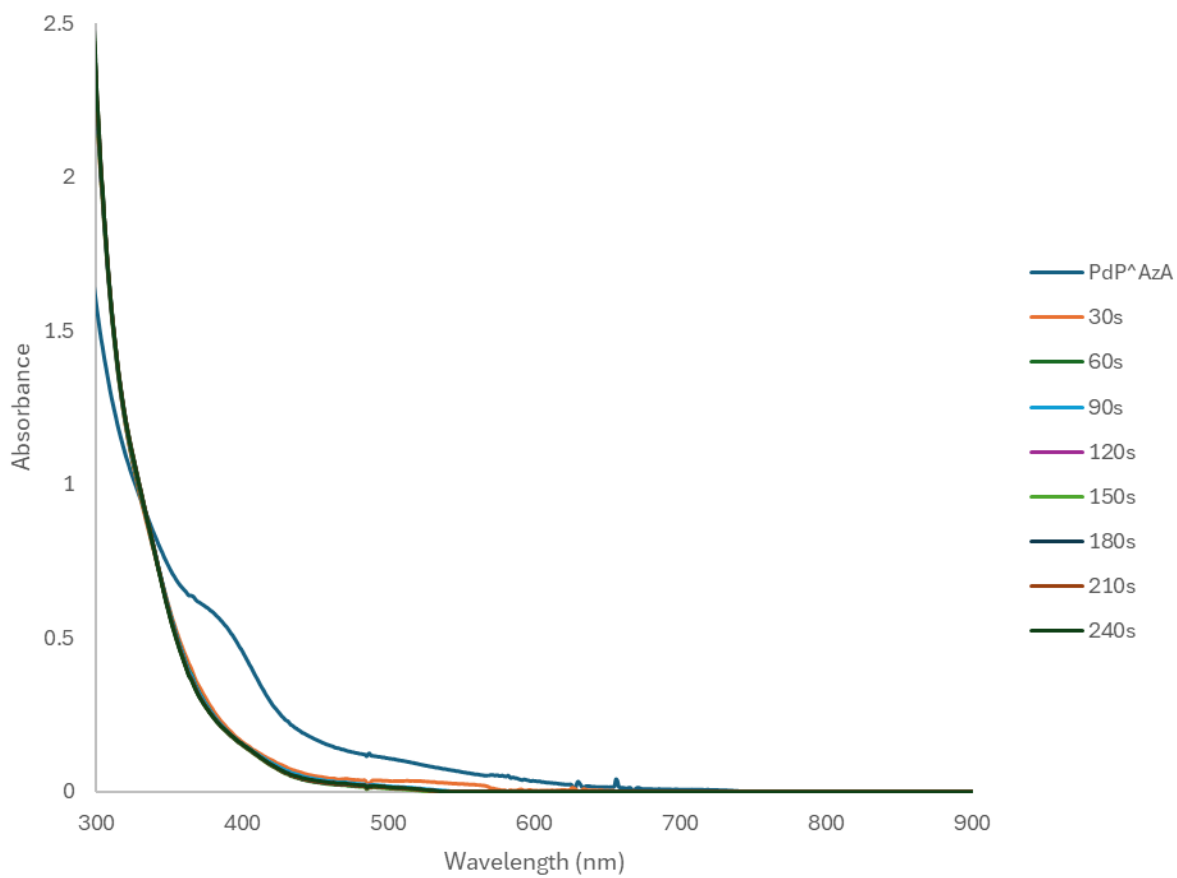
Figure B.13. UV-Vis spectra of P(^{t}Bu)$_3$ reaction time analysis at –80 °C in toluene.

{2 + PR$_3$}
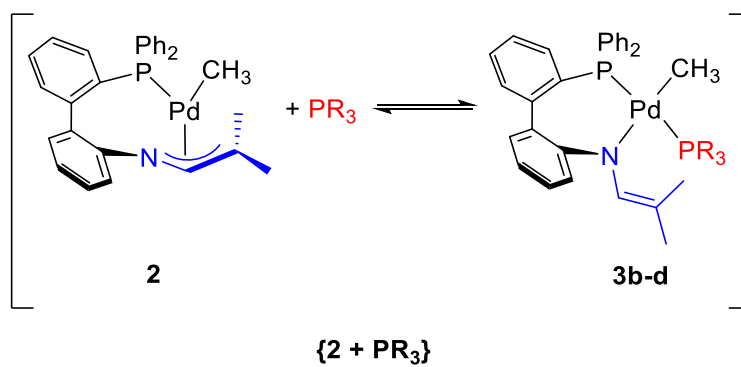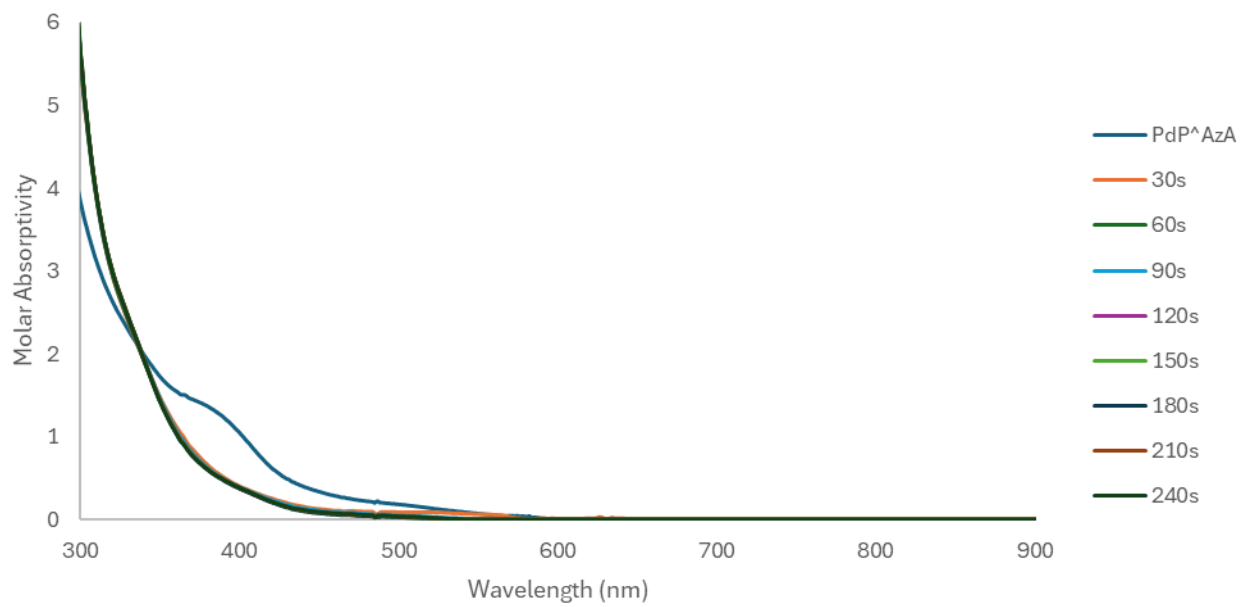
Figure B.14. Plot of molar absorptivity vs wavelength of P(^{t}Bu)$_3$ reaction time analysis at –80 °C in toluene.
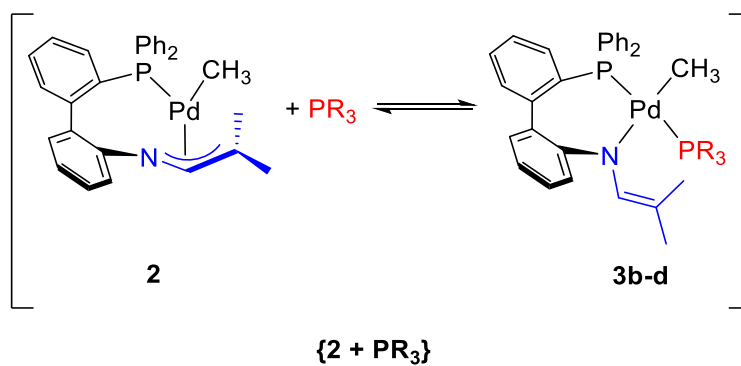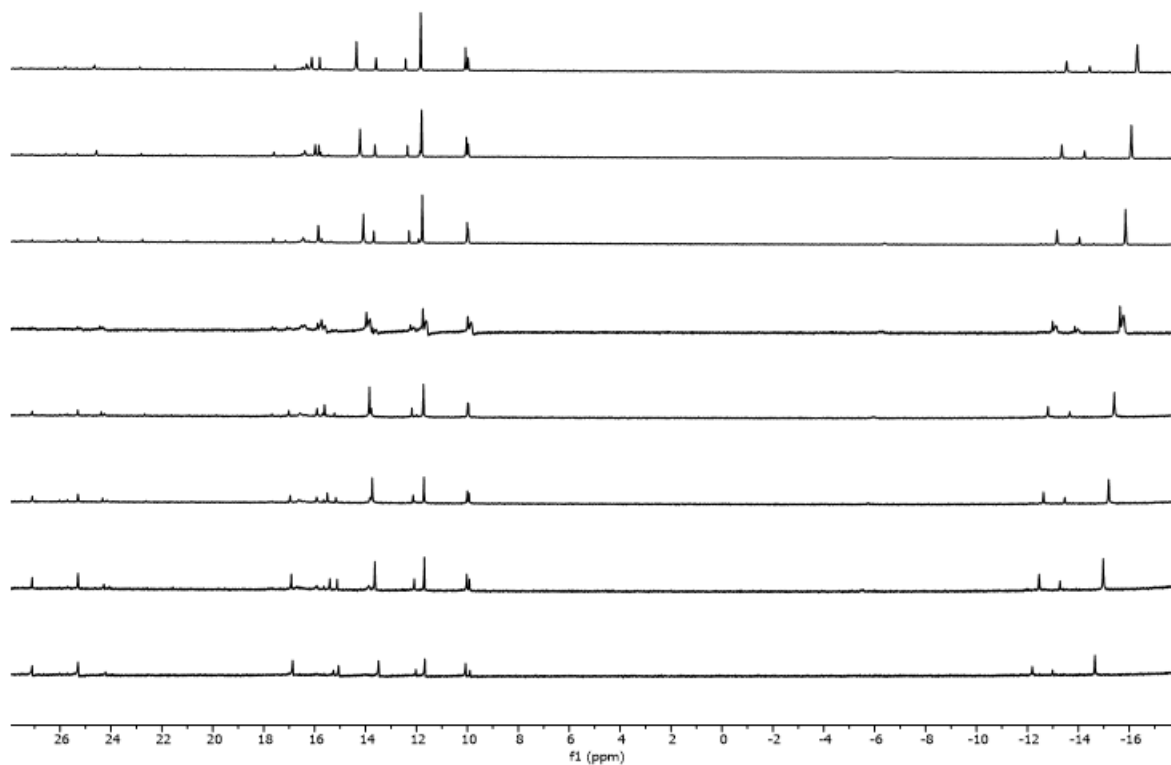
Figure B.15. $^{31}P\{^1H\}$ variable temperature NMR spectra (toluene-d_8, 243MHz) stack plot of the reaction of **2** with one equivalent of PEt₃. From top to bottom: 25 °C, 10 °C, 0 °C, –10 °C, –20 °C, –30 °C, –40 °C, and –50 °C. The free PEt₃ signal at $\delta_P = -19.7$ was cut out.

2   + PEt₃ ⇌   3e

{2 + PEt₃}
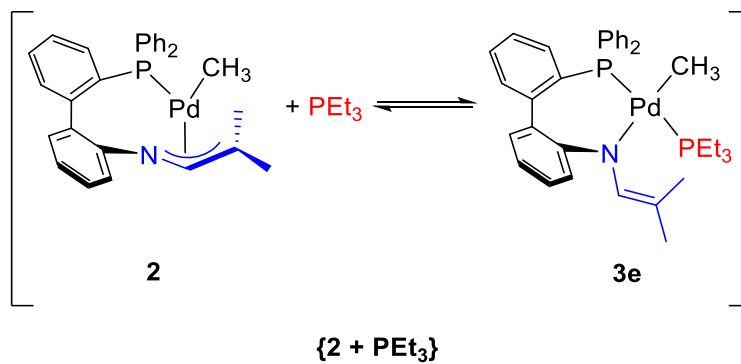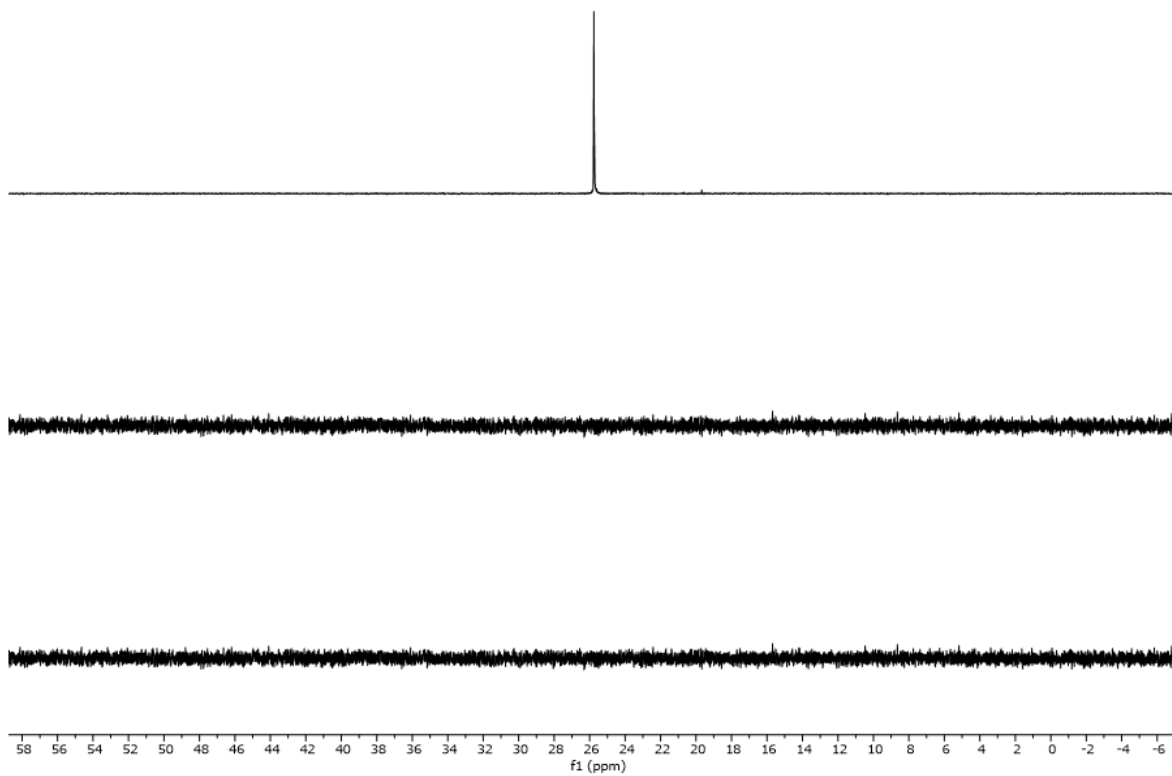
Figure B.16. ^{31}P$\{^{1}$H$\}$ NMR spectra (DMF, 400 MHz) stack plot of the reaction of **2**, one equivalent of CN$^-$, and excess MAH. From top to bottom: **2**, **2** and CN$^-$; **2**, CN$^-$, and MAH.
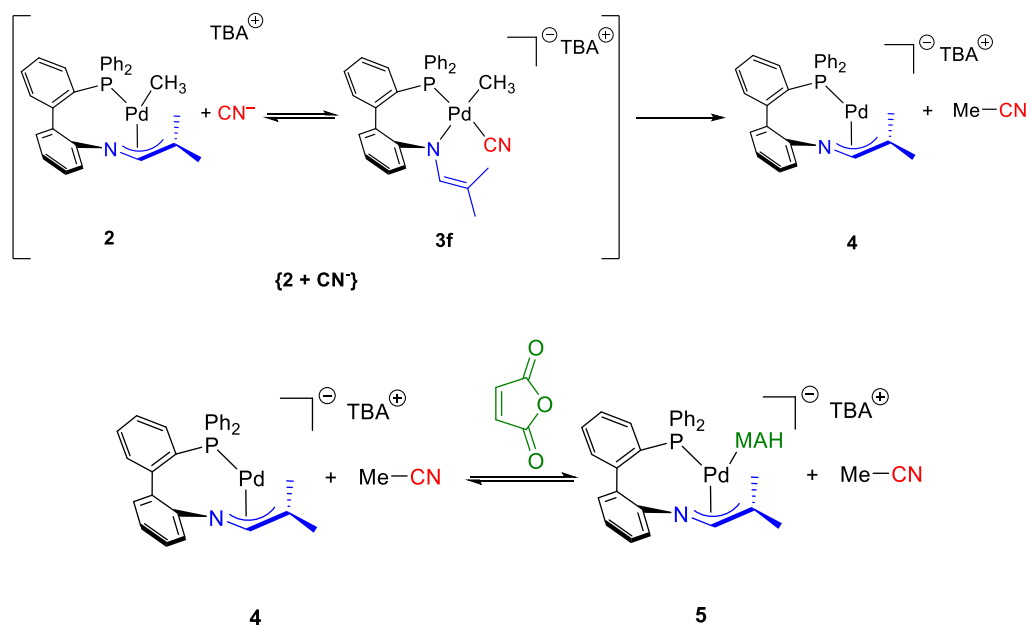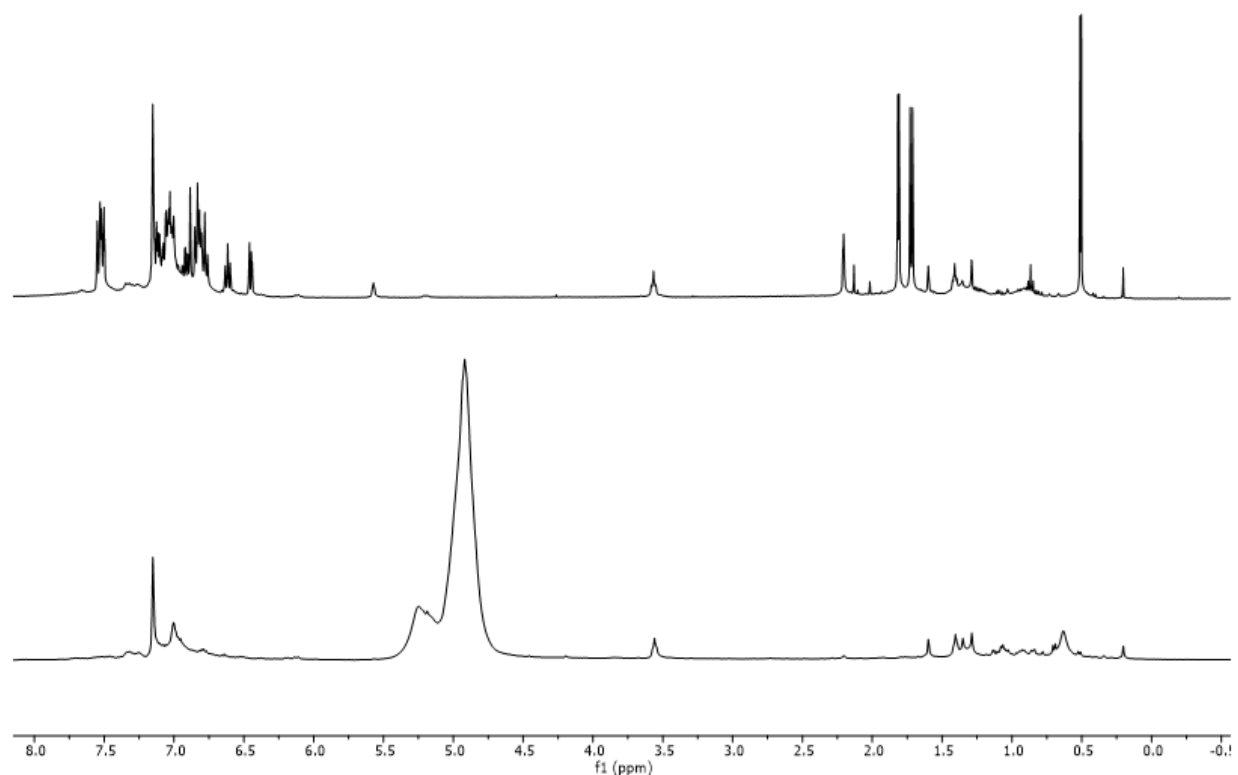
Figure B.17. ^{1}H NMR spectra (C_6D_6, 400 MHz) stack plot of the reaction of **2** and one drop of degassed water. From top to bottom: **2**, **2** and water.
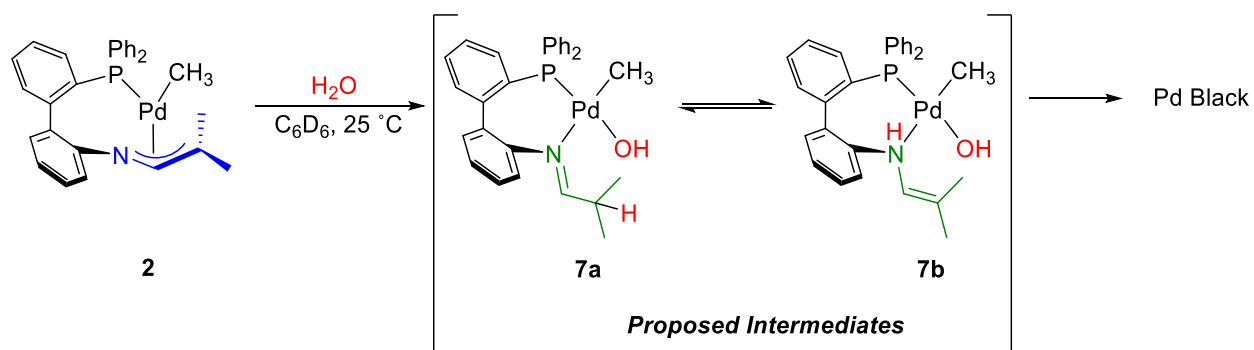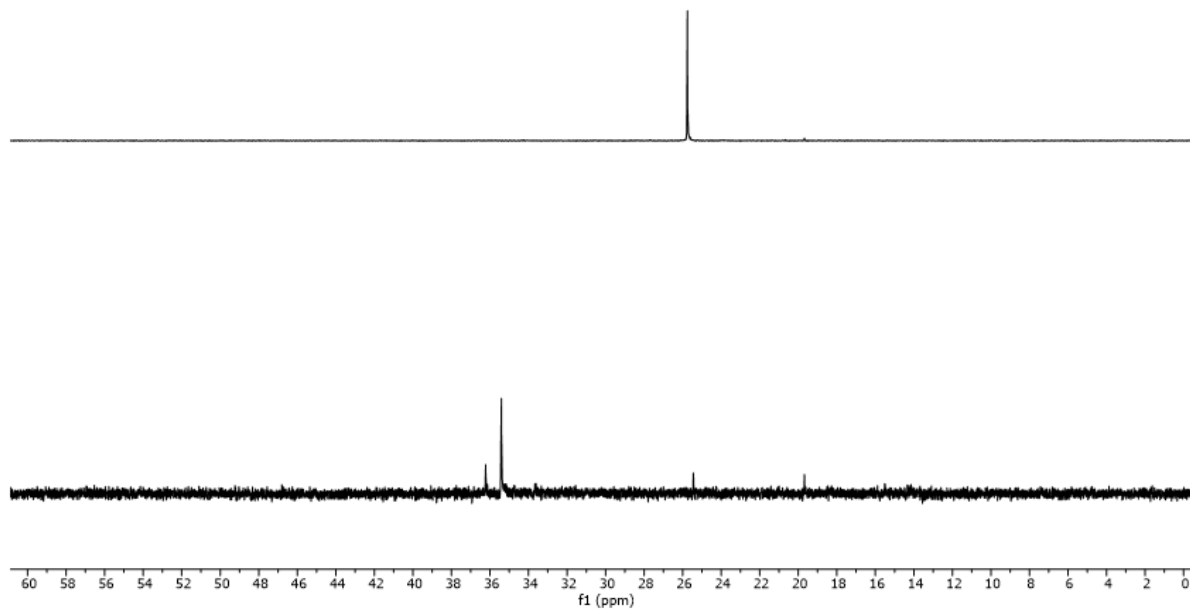
Figure B.18. $^{31}P\{^1H\}$ NMR spectra (C_6D_6, 162MHz) stack plot of the reaction of **2** and one drop of degassed water. From top to bottom: **2**, **2** and water.
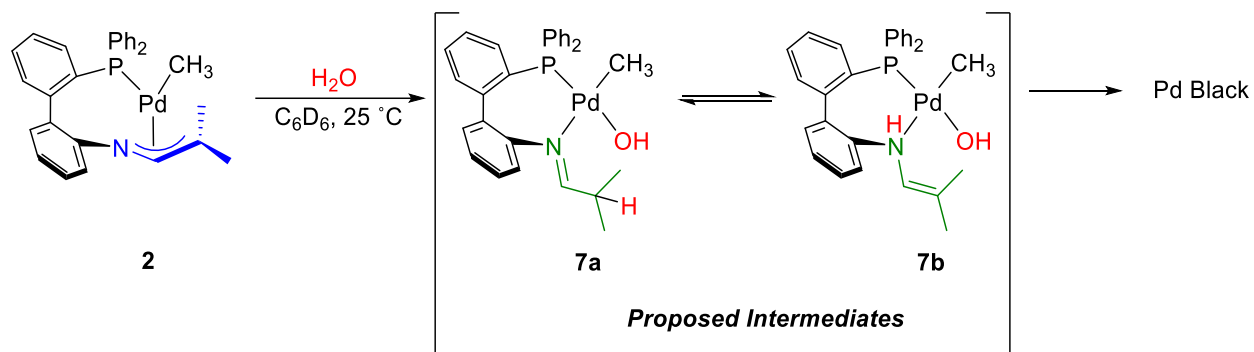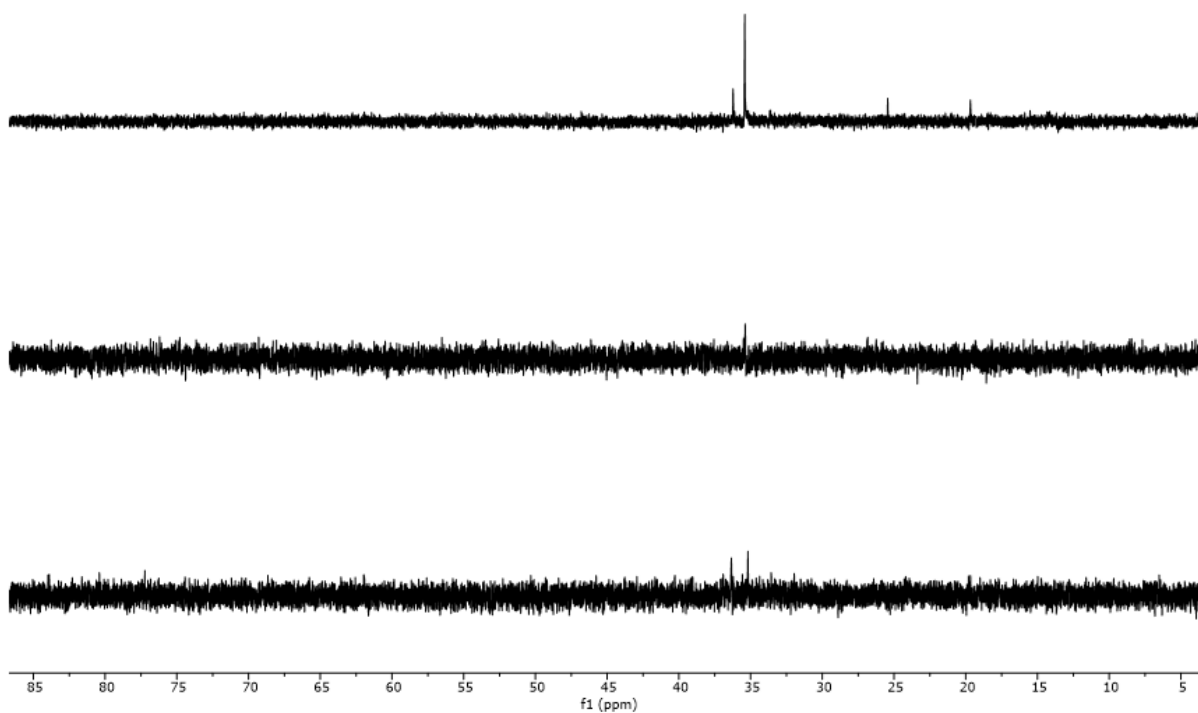
Figure B.19. $^{31}P\{^{1}H\}$ NMR spectra (162 MHz) stack plot of the reaction of **2** and one drop of degassed water in different solvents. From top to bottom: C_6D_6, DMSO, THF.
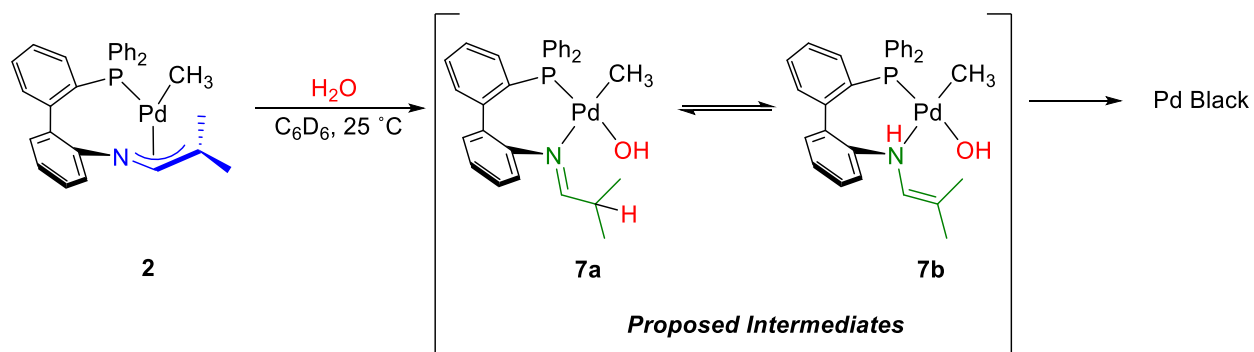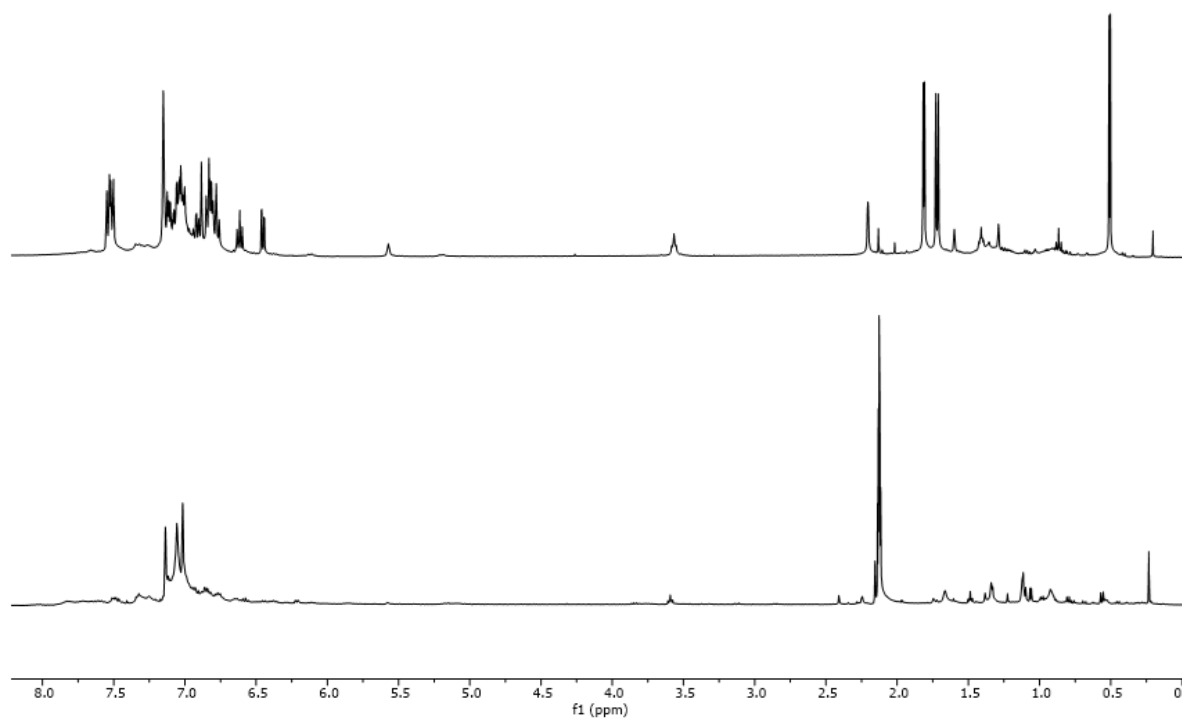
Figure B.20. ^{1}H NMR spectra (toluene-d_8, 400 MHz) stack plot of the reaction of **2** and CO. From top to bottom: **2**, **2** and CO.
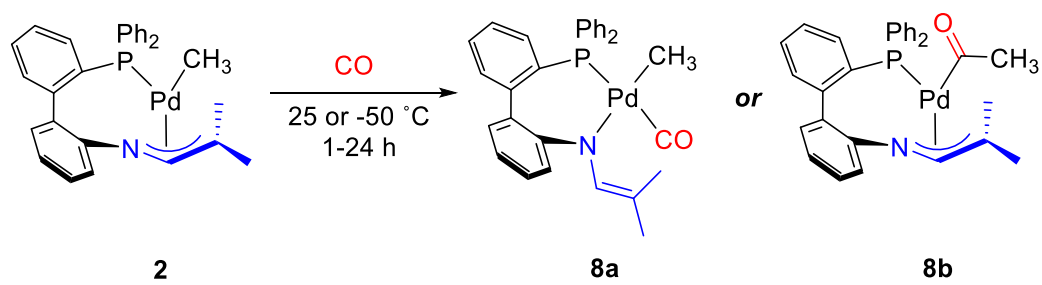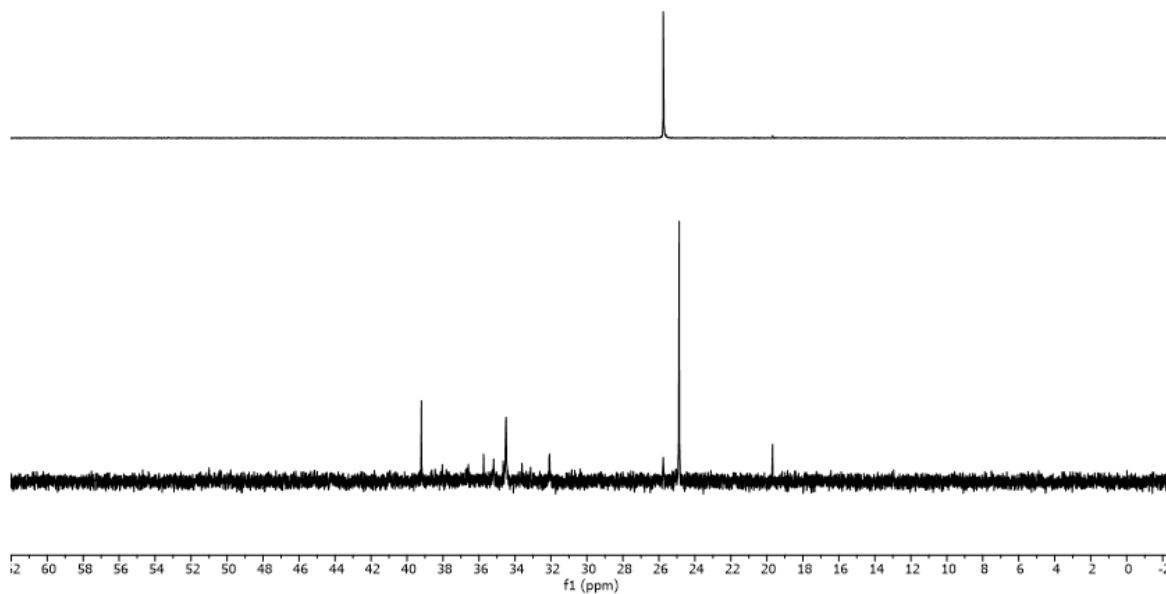
Figure B.21. $^{31}P\{^1H\}$ NMR spectra (toluene-d_8, 162 MHz) stack plot of the reaction of **2** and CO. From top to bottom: **2**, **2** and CO.
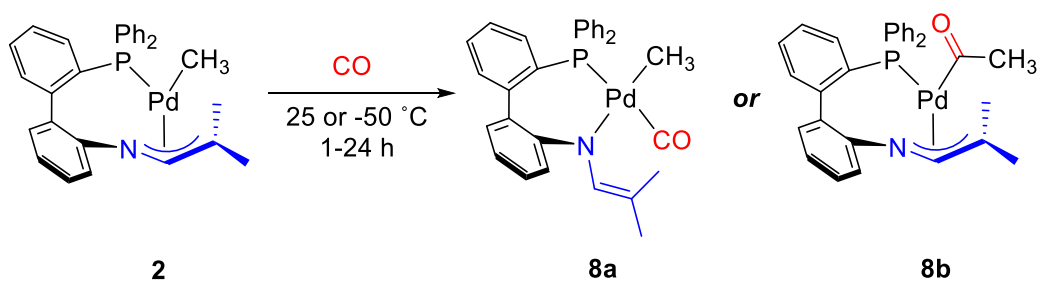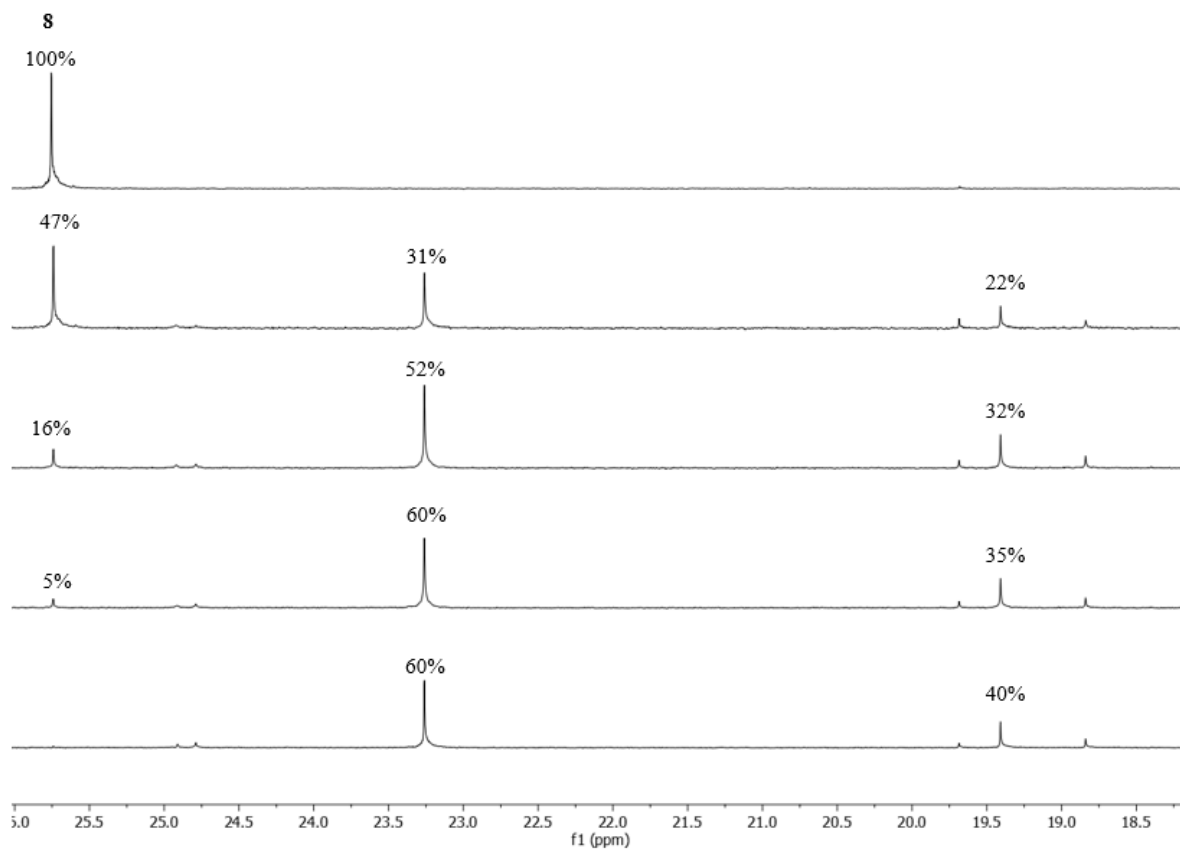
Figure B.22. $^{31}P\{^{1}H\}$ NMR spectra (C$_6$H$_6$, 162 MHz) stack plot of the reaction of **2** and one equivalent of

MA. From top to bottom: **2**, **2** and MA 10 min, **2** and MA 2 h, **2** and MA 4 h, **2** and MA 24 h.
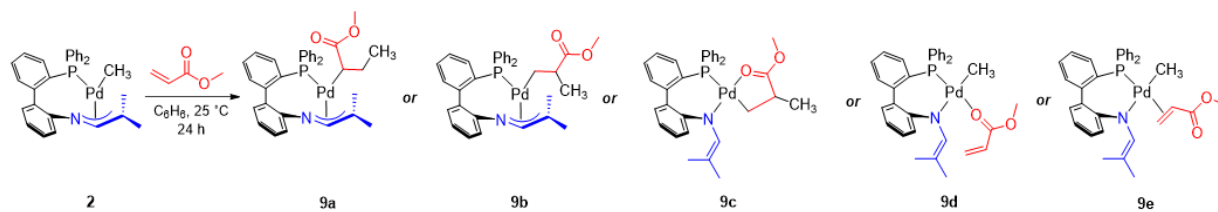
Figure B.23. ^{1}H NMR spectra (toluene-d_8, 600 MHz) stack plot of the reaction of **2** and one equivalent of MA submerged in a -50 ˚C cold bath. From top to bottom: **2**, **2** and MA.

Figure B.24. $^{31}P\{^1H\}$ NMR spectra (toluene-d_8, 243 MHz) stack plot of the reaction of **2** and one equivalent of MA submerged in a -50 ˚C cold bath. From top to bottom: **2**, **2** and MA.
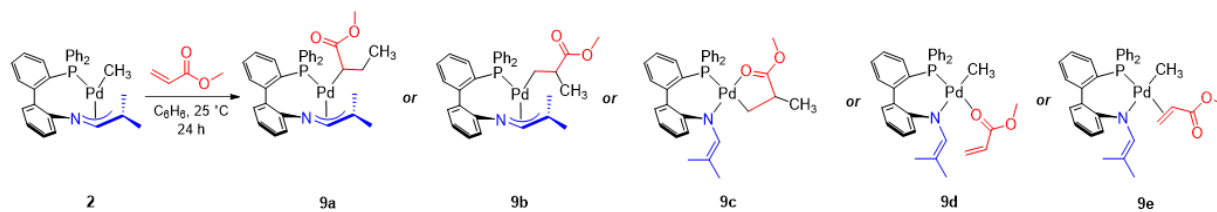
8.3 Appendix C: Supplementary Information for Chapter 4
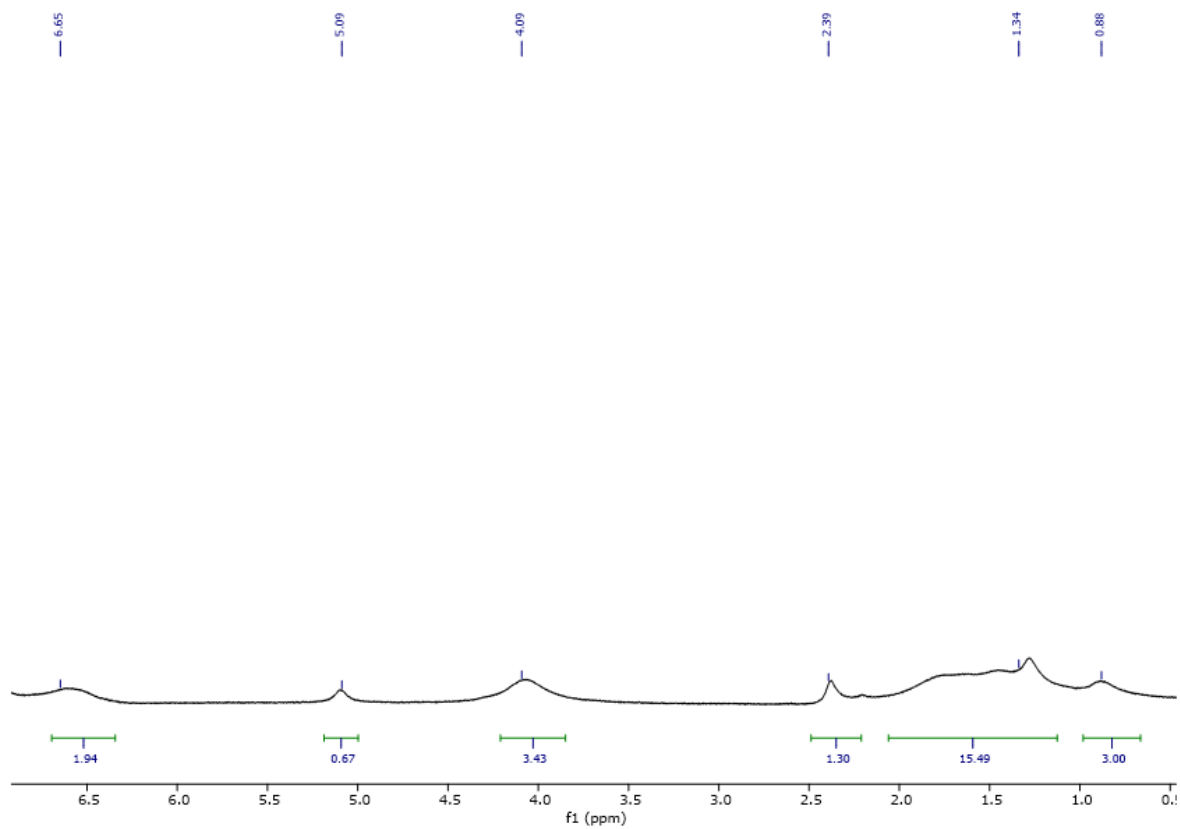
Figure C.1. ¹H NMR spectrum (400 MHz, CDCl₃) of ethylene polymerization control reaction with no catalyst.
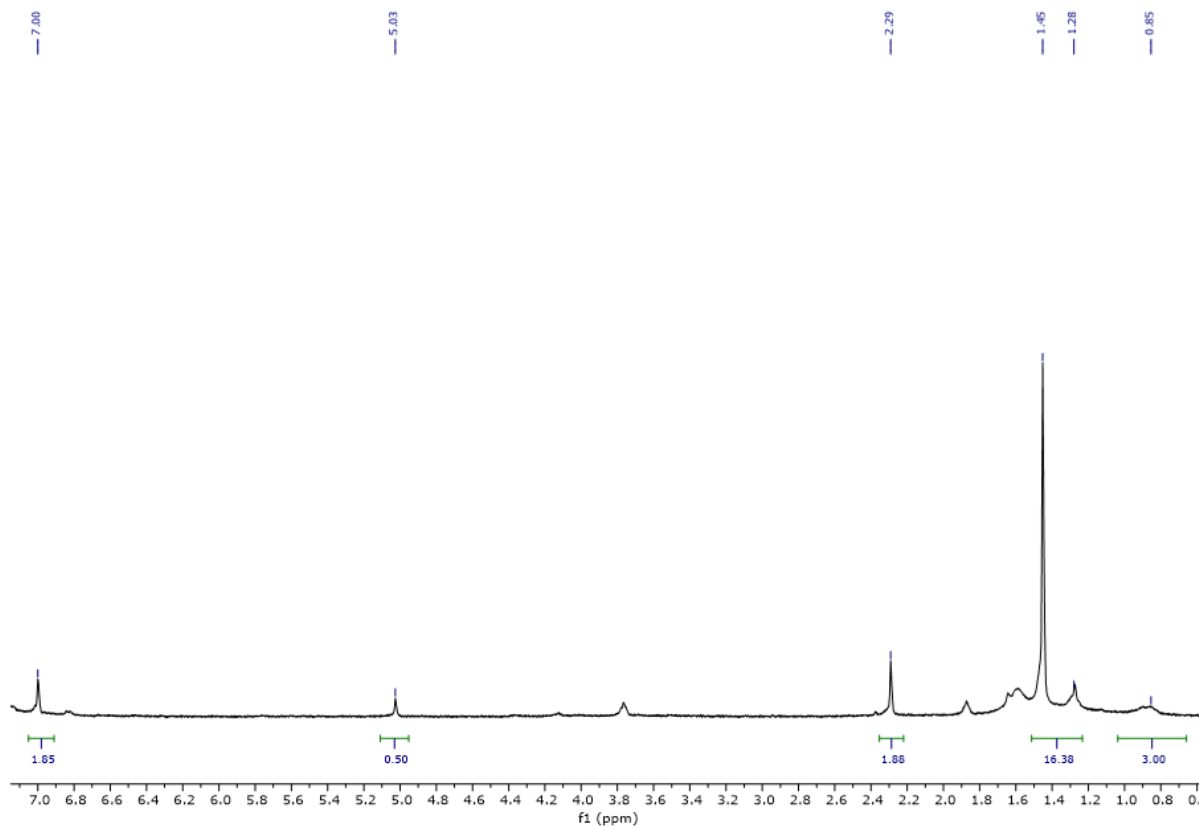
Figure C.2. ^{1}H NMR spectrum (400 MHz, CDCl$_3$) of attempted ethylene polymerization with **2** as a catalyst.
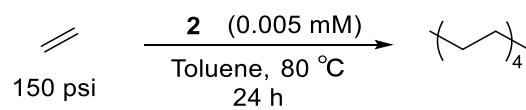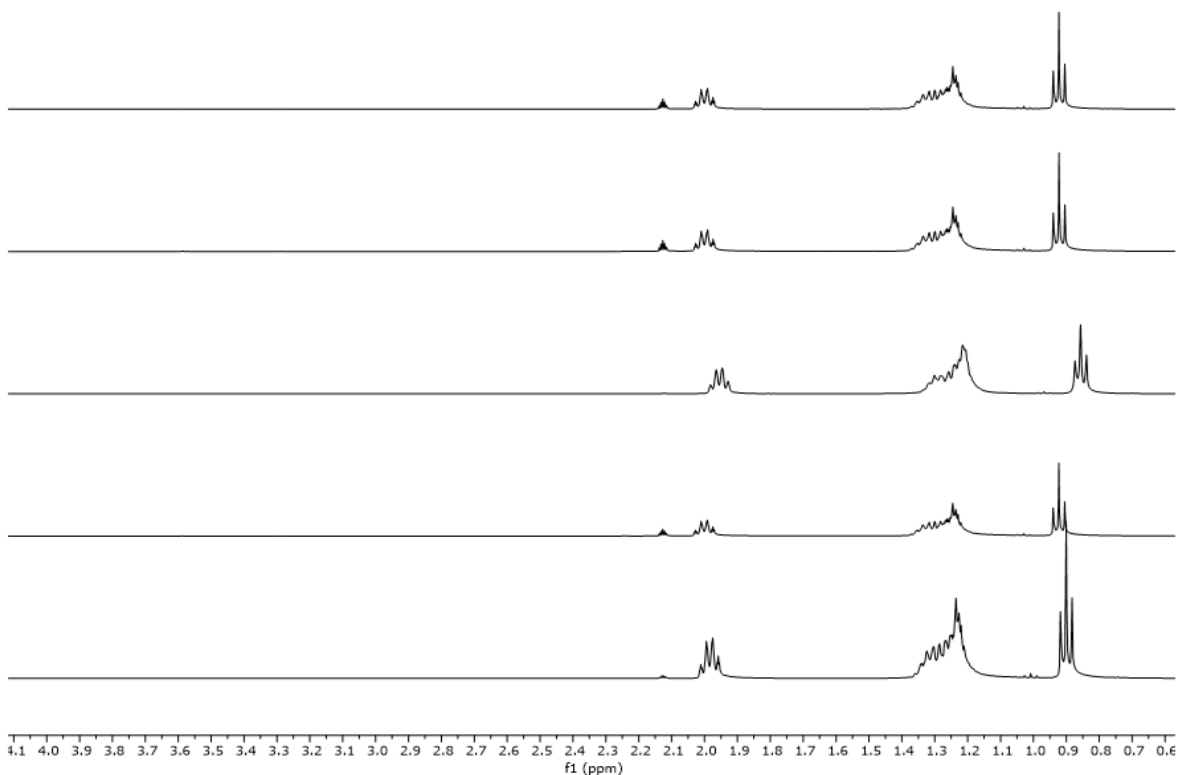
Figure C.3. ^{1}H NMR spectra (600 MHz, toluene-d_8) stack plot of attempted 1-octene oligomerization with

2 as a catalyst. From top to bottom: 1-octene, **2** and one equivalent of 1-octene at room temperature, **2** and

50 equivalents of 1-octene at room temperature, **2** and one equivalent of 1-octene at 80 ˚C, **2** and 50

equivalents of 1-octene at 80 ˚C.
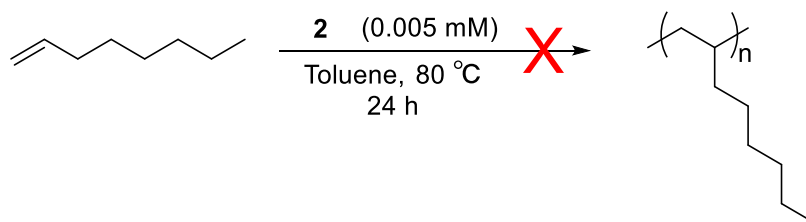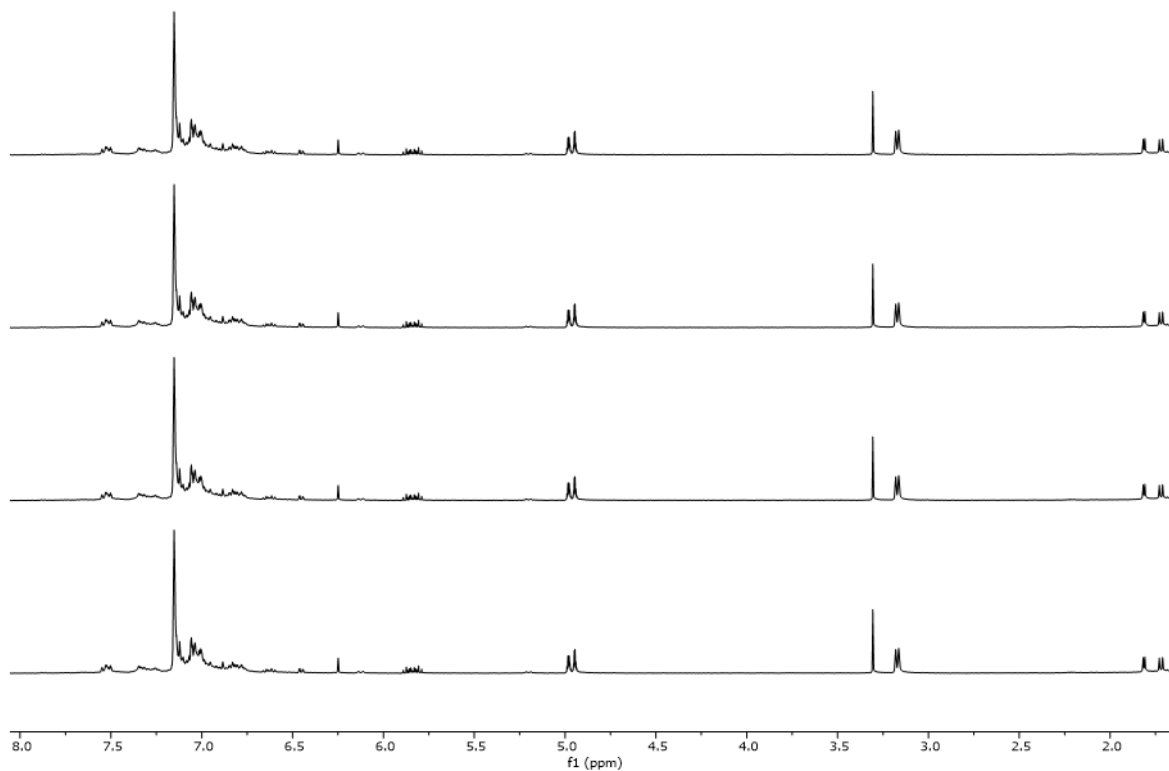
Figure C.4. ¹H NMR spectrum (600 MHz, C₆D₆) of attempted allyl benzene isomerization with **2** as a catalyst. From top to bottom: **2** and allyl benzene 10 minutes at room temperature, **2** and allyl benzene 24 h at room temperature, **2** and allyl benzene 10 minutes at 80 ˚C, **2** and allyl benzene 24 h at 80 ˚C.
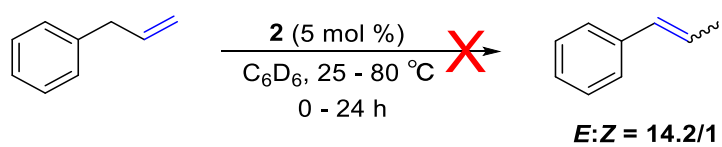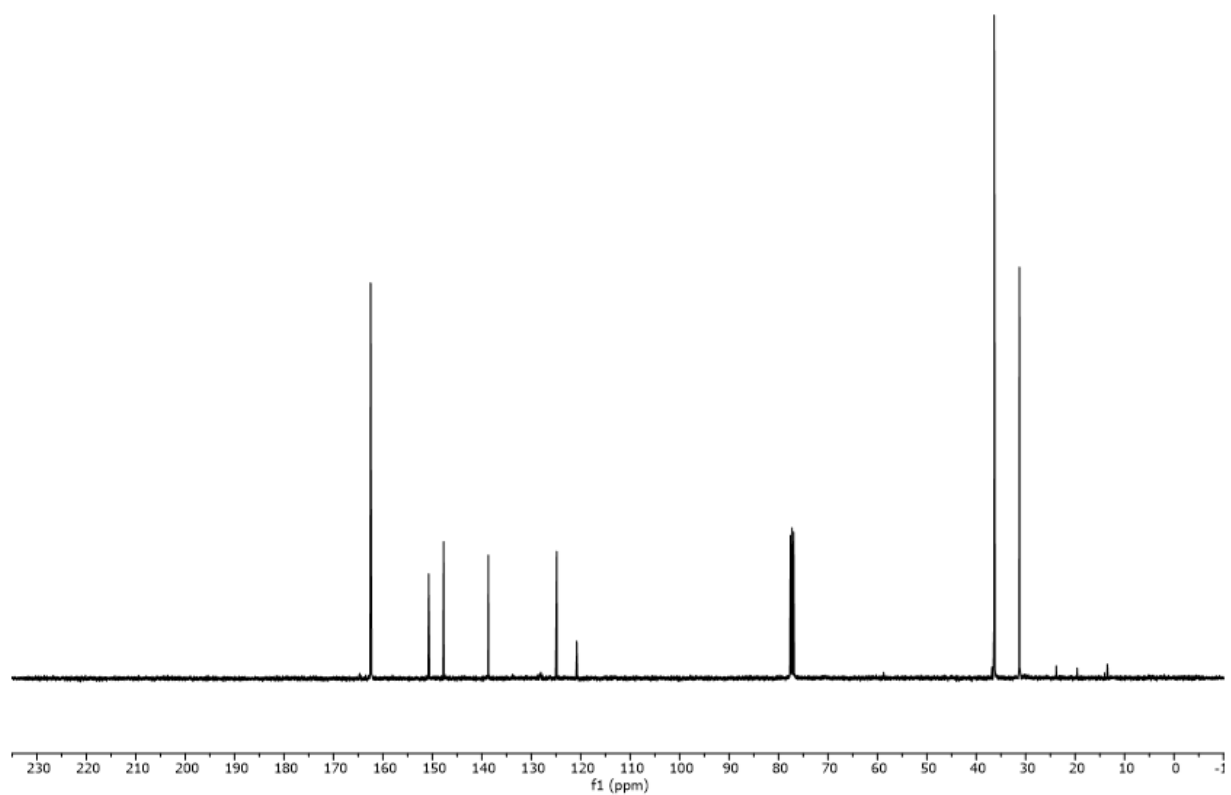
Figure C.5. $^{13}C\{^1H\}$ NMR spectrum (151 MHz, DMF) of attempted cyanation of 3-bromopyridine with **2** as a catalyst at 65 ˚C.
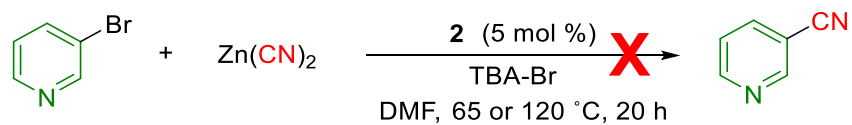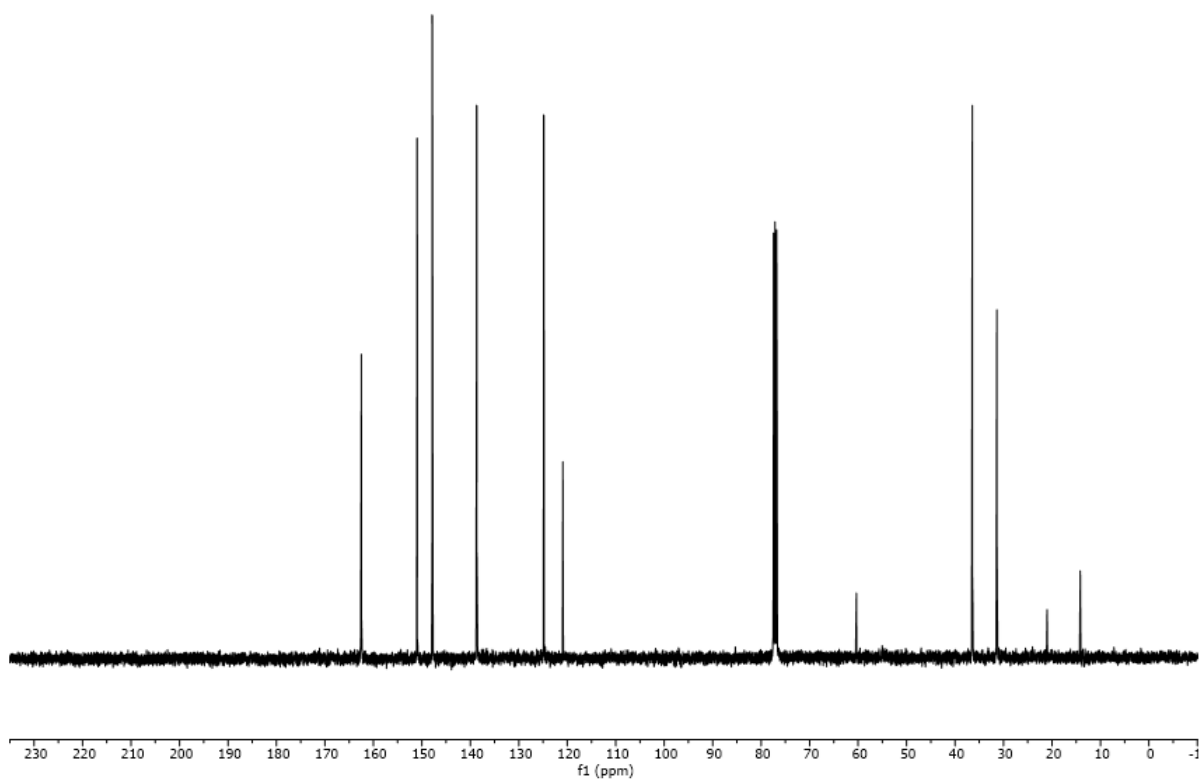
Figure C.6. $^{13}C\{^{1}H\}$ NMR spectrum (151 MHz, DMF) of attempted cyanation of 3-bromopyridine with **2** as a catalyst at 120 ˚C.
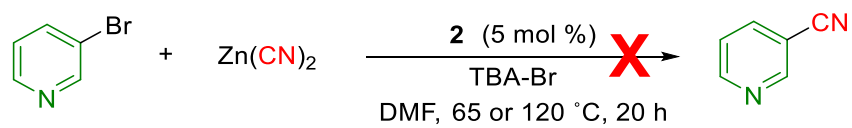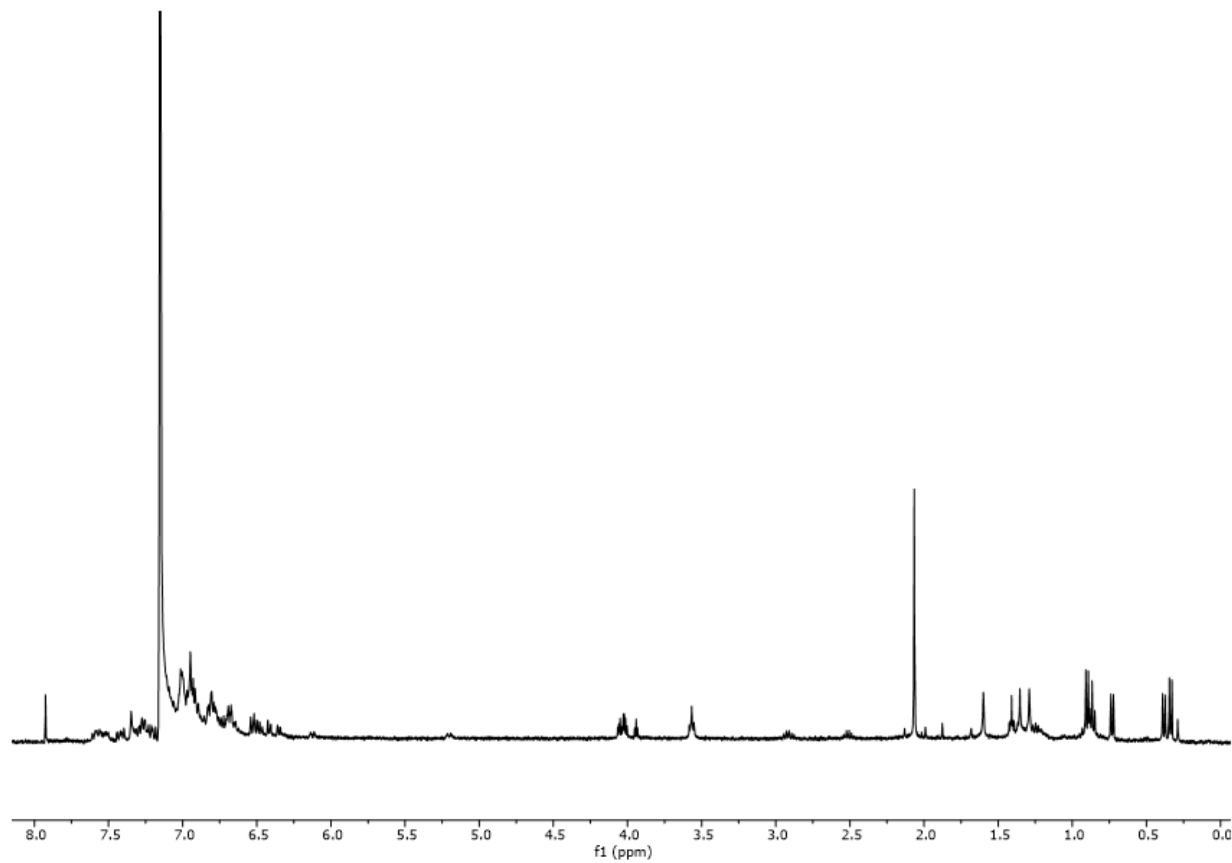
Figure C.7. ^{1}H NMR spectrum (C$_6$D$_6$, 400 MHz) of [Pd(MAH)(**H[L2]a**)], **12a**, and [Pd(MAH)(**H[L2]b**)], **12b**.
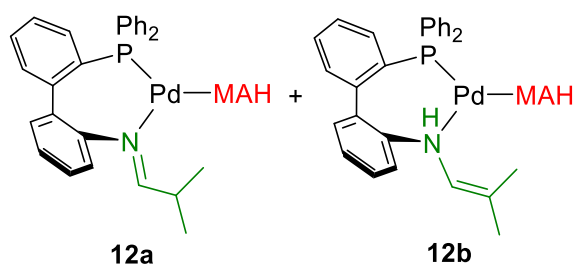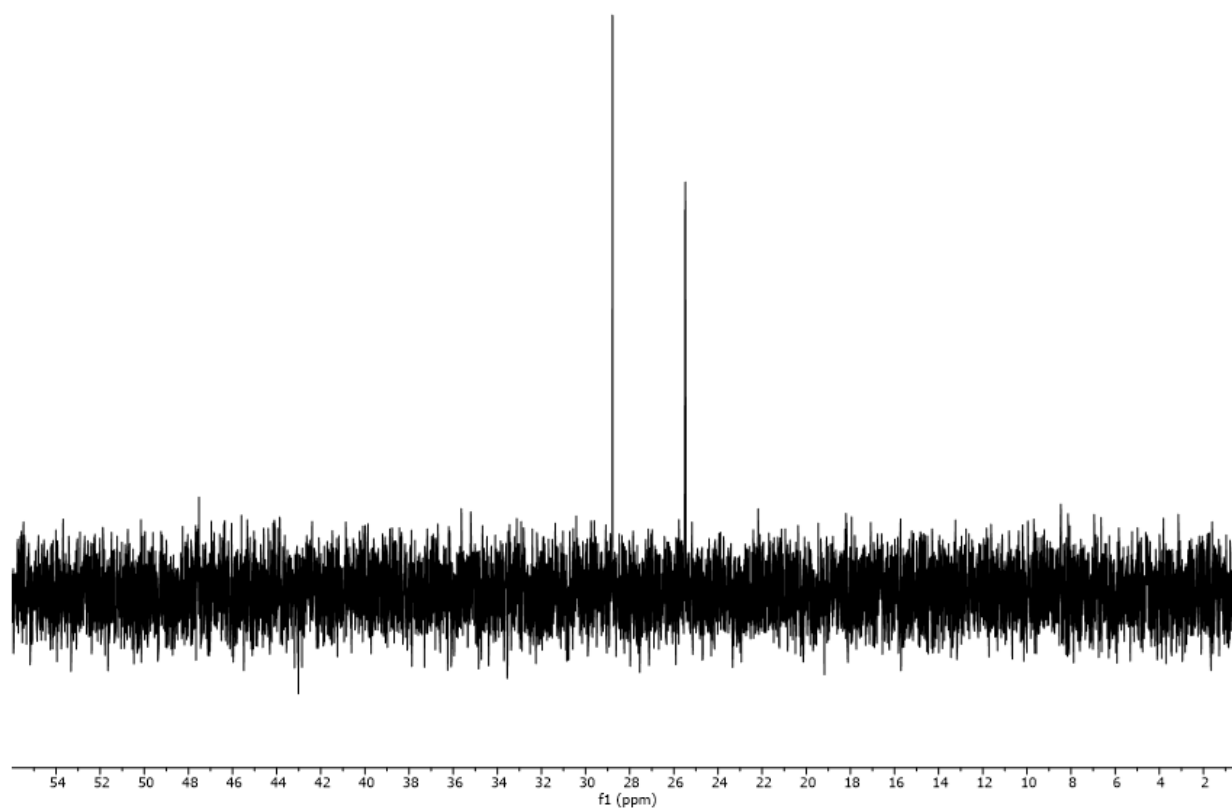
Figure C.8. ^{31}P{^{1}H} NMR spectrum (C$_6$D$_6$, 162 MHz) of [Pd(MAH)(**H[L2]a**)], **12a**, and [Pd(MAH)(**H[L2]b**)], **12b**.

12a   12b
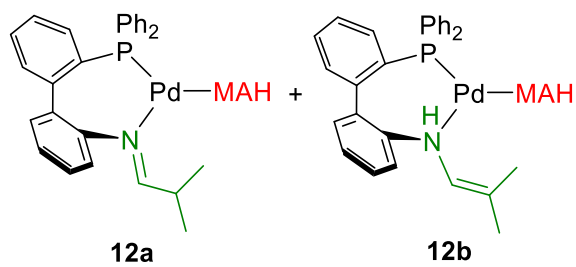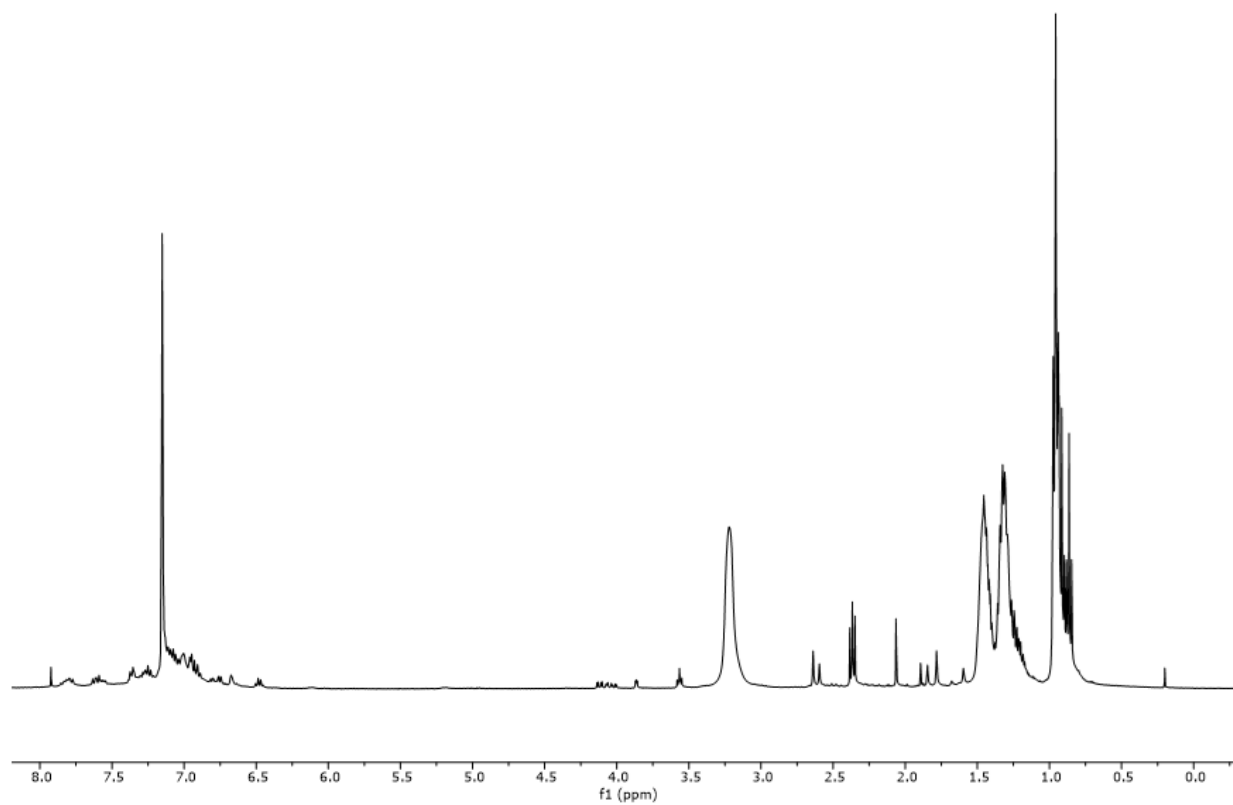
Figure C.9. ^{1}H NMR spectrum (C_6D_6, 400 MHz) of [Pd(MAH)(**[L2]**)], **5**.
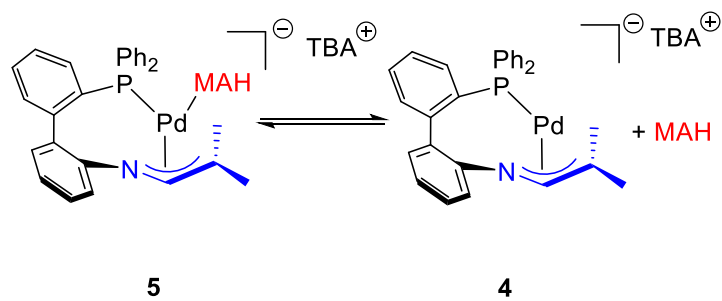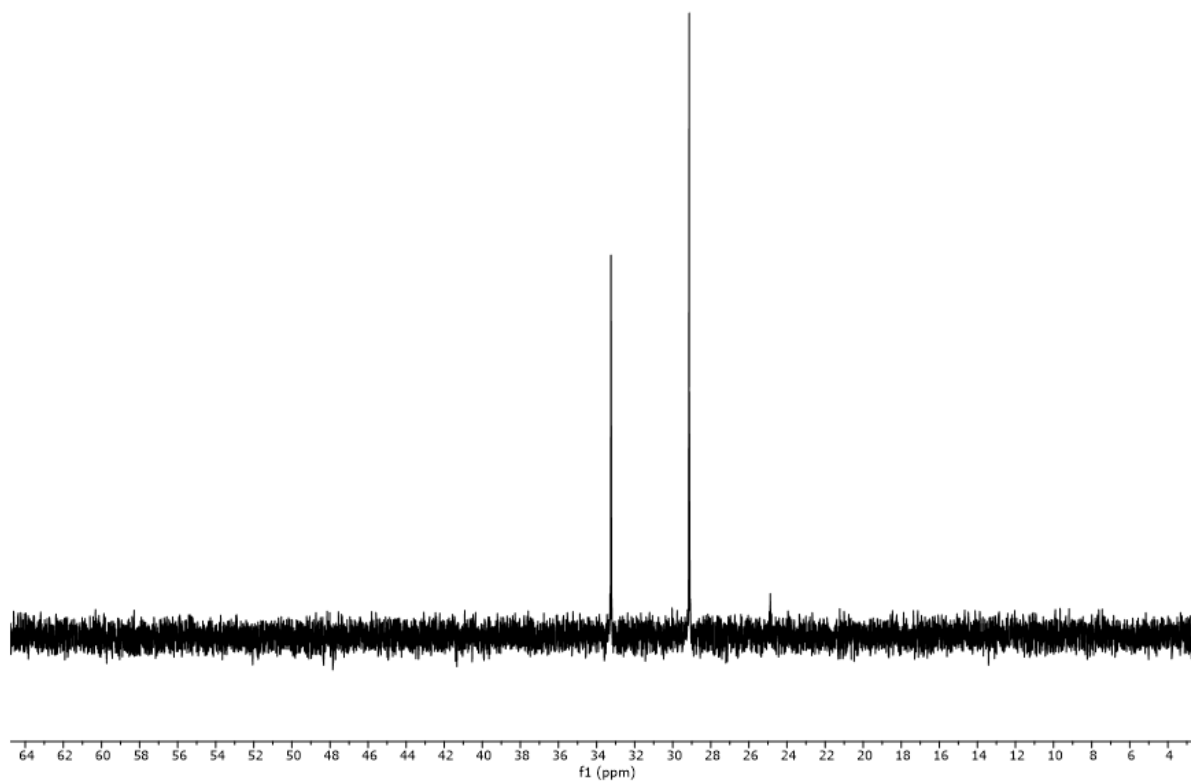
Figure C.10. $^{31}P\{^1H\}$ NMR spectrum (C$_6$D$_6$, 162 MHz) of [Pd(MAH)(**[L2]**)], **5**.
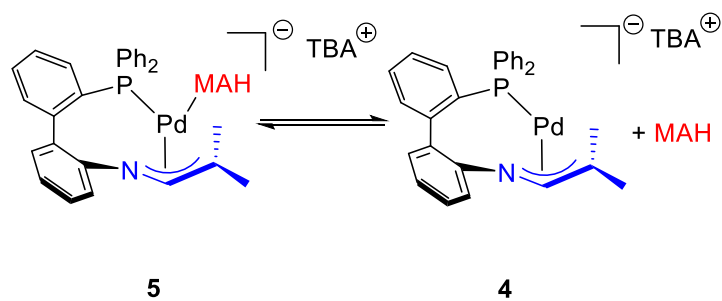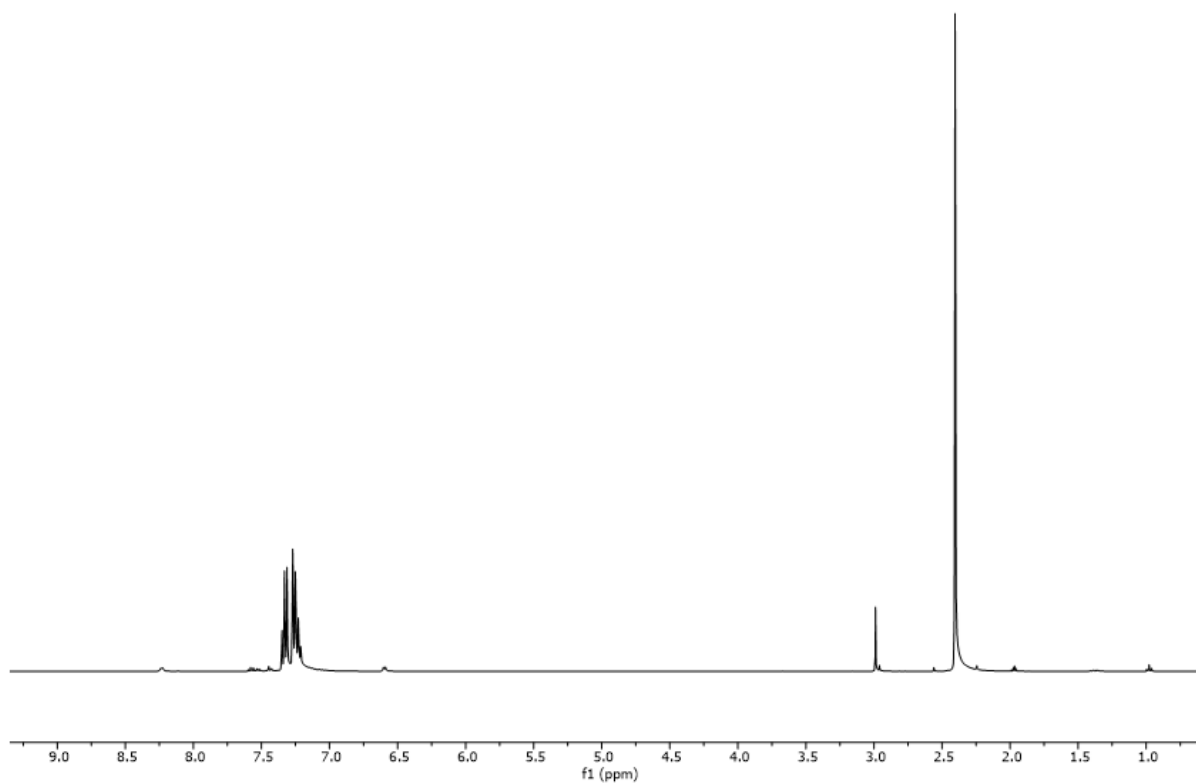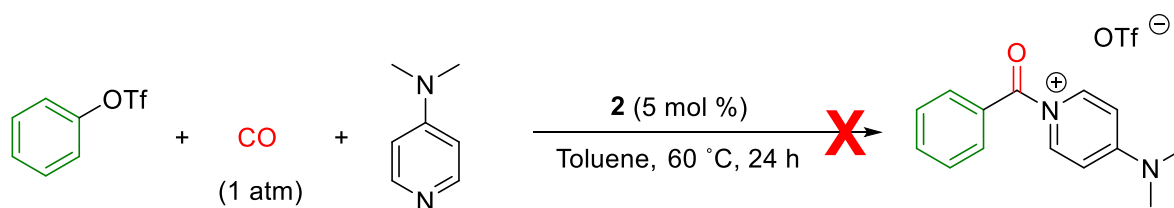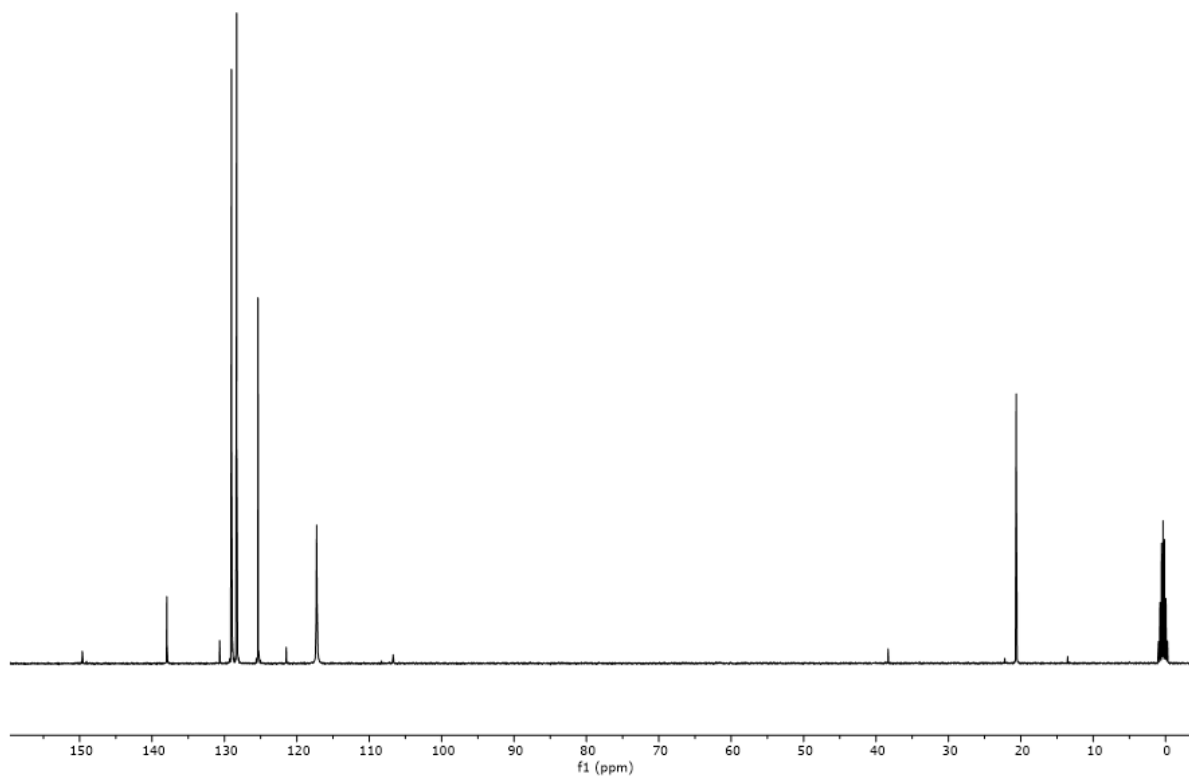
Figure C.11. ^{1}H NMR spectrum (400 MHz, toluene-d_8) of attempted carbonylation of phenyl triflate with **2** as a catalyst at 60 ˚C.
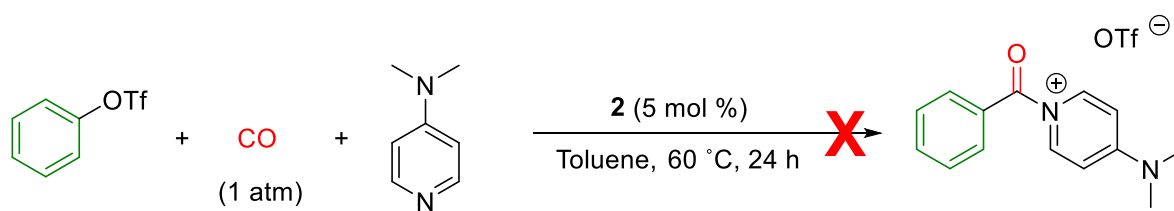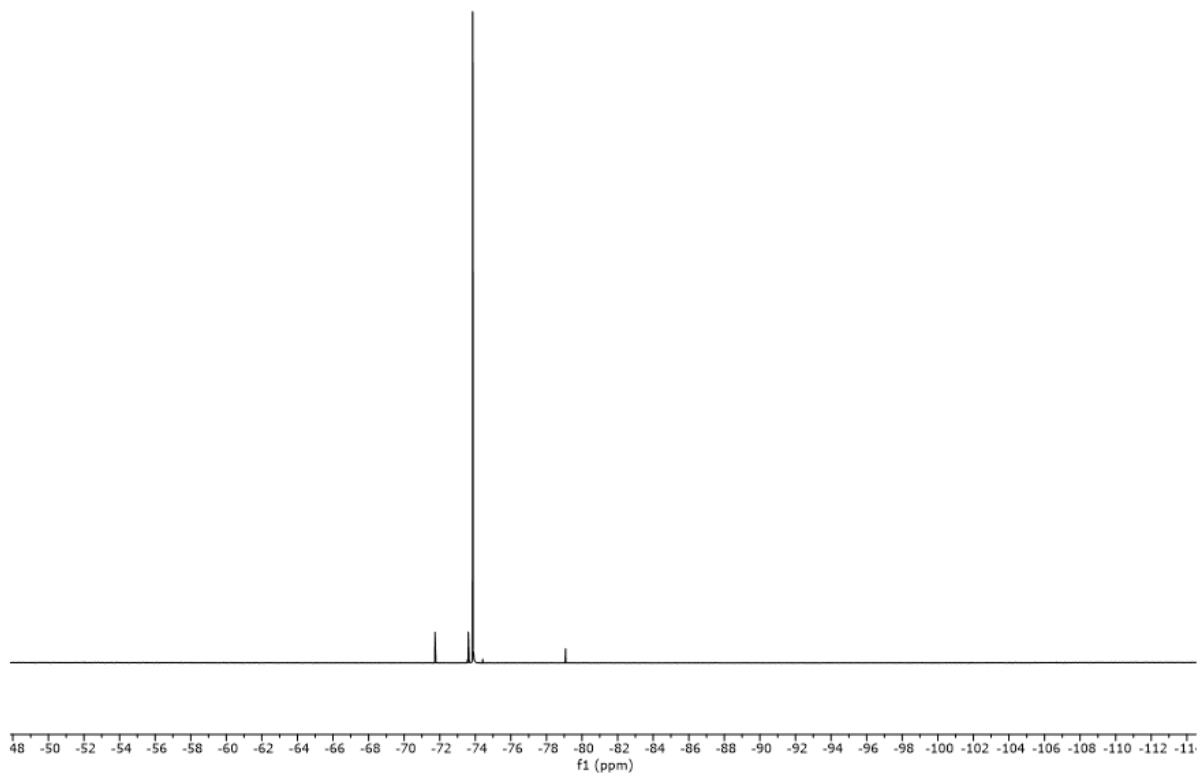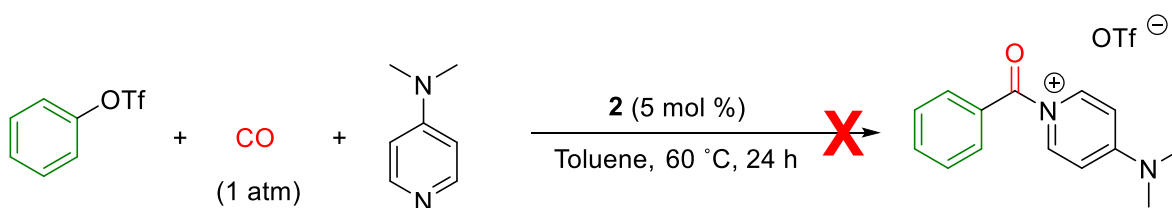
Figure C.12. ^{19}F{^{1}H} NMR spectrum (376 MHz, toluene-d_8) of attempted carbonylation of phenyl triflate with **2** as a catalyst at 60 ˚C.
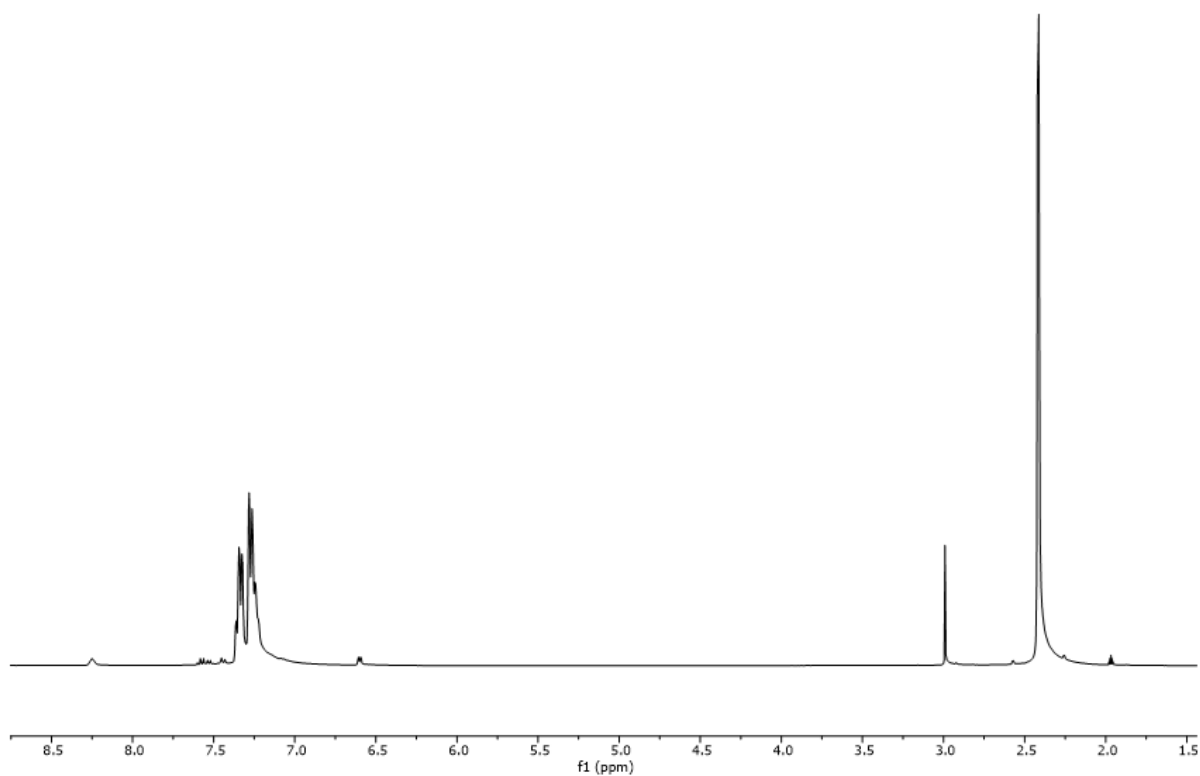
Figure C.13. $^{13}C\{^1H\}$ NMR spectrum (151 MHz, toluene-d_8) of attempted carbonylation of phenyl triflate with **2** as a catalyst at 60 ˚C.

Figure C.14. ^{1}H NMR spectrum (400 MHz, toluene-d_8) of attempted carbonylation of phenyl triflate with

2 as a catalyst at room temperature.

Figure C.15. ^{19}F{^{1}H} NMR spectrum (376 MHz, toluene-d_8) of attempted carbonylation of phenyl triflate with **2** as a catalyst at room temperature.
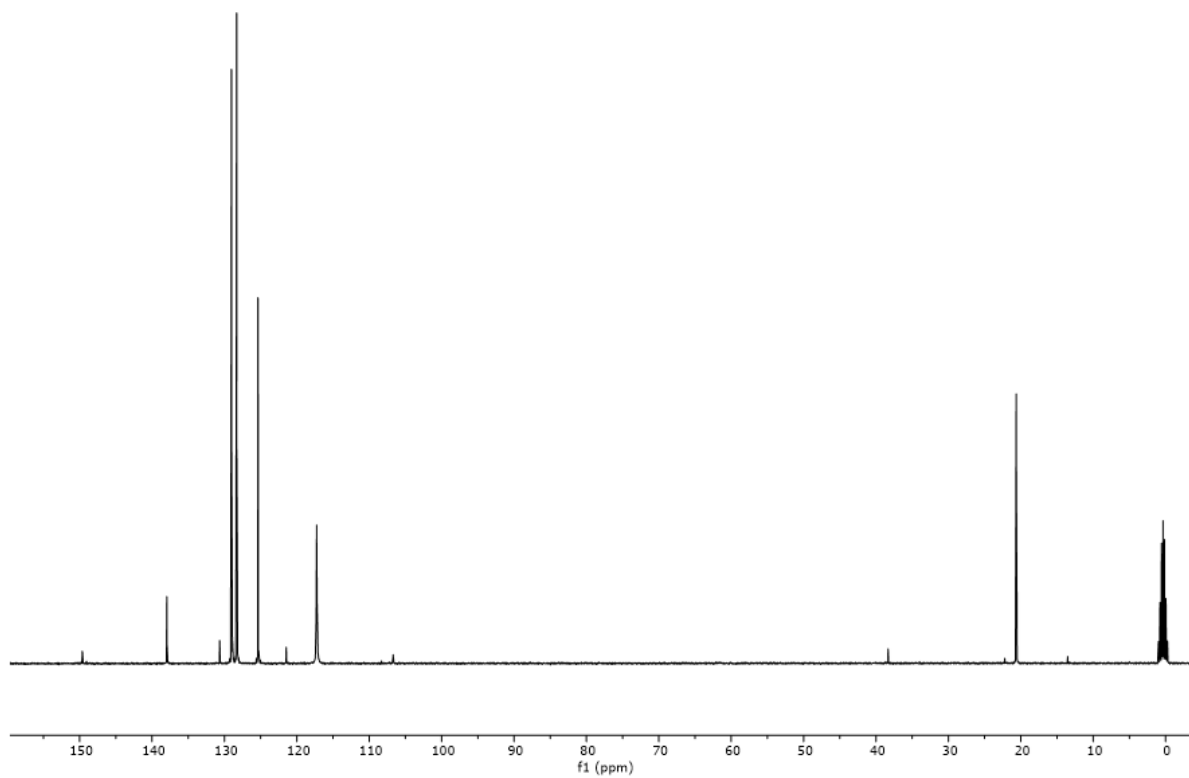
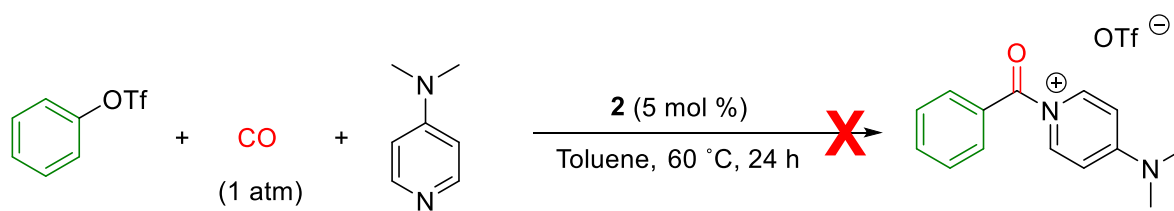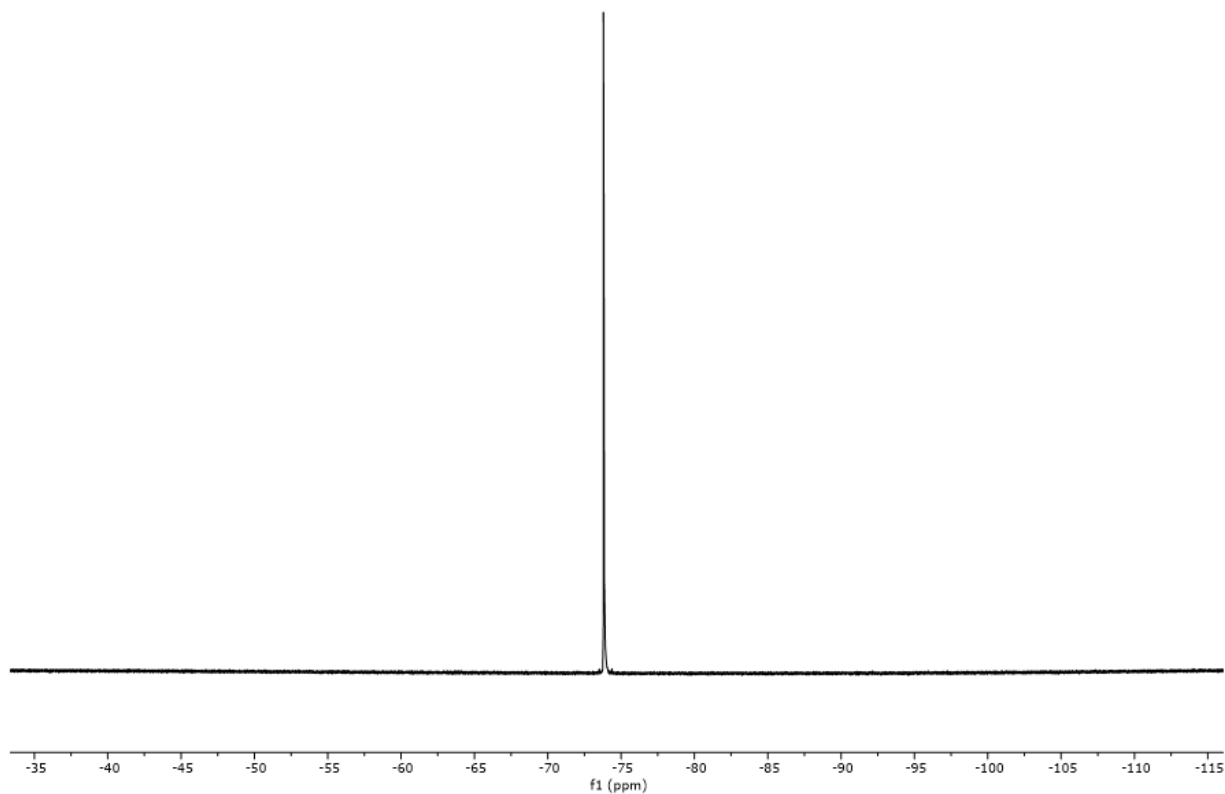**Figure C.16.** ^{13}C{^{1}H} NMR spectrum (151 MHz, toluene-d_8) of attempted carbonylation of phenyl triflate
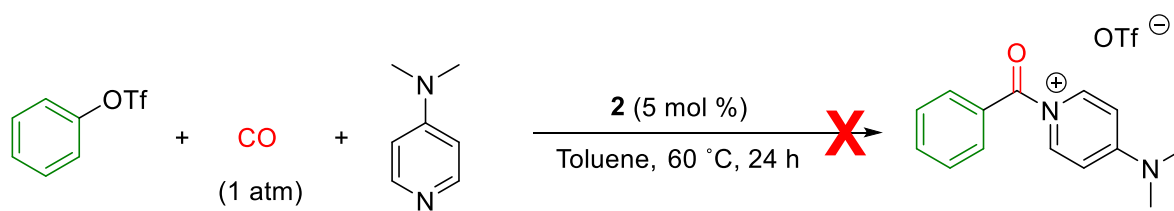
with **2** as a catalyst at room temperature.

Figure C.17. ^{1}H NMR spectrum (400 MHz, toluene-d_8) of attempted carbonylation of *p*-tolyl triflate with **2** as a catalyst at 120 ˚C.

Figure C.18. $^{19}F\{^{1}H\}$ NMR spectrum (376 MHz, toluene-d_8) of attempted carbonylation of *p*-tolyl triflate with **2** as a catalyst at 120 ˚C.

Figure C.19. $^{13}C\{^1H\}$ NMR spectrum (151 MHz, toluene-d_8) of attempted carbonylation of *p*-tolyl triflate with **2** as a catalyst at 120 ˚C.

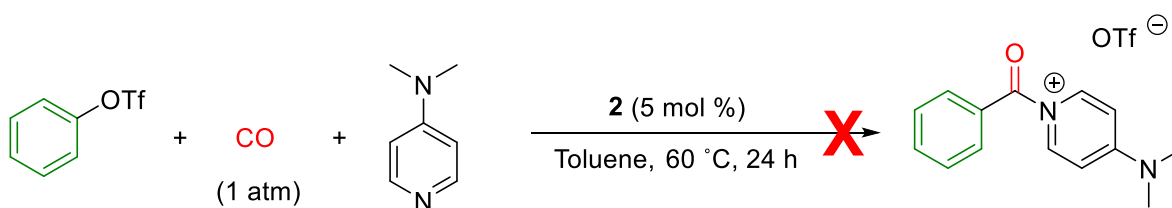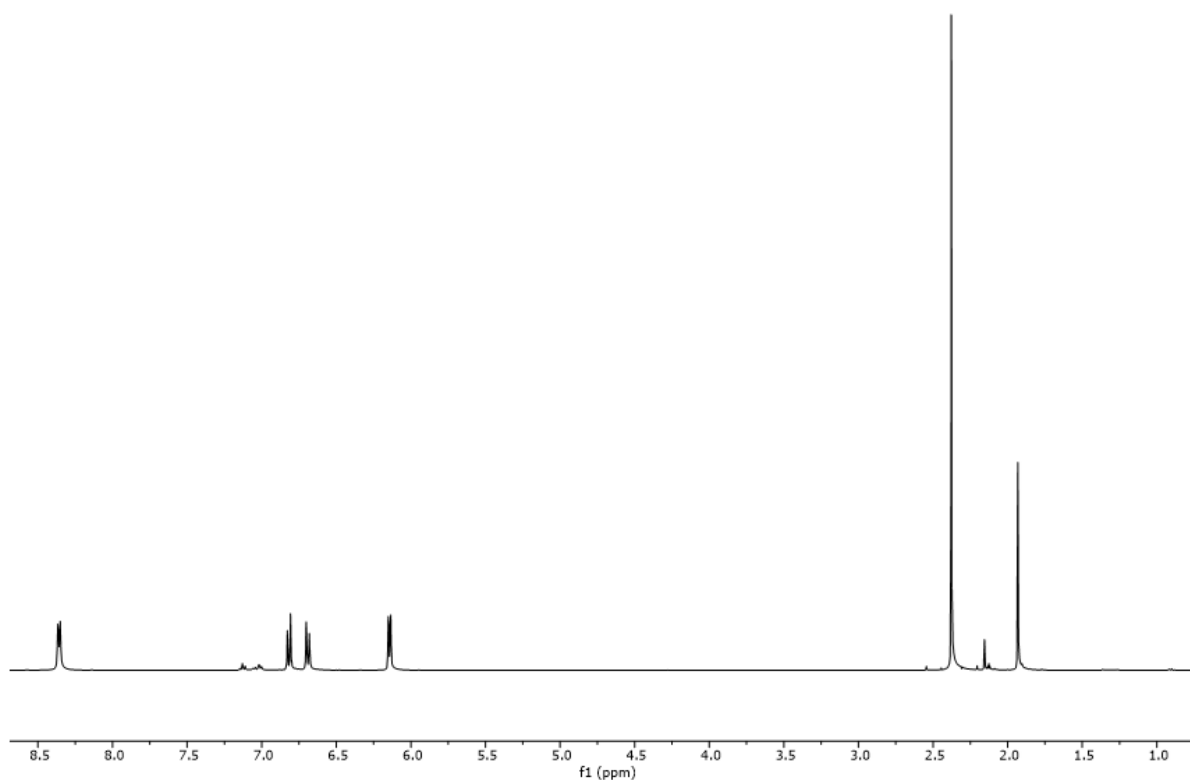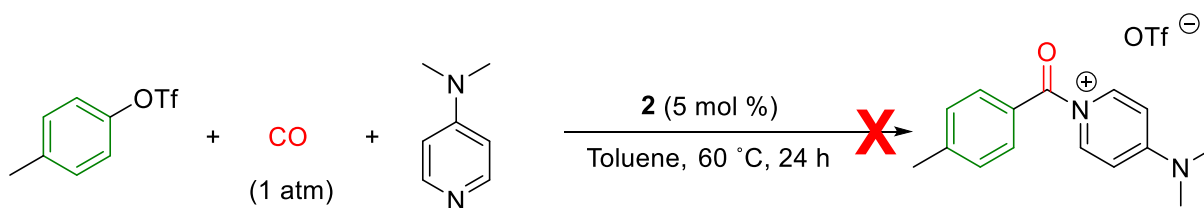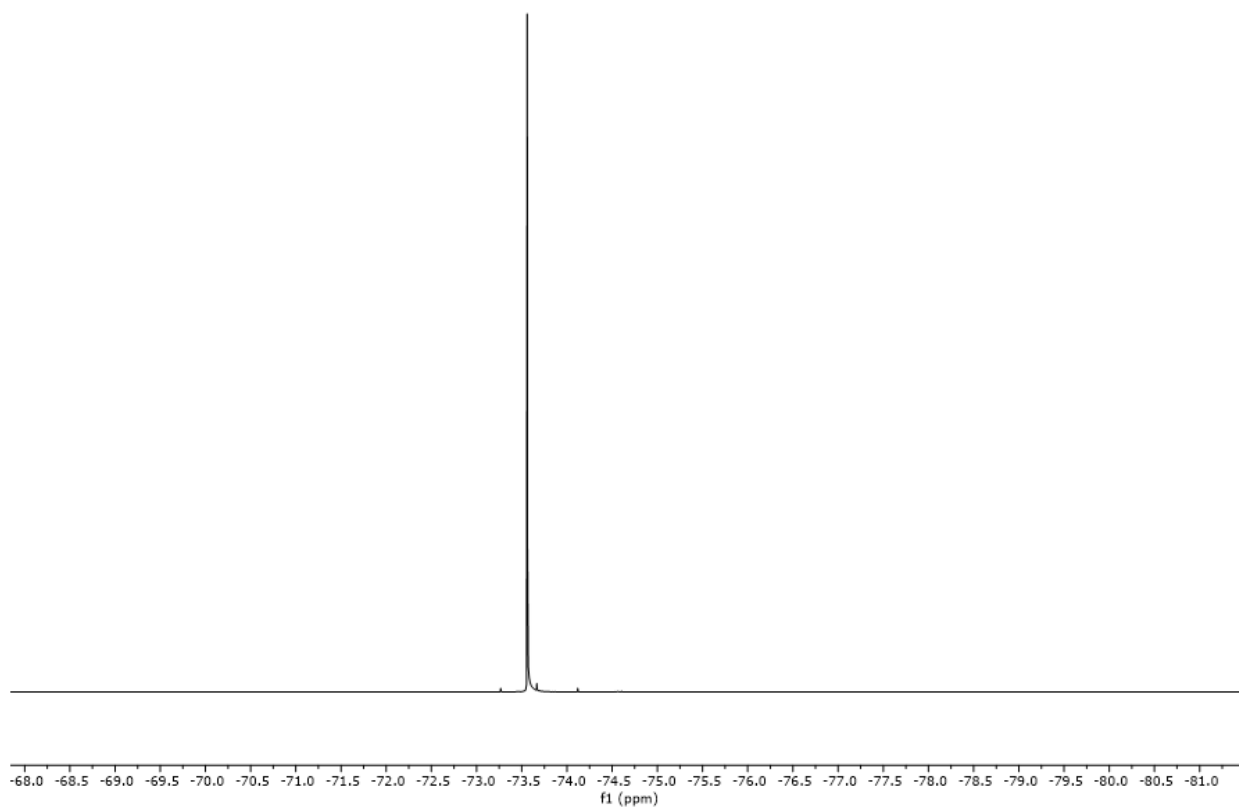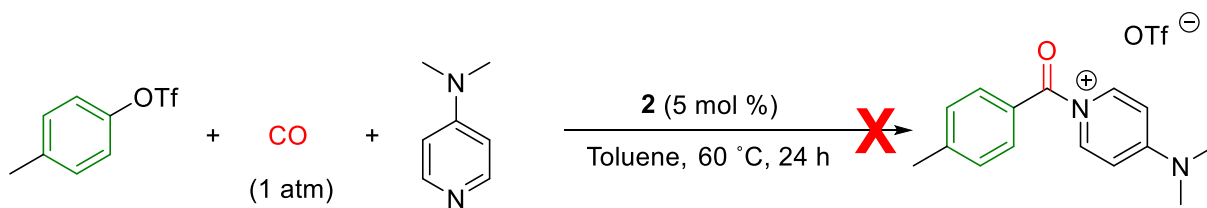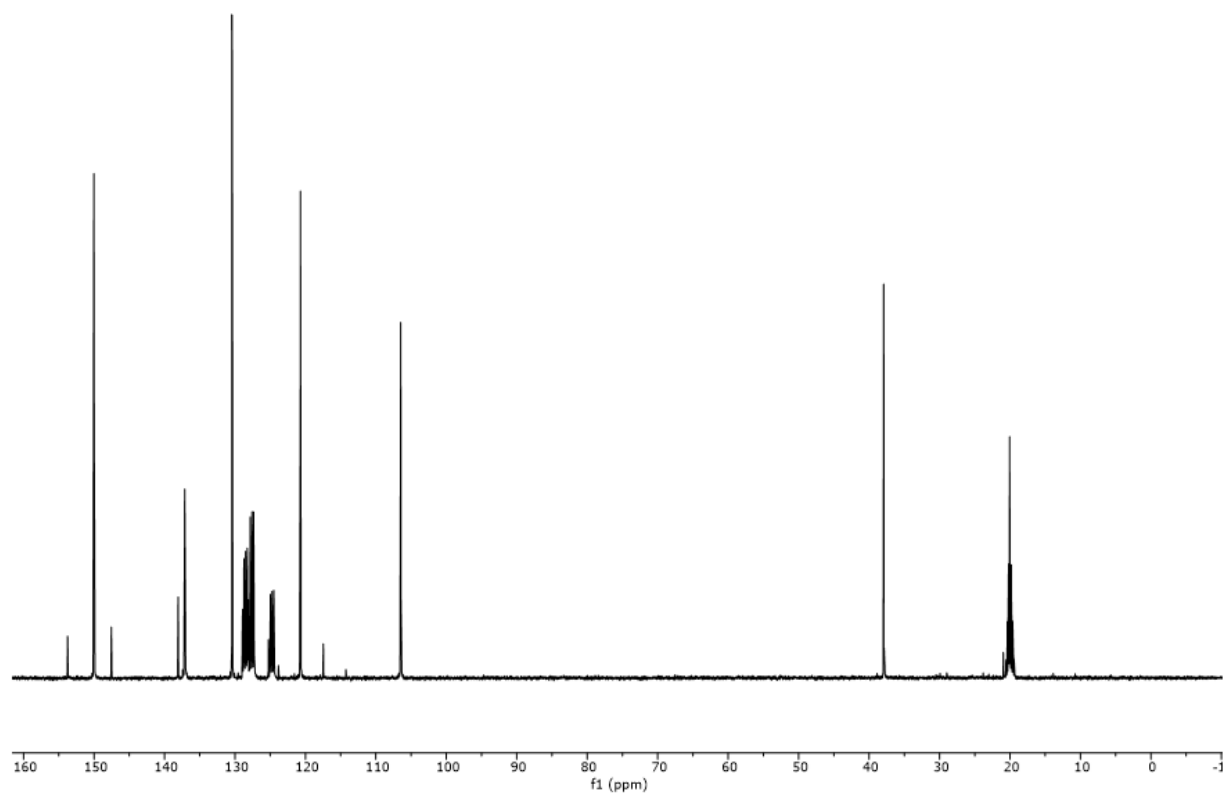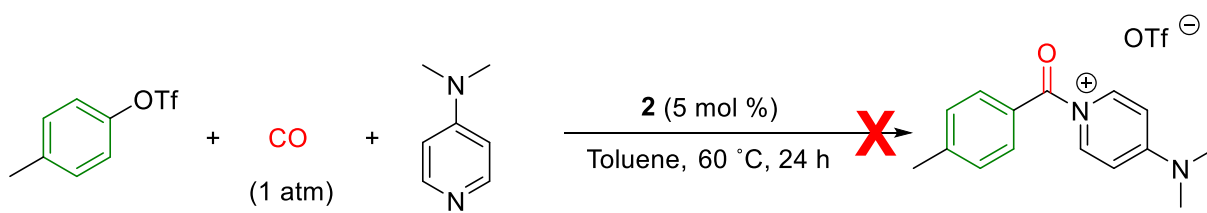**9.0 Curriculum Vitae**

Leslie Kelley

Education

M.Sc. in Chemistry, Western University   **2022– Present**
- Graduate Project: Coordination Chemistry and Reactivity of Biaryl Pd Phosphine 1-Azaallyl Complexes
  - Synthesis of air-sensitive P-N ligands and their coordination modes with group 10 transition metals were analyzed. Characterization techniques include NMR spectroscopy, UV-Vis spectroscopy, IR Spectroscopy, and MALDI. Reactivity with the synthesized complexes towards various Lewis base donors, polar olefin monomers, and CO was investigated and analyzed. Catalytic behaviour with the synthesized complexes towards polymerization, oligomerization, isomerization, cyanation, carbonylation was investigated and analyzed.
- Supervisor: Johanna M. Blacquiere

B.Sc. Honours Specialization in Chemistry, Western University   **2017 – 2022**
- Thesis: Coordination Chemistry of a New Phosphine 1-Azaallyl Ligand
  - An air-sensitive P-N ligand was synthesized using standard Schlenk techniques and coordinated to a monoalkyl Pd(II) precursor in a glovebox. The complex and ligand were characterized by NMR spectroscopy. Homopolymerization of ethylene was attempted with this complex in a Parr reactor.
- Supervisor: Johanna M. Blacquiere

Publications

1. Kindervater, M. B.; Staroverov, V. N.; Jackman, K. M. K.; Fogh, A. A.; Kelley, L. S. G.; Lim, L.; Sirohey, S. A.; Boyle, P. D.; Blacquiere, J. M. Operationally Unsaturated Ruthenium Complex Stabilized by a Phosphine 1-Azaallyl Ligand. *Dalton Trans.* **2023**, *52*, 10744 – 10750.
2. Kelley, L. S. G.; Jackman, K. M. K.; Staroverov, V. N.; Sham, T. K.: Blacquiere, J. M. Coordination Chemistry and Reactivity of Biaryl Pd Phosphine 1-Azaallyl Complexes. *Manuscript in progress*.

Presentations (OP = Oral, PP = Poster)

1. OP: <u>Leslie S.G. Kelley</u>, Kyle M.K. Jackman, and Johanna M. Blacquiere* 'Coordination Chemistry and Reactivity with a Palladium Phosphine 1-Azaallyl Complex.' *Inorganic Discussion Weekend*, Windsor, ON, November 2023.

Awards and Scholarships

- Purple Blanket Award   **2024**
- Championship Legacy Award   **2024**
- John P. Metras Bursaries   **2024**
- Station Park All Suite Hotel 125th Anniversary Alumni Athletic Award   **2024**
- Elizabeth Matthews Memorial Award   **2024**
- London Ontario Winter/Summer Games Legacy Award   **2019**

- Four Year Continuing Admission Scholarship **2017**

Mentoring / Teaching

Graduate Student Mentor **2022– Present**
- Primary in lab mentor for Inorganic Chemistry Exchange and NSERC USRA student Omar Castro-Sandoval and WUSRI student Bradley Cooper.
- Provided additional secondary support and assistance to 4491 students and undergraduate volunteers.
- Offered technical assistance and trained new students in laboratory techniques.

Laboratory and Marking Teaching Assistant **2022– Present**
- Chemistry 2283G – Organic Chemistry II: Mechanisms and Reactivity **Winter 2024**
- Chemistry 2211A – Inorganic Elements in Life **Fall 2023**
- Chemistry 2213A – Organic Chemistry for Life Sciences **Fall 2023**
- Chemistry 2223B – Organic Chemistry for Biological Molecules **Winter 2023**
- Chemistry 2213A – Organic Chemistry for Life Sciences **Fall 2022**

Outreach Program Volunteer **2022– Present**
- Assisted in the operation of experiments for groups of 25 – 30 high school students at Western University.

Extracurricular Activities

Member of the Western Women's Rowing Team **2017– Present**
- Women's Coxed Eight National Champions 2019
- Women's Team Provincial Champions in 2018, 2019, 2021, 2022, 2023
- Canadian University Rowing Championship All-Star 2019
- Ontario University Athletics All-Star 2019, 2021, 2022, 2023
- Women's Team Captain 2023, Summer Captain 2021, 2022, 2023
- Purple Blanket Award

Assistant Coach / Performance Analyst Western Women's Basketball Team **2017– Present**
- Assistant to the head coach at practices and games.
- Collected and analyzed statistics from practices and games, prepared statistics reports for players.
- Managed a group of student statisticians.
- Filmed practice and games for team video sessions.

Member of the Western Student Athlete Mental Health Initiative (SAMHI) **2018 – 2020**
- Focused on eliminating the stigma surrounding mental health in sports by spreading awareness, educating, and connecting athletes to Western University campus resources.